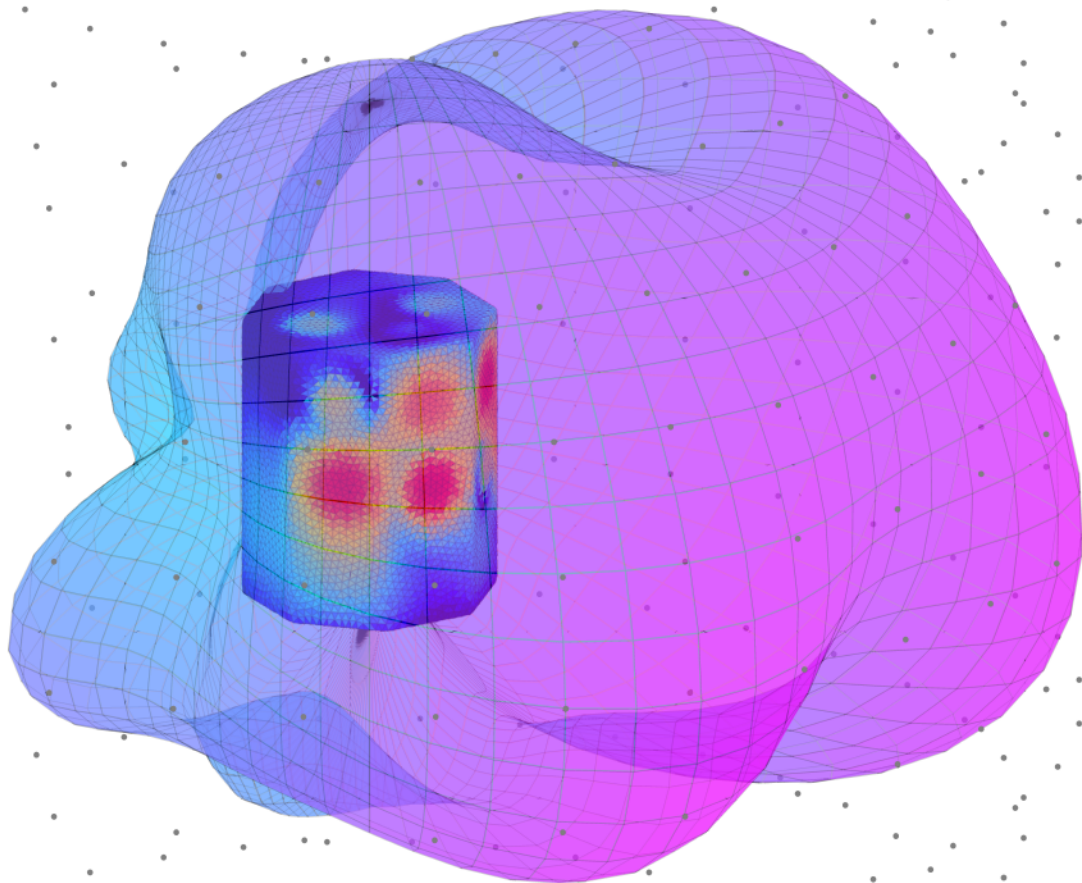


# Compact Loudspeaker Array for Synthesizing the Radiation Pattern of an Acoustic Guitar



Andrea D'Onofrio  
Rasmus Bo Bertelsen  
Tim Hede Stenholt Jensen  
Aalborg University  
2021-06-03



AALBORG  
UNIVERSITY



**AALBORG UNIVERSITY**  
DENMARK

**Signal Processing and Acoustics**  
Aalborg University  
<http://www.aau.dk>

**Title:**

Compact Loudspeaker Array for Synthesizing the Radiation Pattern of an Acoustic Guitar

**Theme:**

Signal Processing and Acoustics

**Project Period:**

Spring Semester 2021

**Project Group:**

Group 1071

**Participant(s):**

Andrea D'Onofrio  
Rasmus Bo Bertelsen  
Tim Hede Stenholt Jensen

**Supervisor(s):**

Flemming Christensen

**Copies:** 1

**Number of Pages**

(including appendices): 197

**Date of Completion:**

June 2, 2021

**Abstract:**

Acoustic guitarists performing for medium to large audiences often need amplification of their guitar in order for the audience to be able to hear the performance. Unfortunately, this amplification is generally provided by traditional guitar amps/loudspeakers, which often results in a different spatial sound impression due to the different sound radiation pattern of the loudspeaker compared to the actual guitar.

This project aims to investigate methods for synthesizing the radiation pattern of an acoustic guitar with a compact loudspeaker array. Based on acoustic measurements of the radiation pattern of a guitar and numerical simulations of different loudspeaker arrays, a prototype with 20 loudspeakers is designed to specifically recreate this radiation pattern.

Methods for designing optimal FIR filters for recreating the directional magnitude response of the guitar are also investigated. These filters are implemented using both all 20 loudspeakers as well as 12 selected loudspeakers on the array.

The performance of the loudspeaker array is tested objectively by measurement of the loudspeaker array radiation pattern, which afterward is compared to the measured guitar radiation pattern. Results show that the loudspeaker array is able to synthesize the desired guitar radiation pattern very well up to around 2 kHz, but a rough approximation of the guitar radiation pattern is still seen at higher frequencies.

Using only 12 loudspeakers resulted in a slightly reduced performance in an objective sense, but the question of how similar a synthesized radiation pattern needs to be in order to perceptually recreate the spatial sound impression of a guitar remains to be fully revealed.

# Preface

---

This report presents the master thesis of the authors during the 10th semester of their Master's programme in Signal Processing and Acoustics at Aalborg University in the spring of 2021.

References are given in IEEE style with square brackets like [0] in the order of appearance, and the bibliography can be found on page 107. A glossary of project-specific terms can be found on page 112. Associated appendices relevant for the main report can be found from page 115. Throughout the report, magnitude responses are plotted with a 50 dB/decade aspect ratio unless otherwise stated.

Vectors are given as bold lowercase numbers, like **a**, and matrices are given as bold uppercase letters, like **B**.

Many of the results from this work are visualized using color-coded figures, it is therefore recommended that any print-out of this thesis is printed in color.

Various files and scripts can be found bundled with this thesis in the archive `File_Submission_GR1071.zip`.

The authors would like to thank Flemming Christensen for supervision throughout the project as well as Jesper Lumbye Andersen and Knud Bank Christensen at MUSIC Tribe for good discussions and their valuable feedback and inputs throughout the project.

The authors also owe a huge thank you to Claus Vestergaard Skipper and Kenneth Knirke for their help with prototype construction and equipment throughout the project, especially Claus for his valued help with different measuring setups.

Lastly, the authors would like to thank our friends and families for their continued support throughout the authors' university studies.

Aalborg University, June 2, 2021

---

Andrea D'Onofrio  
<adonof19@student.aau.dk>

---

Rasmus Bo Bertelsen  
<rberte15@student.aau.dk>

---

Tim Hede Stenholt Jensen  
<thsj19@student.aau.dk>

# Contents

---

<b>Preface</b>	<b>iii</b>
<b>1 Introduction</b>	<b>1</b>
1.1 Scope of the Project . . . . .	1
<b>2 Background Theory</b>	<b>3</b>
2.1 The Acoustic Guitar . . . . .	3
2.2 The Electro-dynamic Loudspeaker . . . . .	6
2.3 Radiation Patterns . . . . .	7
2.4 Spatial Aliasing . . . . .	11
2.5 Summary of Previous Research . . . . .	12
<b>3 Delimitation and Specification of the Project</b>	<b>18</b>
<b>4 Measurements of the Directivity Pattern of an Acoustic Guitar</b>	<b>20</b>
4.1 Initial 2D Measurement in an Anechoic Chamber . . . . .	20
4.2 Spherical 3D Measurement in an Anechoic Chamber . . . . .	28
<b>5 Simulations of Compact Loudspeaker Arrays</b>	<b>35</b>
5.1 Model of a Compact Loudspeaker Array . . . . .	35
5.2 The Boundary Element Method . . . . .	36
5.3 Optimal Piston Velocities via BEM Simulations . . . . .	40
5.4 Summary of Simulation Results . . . . .	46
<b>6 Design of Filters</b>	<b>53</b>
6.1 Least-Squares Multichannel Inversion . . . . .	53
6.2 The Fast Deconvolution Algorithm . . . . .	56
6.3 The Iterative Magnitude Fast Deconvolution Algorithm . . . . .	57
6.4 Target Response Filter . . . . .	58
6.5 Solution on Logarithmic Frequency Grid and Complex Interpolation . . . . .	59
<b>7 Design of the Loudspeaker Array</b>	<b>63</b>
7.1 Physical Design Constraints . . . . .	63
7.2 Strategies for Intelligent Loudspeaker Placement on the Array . . . . .	66
7.3 Description of Prototype Loudspeaker Array . . . . .	70
7.4 Measurement of the Prototype Transfer Functions . . . . .	73
<b>8 Performance of the Loudspeaker Array</b>	<b>75</b>
8.1 Description of Measurements . . . . .	75
8.2 Loudspeaker Sonograms . . . . .	76
8.3 Loudspeaker Balloon-style Directivity Plots . . . . .	78
8.4 Weighted MSE . . . . .	84
8.5 Frequency and Time Response . . . . .	86
8.6 Results with a Reduced Number of Loudspeaker Driver Units . . . . .	88

<b>9 Discussion</b>	<b>95</b>
9.1 Uncertainties from the Measurement Setup . . . . .	95
9.2 Measured Guitar Radiation as Target Function . . . . .	96
9.3 The use of BEM - Simulations . . . . .	97
9.4 On the Prototype Loudspeaker Array . . . . .	99
9.5 On the Different Filter Design Algorithms . . . . .	100
9.6 Perceptual Considerations . . . . .	101
<b>10 Conclusion</b>	<b>103</b>
<b>11 Future Work</b>	<b>104</b>
11.1 Multi-way System . . . . .	104
11.2 Real Time Filter Implementation Issues . . . . .	104
11.3 Synthesis of Other Instruments . . . . .	105
11.4 Listening Tests . . . . .	106
<b>Bibliography</b>	<b>107</b>
<b>Glossary</b>	<b>112</b>
<b>A Loudspeaker Model</b>	<b>115</b>
A.1 Loudspeaker Model . . . . .	115
<b>B 2D Guitar Measurement Description</b>	<b>119</b>
B.1 Equipment List . . . . .	119
B.2 Setup . . . . .	119
B.3 Procedure . . . . .	121
B.4 Polar Plots Results . . . . .	123
<b>C 3D Guitar Measurement Description</b>	<b>130</b>
C.1 Equipment List . . . . .	130
C.2 Setup . . . . .	130
C.3 Procedure . . . . .	133
C.4 Balloon-style Directivity Plots Results . . . . .	135
<b>D Comparison of Optimization Methods with Simulations</b>	<b>140</b>
D.1 Simulation Parameters . . . . .	140
D.2 Results . . . . .	141
D.3 Discussion . . . . .	152
<b>E Effect of the Number of Speakers on Radiation Synthesis Performance</b>	<b>153</b>
E.1 Simulation Parameters . . . . .	153
E.2 Results . . . . .	154
E.3 Discussion . . . . .	160
<b>F Simulation of the Effect of the Shape of the Enclosure</b>	<b>162</b>
F.1 Simulation Parameters . . . . .	162
F.2 Results . . . . .	163
<b>G Simulation of the Effect of the Enclosure Size on Radiation Synthesis Performance</b>	<b>167</b>
G.1 Simulation Parameters . . . . .	167

G.2 Results . . . . . 168

**H Simulations of Different Placement Strategies on Octagonal Prism 169**

H.1 Simulation Parameters . . . . . 169

H.2 Results . . . . . 170

H.3 Summary . . . . . 181

**I Measurement of Speaker Impulse Responses 182**

I.1 Equipment List . . . . . 182

I.2 Measurement Setup . . . . . 182

I.3 Measurement Procedure . . . . . 185

I.4 Results . . . . . 186

**J Loudspeaker Balloon-style Directivity Plots 189**

J.1 MLS . . . . . 190

J.2 MLS-CI . . . . . 194

One of the biggest challenges for musicians performing for medium to large audiences is the need for amplification of their instruments in order for the audience to be able to hear the performance. Loudspeakers are often used in these situations to reproduce electronically amplified instrument signals. Unfortunately, the use of loudspeakers also means that some of the important and exciting features such as the spatial interaction between an acoustic instrument and a room of a live performance can be lost by this kind of reproduction [1][2][3]. It is a shame since this spatial interaction or excitation of the room is often a desired feature of the performance when performing in e.g. a church. The sound of e.g. an acoustic guitar reproduced over a loudspeaker is missing some of the spatial properties which make the sound of the instrument feel lively and present and the sound can be judged as lacking some of its personality[1].

Musical instruments such as an acoustic guitar have a rather complicated and complex sound radiation characteristic/pattern where the sound directivity is highly frequency-dependent, and this characteristic can be seen as the spatial signature of the particular instrument[4]. Loudspeakers impose their own spatial signature on the sounds they are trying to reproduce, which results in a different sound radiation characteristic. It is this difference in the spatial signatures between an instrument playing and the corresponding loudspeaker playback that we humans are able to perceive [5] and thereby distinguish loudspeaker playback from sound radiated by a real guitar, violin, piano, etc.

However, if the sound radiation pattern or sound directivity of a musical instrument can be captured and synthesized approximately correct over a loudspeaker system, then the loudspeaker could create an auditory illusion of an instrument playing on stage[6] as it will provide a more natural spatial sound impression of the musical instrument. In other words, the loudspeaker should try to mimic the radiation characteristics of a musical instrument so that the audience will feel the instrument being alive and present in the room of e.g. a live performance.

In this project, a loudspeaker array with a specified frequency-dependent sound radiation pattern, which for example can emulate the sound radiation of an acoustic guitar held by a musician, is investigated and implemented. This also includes investigations and measurements of the radiation pattern for an acoustical guitar, in order to specify a realistic target radiation pattern for the loudspeaker.

## 1.1 Scope of the Project

This project aims to recreate the sound radiation pattern of an acoustic guitar using a loudspeaker array. It has been chosen to solely focus on the acoustic guitar in order to limit the scope of the investigations in this project. This problem involves different areas to be investigated and questions to be answered.

First, an investigation of the directivity of a guitar held by a musician is needed. This includes measurement of the frequency-dependent radiation pattern of the instrument in two or three dimensions in order to clarify how the loudspeaker array should imitate the sound radiation of the acoustic guitar. It also includes research of optimal and possible measurement setups, instrument excitation methods, and analysis methods based on

literature, articles, and similar studies concerning the measurement of instrument sound radiation patterns.

Experimentation or simulations of optimal loudspeaker array(s) are desired to compare the impact of different amount of drivers (loudspeaker units), enclosure shapes, and driver locations, which can be used to specify the physical requirements in order to achieve a desired sound radiation pattern in the best possible way.

Digital signal processing can be used to synthesize a desired radiation pattern with a given loudspeaker array. Research, development, and implementation of digital filter algorithms (such as FIR and IIR filters), which make it possible to reproduce the desired sound field with the selected loudspeaker array, are thus also within the scope of the project.

Lastly, a prototype of a loudspeaker array is desired to be constructed in order to evaluate the investigated methods through measurements by comparing the synthesized radiation patterns to the desired/measured sound radiation of an acoustic guitar.

Additionally, if time allows, subjective listening experiments could be performed to establish what effect the synthesized sound radiation pattern provides to the listening experience and the impression of a real guitar playing.

In summary, the following research questions can be formulated to serve as a basis for the project:

- *How can the directive radiation characteristic of an acoustic be accurately described?*
- *How can this radiation pattern be reproduced through a loudspeaker system to a sufficient accuracy?*

# Background Theory 2

Before the scope of the project can be further specified, it is a good idea to start by briefly going over some of the relevant theories for this topic of research.

These topics include some descriptions of the characteristics of the relevant sound sources to be worked with, namely acoustic guitars and loudspeakers. Additionally, a few theoretical topics useful for describing/recreating arbitrary radiation patterns will also be outlined.

Lastly, some of the previous work and research on the topic of measuring the radiation patterns of instruments and synthesizing radiation patterns with loudspeaker arrays will also be summarized.

## 2.1 The Acoustic Guitar

In this section, the physical and acoustical aspects of a typical acoustic guitar will be briefly summarized. This is both to get an intuitive understanding of the behaviour of the guitar as a sound source and to identify certain aspects of acoustic guitar playing relevant for the design of the directive loudspeaker, like the process at which it radiates sound energy and at which frequency range this sound radiation occurs.

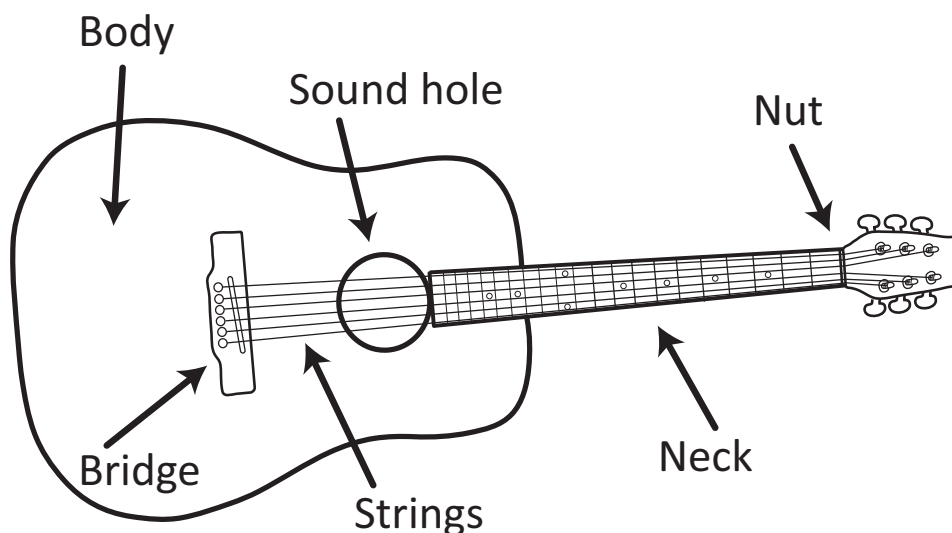


Figure 2.1: Diagram of front of a typical acoustic guitar.

A typical acoustic guitar consists of a hollow wooden chamber usually called the *body* or *soundbox*, which is attached to a flat narrow piece of wood called the *neck*. A set of guitar strings<sup>1</sup>, six usually, are suspended

<sup>1</sup>The material which the strings are made of can be used to categorize the acoustic guitar. Guitars with nylon strings are

a few millimeters over the neck, held up by the *bridge* on the hollow body, and the *nut* at the far-end of the neck, allowing the strings to vibrate freely between these two points. The ends of the guitar strings are fastened just behind the bridge at one end and behind the nut on the other end, where they are wrapped around a rotatable coil. This allows the guitarist to increase the tension of the strings simply by winding up more of the guitar string into the rotatable coil.

Sound is produced on the guitar by applying motion to a suspended string, causing it to vibrate in a standing wave pattern[7, Ch 2] at a number of normal modes i.e. a fundamental frequency and a number of harmonics, which creates a complex tone. As the first normal mode has nodes at both ends of the guitar string, the fundamental frequency of the string [7, Ch. 2][8, Ch. 4] can be found as:

$$f_0 = \frac{c}{\lambda_0} = \frac{1}{2L} \sqrt{\frac{T}{\rho}} \quad [\text{Hz}] \quad (2.1)$$

where  $c$  is the speed of sound on the string,  $\lambda_0$  is the wavelength of the fundamental,  $L$  is the length of the guitar string,  $T$  is the tension of the guitar string, and  $\rho$  is the density per unit length of the string

The fact that the fundamental is inversely proportional to the string length is used to produce different tones by pressing a finger between the *frets*, a set of raised strips, thus shortening the length of the vibrating string. The frets are placed such that every note of some musical tuning system can be reproduced between the lowest open string and the highest fret on the highest string.

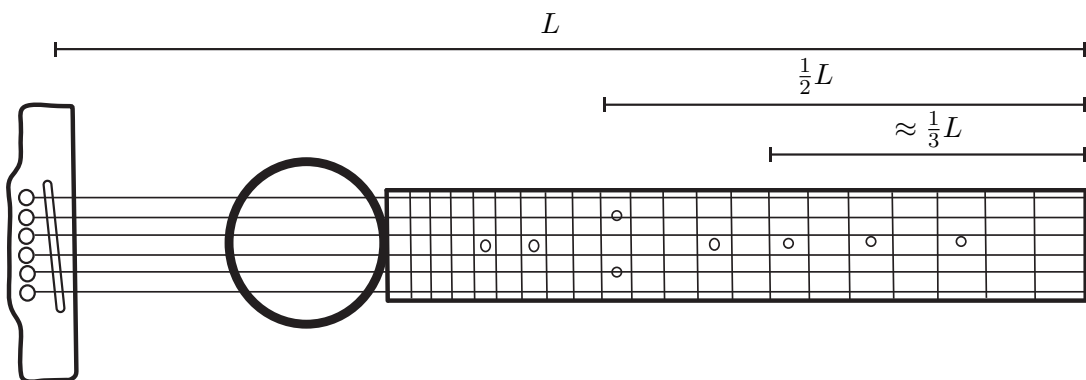


**Figure 2.2:** Examples of the resulting string lengths due to placing down the finger at certain frets.

A conventionally tuned guitar with 20 frets like the one shown on Figure 2.2 can produce tones with fundamental frequencies roughly in the range of 82-1040 Hz[9]. However, the frequency range extends much higher when you take the harmonics into account.

However, the vibrating string does not produce much sound by itself. Instead, the body of the guitar is utilized as the vibrational energy is more efficiently transmitted to the bridge and the top plate of the body [10, Chapter 3] compared to the air transmission. The energy of the vibrations of the bridge and top plate is further transmitted to the air cavity inside the body and the backplate via the sides or *ribs*. It results in sound radiating through the backplate and the *sound hole* on the top plate.

Typically an acoustic guitar can radiate sound with energy up to around 5 kHz[11, Ch. 14.3]. The coupling of the different vibrating elements is illustrated in Figure 2.3.

The shape of the body, along with the wooden support braces on the inside of the body, causes the vibrations of the body to have modal resonances with some quite complex shapes [10, 12].

mostly used for classical and flamenco music, while the acoustic guitars used for most modern music have guitar strings made of metal.

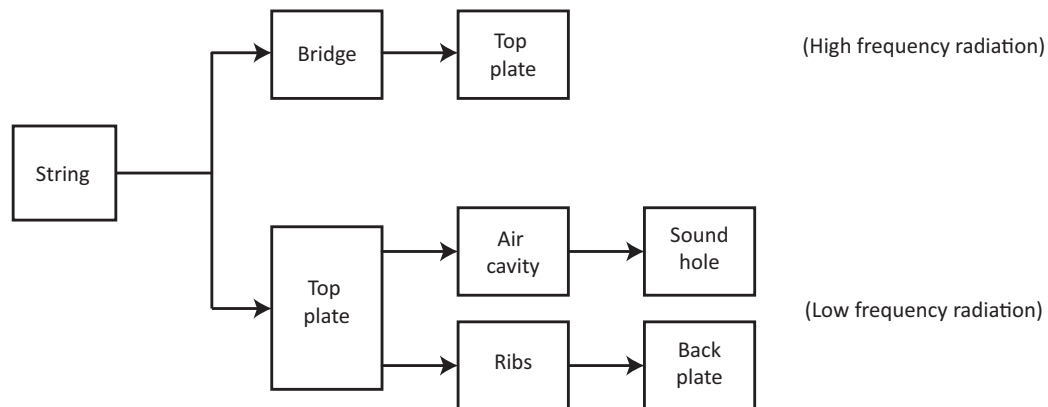


**Figure 2.3:** Transmission of vibration energy through the different elements of the guitar. Adapted from [10].

This complex interaction of vibrating elements causes the guitar to have a complicated radiation characteristic both spatially and in terms of frequency[13]. Similar results have been shown more thoroughly for orchestral string instruments [14, 15].

### 2.1.1 The Pickup

The *guitar pickup* is a transducer that is able to convert the sound of a guitar into an electric signal. The first appearance of the pickup goes back to the early 20's[16].

The pickup finds its applications in situations where the sound power radiated by the guitar needs to be amplified. This conventionally requires the sound signal to be converted to an electrical signal. In many situations, it is desirable to only capture the sound from the guitar itself, and therefore it is often infeasible to use a microphone. Instead a pickup is used. In this way, the vibrations of the guitar are converted into an electrical signal that can be fed through a wire to an amplifier and eventually to a loudspeaker.

The pickups are generally divided into two types: Contact pickups and Electromagnetic pickups. Those two are in turn divided into different kinds depending on the mechanism adopted in the transduction. The contact pickups are divided into a condenser, dynamic and piezoelectric. The electromagnetic pickups are instead divided into low, mid, and high impedance and in a single, double and triple coil.

However, for acoustic guitars, electromagnetic pickups will significantly alter the sound character of the instruments since the electric signal is more analogous to the vibrations of the strings than the vibrations of the body. Instead, contact pickups can be placed at some point of the body, often around the bridge, and are able to generate a small voltage in response to a change in mechanical pressure. This type of pickups often come pre-installed on an acoustic guitar, along with a pre-amplifier to raise the signal level to a more appropriate one for transmission through a cable.

#### Condenser Pickup

In the same way, as for the condenser microphones, condenser pickups make use of two plates separated by a small gap. The two plates are subject to sound vibrations, which move them back and forth, thus allowing a current to flow either more or less. That is because, when closely spaced, the plates reduce the resistance shown by the gap allowing for more current to flow, and vice-versa. Usually, an external voltage keeps the plates charged.

## Dynamic Pickup

As in the dynamic microphones, the dynamic pickups create a flow of current based on Faraday's law. A coil wrapped around a strong magnet is moved up and down by the impacting sound vibrations and thus creating a flow of current along the wire. At this point, the electric signal is available to be picked up and amplified.

## Piezoelectric Pickup

Piezoelectric pickups make use of crystalline materials (piezo-materials) discovered by Pierre and Paul-Jacques Curie back in 1880. These materials, evenly charged in steady situations, have the characteristic of inducing electrical charges from one surface to another under the application of pressure. Thus electrical flow is linked to the amount of pressure given by the mechanical vibrations.

## 2.2 The Electro-dynamic Loudspeaker

In this section, the electro-dynamic loudspeaker is described shortly to get an understanding of the loudspeaker's dynamic behavior. A more complete mathematical model of the loudspeaker can be found in Appendix A.

The most common type of loudspeaker, namely the electro-dynamic loudspeaker[17, Ch. 17.2][18, Ch. 7][19, Ch 2.16] makes use of a lightweight and stiff diaphragm or cone, which is set in motion by an electromagnetic force to transfer energy to the air. A cross-section model of the electro-dynamic loudspeaker transducer can be seen in Figure 2.4 as an overview of the components which determine the dynamic behavior of the loudspeaker.

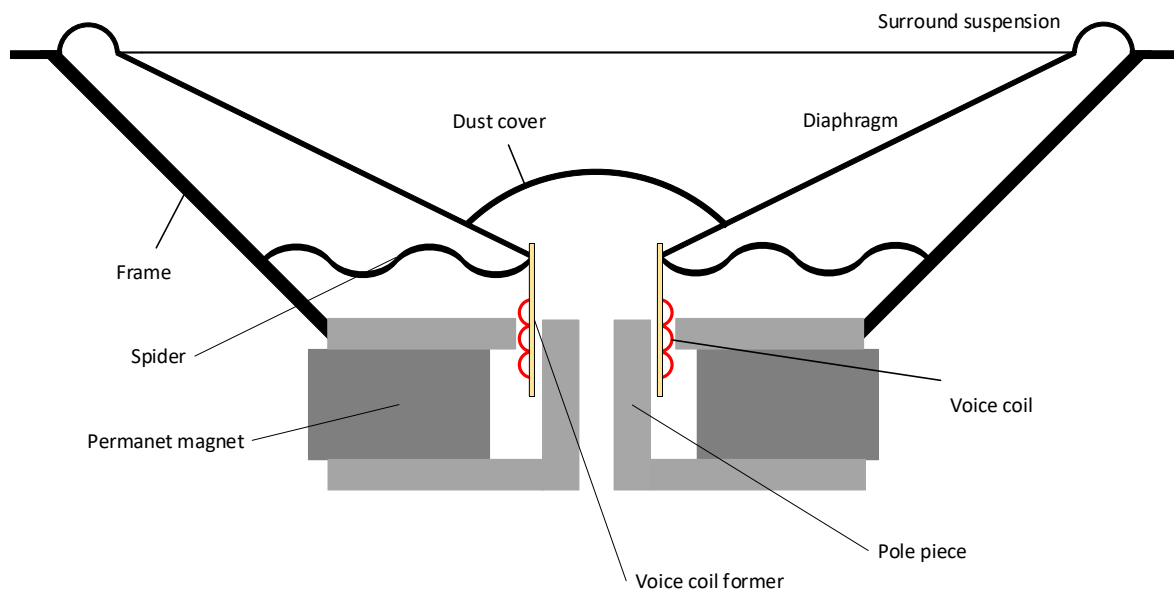


**Figure 2.4:** Cross-section model of a (vented) electro-dynamic loudspeaker

The diaphragm or cone is the moving part of the loudspeaker that pushes to the air and causes air pressure variations, to which the audible sound is produced as waves of pressure. The voice coil is suspended in an air gap between the poles of the permanent magnet and will affect the diaphragm with a force given by

$F = Bl \cdot I$  (the Lorentz force) [18, Ch. 4.7], where  $B$  is the flux density of the magnetic field,  $l$  is the length of coil wire immersed in magnetic flux and  $I$  is the current applied to the voice coil. This results in a movement of the voice coil and the attached diaphragm when a current is applied to the voice coil [17, Ch. 17.2]. An alternating current will cause the voice coil to move rapidly back and forth, but the movement with a velocity  $v$  will also induce a voltage in the voice coil given by  $U = Bl \cdot v$  according to Faraday's induction law which counteracts the applied current in the voice coil (back electromotive force, back EMF)[17, Ch. 32.2][18, Ch. 4.7].

To keep the voice coil free from dust, a dust cover is used to seal the voice coil from the environment and thereby reduce the amount of dust and dirt that can get into the air gap of the magnet[18, Ch. 7.1]. The surround suspension is required to center the movement of the diaphragm axially and to avoid air leakage from the internal volume of the loudspeaker enclosure. The surround suspension often consists of a rubber or foam surround attached to the periphery of the diaphragm, which seals the internal volume and allows for flexible movement[17, Ch. 17.2]. The spider is attached to the voice coil former and is used to keep the voice coil centered in the air gap between the poles of the permanent magnet to allow free axial movement of the diaphragm but it provides the most suspension and damping of the diaphragm movement. The frame provides a rigid structure to which the driver components are mounted and is the static part used to mount the loudspeaker solidly in an enclosure[18, Ch. 7.1].

The loudspeaker can be modeled as an equivalent circuit for a more detailed analysis of the dynamics in both the electrical, mechanical, and acoustic domains. A model of the electro-dynamic loudspeaker mounted in a sealed enclosure can be found in Appendix A

## 2.3 Radiation Patterns

As this work is very much concerned with the directional radiation characteristics of both the acoustic guitar and loudspeakers, it is good to have a clear understanding of this concept.

The term *directivity pattern* is well known in the field of receivers, like microphones or antennas, where it is used to describe how strong a signal is received depending on the direction of the source.

One can also talk about directivity patterns in the reciprocal sense, i.e. for sources[19, Ch. 1] like loudspeakers or musical instruments. In this sense, the directivity pattern or *Radiation pattern* becomes a measure of how much sound is transmitted in a certain direction.

### 2.3.1 Sound Source Related Coordinate System

To get a common reference when describing some direction, we can define the spherical coordinate system as shown in Figure 2.5.

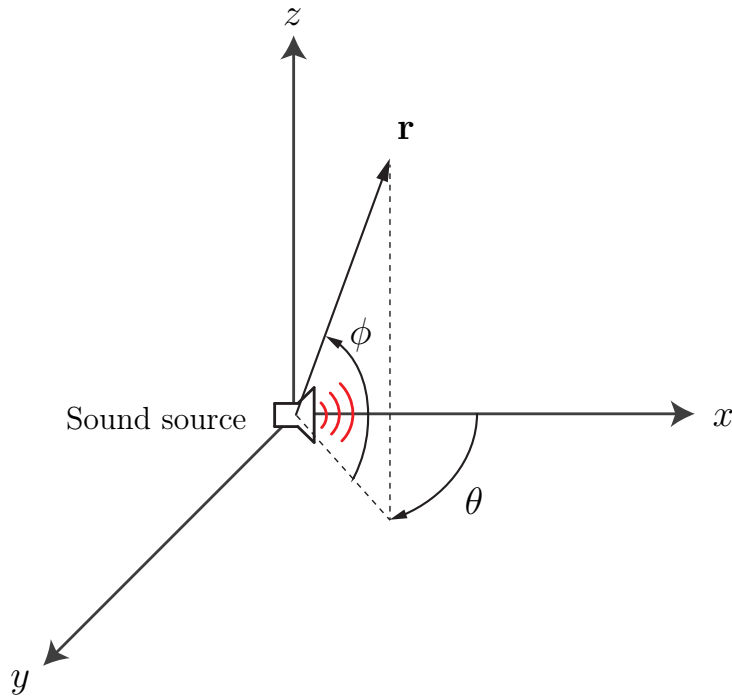


**Figure 2.5:** Spherical coordinate system oriented in relation to a sound source

A point  $\mathbf{r} = (r, \theta, \phi)$  can be given in terms of the radius  $r$ , the azimuth angle  $\theta \in [0, 2\pi)$  or  $[0^\circ, 360^\circ)$  with the counter-clockwise direction being positive, and the elevation angle  $\phi \in [-\frac{\pi}{2}, \frac{\pi}{2}]$  or  $[-90^\circ, 90^\circ]$ , with an upwards direction being positive.

In this work, sound sources will generally be placed at the origin of the coordinate system. Likewise, the sound source will be oriented such that the "front" of the sound source will point in the  $\theta = 0, \phi = 0$  direction, i.e.  $+x$ .

### 2.3.2 Far-field Response of an Acoustic Source

In this spherical coordinate-system a complex sound pressure can be described as a function of space and frequency  $p(\omega, r, \theta, \phi)$ , assumed to be a solution of the Helmholtz equation[7, Ch. 4]. We can also denote the pressure simply as  $p(r, \theta, \phi)$  assuming constant frequency.

The sound field generated by a source can be split up into the near field, far field, and a transition area in between. A point in space is said to be in the far-field when the distance to the source is significantly larger than the dimensions of the source[7, Ch. 7].

At the far-field, the pressure can be decomposed into a product of the on-axis response and a direction-dependent part.

$$p(r, \theta, \phi) = p(r, 0, 0)g(\theta, \phi), \quad r \in \text{Far - field} \quad (2.2)$$

This is very useful as it allows you to describe the directivity or radiation pattern of a sound source in terms of just two spatial variables  $\theta$  and  $\phi$ .

### 2.3.3 Directivity of Loudspeaker as a Plane Piston

As a practical example of a radiation pattern, we can look at a simplified model of a loudspeaker.

The shape of the loudspeaker diaphragm or cone can be somewhat complex, which makes it difficult to calculate the exact radiation pattern of the loudspeaker. However, the electro-dynamic loudspeaker can

be modeled as a circular piston with radius  $a$  mounted in infinite baffle/enclosure moving with a uniform velocity normal to the baffle[7, Ch. 7.4] and thereby be used to approximate the directivity of a loudspeaker.

Due to the symmetry of the piston, we will only look at the directivity in 2D in the horizontal plane given by  $\phi = 0$ . In far-field ( $r \gg a$ ) the acoustic pressure amplitude[7, Ch. 7.4] can be written as

$$p(r, \theta) = p(r, 0)g(\theta) \tag{2.3}$$

$$p(r, 0) = \frac{j}{2}\rho_0cv\frac{ka^2}{r}e^{-jkr} \tag{2.4}$$

$$g(\theta) = \frac{2J_1(ka \cdot \sin(\theta))}{ka \cdot \sin(\theta)} \tag{2.5}$$

where  $p(r, 0)$  is the far-field axial pressure amplitude in a distance  $r$  and  $g(\theta)$  is directional factor describing the dependence of angle  $\theta$ .  $J_1(x)$  is the Bessel function of the first kind,  $k = \frac{2\pi f}{c}$  is the wavenumber,  $v$  is the particle (or piston) velocity normal to the baffle,  $\rho_0$  is the density of air and  $c$  is the speed of sound.

From the directional factor  $g(\theta)$ , it can be seen that pressure nodes (minima) will appear at the angles which reduce the Bessel function to zero and that the maximum pressure will appear when  $\theta = 0$ . Pressure side lobes will appear between the angles yielding minima and maxima with a decreasing amplitude going away from  $\theta = 0$ . This can be illustrated by the beam pattern  $b(\theta) = 20 \cdot \log_{10} |g(\theta)|$  plotted in Figure 2.6

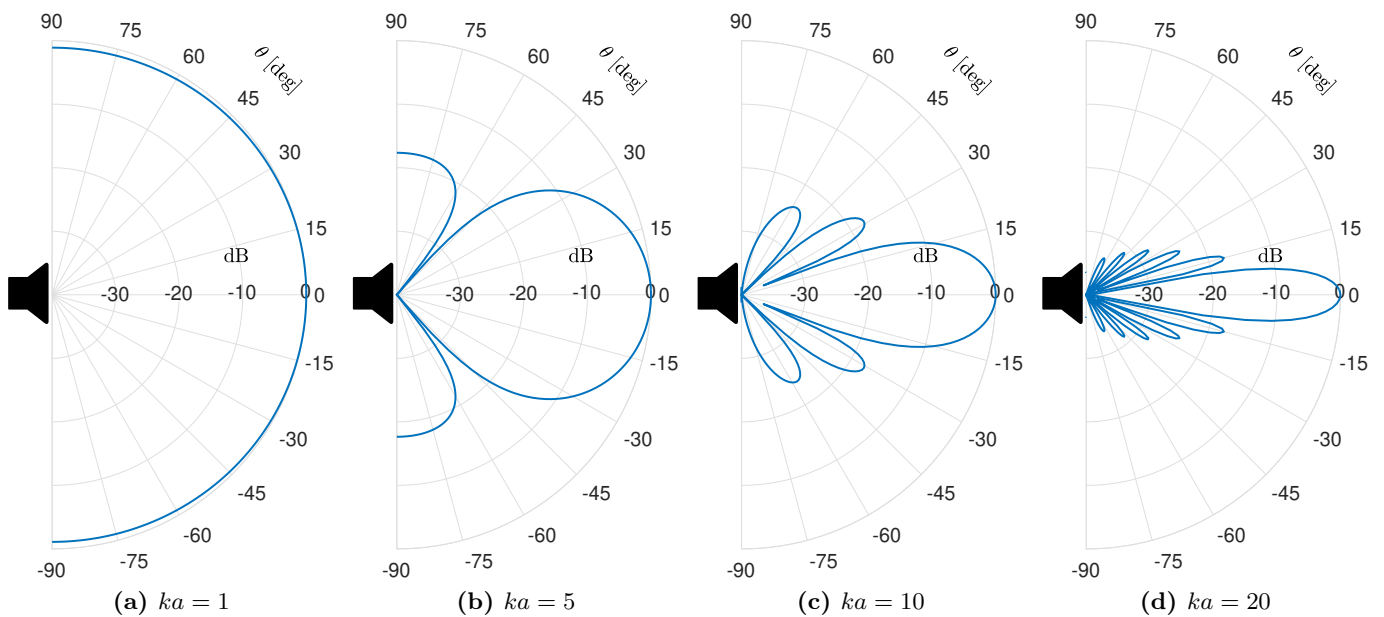


**Figure 2.6:** Beam pattern  $b(\theta)$  for a circular piston of radius  $a$  and with different values of  $ka$

For wavelength much larger than the radius of the piston ( $ka \ll 1$ ), the directional factor  $|g(\theta)|$  becomes nearly unity for all angles with which the radiation pattern of the source will be omnidirectional. When the wavelength becomes small relative to the radius of the piston ( $ka \gg 1$ ), then the main radiation lobe becomes narrow and begins to “beam” directly ahead on-axis while many side lobes will begin to occur at the off-axis angles

### 2.3.4 Multipole Expansion

Another useful tool in describing a far-field radiation pattern is through its *multipole expansion*. This expansion can be performed for a function defined on the surface of a sphere i.e.  $g(\theta, \phi)$  defined over some sphere of radius  $r$ .

In the multipole-expansion, the function  $g$  can be expressed as a weighted sum[20]

$$g(\theta, \phi) = \sum_{n=0}^{\infty} \sum_{m=-n}^n C_{n,m} Y_n^m \tag{2.6}$$

in terms of a set of coefficients  $C_{n,m}$  and their associated *Spherical Harmonics* (SH)  $Y_n^m$ , defined as

$$Y_n^m = \sqrt{\frac{2n+1}{4\pi} \frac{(n-m)!}{(n+m)!}} P_n^m(\cos(\theta)) e^{jm\phi} \tag{2.7}$$

where  $P_n^m$  is a legendre function [20, Ch. 6.3], defined from the legendre polynomials  $P_n$  [21, Ap. A] as

$$P_n^m(x) = (-1)^m (1-x^2)^{\frac{m}{2}} \frac{d^m}{dx^m} P_n(x) \tag{2.8}$$

$$P_n(x) = \frac{(-1)^n}{2^n n!} \frac{d^n}{dx^n} (1-x^2)^n \tag{2.9}$$

It can of course be seen that  $P_n^0 = P_n$ .

The number  $n$  is termed the *order* of the spherical harmonics and  $m$  is called its *degree*. The 0th order spherical harmonic corresponds to a monopole pattern. The real part of the first-order SH for  $m = -1, 0, 1$  corresponds to dipole patterns along the  $x, y$  and  $z$  axes. The real part of the second-order SH corresponds to quadrupoles, and so on.

The spherical harmonics up to order  $N = 3$  are showed in Figure 2.7

The radiation pattern of many real sources can be well approximated by the multipole expansion truncated at some order  $n$ , similar to how a waveform can be well approximated by Fourier expansion<sup>2</sup>. For example,

<sup>2</sup>The act of producing virtual microphone patterns using SH is well known as the field of ambisonics[21], where first-order ambisonics (FOA) creates a microphone directivity pattern using the first four SH, and higher-order ambisonics (HOA) uses even more.

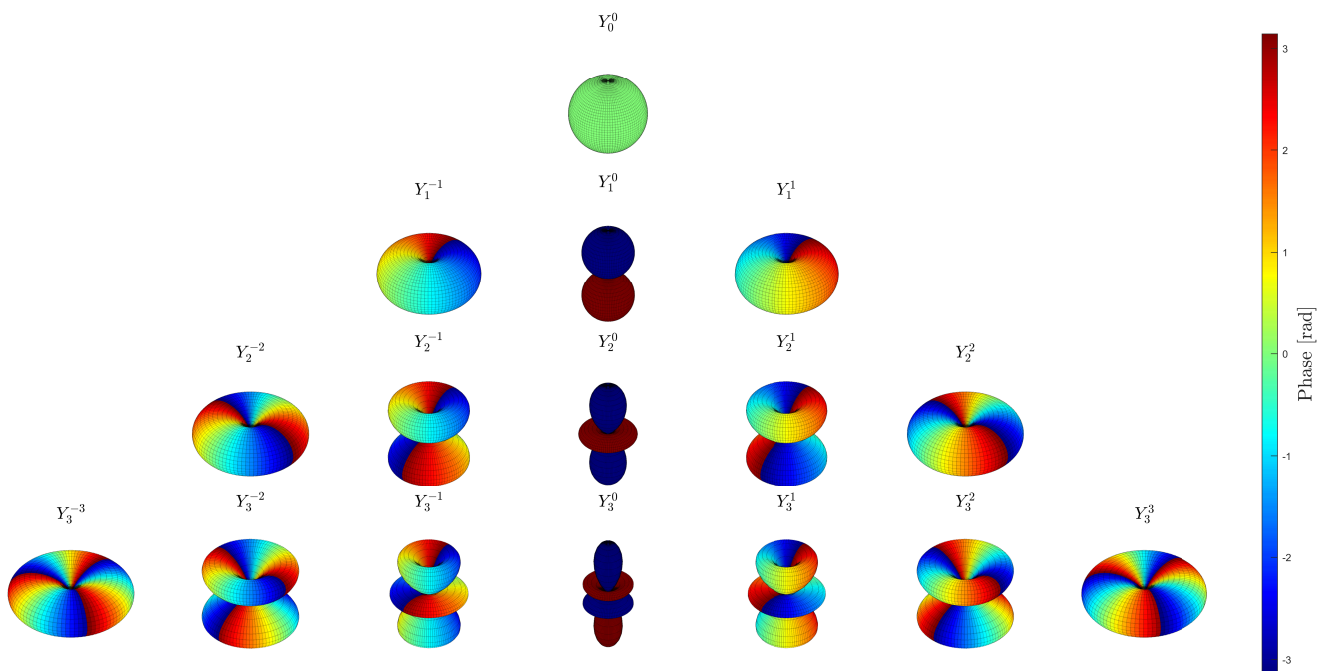


**Figure 2.7:** Complex-valued spherical harmonic components up to order  $N = 3$ .

the beam pattern in Figure 2.6(a) might be somewhat approximated by a monopole, i.e. 0th order SH, while the rest may be approximated by an increasing number of SH.

However, SH used for multipole expansion are limited by the maximum truncation order  $N$  restricted by  $N \leq \sqrt{L}-1$  where  $L$  is the number of loudspeaker drivers [22]. This specifies that the number of loudspeakers  $L$  must be greater or equal to the number of the total SH components for a given truncation order  $N$ [23].

$$L \geq (N + 1)^2 \quad (2.10)$$

## 2.4 Spatial Aliasing

For a given loudspeaker array, the performance of a desired radiation pattern reproduction is limited at high frequencies due to spatial aliasing. Spatial aliasing occurs when spacing a finite number of loudspeakers in some grid. It can be seen as a kind of sampling process in the spatial domain very similar to sampling in the time domain.

When a sound radiation surface is spatially discretized in intervals that are smaller than a half wavelength, then spatial aliasing will occur and reduce the reproducibility of the desired sound field [24] due to distortions in the reproduced sound field.

For a linear loudspeaker array, the aliasing frequency  $f_A$  depends on the distance  $\Delta x$  between the loudspeaker membrane centers and the angle  $\alpha$  between the loudspeaker array and the outgoing wavefront direction of a plane wave[25, p.321-323] given by:

$$f_A = \frac{c}{2 \cdot \Delta x \cdot \sin \alpha} \quad (2.11)$$

where  $c$  is the speed of sound. From Equation 2.11 it can be seen that aliasing frequency is infinitely high at an angle  $\alpha$  of  $90^\circ$  (wavefront direction orthogonal to the line array). But the aliasing frequency quickly decreases when the angle  $\alpha$  deviates from this direction, and with the lowest aliasing frequency occurring when the wavefront direction is parallel the line array ( $\alpha = 0^\circ \vee 180^\circ$ ). At this lowest aliasing frequency, the Equation 2.11 reduces to:

$$f_A = \frac{c}{2 \cdot \Delta x} = \frac{c}{\lambda_{min}} \quad (2.12)$$

where  $\lambda_{min}$  is the shortest wavelength of the plane waves that can be accurately reconstructed with a loudspeaker spacing of  $\Delta x$  for the given array.

However, for a spherical or platonic solid loudspeaker array, the loudspeaker units are not uniformly spaced on a line by which the spacing  $\Delta x$  of adjacent loudspeaker membrane centers is different depending on the number of loudspeakers fitted into the array geometry. A lower bound for the upper-frequency limit where spatial aliasing is starting can be found using the outer radius  $r_0$  of the array as the loudspeaker spacing  $\Delta x$  according to [26]. This approach agrees well with Equation 2.12 for arrays with only 6 loudspeakers placed uniformly, like on the midpoints on the faces of a cube, which indicates that one way to increase the aliasing frequency is by making the array radius as small as possible.

Unfortunately, a very small loudspeaker array requires small loudspeaker dimensions limiting the low-frequency power output and thereby bound the performance of a desired radiation pattern reproduction at the low frequencies. The loudspeaker array design, therefore, becomes a compromise between low and high-frequency reproduction[4] when the array aperture is desired to be as small as possible and output enough acoustic power in the low-frequency range. The rough estimate of the upper-frequency limit from[26] does however not account for loudspeaker array geometries with a large number of loudspeakers closely spaced next to each other. The aliasing frequency should increase with the number of loudspeakers as the sound radiation surface will be spatially discretized in smaller intervals, and in theory, become one continuously radiating surface if spatially discretized in infinitely small intervals.

### 2.4.1 Properties of Spatial Aliasing

In general spatial aliasing will mostly distort the desired sound field close to the loudspeaker array while the amount of distortion artifacts decrease with the distance away from the loudspeaker array[25, p. 321-323] making the far-field less affected by spatial aliasing problems.

Regarding perceived audio quality, spatial aliasing does not seem to have a huge impact on the human auditory system [27], and spatial aliasing has been found to be often inaudible during listening tests[25, p.321-323]. It is properly due to several reasons. One argument is spatial aliasing causing sound pressure dips instead of peaks in the reconstructed sound field [25, p.321-323] which is less audible and disturbing than sound pressure peaks. Another reason is that spatial aliasing only distorts a sound field slightly in the frequencies just above the aliasing frequency. Whereas spatial aliasing distorts a sound field the most at higher frequencies in very narrow frequency bands, where the human auditory system has poor resolution, by which the distortion is only audible for exceptionally narrow band signals[25, p.321-323]. These deep and very narrow band sound pressure dips at higher frequencies are also getting averaged out a little by the outer ear, making the sound pressure distortion dips difficult to perceive[25, p.321-323]. Lastly, the environments in which a loudspeaker array is operating inside will also naturally introduce narrowband sound coloration originating from all the reflections present, by which it can be difficult to separate spatial aliasing effects from the room or environment effects[25, p.321-323]

However, sound field distortion or sound coloration from spatial aliasing might become audible if the sound field is clearly different at each ear of the listener, or if the listener/loudspeaker array is not positioned stationarily in the environment but are moving quickly within the environment [25, p. 321-323].

## 2.5 Summary of Previous Research

With the basic theories surrounding sound radiation patterns in place, a summary of the previous work relevant for this project can be provided. This summary is divided into two sections: The first one going over previous work in measuring the sound radiation of musical instruments, and the following section going over previous work in using loudspeaker arrays to synthesize a chosen radiation pattern.

### 2.5.1 Measurements of the Directivity of Musical Instruments

In 1972, Meyer from Physikalisch-Technisch Beundesanstalt, Braunschweig, West Germany, measured the directivity of bowed stringed instruments in order to evaluate their impact in different audience positions in concert hall arrangements [28]. The measurements were performed in an anechoic chamber with a single microphone placed at a fixed distance dependant on the instrument to be measured. The instruments were placed on a turntable and excited by an electrodynamic oscillation system at the bridge. It was found that all the instruments measured had highly directional and frequency dependant sound radiation in middle and high frequencies.

In 2009, Pollow *et al.* from the Institute of Technical Acoustics, RWTH Aachen University, Germany, measured the directivity of 41 instruments for symphony orchestras with a spherical microphone array [29]. The microphone array with the sound source in its center had a radius of 2.1 m and consisted of 32 electret microphones. The instruments were recorded in an anechoic chamber while played by musicians. Since the center of the instruments was hard to define, the phase information from the measurements was discarded, as it would otherwise result in phase displacement error. However, no comprehensive results have been shown and no listening tests were performed to confirm the impact of discarding the phase information.

In a paper of 2010 [14], Pätynen *et al.* from Helsinki University of Technology, Helsinki, Finland, described the

measurements of the directivity of 14 symphony orchestra instruments. The measurements were performed with professional musicians in an array of 22 large condenser microphones inside a cubical anechoic chamber. 20 of the microphones were mounted in the vertices of a dodecahedron, while the other two were placed in front and above the musicians at the average distance of 2.13 m from the center (here defined as the musicians head). It was found that different dynamics did alter the timbre of the sound sources, but not the directivity. Moreover, the directivity patterns were influenced by tone variations in string and woodwind instruments, while they did not affect brass instruments, which radiated consistently with a bell pattern.

A year later, Pérez Carrillo *et al.* published their work for measuring the sound radiation of a violin [15]. The violin was excited with a bowed glissandi<sup>3</sup> played by a musician and recorded inside an anechoic chamber with a spherical array of 21 microphone arranged over two pentagonal antiprisms. The body impulse response of the instrument was obtained through a deconvolution in between the signal captured by the microphones and the signal captured by the pickup placed at the bridge of the violin.

In 2012, Bader from University of Hamburg, Germany, measured the radiation characteristics of multiple and single sound hole violas and a classical guitar by placing a grid array of 121 microphones 3 cm in front of the instruments [30]. A few years later, Bader *et al.* measured the 2D radiation pattern of instruments by placing the musicians in the center of an array of 128 microphone (with a  $2.8^\circ$  spacing) [31]. The microphone array had the shape of a ring with a radius of 1 m.

In 2014 Perry published his PhD-thesis on sound radiation measurements on stringed musical instruments [13]. In the research, many different excitation techniques alternative to a musician playing the instrument are mentioned and evaluated for the measurements. Considerations upon the influence of added mass on the plate of the guitar (an effect that a guitarist could have on the guitar) are also exposed. Perry measured the radiation efficiency of guitars with 2 microphones on two concentric spheres of radii 45 cm and 71 cm while the guitars were suspended with elastic bands and excited with an impact hammer. However, the directivity patterns in the far-field of the instruments were not investigated in the research.

In 2015 Shabtai *et al.* measured the radiation pattern of a violin using a single microphone [32]. The violin was excited with a sweep using the Lorentz force law by a conductive wire leaned against the violin's bridge, while the violin strings were prevented from vibrating. In order to acquire the full sphere pattern, the violin was turned and tilted for every measurement. In 2017, Shabtai *et al.* collected the radiation pattern of 41 musical instruments [33]. The measurements were conducted inside a 2.1 m radius spherical array of 32 microphones inside an anechoic chamber with musicians playing the instruments. Particular attention was given to the localization of the right acoustic center of the instruments to be measured in both studies.

---

<sup>3</sup>A glissandi consists of a constant glide going from one pitch to another, either by lowering or raising it, somewhat analogous to a 'sweep signal'.

Study	Year	No. Microphones	Microphone placement & distance	Excitation technique	Motivation of the measurements
Meyer[28]	1972	1	Dependent on the instrument	Electrodynamic oscillation system	Directivity of orchestra instruments for seat arrangement
Pollow[29]	2009	32	Spherical array of 2.1 m radius	Played by musicians	Directivity of 41 orchestra instruments
Pätynen <i>et al.</i> [14]	2010	22	20 in a dodecahedral and 2 above and in front at 2.13 m	Played by musicians	Directivity of 14 symphony orchestra instruments
Pérez Carrillo <i>et al.</i> [15]	2011	21	Spherical array of two pentagonal antiprisms	Played by musicians	Sound radiation of a violin
Bader <i>et al.</i> [31]	2015	128	2D in a ring of 1 m	Played by musician	2D radiation pattern of instruments
Perry[13]	2014	2	2 concentric spheres of radii 45 cm and 71 cm	Excited with a hammer at the bridge	Radiation efficiency of guitars and stringed instruments
Shabtai <i>et al.</i> [32]	2015	1	Fixed at 68 cm while instrument is turned and tilted	Sweep with a conductive wire	Radiation pattern of a violin
Shabtai <i>et al.</i> [33]	2017	32	Spherical array of 2.1 m	Played by musicians	Radiation pattern of 41 musical instruments

**Table 2.1:** Overview of the different instrument measurement setups of the previous research and studies

### 2.5.2 Synthesis of Directivity Patterns with Compact Loudspeaker Arrays

A decent amount of previous work has been done on the use of compact loudspeaker arrays to recreate selected or arbitrary radiation patterns.

In 1992 researchers from IRCAM (Institut de Recherche et Coordination Acoustique/Musique, Paris) first raised the problem of loudspeakers not being able to reproduce the radiation pattern of the sound sources aimed to be reproduced [34]. Later in a 1995 paper [35] the researchers described a method of synthesizing a given radiation pattern by finding an optimal set of weightings to a set of loudspeakers in a compact loudspeaker array. Such an array was built with twelve loudspeaker units driven by four channels and mounted on the faces of a dodecahedron contained in a 35 cm radius sphere. This allowed them to recreate the first-order spherical harmonics up to 500 Hz.

In a successive research in 2001, IRCAM developed a new compact loudspeaker array improving the bandwidth of the previous model [2]. The new prototype was made by three concentric cubes of decreasing size: A sub-bass system with four horizontal drivers, six mid-frequencies 7" drivers in a 25 cm cube and six tweeters mounted in an 8 cm cube. The system was able to resemble the radiation pattern of e.g. musical instruments by combining four elementary directivity patterns: a monopole (0<sup>th</sup> order spherical harmonic) and three dipoles (1<sup>st</sup> order spherical harmonics) for the X, Y, and Z axes.

In a paper of 2003 [3], Kassakian and Wessel from CNMAT (Center for New Music and Audio Technologies, U.C. Berkeley, CA) described a new filter implementation for a dodecahedral loudspeaker array made by twelve independent 4" driver units, each of them embedded and isolated in its separate enclosure. The new driving system of filters was shown as an improvement of the least-squares minimization, enhancing the spatial synthesis up to the second-order of spherical harmonics. However, the system showed deterioration as the frequency increased.

Further studies conducted by the CNMAT at the Meyer Sound Labs were documented in [36]. In this work, a 12.7 cm radius icosahedral loudspeaker array is presented. The loudspeaker array is composed of 120 1.25"

driver units driven independently by 120 digital audio channels. The loudspeaker array is theoretically able to spatially synthesize up to the 8th order spherical harmonics in the frequency range up to approximately 7 kHz (with the error increasing with frequency). However, only simulated results were presented in this study.

Zotter *et al* from IEM (Institute of Electronic Music and Acoustics, Graz, Austria) introduced a 'Spherical Cap' model to describe the compact loudspeaker array as a sphere with several moving 'Caps' of constant velocity [22]. This study served as a base for future works. During 2006 they built a 33 cm radius icosahedral loudspeaker array able to playback with a frequency range of approximately 40 Hz to 4 kHz [37]. A coaxial pair of driver units of 6.5" and 1" were mounted on each face of the solid with a spacing dictated by the distance in between the corners of a 19 cm radius dodecahedron placed inside the icosahedral structure. Later on, the array was subjected to changes in radius, which was reduced to 28 cm [38], and in the size of the drivers being reduced to 6". The IKO array was able to synthesize up to the 3rd order spherical harmonics [39]. The system, which is based on microphone array measurements, was utilized in subsequent papers [38] [40].

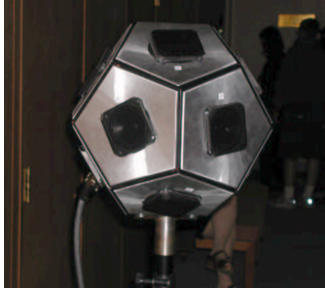
In his PhD-thesis from 2010, Pasqual documented an extended theory on the sound directivity of loudspeaker arrays. In particular, he introduced the idea of using acoustic radiation modes (ARM's) for the synthesis of the spatial information of a 3D source [4]. To evaluate the validity of the model, he built a 7.5 cm radius spherical loudspeaker array prototype. The array contained twelve 2" driver units distributed as the faces of a dodecahedron, while the inner part was used as a common enclosure for all the loudspeakers. In a later paper, [41] the author discussed and compared the different platonic solids used as 3D sound sources, with special attention given to the dodecahedron.

In 2016 Farina *et. al.* from UNIPR (University of Parma, Parma, Italy) built up a new spherical loudspeaker array system embedded with 32 2" driver units[6] distributed as the faces of a truncated icosahedron. The system, relatively light and compact (3 kg per 10 cm radius), was able to work as a good omnidirectional source at a high level of reproduction within a frequency range of 125 Hz to 4 kHz, being superior to larger dodecahedron sources already built. The loudspeaker array was also adopted to synthesize 3D sources at a full range up to the 2nd order spherical harmonics.

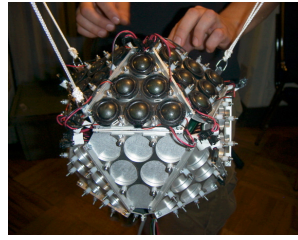
The most recent large scale work on synthesized directivity patterns with loudspeaker arrays was published in 2020 by researchers from Pennsylvania State University, PA, USA [23]. Here, a compact spherical loudspeaker array was built in order to reproduce the directivity pattern of many different musical instruments from an orchestra. This was done by decomposing all the instrument radiation patterns into a number of SH up to 3rd order. It provided a set of filter banks able to synthesize these SH patterns. A specific radiation pattern of an instrument could afterward be synthesized as a weighting of these SH filters. The loudspeaker array was very compact in dimension, 7.6 cm radius, was built up by equipping 20 faces of a truncated icosahedron with 1,57" drivers, for a total of 20 driver units. This made it possible for the array to work with limited spatial aliasing problems, which first started to affect the directional accuracy of the array around 3-4 kHz.

Study	Year	Array type	Array radius	No. speakers	Speaker size	Desired pattern
IRCAM[35]	1995	Dodecahedron	35cm	12	N/A	1st order spherical harmonics up to 500 Hz
IRCAM[2]	2001	3 Cubes	N/A 25cm 8cm	4 6 6	N/A 7" N/A	Combination of one 0th and three 1st order spherical harmonics
Kassakian & Wessel[3]	2003	Dodecahedron	N/A	12	4"	Up to 2th order of spherical harmonics
CNMAT[36]	2006	Icosahedron	12.7cm	120	1.25"	Up to 8th order of spherical harmonics up to 7 kHz
Zotter <i>et al</i> [37]	2007	Icosahedron	33cm	20	6.25"+1"	3rd order spherical harmonics in a range of 40 Hz to 4 kHz
Zotter <i>et al</i> [38]	2008	Icosahedron	28cm	20	6"	3rd order spherical harmonics in a range of 40 Hz to 4 kHz
Pasqual[4]	2010	Sphere	7.5cm	12	2"	Arbitrary radiation patterns as well as pure spherical harmonics
Farina <i>et al</i> [6]	2016	Sphere	10cm	32	2"	Omnidirectional source within 125 Hz to 4 kHz and 2nd order spherical harmonics in full range
Neal <i>et al</i> [23]	2020	Truncated Icosahedron	7.6cm	20	1.57"	Orchestral instruments pattern reproduced until 3-4 kHz

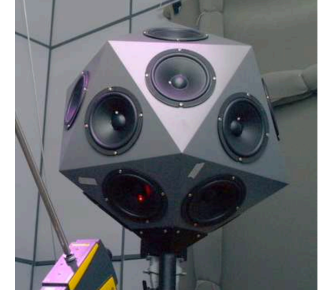
**Table 2.2:** Overview of the different loudspeaker arrays of the previous research and studies



(a) The dodechadral loudspeaker array built by CNMAT researchers Kasakian & Wessel. Figure from [3]



(b) The icosahedral loudspeaker array of 120 drivers by CNMAT. Figure from [42]



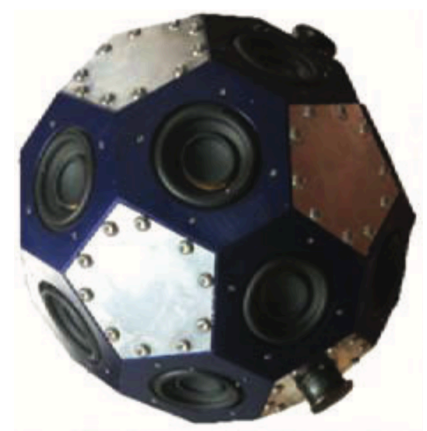
(c) The icosahedral loudspeaker array by Zotter. Figure from [40]



(d) The spherical loudspeaker array (12 drivers) by Pasqual. Figure from [43]



(e) The spherical loudspeaker array (32 drivers) by Farina *et al.*. Figure from [6]



(f) The truncated icosahedral loudspeaker array from the Pennsylvania State University. Figure from [23]

**Figure 2.8:** Illustration of the different loudspeaker arrays from previous research and studies

# Delimitation and Specification of the Project 3

---

After reviewing some of the theory behind sound radiation and after looking at the body of previous work on the topic, it is now possible to further narrow down the scope of the project.

In general, it seems that most previous work on radiation synthesis with compact loudspeaker arrays have been focused on creating arbitrary radiation pattern, often up to some upper limit of spherical harmonics as outlined in Section 2.5.2. For that reason, it has been taken as a given that the loudspeaker driver units should be distributed evenly around the loudspeaker array surface.

However, in this work, a different angle is taken by focusing on recreating a specific radiation pattern, which in this case is the acoustic guitar.

By carefully placing the loudspeaker driver units on a loudspeaker array with the desired target pattern in mind, then superior results might be possible compared to a uniform placement on e.g. a platonic solid array geometry.

For example, the directivity pattern of the sound radiated behind the guitar player might not need the same level of detail as the radiation to the front in order to secure a faithful recreation of the guitar radiation pattern. Thus it might be better to place fewer loudspeakers on the backside of the array while providing a more dense driver distribution on the front side of the loudspeaker array.

This creates another challenge as not a lot of high-quality data on the far-field radiation pattern of an acoustic guitar seems to be available to the authors' knowledge. Therefore several measurements on the radiation pattern of a guitar need to be performed in an anechoic chamber. It is chosen to measure the radiation pattern of a guitar as played by a musician based on the results of the previous research outlined in Section 2.5.1. These measurements may also be used as a basis to further delimit the project by identifying which frequency ranges it is even feasible to steer the radiated sound due to the narrow beamwidth of a typical loudspeaker at higher frequencies modeled in Section 2.3.3.

As the sound radiation of the guitar is highly frequency-dependent, the radiation pattern should at least be described and synthesized by the loudspeaker array throughout the typical frequency spectrum of the guitar from around 80 Hz - 5 kHz. However, the loudspeaker array should preferably also allow reproduction of harmonics/transients sounds going further up in frequency to ensure some high-frequency details in the listening experience, even though the synthesized radiation pattern might be incorrect in high frequencies.

In order to find out how to design a compact loudspeaker array that is built specifically for recreating the sound radiation of a guitar, some investigation into how different aspects of the loudspeaker array affect the performance. These aspects both include the signal processing that should be applied to each loudspeaker driver unit but also the physical aspects of the loudspeaker array, e.g. different enclosure shapes, the number of drivers, and the placements of the drivers.

These investigations would obviously take a lot of time if they had to be done on many different physical

loudspeaker arrays. A much easier option is to set up a mathematical model for a compact loudspeaker array for synthesizing radiation patterns and look at how the different parameters affect the performance using computer simulations. This model will need to encapsulate both an acoustical part describing the sound radiation from the array and into the far-field and a signal processing part describing how the individual driver units should behave in order to best approximate the target radiation pattern of a guitar.

Based on these simulations, it should be possible to construct a physical loudspeaker array in a well-thought-out way.

A set of filters can then be constructed specifically for this loudspeaker array, such that a common input signal can be sent to the filters, e.g. the electric signal from a guitar pickup. The filters should transform the pickup signal to an appropriate input signal to each driver unit, so the sound radiation of the whole loudspeaker array will approximate the radiation pattern of an acoustic guitar. This can overall be seen as a single-input multiple-output (SIMO) system illustrated in Figure 3.1.

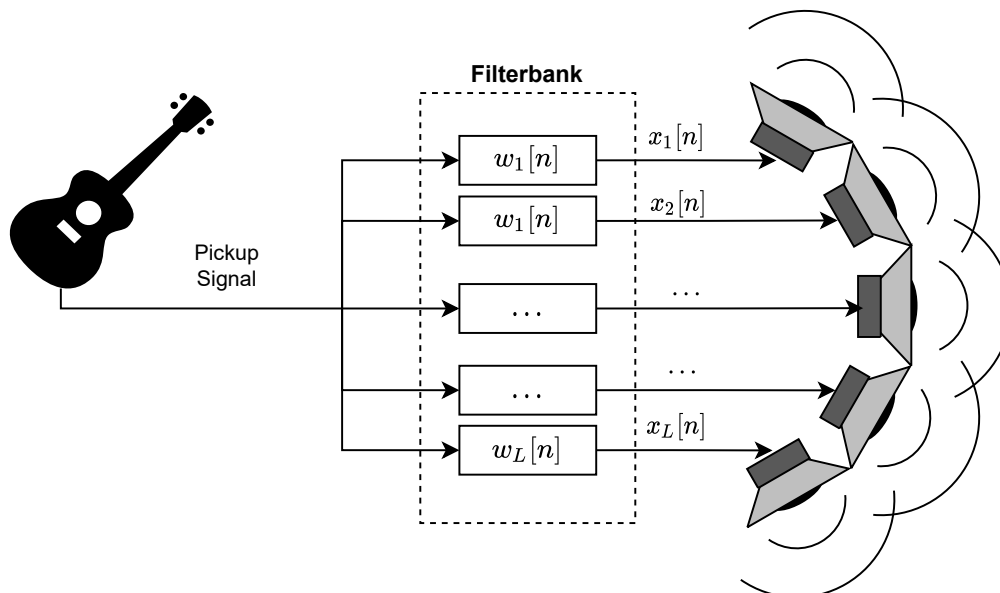


**Figure 3.1:** Block diagram of the SIMO system consisting of a loudspeaker-array with  $L$  loudspeakers and  $L$  corresponding filters feed by the pickup signal of a single guitar.

To limit the scope of the project, it has been chosen to focus on imitating the sound radiation in the spatial- and frequency domains. The time-domain characteristics of the sound radiation of both the guitar and the compact loudspeaker array will therefore not be given a lot of attention in this work.

It also means that the filters will not be required to run in real-time with no audible latency, even though this would be a necessary feature in a commercial product aimed at guitarists.

Instead, the filters can just be implemented as digital FIR filters of arbitrary length on a PC, while effort can instead be concentrated towards making the best possible radiation patterns. Due to the limited frequency range of the guitar, a sampling frequency of  $f_s = 32$  kHz has been decided to be used throughout this project, instead of the more commonly used sampling frequency of 44,1 kHz or 48 kHz.

# Measurements of the Directivity Pattern of an Acoustic Guitar

# 4

As it is desired to design a loudspeaker array made for one specific radiation pattern, then a good place to start is by measuring this radiation pattern to the required degree of accuracy.

In this chapter, measurements of the directivity pattern or sound radiation pattern of an acoustic guitar are presented. The measurements are performed in both 2D and 3D, where the 3D measurements will form the basic target radiation pattern for the desired loudspeaker array system.

## 4.1 Initial 2D Measurement in an Anechoic Chamber

In order to determine the amount of details in the radiation pattern of a guitar and clarify which directions are “important” or dominant for the guitar radiation pattern as well as the amount of spatial resolution necessary for obtaining enough details, a measurement of the radiation pattern was performed in 2D for the horizontal plane. This was followed by another 2D measurement being an attempt to determine the overall radiation pattern in the frontal plane.

The 2D measurement setup consisted of a semicircle arch of 1.7 meters in radius in the horizontal plane, filled with 31 microphones distributed at every  $6^\circ$  in the range  $-90^\circ < \theta < 90^\circ$ .

The arch was placed horizontally in an anechoic chamber<sup>1</sup>. An acoustic guitar, held by a musician, was placed at the center of the arch in such a way that all microphones had the same distance to a fixed point on the guitar when the guitar front side was pointing at the microphone at  $\theta = 0^\circ$ .

The semicircle arch was fixed in a vertical height of 1.1 meters which also roughly corresponded to the height of the guitar’s center when the musician was sitting on a chair.

Overall the measurement procedure consisted of a musician playing a short music section<sup>2</sup> for about 20 seconds while the pickup signal from the guitar itself and the output signal at the 31 microphones on the semicircle arch were recorded simultaneously. A more complete description of the measurement setup, equipment, and procedure can be found in Appendix B.

The measurements were performed with an acoustic guitar of the model ‘Fender CD-60 CE’ equipped with a piezoelectric pickup from Fishman of the model ‘Fishman Isys’.

### 4.1.1 Observations and Preliminary Results of Guitar Radiation Pattern

These measurement results are only used to get an idea of how the guitar radiates the sound and will thus not tell the full story of the radiation pattern of the guitar in the surrounding dimensions. The focus is to determine the radiation pattern for both the half and the full horizontal plane as well as an attempt to

---

<sup>1</sup>The specific anechoic chamber was the ‘large anechoic chamber’ at AAU which is anechoic down to around 65 Hz.

<sup>2</sup>like open chords, barre chords, a sequence of single notes, etc.

obtain the overall radiation pattern in the frontal plane using an offset of around 1 meter in the guitar front direction.

The calibrated microphone measurements  $y_\theta[n]$  are analyzed in 1/3 and 1/6 octave bands from 79 Hz - 10 kHz before the RMS value is calculated for each frequency band of each microphone channel. Afterward, RMS values of each frequency band get divided by the corresponding RMS value of the reference pickup signal  $x[n]$  for the same frequency bands. It provides a set of 'gains' relative to the observed pickup signal for all the frequency bands acting as a discretized representation of the beam pattern of the sound going from the guitar to each microphone position. Since the microphone signals are calibrated these gains can be given in terms of sound pressure in Pascal over full-scale digital signal level.

This process is illustrated in Figure 4.1.

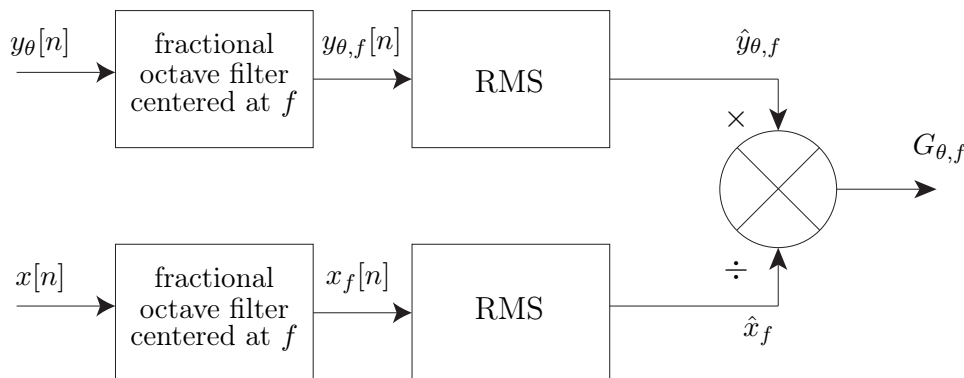


**Figure 4.1:** Computation of the frequency dependant gain factors from the recorded signals.

For the sake of visualization, the gains are normalized to the maximum RMS value of all the frequency bands for one measurement at a time to get a common scale for different results.

Polar plots showing the beam pattern gains from the 2D measurement can be found in Section B.4, while directivity sonograms of the measurements will be presented in this section.

The guitar radiation pattern at high frequencies should be taken with caution as it only shows how the guitar will beam the frequencies with a certain gain but not the actual sound pressure level. The guitar will often only produce very small signal levels in the high-frequency area and hence often not radiate much energy in this frequency area even though the high frequencies are greatly amplified in the microphone recordings compared to the pickup recordings.

An example of this situation can be seen by comparing the power spectrum of the peak signal in Figure 4.2a with the SPL directivity sonogram of Figure 4.2b, which is instead showing the actual sound pressure level over frequency at different measurement points.

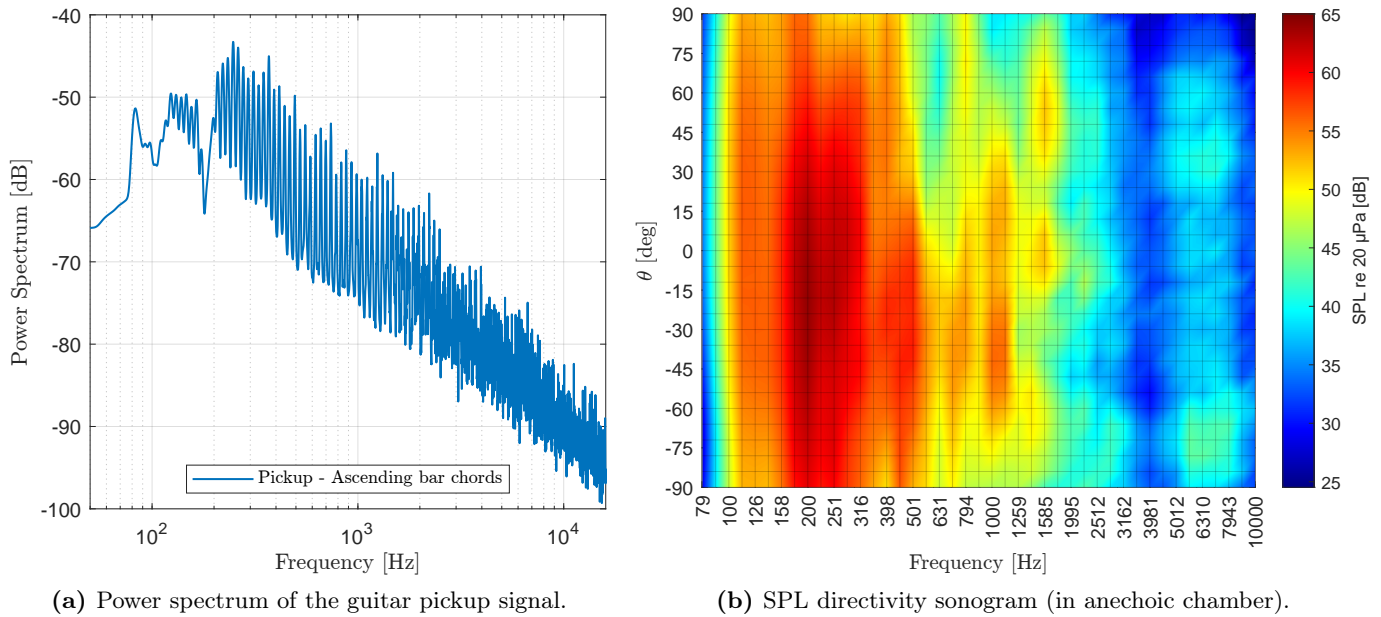


**Figure 4.2:** The left plot is the power spectrum of the guitar pickup signal when playing 20 seconds of ascending barre chords (25dB/decade). The right plot is the SPL directivity sonogram in the half horizontal plane at a distance of 1.7m when playing ascending barre chords using interpolated 1/6 octave bands to plot frequency vs. azimuth angle  $\theta$ . Front direction is  $\theta = 0^\circ$

From the plots of Figure 4.2 it can be seen that the guitar only produces very small pickup signals at middle and high frequencies when playing ascending barre chords. It agrees with the assumption that this frequency range mainly consists of the higher harmonic tones of the guitar. It can also be seen from the SPL directivity sonogram that the guitar does not produce high sound pressure levels above 2000 Hz, which corresponds well with the smaller pickup signal level at these frequencies. However, there are small to medium-sized peaks in the SPL directivity sonogram around 7000 Hz.

This might be due to some analog low-pass filtering being applied at the pickup. The frequency content at 5 - 8 kHz probably does not include much complex tonal content, but rather it could be transient content produced when the strings are initially set into motion. For example, impulsive sound events of this kind could be produced from the hand of the guitarist physically hitting the guitar strings. This might not cause the same vibration at the point where the pickup is as the eventual standing waves of the guitar strings, but this is mostly speculation.

### Different Playing Styles in the Half Horizontal Plane

In order to see the impact of different types of excitation on the radiation pattern, different guitar radiation patterns for different playing styles have been measured in the front half of the horizontal plane. The musician was sitting on a chair facing the guitar front at  $\theta = 0^\circ$  while playing the different pieces of music.

Polar plots, in the half horizontal plane, showing the beam pattern for different 1/3 octave bands with different playing styles can be found in Figure B.4 in the appendices. In addition directivity sonograms of the guitar in the half horizontal plane with different playing styles can be seen plotted in Figure 4.3 using 1/6 octave bands and interpolation to smooth the plots out.

In the polar plots of Figure B.4 it can be seen that the general beam patterns for each 1/3 octave bands are very similar for all playing styles and that the patterns follow the same trends over frequency. The polar plots for different playing styles do have some magnitude differences for some frequency bands, which indicates

that the guitar playing style does have an impact on the energy radiated at some frequency. However, these magnitude differences do not change the general beam pattern significantly.

A better overview of the influence that different playing styles provide in the horizontal plane is shown in the directivity sonograms of Figure 4.3. From these directivity sonograms, it can again be seen that the overall sound radiation pattern is very similar for all the playing styles. The only big difference between them lays in the amount of energy radiated in different directions at some frequency bands.

From Figure B.4 in the appendix and Figure 4.3 it can also be seen that the guitar is radiating sound in a pretty omnidirectional pattern for the low frequencies up to around 200 Hz and has its peak gain at around 180 Hz. At around 500 Hz the beam pattern seems concentrated to an angle of around  $\theta = -30^\circ$ , while at 1000 Hz the beam pattern gets centered to the front direction again. From around 1500 Hz the guitar starts to beam in different directions (around  $\theta = 60^\circ$ ,  $\theta = 0^\circ$ ,  $\theta = -60^\circ$  azimuth) followed by a frequency interval from 2500 Hz to 5000 Hz characterise by a low gain in all the directions. Lastly, around 7000 Hz to 8000 Hz the guitar is highly directional to around  $\theta = -70^\circ$  and in part also in between  $\theta = 40^\circ$  and  $\theta = 60^\circ$ .

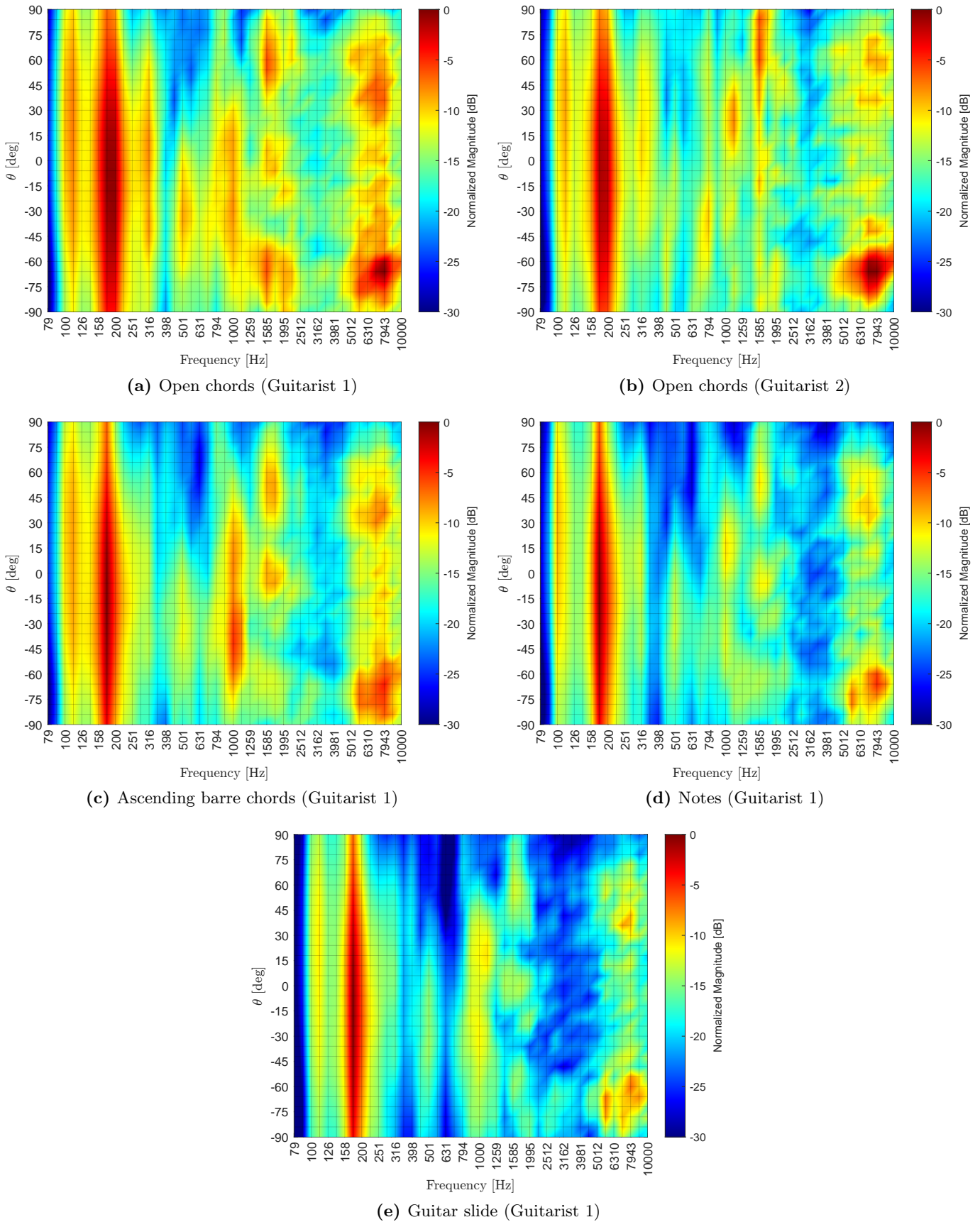


**Figure 4.3:** Directivity sonogram of the guitar in the half horizontal plane with different playing styles as the excitation signal. The figures are obtained by using 1/6 octave bands and are afterward interpolated to have a smoothed plot of frequency vs. azimuth angle  $\theta$ . Front direction is  $\theta = 0^\circ$ .



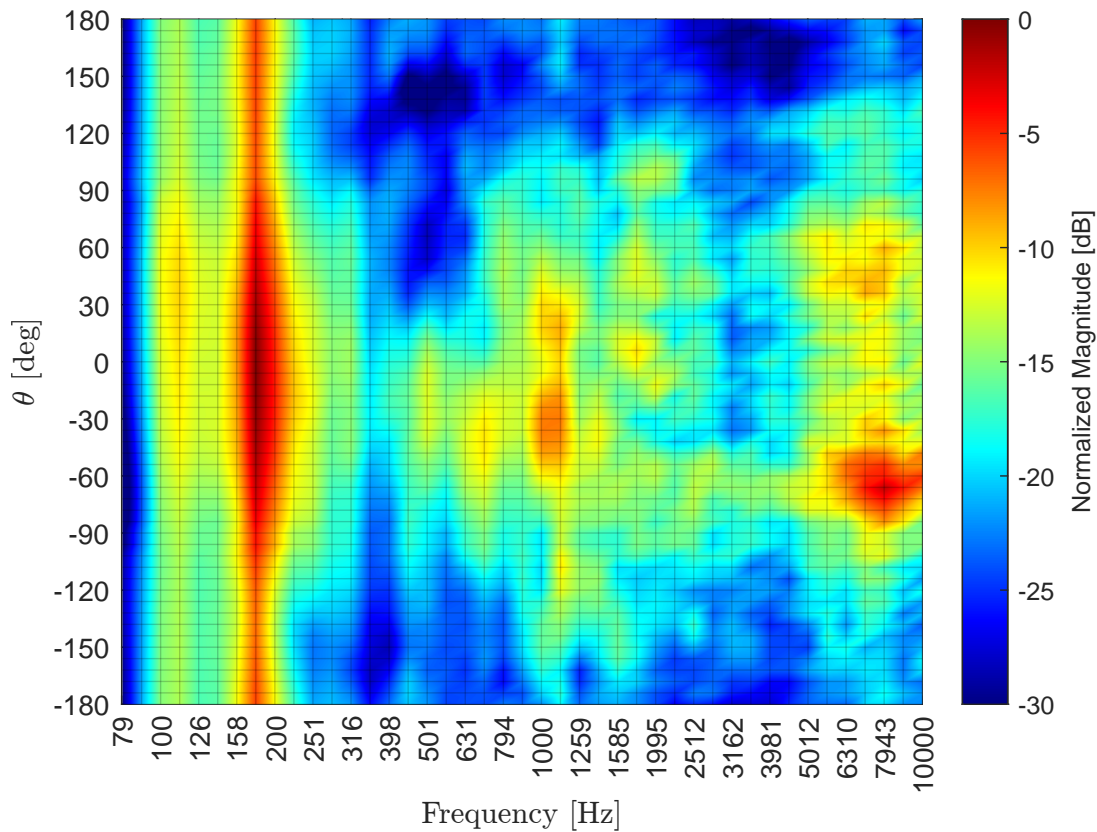


**Figure 4.5:** Directivity sonogram of the guitar in the full horizontal plane using interpolated 1/6 octave bands to plot frequency vs. azimuth angle  $\theta$ . Front direction is  $\theta = 0^\circ$ .

Similarly to the half horizontal plane, the guitar radiation pattern in the full horizontal plane can be seen from the polar plots in Figure B.5 and the directivity sonogram in Figure 4.5. This time the musician is no longer seated on a chair but standing up.

However, more information about the guitar radiation pattern in the horizontal plane is now provided since the back radiation pattern (half-circle centered at  $\theta = 180^\circ$ ) of the guitar is also included. It can be seen that overall the energy radiated to the backside of the guitar is much lower compared to the energy radiated to the front side of the guitar. This effect is probably due to a combination of the sound radiation of the guitar itself as well as the shadowing effect caused by the guitarist holding the guitar.

The guitar radiation pattern behaves more like a cardioid for frequencies above 200 Hz. At these frequencies, the sound radiation to the back starts being negligible compared to the energy radiated to the front of the guitar player, whereas the sound radiation to the sides (around  $\theta = 90^\circ$  and  $\theta = -90^\circ$ ) still have a decent role to play.

### Full "Frontal" Plane

The guitar radiation pattern has been measured twice in the half frontal plane. The measurements were taken with an offset of around 1 meter in the guitar front direction, which made it so that the measurement points were not exactly on the frontal plane but rather on an offset frontal plane. The musician lying on the floor was playing ascending barre chords with the head pointing at  $\phi = 90^\circ$  and  $\phi = -90^\circ$  respectively. The two measured radiation patterns in the half frontal plane are then combined to a single radiation pattern for the full frontal plane.

The full frontal plane can be seen from the polar plots of Figure B.6 of Appendix B where the beam patterns

for different 1/3 octave bands are shown. The directivity sonogram is instead shown in Figure 4.6 and obtained using 1/6 octave bands. The resulting discrete beam pattern values are linearly interpolated for the sake of visualization.

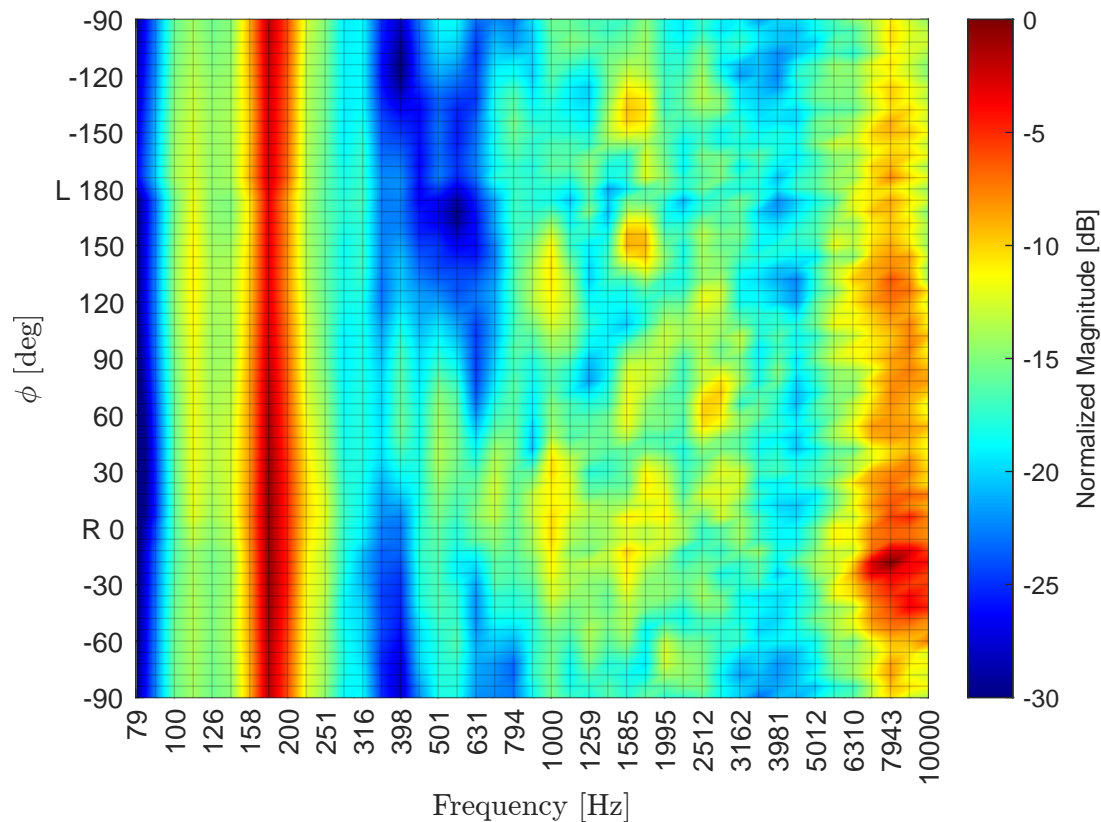


**Figure 4.6:** Directivity sonogram of the guitar in the full frontal plane using interpolated 1/6 octave bands to plot frequency vs. elevation angle  $\phi$ . Right is  $\phi = 0^\circ$ , left is  $\phi = 180^\circ$  and top/head is  $\phi = 90^\circ$ .

The full frontal plane provides some new information about the radiation pattern compared to the horizontal plane. The guitar radiation pattern is very omnidirectional in the frontal plane up to about 300 Hz, where the guitar starts to radiate the energy more above ( $\phi = 90^\circ$  in elevation) than below ( $\phi = -90^\circ$  in elevation) the guitar and slightly to the right side ( $\phi = 0^\circ$  in elevation) of the guitar. However, around 1000 Hz, the guitar starts to beam the sound more in specific directions depending on frequency. Examples of beam direction are  $\phi = 130^\circ$  and  $\phi = 0^\circ$  at 1000 Hz, or  $\phi = -140^\circ$ ,  $\phi = 150^\circ$ ,  $\phi = 60^\circ$  and  $\phi = 0^\circ$  at around 1600 Hz. At the higher frequencies, the guitar radiates the sound in many specific directions with high gain, but predominantly with a beam to the lower right, at around  $\phi = -20^\circ$ .

However, the results from this full "frontal" plane should be taken with caution since the frontal plane was measured with an offset from the true frontal plane. For example, parts of the musician's body, like the head, are not shadowing as much the guitar sound radiation as they would do in the situation of a true frontal plane.

### Partial Conclusion for the 2D Measurements of the Guitar Radiation Pattern

It can be concluded from the different measurements of the guitar radiation pattern in both the horizontal and frontal plane, that the general beam/radiation patterns for each 1/3 octave band are similar for all playing styles. It can also be concluded, that the radiation patterns follow the same trends over frequency, even though the playing style might influence the overall magnitude for some frequency bands. Anyway,

playing ascending barre chords is found to be the most robust and easy to reproduce, and therefore chosen as the guitar excitation signal.

Overall, at the low frequencies, the guitar radiates sound in a somewhat omnidirectional pattern, but as the frequency increases, the radiation to the back starts to decrease. From 1000 Hz on, the guitar radiation pattern becomes more complex and begins to beam the sound more in specific directions depending on frequency, which requires both good spatial resolution and narrow bandwidth in analysis to be determined exactly. However, even if the musician is sitting still on a chair and playing, it was found that small movements or rotations of a few degrees of the guitar will occur naturally, which can result in large uncertainties of the actual radiation pattern at the measurement points. A too high spatial resolution might not be worthwhile as it does not allow these small natural movements of the guitar.

A spatial resolution of  $10^\circ$  might therefore be a better and less complex compromise between the amount of details and uncertainties caused by the guitar movement compared to e.g. a spatial resolution of  $6^\circ$ . A resolution of  $10^\circ$  will still result in a very large number of measurement points on a sphere if both the azimuth and elevation angles are sampled. This should be enough to characterize the overall radiation pattern of the guitar.

## 4.2 Spherical 3D Measurement in an Anechoic Chamber

In order to determine the basic target radiation pattern for the desired loudspeaker array system, a measurement of the guitar radiation pattern was performed in 3D, with measurement points covering a sphere surrounding the guitar.

The 3D measurement setup consisted of a semicircle arch of 1.7 meters in radius, positioned in the vertical plane orthogonal to the floor. The metal arch was filled with 17 microphones attached to plastic flat bars distributed at every  $\phi = 10^\circ$  in the range  $-70^\circ < \phi < 90^\circ$  creating a free-field microphone semicircle with radius 1.53m. The musician holding the acoustic guitar of interest was placed on a high chair fixed to a turning table allowing the guitarist to be rotated horizontally. The chair and guitarist were placed in such a way that the guitar soundhole center was located in the origin of the semicircle arch even when the musician was rotated around by the turning table.

The measurement procedure consisted of a musician playing 20 seconds of ascending barre chords on a guitar while simultaneously recording the pickup signal of the guitar and the signal at the 17 microphones on the arch. The procedure was repeated for multiple turntable steps with a step-size of  $5^\circ$ , so the guitar front was facing at  $\theta = 0^\circ, 5^\circ, \dots, 360^\circ$ . A more complete description of the measurement setup, equipment, and procedure can be found in Appendix C.



**Figure 4.7:** Picture of the setup for the 3D measurement of the sound radiation of the acoustic guitar. The guitarist is seated on a chair located on a turntable in the middle of an arch of microphones.

#### 4.2.1 Analysis of Recordings

The measurements are analyzed in 1/3 octave and 1/6 bands from 79 Hz-10 kHz. First, the RMS value is calculated for each frequency band for all turntable step recordings and afterward scaled with the corresponding RMS value of the reference pickup signal. This provides a transfer beam pattern matrix of gains relative to the observed pickup signal for all frequency bands.

Due to the nature of the measurement procedure, some directions were measured several times, like  $\phi = 90^\circ$ . A recording at both  $0^\circ$  and  $360^\circ$  was also obtained to compensate for the movements that might have occurred between the first and last measurement. In all these cases an average of all the RMS-values was calculated for overlapping directions.

In order to account for the differences in guitar playing between the 73 rotations of the chair, the transfer beam pattern matrix is transformed into a new smaller matrix with  $10^\circ$  spatial resolution in both azimuth and elevation angles by averaging every azimuth step size of  $\theta = 10^\circ$  with  $\pm 5^\circ$  of the transfer beam pattern matrix.

To be able to compare the measured radiation patterns in 3D to the previous measurements, the gains have again been normalized to the maximum RMS-value of all recorded directions for the visualizations<sup>3</sup>.

At high frequencies, the guitar radiation pattern should again be taken with caution as it only shows how the guitar will beam the frequencies with a certain gain, but not the actual sound pressure level. As already mentioned and shown in Figure 4.2 the guitar will often only produce very small pickup signals for the high frequencies, and hence often not radiate much energy or produce high sound pressure levels in this frequency area.

In order to visualize the radiation pattern of the guitar in 3D, the gains at all the measurements point in a

<sup>3</sup>The absolute gain is not really of great significance to the project as a whole, since the point of using a loudspeaker is often to get more overall gain compared to the guitar

single frequency band are visualized as a surface or 'balloon' where the distance of every point on the surface to the origin corresponds to the gain at this direction. The 'balloons' have also been colored according to these same gains for better visual clarity.

All balloon-style directivity plots from the 3D measurement can be found in Section C.4, while a few selected balloon-style directivity plots and different directivity sonograms of the measurements will be presented in this section.

#### 4.2.2 Results of the Guitar Radiation in a 3D Sphere

The balloon-style directivity plots in Figure C.6 and Figure C.7 show the full 3D guitar radiations for different 1/3 octave bands with  $10^\circ$  spatial resolution ( $\theta = 10^\circ$  averaged from  $\pm 5^\circ$ ) from the 3D view and from the top-view (horizontal plane) respectively. These patterns will form the basis for the target radiation pattern for the desired loudspeaker array system. Anyway, few balloon-style directivity plots for some selected 1/3 octave bands can be seen in Figure 4.8, so to get an idea of how the guitar radiation pattern evolves with frequency.

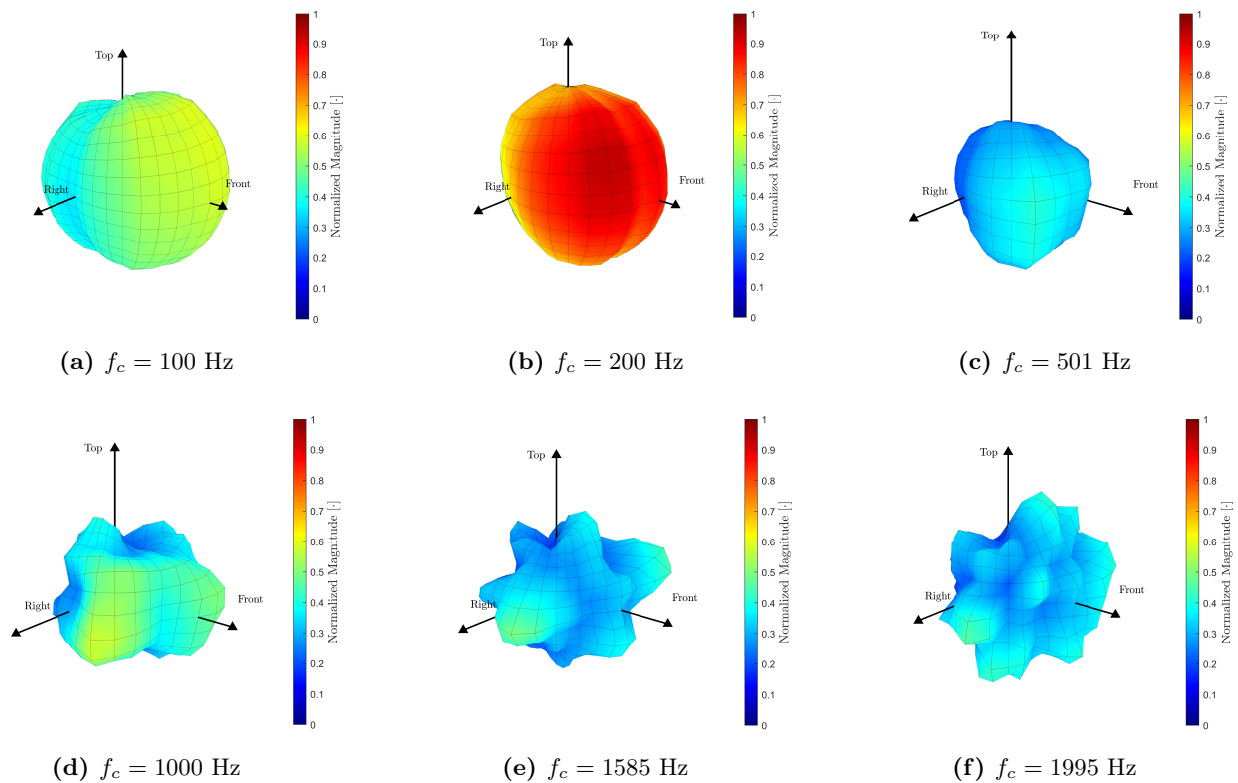


**Figure 4.8:** 3D Balloon-style directivity plots (3D view) for the guitar radiation for a few selected 1/3 octave bands with  $10^\circ$  spatial resolution ( $\theta = 10^\circ$  averaged from  $\pm 5^\circ$ ). The plots are normalized over the maximum magnitude for all 1/3 octave bands in between 79 Hz to 10 kHz.

However, to get an overview over this radiation pattern in the horizontal, frontal and median plane, the directivity sonograms of the guitar in the horizontal, frontal and median plane are plotted in Figure 4.9, Figure 4.10 and Figure 4.11 using 1/6 octave bands. These can also serve as a good comparison with the 2D measurement results.

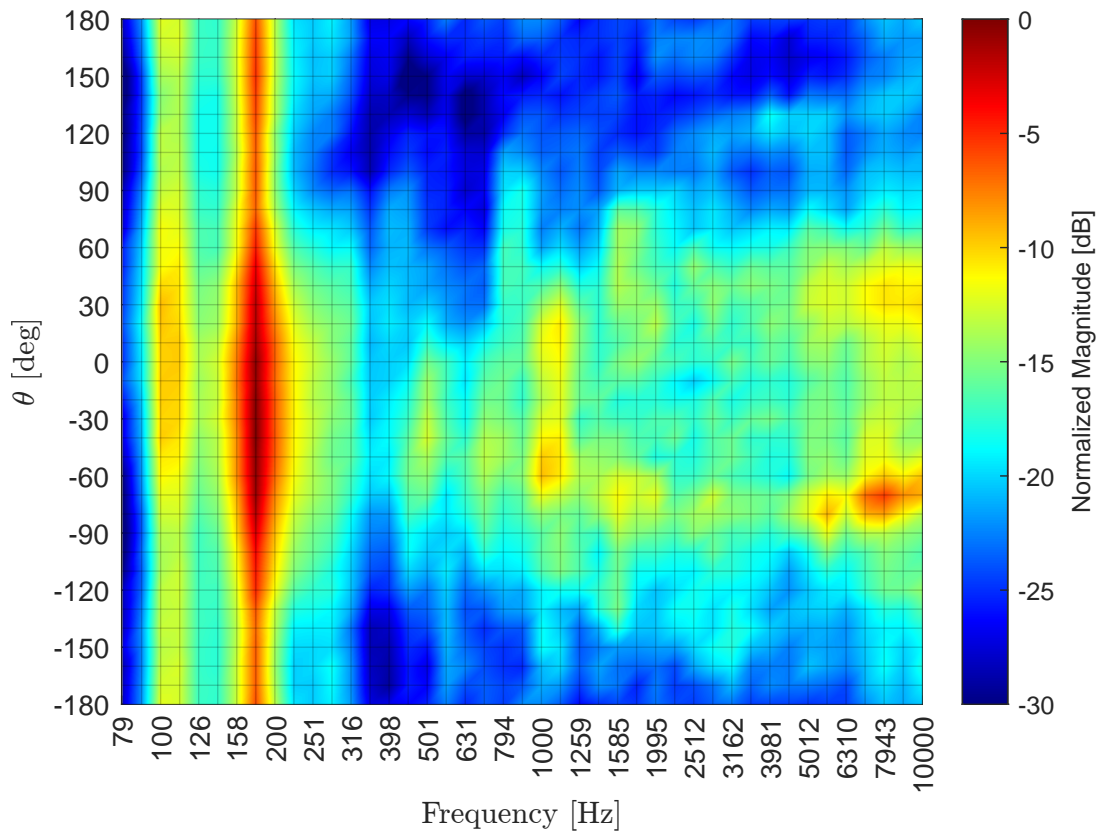


**Figure 4.9:** Directivity sonogram of the guitar in the full horizontal plane from the 3D measurement using interpolated 1/6 octave bands to plot frequency vs azimuth angle  $\theta$ . Front direction is  $\theta = 0^\circ$

From Figure 4.9 it can also be seen that the guitar radiation pattern in the horizontal plane is very similar to the results obtained in the 2D measurement of Figure 4.5. The guitar radiates sound in an omnidirectional pattern for the low frequencies up to around 200 Hz and peaks in gain around 180 Hz. Above 200 Hz, the body of the musician is shadowing the sound radiation of the guitar going to the back, making the guitar radiation pattern behave more like a cardioid pattern. The beam pattern is concentrated to an angle of around  $\theta = -40^\circ$  azimuth at around 500 Hz, and to angles around  $\theta = -60^\circ$  and  $\theta = 10^\circ$  at 1000 Hz. Above 1000 Hz the guitar starts to beam in different directions in between around  $\theta = -80^\circ$  and  $\theta = 60^\circ$ . In the high frequencies, around 8000 Hz, the guitar is again highly directional to  $\theta = -70^\circ$  and to  $\theta = 40^\circ$ .

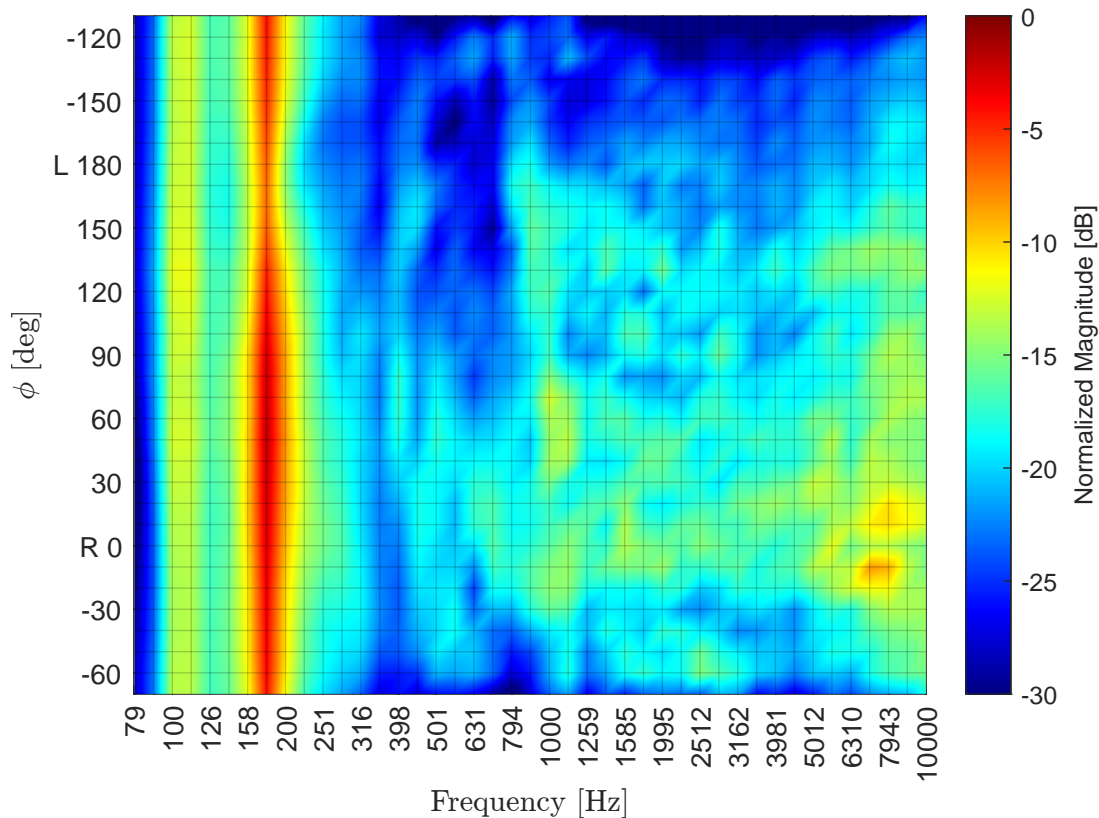


**Figure 4.10:** Directivity sonogram of the guitar in the frontal plane from the 3D measurement using interpolated 1/6 octave bands. The plot is shown in elevation angle  $\phi$  vs. frequency. To get a reference,  $\phi = 0^\circ$  is the right side, while left is  $\phi = 180^\circ$  and top/head is  $\phi = 90^\circ$ .

The guitar radiation pattern in the frontal plane of the 3D measurement can be seen in Figure 4.10. Unlike the roughly "frontal" plane of the 2D measurements seen in Figure 4.10, the frontal plane of the 3D measurements is only obtained down to an elevation angle of  $\phi = -70^\circ$  both in the right and left side of the plane. However, this time the frontal plane is in fact the true frontal plane as it was not measured with any offset in the guitar front direction<sup>4</sup>.

The radiation pattern provided in the frontal plane is omnidirectional only up to about 200 Hz. Above those frequencies, the guitar starts to radiate more to the right side. In general, it seems like the guitar radiates the sound to the bottom of the frontal plane with lower gain (e.g. angles in between  $\phi = -150^\circ$  to  $\phi = -60^\circ$  below the horizontal plane) compared to the upper part. However, it must be said that the turning table platform on which the chair was mounted starts to shadow the guitar sound radiation from around  $\phi = -70^\circ$ . For this reason, no measurements were performed below that angle.

The reason for the presence of this gain difference in between the top and bottom part of the frontal plane may be given to multiple reasons. One likely reason could be the shadowing effect that both the musician and the chair are imposing to the guitar's sound radiation. The guitar is indeed more free to radiate to the top of the plane, which is left empty, compared to the bottom part, instead occupied by the musician sitting on the chair.

However, the top part of the frontal plane does also show low gain at around  $\phi = 90^\circ$ . This is thought to be caused by the shadowing effect of the head, which starts to interfere with the guitar's sound radiation for wavelengths comparable with dimensions of the head itself, i.e. frequencies above 1000 Hz. At the higher

<sup>4</sup>Of course disregarding the small inaccuracy there might be in the placement of microphones on the arch and the turning of the turning table.

frequencies, the guitar radiates the sound with high gain predominantly towards the lower right angles at around  $\phi = -20^\circ$  elevation.

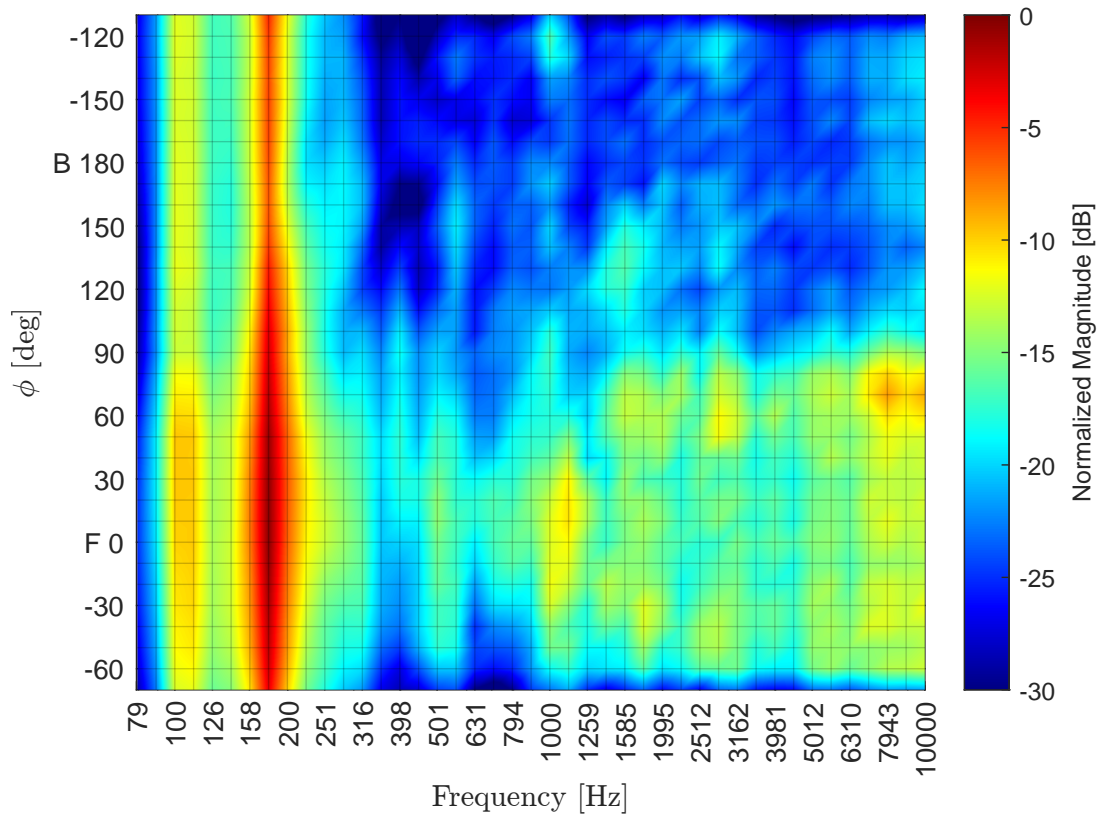


**Figure 4.11:** Directivity sonogram of the guitar in the median plane from the 3D measurement using interpolated 1/6 octave bands to plot elevation angle  $\phi$  vs. frequency. Front is  $\phi = 0^\circ$ , back is  $\phi = 180^\circ$  and top/head is  $\phi = 90^\circ$ .

Lastly, the radiation pattern for the median plane is shown in Figure 4.11. This plot helps one get a different view of how the guitar radiates sound to the front compared to the back. Once again, the radiation pattern is omnidirectional up to around 200 Hz. Above this frequency, the guitar predominantly radiates the sound to the front, beaming within the angles  $\phi = -60^\circ$  and  $\phi = 90^\circ$  for almost all the frequency bands.

Some of this behavior can probably be attributed to the shadowing effect of the body of the musician seated on the chair. This effect starts at  $\phi = 90^\circ$  which corresponds to when the head begins shadowing the direct sound and should theoretically end at  $\phi = -90^\circ$ . Unfortunately, not much can be said about the bottom angles going in between  $\phi = -90^\circ$  to  $\phi = -70^\circ$ , as no measurements were taken within  $-110^\circ < \phi < -70^\circ$  due to the already mentioned shadowing effect of the turntable.

### 4.2.3 Partial Conclusion for the 3D Measurement of the Guitar Radiation Pattern

After having analyzed the measurements done in 3D, it is now possible to get conclude on the results. The radiation patterns observed follow a similar trend to the 2D measurements, but with additional information for the points on the sphere not previously measured.

Generally, it can be deduced from both the 3D balloon plots and from the different sonograms that the radiation pattern is mainly omnidirectional for frequencies below 200 Hz. Then, as the frequency increases, the guitar loses its omnidirectionality and starts to beam the sound into some specific zones but with less gain than before. Around 1000 Hz, many factors start to play a role in the radiation. The guitar gets shadowed by the body of the musician, and the radiation of the sound gets mostly concentrated to the front-right side.

An example of that is shown in Figure 4.11 as well as in the top-view of the balloon plots of Figure C.7 in the Appendix C.

For higher frequencies, the radiation pattern gets very intricate, and the sound gets beamed towards many narrow spots in space. The predominant direction is the front, even though it gets more spread to the right or the left side at certain frequencies. However, it is difficult to make a general argument or trend, as the directivity pattern continuously varies even for adjacent frequency bands, as it can be also seen from Figure C.6 and Figure C.7 in the Appendix C.

Overall, the measurements have provided a great deal of insight into the overall radiation patterns of an acoustic guitar. While the angular resolution of  $10^\circ$  puts a limit to how detailed the sound radiation can be described, it was still possible to observe well defined 'lobes' in the sonograms, even up to high frequencies<sup>5</sup>.

Above 200 Hz, the sound is primarily radiated towards the front of the guitar, roughly in between  $\theta = -90^\circ$  and  $60^\circ$  in the horizontal plane and the front part of the median plane. This information may be very useful in designing the loudspeaker system to recreate this pattern, as it might be beneficial to give special attention to these directions.

---

<sup>5</sup>Some details might be lost at frequencies with wavelengths smaller than the distance between adjacent microphone positions, but this level of detail in the radiation pattern would probably be extremely hard to recreate anyway.

# Simulations of Compact Loudspeaker Arrays

# 5

With a suitable description of the target radiation pattern in place, due to the measurements, it is now possible to look into how a specific radiation pattern can be approximated with a compact loudspeaker array. In order to fully investigate how well this can be done with different loudspeaker arrays and methods, a method for simulation of the free-field radiation of a compact loudspeaker array is needed. Such a method will be described in this chapter by first setting up a generalized model for the compact loudspeaker array and describing the numerical methods used for computing the far-field sound pressure produced by this array.

## 5.1 Model of a Compact Loudspeaker Array

In order to simulate the radiation of a loudspeaker array for the synthesis of radiation patterns, a general model will be established.

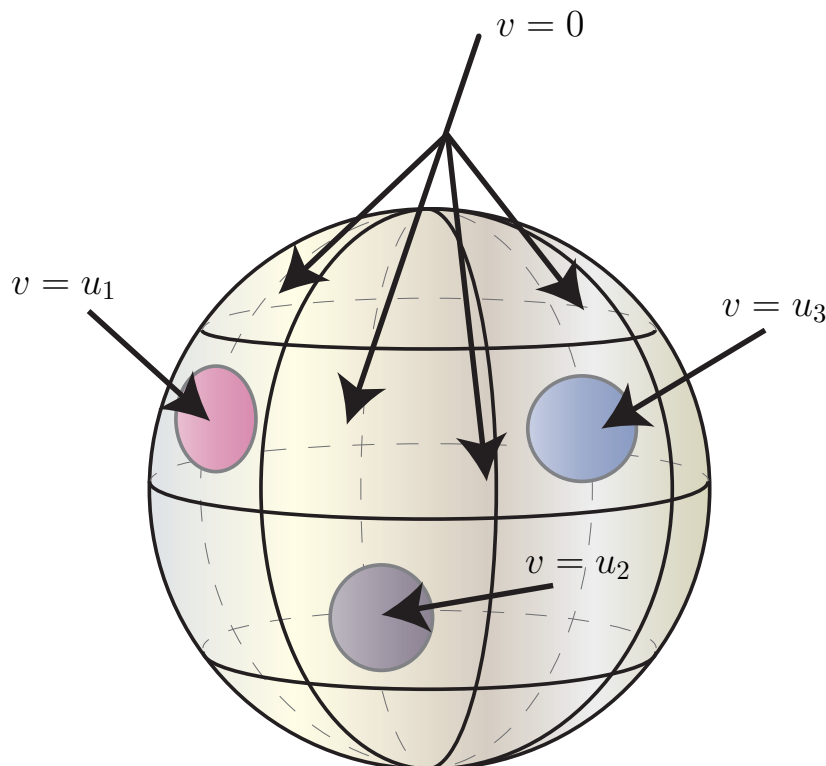


**Figure 5.1:** Simplified model of a loudspeaker array (Even though it is illustrated as a sphere here, the shape of the enclosure is only assumed to some shape with a closed surface).

The physical part of the loudspeaker system can be modeled as a closed surface in three-dimensional space, with several 'pistons' placed on parts of the surface. The surface of each piston has a constant particle velocity  $u_i$ , and each piston is assumed to be able to vibrate at an arbitrary velocity independent of the

other pistons. The remaining part of the surface is assumed to be acoustically rigid, and therefore every point of the surface not on a piston will have zero velocity, as illustrated in Figure 5.1.

This model is similar to the 'Spherical Cap' model used in [22, 40], except that the spherical cap model assumes the surface to always be a sphere. This gives the spherical cap model a nice analytical solution to the pressure at the far-field due to the vibrating pistons when the loudspeaker is assumed to be a sphere.

In order to keep the simulations more general in regards to the geometry of the loudspeaker array, solving the pressure in the far-field analytically quickly becomes an infeasible task. Instead, a numerical method is used.

## 5.2 The Boundary Element Method

The Boundary Element Method (BEM) is a numerical method for solving partial differential equations that can be transformed to a *Boundary Integral Equation* (BIE). Particularly in the field of acoustics, BEM is useful in situations where the Helmholtz equation can be transformed into the Kirchhoff-Helmholtz integral equation[44, Chapter 4].

By posing the solution to an acoustic field governed by the Helmholtz equation into an integral over some boundary surface only the solution on the surface is needed to determine the pressure at every point in the sound field. Thus only the surface has to be discretized in the numerical calculations.

This gives BEM some advantages over other numerical methods like Finite Element or Finite difference, where the whole domain will have to be discretized. BEM especially has some advantages in problems in an exterior (i.e. infinite) domain, e.g. the sound radiation of a loudspeaker in a free-field, with which BEM has been used in several studies[45].

Consider a vibrating body with a surface  $S$  vibrating at a frequency  $f$  radiating sound out into an exterior domain  $E$ , as illustrated in Figure 5.2.

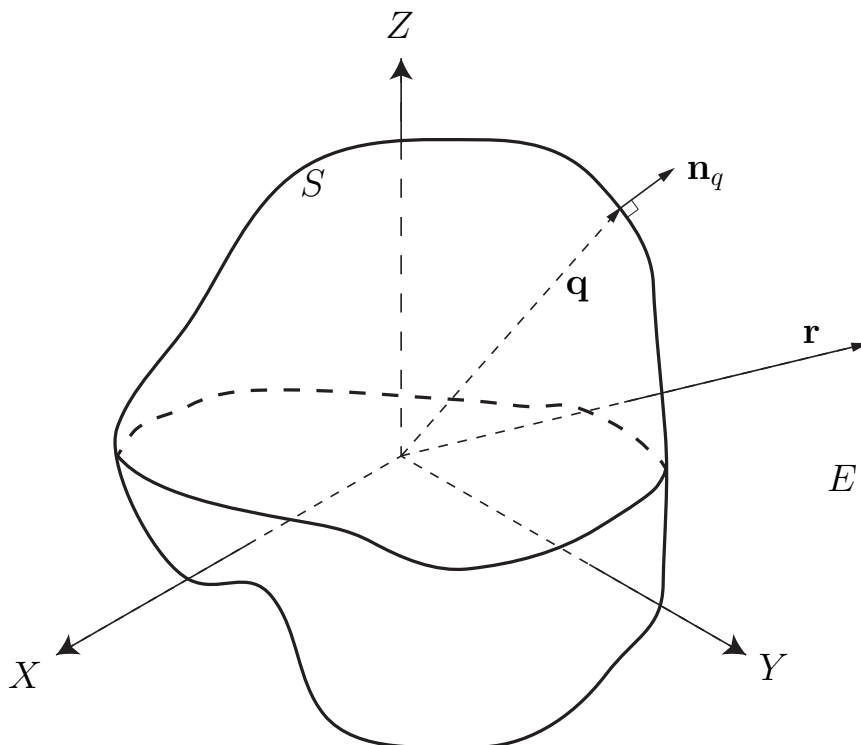


**Figure 5.2:** Vibrating body with surface  $S$  in exterior domain  $E$ . Adapted from [46, Ch. 2]

The pressure  $p$  at a point  $\mathbf{r}$  resulting from this vibrating surface can be expressed with the Kirchhoff-Helmholtz integral equation as[46]

$$\mu(\mathbf{r})p(\mathbf{r}) = \int_S p(\mathbf{q}) \frac{\partial G_k(\mathbf{r}, \mathbf{q})}{\partial \mathbf{n}_q} + jk\rho_0cv(\mathbf{q})G_k(\mathbf{r}, \mathbf{q}) dS(\mathbf{q}) \quad (5.1)$$

where  $\mathbf{q}$  is a dummy variable representing every point on the surface  $S$ ,  $k = \frac{2\pi f}{c}$  is the wavenumber,  $v$  is the particle velocity in the outwards pointing normal direction to the surface given by the unit vector  $\mathbf{n}_q$ ,  $G_k(\mathbf{x}, \mathbf{y}) = \frac{e^{jk\|\mathbf{x}-\mathbf{y}\|}}{4\pi\|\mathbf{x}-\mathbf{y}\|}$  is the free space Green's function for three dimensions.

The free space Green's function corresponds to the sound pressure at a point in free space  $\mathbf{x}$  resulting from an acoustic point source, or monopole at  $\mathbf{y}$  also in free space<sup>1</sup>. Its derivative with respect to the normal vector  $\mathbf{n}_x$  can be expressed as  $\frac{\partial G_k(\mathbf{r}, \mathbf{q})}{\partial \mathbf{n}_x} = \frac{e^{jk\|\mathbf{x}-\mathbf{y}\|}}{4\pi\|\mathbf{x}-\mathbf{y}\|} \left( ik - \frac{1}{\|\mathbf{x}-\mathbf{y}\|} \right) \frac{\partial \|\mathbf{x}-\mathbf{y}\|}{\partial \mathbf{n}_x}$  which corresponds to a dipole[44, Ch 4].

$\rho_0$  and  $c$  are the medium density and speed of sound respectively. The function  $\mu$  is a factor depending on whether  $\mathbf{r}$  is directly on the surface or not, such that

$$\mu(\mathbf{r}) = \begin{cases} 1, & \mathbf{r} \in E \\ \frac{1}{2}, & \mathbf{r} \in S \\ 0, & \text{otherwise} \end{cases} \quad (5.2)$$

A derivation of this integral equation can be found in great detail in [44, Chapter 5] or [46, Chapter 2].

If either the pressure or velocity on the surface is known beforehand, then the other one can be determined by manipulating Equation 5.1. Once the full solution on the surface is known, then the pressure at any point in space can be uniquely determined. In practice, the integral equation can only be solved analytically for simple geometrical shapes, and even then it is not always a trivial thing to do.

Instead, the boundary element method approximates the solution by decomposing the surface into  $N$  panels of simpler shape  $S_1, \dots, S_N$  where the integral can more easily be computed, for example, triangles and rectangles.

$$\mu(\mathbf{r})p(\mathbf{r}) \approx \sum_{n=1}^N \int_{S_n} p(\mathbf{q}) \frac{\partial G_k(\mathbf{r}, \mathbf{q})}{\partial \mathbf{n}_q} + jk\rho_0cv(\mathbf{q})G_k(\mathbf{r}, \mathbf{q}) dS_n(\mathbf{q}) \quad (5.3)$$

These smaller surfaces are usually referred to as 'Elements' in BEM terminology. It should be obvious that the accuracy of the approximation improves by using a large number of small elements instead of a smaller number of large elements. It is often reported that an element length of six elements per wavelength tends to yield a result without too much error[47].

### 5.2.1 Collocation

The solution on the surface can be found in several ways. The simplest and probably most often used in the field of acoustics is the "Collocation Method"[45, 46, 48].

<sup>1</sup>The free field Green's functions is found as a solution to the inhomogenous Helmholtz equation  $(\nabla)^2 + k^2)G(\mathbf{x}, \mathbf{y}) = \delta(\|\mathbf{x} - \mathbf{y}\|_2^2)$ , constrained to fulfill Sommerfield's radiation condition  $\lim_{r \rightarrow \infty} [r \left( \frac{\partial p}{\partial r} - jkp \right)] = 0$  [44, Ch 4]

The collocation method starts with assuming that the surface of each element  $S_n$  has a constant pressure  $p_n$  and velocity  $v_n$ . As long as the elements are sufficiently small compared to the wavelength, this is still a pretty good approximation. This allows the acoustic variables to be taken outside of the integral.

$$\mu(\mathbf{r})p(\mathbf{r}) \approx \sum_{n=1}^N \left[ p_n \int_{S_n} \frac{\partial G_k(\mathbf{r}, \mathbf{q})}{\partial \mathbf{n}_q} dS_n(\mathbf{q}) + v_n \int_{S_n} jk\rho_0 c G_k(\mathbf{r}, \mathbf{q}) dS_n(\mathbf{q}) \right] \quad (5.4)$$

The next step is to place  $N$  points  $\mathbf{r}_i$  on the surface, conventionally at the midpoint of each element [48, Ch. 1]. This allows you to put up  $N$  equations for the pressure at each point  $\mathbf{r}_i$

$$\frac{1}{2}p_i = \sum_{n=1}^N \left[ p_n \int_{S_n} \frac{\partial G_k(\mathbf{r}_i, \mathbf{q})}{\partial \mathbf{n}_q} dS_n(\mathbf{q}) + v_n \int_{S_n} jk\rho_0 c G_k(\mathbf{r}_i, \mathbf{q}) dS_n(\mathbf{q}) \right] \quad (5.5)$$

$$= \sum_{m=1}^M p_n a_{i,m} + v_n b_{i,m} \quad (5.6)$$

where  $a_{i,n} = \int_{S_n} \frac{\partial G_k(\mathbf{r}_i, \mathbf{q})}{\partial \mathbf{n}_q} dS_n(\mathbf{q})$ , and  $b_{i,n} = jk\rho_0 c \int_{S_n} G_k(\mathbf{r}_i, \mathbf{q}) dS_n(\mathbf{q})$  which can be written on matrix form as

$$\frac{1}{2}\mathbf{p} = \mathbf{A}\mathbf{p} + \mathbf{B}\mathbf{v} \quad (5.7)$$

where the entries of the matrices  $\mathbf{A}$  and  $\mathbf{B}$  are given by  $a_{i,n}$  and  $b_{i,n}$  respectively i.e.

$$\mathbf{A} = \begin{bmatrix} a_{1,1} & \dots & a_{1,N} \\ \vdots & \ddots & \vdots \\ a_{N,1} & \dots & a_{N,N} \end{bmatrix} \quad (5.8)$$

and the vectors  $\mathbf{p}$  and  $\mathbf{v}$  are vectors of the the acoustic variables  $p$  and  $v$  on the collocation points e.g.  $\mathbf{p} = [p(\mathbf{r}_1), \dots, p(\mathbf{r}_N)]^T$

With the velocities on the surface given, the solution for the pressure can be found using simple matrix manipulation as

$$\frac{1}{2}\mathbf{p} = \mathbf{A}\mathbf{p} + \mathbf{B}\mathbf{v} \quad (5.9)$$

$$\iff (\mathbf{A} - \frac{1}{2}\mathbf{I})\mathbf{p} = -\mathbf{B}\mathbf{v} \quad (5.10)$$

$$\iff \mathbf{p} = (\mathbf{A} - \frac{1}{2}\mathbf{I})^{-1}(-\mathbf{B})\mathbf{v} \quad (5.11)$$

where  $\mathbf{I}$  is the  $N \times N$  identity matrix

Once the pressure on the surface has been obtained, the pressure at any point  $\mathbf{r}_e$  in the exterior domain can be determined using Equation 5.4. Given a set of  $M$  field points then a new set of matrices  $\mathbf{A}_{fp}$  and  $\mathbf{B}_{fp}$  can be constructed similarly to  $\mathbf{A}$  and  $\mathbf{B}$  such that

$$\mathbf{p}_{fp} = \mathbf{A}_{fp}\mathbf{p} + \mathbf{B}_{fp}\mathbf{v} \quad (5.12)$$

### 5.2.2 Non-uniqueness Problem & the CHIEF Method

A well-known issue with using BEM is the problem of 'irregular frequencies' [47, Ch. 15], also referred to as the 'non-uniqueness problem'. This issue occurs at the 'eigenfrequencies' or resonance frequencies of the corresponding interior problem and will show up as narrow peaks and dips in the frequency response at these frequencies. However, for exterior problems, they make no physical sense and are purely due to the mathematical formulation of the BIE[46, Ch. 5].

Luckily there are multiple ways of dealing with this issue. A very useful one was proposed by Shenck[49] often called the CHIEF (Combined Helmholtz Integral Equation Formulation) method.

This method is based on placing  $N_{ch}$  additional points  $\mathbf{r}_{ch}$ , called 'CHIEF points', in the interior space bounded by the surface and setting up Equation 5.4 for their pressures with  $\mu(\mathbf{r}_{ch}) = 0$ , i.e.

$$0 = \sum_{n=1}^N \left[ p_n \int_{S_n} \frac{\partial G_k(\mathbf{r}_{ch}, \mathbf{q})}{\partial \mathbf{n}_q} dS_m(\mathbf{q}) + v_n \int_{S_n} jk\rho_0 c G_k(\mathbf{r}_{ch}, \mathbf{q}) dS_n(\mathbf{q}) \right] \quad (5.13)$$

This adds an additional  $N_{ch}$  equations to the linear systems, making it an over-determined system that can be solved in a least-squares sense. This leads to the matrices  $\mathbf{D} = (\mathbf{A} - \frac{1}{2}\mathbf{I})$  and  $\mathbf{B}$  becoming tall like

$$\mathbf{D}_+ = \begin{bmatrix} a_{1,1} - \frac{1}{2}\delta_{1,1} & \dots & a_{1,N} - \frac{1}{2}\delta_{1,N} \\ \vdots & \ddots & \vdots \\ a_{M,1} - \frac{1}{2}\delta_{M,1} & \dots & a_{N,N} - \frac{1}{2}\delta_{N,N} \\ \hline a_{N+1,1} & \dots & a_{N+1,N} \\ \vdots & \ddots & \vdots \\ a_{N+N_{ch},1} & \dots & a_{N+N_{ch},N} \end{bmatrix} \quad (5.14)$$

$$\mathbf{B}_+ = \begin{bmatrix} b_{1,1} & \dots & b_{1,N} \\ \vdots & \ddots & \vdots \\ b_{N,1} & \dots & b_{N,N} \\ \hline b_{N+1,1} & \dots & b_{N+1,N} \\ \vdots & \ddots & \vdots \\ b_{N+N_{ch},1} & \dots & b_{N+N_{ch},N} \end{bmatrix} \quad (5.15)$$

where  $\delta_{x,y}$  denotes the Dirac-delta function  $\delta(x-y)$ . A solution to the surface pressure can then be found as

$$p = (\mathbf{D}_+^H \mathbf{D}_+)^{-1} \mathbf{D}_+^H (-\mathbf{B}_+) \mathbf{v} \quad (5.16)$$

Where the  $\mathbf{D}^H$  superscript denotes the Hermitian transpose of  $\mathbf{D}$ .

However, there are a few things to be mindful of when using the CHIEF method. One needs to determine the number of CHIEF points that are needed (if even necessary) and where to place them. It was shown in [46, Ch. 7] that the number CHIEF points needed can be found from the rank deficiency of the BEM matrices ( $\mathbf{A}$  and  $\mathbf{B}$ ). Another concern is where to place them. If a CHIEF point is placed at a node inside the interior, then the point will not provide any benefit to the solution. Most approaches in the literature seem to suggest picking the point semi-randomly and then either testing whether the point adds any benefit or just adding enough points to be safe[46, 50].

Another way of dealing with the non-uniqueness problem comes from Burton and Miller[51]. In the 'Burton-Miller' method a weighted sum of the conventional BIE in Equation 5.1 and its normal derivative with respect to  $\mathbf{r}$  is taken

$$\text{BIE} + \beta \frac{\partial}{\partial \mathbf{n}_r} \text{BIE} \implies \quad (5.17)$$

$$\begin{aligned} \mu(\mathbf{r}) \left[ p(\mathbf{r} + \beta \frac{\partial}{\partial \mathbf{n}_r} p(\mathbf{r})) \right] &= \int_S p(\mathbf{q}) \frac{\partial G_k(\mathbf{r}, \mathbf{q})}{\partial \mathbf{n}_q} + jk\rho_0 cv(\mathbf{q}) G_k(\mathbf{r}, \mathbf{q}) dS(\mathbf{q}) \\ &+ \beta \int_S p(\mathbf{q}) \frac{\partial^2 G_k(\mathbf{r}, \mathbf{q})}{\partial \mathbf{n}_q \partial \mathbf{n}_r} + jk\rho_0 cv(\mathbf{q}) \frac{\partial G_k(\mathbf{r}, \mathbf{q})}{\partial \mathbf{n}_r} dS(\mathbf{q}) \end{aligned} \quad (5.18)$$

It can be shown that using this combined BIE always yields a unique solution as long as  $\beta$  is a complex number (usually  $j/k$ ). This is especially useful in higher frequencies where the nodes are really closed together, making it hard to place CHIEF points. However, computing the BEM matrices becomes significantly harder, especially for the  $\frac{\partial^2 G_k(\mathbf{r}, \mathbf{q})}{\partial \mathbf{n}_q \partial \mathbf{n}_r}$  part, which tend to be hypersingular[47, Ch. 15], which means that special integration methods must be used[52].

Additionally, a comparison between the two methods has previously been made that suggested the Burton-Miller formulation is only worth it when the geometry of the surface is complex or the frequency is high ( $f > 10kHz$ ), neither of which is true for the loudspeaker simulations needed in this project. For that reason, it has been decided that the CHIEF method is "good enough" for the purposes of this project.

### 5.2.3 Software Implementation

The process of assembling the BEM matrices  $\mathbf{A}$  and  $\mathbf{B}$  by computing the integrals numerically is not an easy task. Luckily a number of software libraries exist that can help in doing this for you[45].

In this project, it has been chosen to use openBEM[53]<sup>2</sup> which is an open-source MATLAB implementation of the direct collocation BEM. The BEM formulations are based on the PhD-thesis by Juhl[46] and the 3D implementation of the code was originally implemented in conjunction with the PhD-thesis by Cutanda[54].

This implementation has been chosen due to its ease of use, its open-source nature, and the fact that it is all based on MATLAB, which makes it very easy to integrate into the rest of the scripts for this project. This also means that the main functionality of the OpenBEM is to assemble the BEM matrices, which can then be manipulated with the normal inbuilt MATLAB functions.

OpenBEM more or less follows the same mathematical conventions as this chapter with a few exceptions. Instead of placing the collocation points at midpoints of the panels, the collocation points are placed at the vertices of the 3D mesh. This means that every entry of the BEM matrices will be given by a sum of the  $a_{m,i}$  coefficients of the surrounding panels, similarly to the axisymmetric BEM-formulation described in [46, Ch. 4.4]<sup>3</sup>. In this way, there is a more direct connection between the computer description of the 3D mesh to the collocation points.

Additionally the Green's function is given as  $\frac{e^{jk\|\mathbf{x}-\mathbf{y}\|}}{\|\mathbf{x}-\mathbf{y}\|}$ , and the factor of  $4\pi$  is instead multiplied onto  $\mu$ .

## 5.3 Optimal Piston Velocities via BEM Simulations

As the model, so far, is only describing the performance purely in the acoustic domain, an optimal solution to the synthesized radiation pattern can be found as a set  $L$  complex driver velocities  $u_1, \dots, u_L$  for each piston.

<sup>2</sup>Available from <http://www.openbem.dk/>

<sup>3</sup>The authors would like to thank Peter Møller Juhl for the clarification of this aspect of OpenBEM.

For such a solution to be found via BEM-simulation, a mapping between the  $L$  discrete driver velocities and the velocity vector  $\mathbf{v}$  used in BEM is needed.

An easy way of describing a piston in the model is by a direction given as a unit vector  $\mathbf{d}_l$ , and an aperture angle  $\alpha_l$ , such that every point  $\mathbf{r}$  inside the resulting cone is part of the piston as illustrated in Figure 5.3.

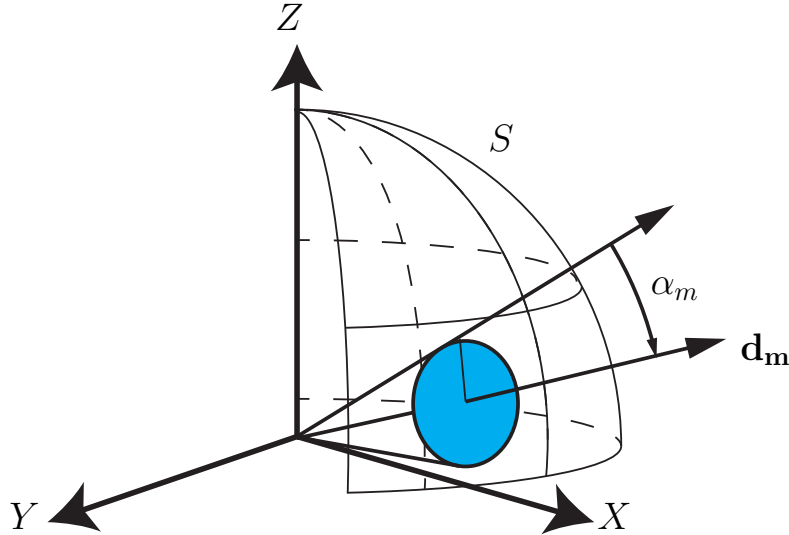


**Figure 5.3:** A piston as an intersection between the surface of the array and the cone around  $\mathbf{d}_m$ .

Whether or not a point  $\mathbf{r}$  on the surface is on the  $l$ th piston can be determined by the following 'aperture function'

$$a_l(\mathbf{r}) = \begin{cases} 1, & \cos^{-1}(\mathbf{d}_l \cdot \frac{\mathbf{r}}{\|\mathbf{r}\|}) \leq \alpha_l \\ 0, & \text{otherwise} \end{cases} \quad (5.19)$$

This function can be applied to all of the  $N$  elements in the BEM-mesh giving the vector  $\mathbf{a}_l = [a_l(\mathbf{r}_1), \dots, a_l(\mathbf{r}_N)]$ . Using these vectors the  $L$  piston velocities  $u_l$  can be mapped onto the velocity vector of the whole mesh  $\mathbf{v}$ .

$$\mathbf{v} = \sum_l^L \mathbf{a}_l u_l \quad (5.20)$$

In some situations it might make more sense to define the pistons in terms of a radius instead of an angle as illustrated in Figure 5.4. If the desired radius, the distance  $d_{center}$  to the surface in the piston direction  $\mathbf{d}_l$  and the distance to the rim of the piston  $d_{rim}$  are known, then the angle can be expressed as

$$\alpha = \cos^{-1} \left( \frac{d_{center}^2 + d_{rim}^2 - r_p^2}{2d_{rim}d_{center}} \right) \quad (5.21)$$

using the law of cosines. Of course, this only makes sense for geometries where  $d_{rim}$  is constant around the intersection between the cone and the surface. Some cases where this holds are if  $S$  is a sphere or if the piston direction is pointing to the midpoint of a flat panel larger than the piston and perpendicular to  $\mathbf{d}_l$ , e.g. on a platonic solid.

In other cases, this simple aperture function might not be so useful. A good example is if you want to place a piston on the side of a box, but not necessarily on the center of the side. In this case, the above model does not hold as the line given by the normal vector of the piston does not go through the origin.

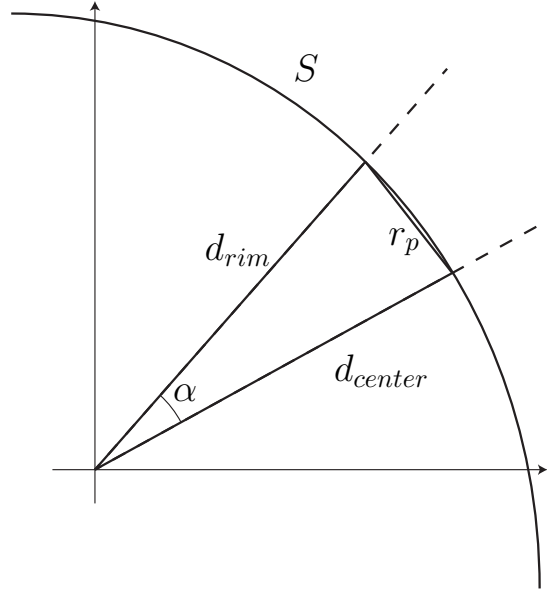


**Figure 5.4:** Approximate relation between the aperture angle and the radius of a piston.

In a case like this, it might be easier to pick a point on the surface  $\mathbf{r}_l$  to act as the center of the piston and define the aperture function by the distance to this point.

$$a_l(\mathbf{r}) = \begin{cases} 1, & \|\mathbf{r}_l - \mathbf{r}\|_2 \leq r_p \\ 0, & \text{otherwise} \end{cases} \quad (5.22)$$

This means that the coordinate of the center of the pistons on the surface needs to be known beforehand, so this function requires a little bit more knowledge of the meshes used compared to just picking a piston direction. However, both methods serve the same function, i.e. a Boolean function used to determine whether or not a point in the mesh is part of a given piston or not.

### 5.3.1 Acoustic Transfer Matrix

The sound pressure at each field point can be seen as a superposition of the sound pressures resulting from the movement of each piston on the array, such that

$$p_{fp,m} = H_{m,1}u_1 + \dots + H_{m,L}u_L \quad (5.23)$$

where  $p_{fp,m}$  is the pressures at the  $m$ th field point, and  $H_{l,m}$  is the transfer function from the velocity of the  $l$ th piston to the sound pressure at the  $m$ th field point evaluated at the same specific frequency as the frequency of the piston velocities.

This makes it possible to write up a linear system describing the pressure at every field point using the  $L$  piston velocities.

$$\mathbf{p}_{fp} = \begin{bmatrix} H_{1,1} & \dots & H_{1,L} \\ \vdots & \vdots & \vdots \\ H_{M,1} & \dots & H_{M,L} \end{bmatrix} \begin{pmatrix} u_1 \\ \vdots \\ u_L \end{pmatrix} = \mathbf{H}\mathbf{u} \quad (5.24)$$

Every column of  $\mathbf{H}$  can be determined by setting the corresponding entry in the piston velocity vector  $\mathbf{u}$  to 1, and every other entry to 0 since

$$\begin{pmatrix} H_{l,1} \\ \vdots \\ H_{l,m} \end{pmatrix} = \mathbf{H}\mathbf{e}_l \quad (5.25)$$

where  $\mathbf{e}_l$  is a vector with a 1 as its  $l$ th entry and zeros otherwise. This is equivalent to the field point solution in BEM with boundary conditions  $\mathbf{v} = \mathbf{a}_l$ , i.e. the  $l$ th piston is moving with unit amplitude and zero phase, and all other pistons are kept still.

Thus every column of  $\mathbf{H}$  can be found using the BEM matrices from Section 5.2 using Equation 5.11 and Equation 5.12 as

$$\begin{pmatrix} H_{l,1} \\ \vdots \\ H_{l,M} \end{pmatrix} = \mathbf{A}_{fp} \mathbf{D}^{-1} (-\mathbf{B}) \mathbf{a}_l + \mathbf{B}_{fp} \mathbf{a}_l \quad (5.26)$$

Assuming no CHIEF points are added, as the inversion otherwise would need to be replaced by a pseudo-inverse.

### 5.3.2 Optimal Solution in the Least Squares Sense

A simple way of choosing the right piston velocity is to minimize the difference between the target vector  $\mathbf{t} = [t_1, \dots, t_M]^T$  defined at every field point and the expression for the pressure at the field points  $\mathbf{p}_{fp} = \mathbf{H}\mathbf{u}$ . For now, we will assume that  $\mathbf{H}$  is both full rank and well-conditioned and that  $M > L$ .

$$\min_{\mathbf{u}} \|\mathbf{t} - \mathbf{H}\mathbf{u}\|_2^2 \quad (5.27)$$

which has the well known least squares solution  $\mathbf{u}^* = \mathbf{H}^\dagger \mathbf{t}$  [55, chapter 6].

For the purposes of this project the target  $\mathbf{t}$  could be based on the measured radiation pattern of the guitar in Chapter 4 at some frequency defined at every measurement point.

#### A Note on the Units of the Target Function and Simulation Variables

The target function as it is computed from the measurements of the guitar is given as a 'pressure gain' in units of Pascal per digital full scale level. This is different from the acoustical units usually used in the BEM simulations namely pressure in Pascal and velocities in m/s.

This can however easily be solved with one of two steps. We could re-imagine the target as a pressure resulting from a flat and unity gain input signal without changing its numerical values, or we could similarly imagine the acoustic variables of the simulations also as 'pressure gains' and 'velocity gains'. The benefit of this latter way of thinking is that the variables are now more related to the transfer functions that the eventual filters will need to have in order to reach the target function. The solution vector  $\mathbf{u}^*$  can then be seen as a set of complex weights applied to every loudspeaker, in order to make them vibrate at different amplitudes and in different phases.

### 5.3.3 Optimal Solution of Magnitude Response

the LS solution might however not be very efficient since the minimization is indiscriminately trying to minimize both the magnitude difference and the phase difference between the pressure response and the target response. The phase of the target function is not seen as being terribly important. In fact, no phase information from the guitar radiation is even present in the target function due to the analysis method described in Chapter 4.

Instead, the optimization problem can be posed in terms of the magnitude response like

$$\min_{\mathbf{u}} \|(|\mathbf{t}| - |\mathbf{H}\mathbf{u}|)\|_2^2 \quad (5.28)$$

Where the  $|\cdot|$  notation denotes an element-wise absolute value. However, this optimization problem is non-convex due to the absolute value function and therefore cannot be solved directly with conventional optimization methods. This problem is known as the 'Magnitude Least Squares' (MLS) problem and is discussed in great detail in [56].

The optimization problem can be reformulated as the following constrained optimization problem [56, Ch. 5].

$$\min_{\mathbf{u}, \mathbf{z}} \quad \|\mathbf{T}\mathbf{z} - \mathbf{H}\mathbf{u}\|_2^2 \quad (5.29)$$

$$\text{s.t.} \quad \text{diag}(\mathbf{z})^H \text{diag}(\mathbf{z}) = \mathbf{I} \quad (5.30)$$

where  $\mathbf{T} = \text{diag}(|\mathbf{t}|)$ . The reformulation is done by adding a phase component to the target function given by the vector  $\mathbf{z}$  and minimizing over it in order to get the best solution for  $\mathbf{u}$  over all possible phases. The equality constraint ensures that  $\mathbf{z}$  is only adding phase to the target.

Several methods for solving this problem are outlined in [56], but a simple iterative solution has been popular in previous studies due to its ease of implementation [3, 4].

By keeping  $\mathbf{z}$  fixed, then a minimizer for  $\mathbf{u}$  can easily be found as the least squares solution  $\mathbf{u}_* = \mathbf{H}^\dagger \mathbf{T}\mathbf{z}$ . Instead, if  $\mathbf{u}$  is kept fixed, the minimizer  $\mathbf{z}_*$  is found when each element of  $\mathbf{z}$  has the same phase as each element of the vector  $\mathbf{H}\mathbf{u}$ , i.e.  $z_* = e^{j\arg(\mathbf{H}\mathbf{u})}$ .

A local minimum can then be approached by alternating between minimizing for  $\mathbf{u}$  and  $\mathbf{z}$ . The conventional LS-solution can be used as a good initial guess for  $\mathbf{u}$  and the phase of the target function (in our case unity) can be used as an initial guess for  $\mathbf{z}$ . The algorithm can thereby be summarized as follows:

Iterative magnitude least squares algorithm:

1. Choose convergence tolerance  $\epsilon$
2. Calculate initial guess of the velocities  $\mathbf{u}_0 = \mathbf{H}^\dagger \mathbf{t}$
3. Calculate initial guess of the phase component  $\mathbf{z}_0 = e^{j\arg(\mathbf{t})}$
4. Repeat until convergence e.g.  $\epsilon < \frac{\|\mathbf{z}_i - \mathbf{z}_{i-1}\|_2^2}{\|\mathbf{z}_i\|_2^2}$  for the iterations  $i = 1, 2, \dots$ 
  - a)  $\mathbf{z}_i = e^{j\arg(\mathbf{H}\mathbf{u}_{i-1})}$
  - b)  $\mathbf{u}_i = \mathbf{H}^\dagger \mathbf{T}\mathbf{z}_i$
5. Optimal solution  $\mathbf{u}_* = \mathbf{u}_i$

### 5.3.4 Spatial Density Weighting

Due to the measuring setup used for obtaining the target function in 3D in Chapter 4, the target function is more densely sampled at certain points in the spherical coordinate system than others. In particular, the top and bottom of the sphere formed by the field points are much more closely spaced than the points in the horizontal plane. This affects the least-squares optimization methods covered in this section since the densely sampled areas of the sphere will be more favored.

A simple solution to this issue could simply consist of removing points at these densely sampled areas, which might only approximate a more uniformly sampled sphere at the cost of losing information. Another solution could be to add a weighting to each field point in order to favor densely sampled points less.

The common way of doing this is to construct a real diagonal matrix  $\mathbf{W}$  and set up the *Weighted Least*

squares problem[55, chapter 6]

$$\min_{\mathbf{u}} \|\mathbf{W}(\mathbf{t} - \mathbf{H}\mathbf{u})\|_2^2 \quad (5.31)$$

which can be solved similarly to the normal LS-problem as  $\mathbf{u}_* = (\mathbf{H}\mathbf{W})^\dagger \mathbf{W}\mathbf{t}$  or  $(\mathbf{H}^H \hat{\mathbf{W}}\mathbf{H})^{-1} \mathbf{H}^H \hat{\mathbf{W}}\mathbf{t}$ , where  $\hat{\mathbf{W}} = \mathbf{W}^H \mathbf{W}$ .

A potential weighting for a point could be chosen based on how much of the sphere is 'covered' by the point when looking at the area of the sphere 'belonging' to the point. The area of a unit sphere can be found as

$$\int_0^{2\pi} \int_0^\pi \sin(\phi) d\phi d\theta = 4\pi \quad (5.32)$$

As described in Chapter 4, the measuring points are spaced horizontally with a constant angular distance  $\Delta\theta$  and spaced vertically with an angular distance  $\Delta\phi$ , both equal to  $10^\circ$  in our case.

The area 'belonging' to a point  $(\theta_i, \phi_i)$  can therefore be described as going from  $[\theta_i - \frac{\Delta\theta}{2}, \theta_i + \frac{\Delta\theta}{2}]$  in azimuth angles and  $[\phi_i - \frac{\Delta\phi}{2}, \phi_i + \frac{\Delta\phi}{2}]$

Since the integral over phi goes from  $[0, \pi]$  instead of  $[-\frac{\pi}{2}, \frac{\pi}{2}]$  the elevation angles are shifted by 90 degrees. Thereby the area of each section can be written as

$$\int_{\theta_i - \frac{\Delta\theta}{2}}^{\theta_i + \frac{\Delta\theta}{2}} \int_{\phi_i + \frac{\pi}{2} - \frac{\Delta\phi}{2}}^{\phi_i + \frac{\pi}{2} - \frac{\Delta\phi}{2}} \sin(\phi) d\phi d\theta \quad (5.33)$$

$$= \int_{\theta_i - \frac{\Delta\theta}{2}}^{\theta_i + \frac{\Delta\theta}{2}} \left( \cos\left(\phi_i + \frac{\pi}{2} - \frac{\Delta\phi}{2}\right) - \cos\left(\phi_i + \frac{\pi}{2} - \frac{\Delta\phi}{2}\right) \right) d\theta \quad (5.34)$$

$$= 2 \sin\left(\phi_i + \frac{\pi}{2}\right) \sin\left(\frac{\Delta\phi}{2}\right) \int_{\theta_i - \frac{\Delta\theta}{2}}^{\theta_i + \frac{\Delta\theta}{2}} 1 d\theta \quad (5.35)$$

$$= 2 \cos(\phi_i) \sin\left(\frac{\Delta\phi}{2}\right) \Delta\theta \quad (5.36)$$

using trigonometric identities. The point at  $90^\circ$  is a little different since it is covering parts of the sphere at every azimuth angle. Therefore, the area for covered by the point at  $90^\circ$  can be written as

$$\int_0^{2\pi} \int_{\pi - \frac{\Delta\phi}{2}}^\pi \sin(\phi) d\phi d\theta \quad (5.37)$$

$$= \int_0^{2\pi} \left( -\cos(\pi) + \cos\left(\pi - \frac{\Delta\phi}{2}\right) \right) d\theta \quad (5.38)$$

$$= 2\pi \left( 1 - \cos\left(\frac{\Delta\phi}{2}\right) \right) \quad (5.39)$$

Thus the diagonal entries of the matrix  $\mathbf{W}$  can be found as

$$w_i = \begin{cases} 2\pi \left( 1 - \cos\left(\frac{\Delta\phi}{2}\right) \right), & |\phi_i| = \frac{\pi}{2} \\ 2 \cos(\phi_i) \sin\left(\frac{\Delta\phi}{2}\right) \Delta\theta, & \text{Otherwise} \end{cases} \quad (5.40)$$

The weighting matrix can be normalized by multiplying by the scalar  $\frac{M}{4\pi}$  such that the sum of every entry equals  $M$  similar to a uniform weighting equivalent to a  $M \times M$  identity matrix.

## 5.4 Summary of Simulation Results

Using the methods described in this chapter, a set of simulations has been carried out to identify how the performance of recreating the target radiation pattern of a guitar is affected by different parameters.

The results will mostly be judged in two different ways - Both subjectively by visually comparing the resulting radiation pattern to the target pattern at different frequencies and objectively by looking at a weighted MSE measure of the magnitude responses at every point where the target function is defined given as

$$WMSE = \frac{1}{M} \sum_{m=1}^M w_m (|p_{fp,m}| - |t_m|)^2 \quad (5.41)$$

where  $M$  is the number of field points,  $w_m$  is the spatial density weighting for the  $m$ th field point as described in Section 5.3.4,  $p_{fp,m}$  is the complex pressure at the  $m$ th field point and  $t_m$  is the target at the  $m$ th field point.

All simulations were done with the measured radiation pattern in 3D from Chapter 4, given as the 'gains' at every measurement point calculated in 1/3 octave bands.

An 'artificial' target point was placed at  $\phi = -90^\circ$ , with a target value found as the average between all gains at  $\theta = -70^\circ$  at a specific frequency. This was done just mostly to limit the sound propagation to the bottom somewhat, as this would otherwise be unspecified. Since the target point is 'artificial' the weighting for this point is only set to 1, even though it covers a relatively large area.

All the 3D meshes used in the simulations were made using the free 3D modelling program `blender 2.9x4`. In cases where the 3D models did not initially consist of uniformly sized triangles, the models were re-meshed using the ACVD algorithm[57] with the python implementation `pyACVD`<sup>5</sup> such that every model is made from approximately equilateral triangles of approximately uniform area. All meshes were created such that the longest edge was smaller than 1/6 of the wavelength corresponding to 3,2 kHz at  $c = 343$  m/s.

This frequency limitation was done in order for the computations of the BEM matrices to be done in a reasonable amount of time (around 10 mins per frequency bin), which still is a considerable amount if simulations are desired at, say, every 1/3 octave center frequency from 79 Hz to 3.16 kHz. To save computation time, the BEM matrices  $\mathbf{A}, \mathbf{B}, \mathbf{A}_{fp}$  and  $\mathbf{B}_{fp}$  of all models for all frequencies of interest were pre-computed so that the matrices would only have to be assembled once, as many of the simulations use the exact same matrices. Because of this storage also became a considerable issue, which also made it unattainable to use much larger 3D meshes.

After every assembly of the BEM matrices, their rank was calculated to check if CHIEF points were needed. However, it does not seem to have been the case for the particular 3D meshes at the particular frequencies used in these simulations.

### 5.4.1 Comparison of Optimization Methods

In Appendix D a test has been performed comparing the effectiveness of the different ways of obtaining an 'optimal' set of driver weightings. Both the LS and MLS solutions have been compared both with and without the spatial density weighting. Additionally, it has also been tried to randomize the initial guess of the MLS algorithm to see if that provides better results. This was done with both 8 and 12 loudspeaker units placed uniformly on a sphere.

<sup>4</sup>Available from <https://www.blender.org/>

<sup>5</sup>Available from <https://pypi.org/project/pyacvd/>

In all cases, the MLS optimization gave a better approximation to the target magnitude response than the simple LS solution. Moreover, the MLS solutions with the LS solution as an initial guess generally arrived at a solution without any huge phase variations over short distances.

Giving the MLS algorithm a random vector as the initial guess did at certain times result in a slightly lower error. More often than not, the result was equivalent or worse than with the LS solution as a starting guess, in addition to the phase not looking as "nice". For these reasons, it has been decided to move forward with the MLS method with the LS solution as a starting guess.

Interestingly the weighting function did not seem to make a big difference in the MSE even when the weighting was applied to the error calculations, such that the more highly weighted points were weighted higher in the error measure. This suggests that it might not be that important that the field points of the target pattern are sampled completely uniformly in space. Additionally, when the problem is so over-determined (578 target points with 12 degrees of freedom), the optimal solution will probably be very similar anyway. It could also be that using the weighting matrix results in a slightly higher error at the top and bottom but a slightly lower error in the horizontal plane, but that the final total error is more or less the same.

Since it is relatively cheap to apply the weighting, it has been decided to stick with it for now, as it is deemed slightly more important to have a good result in the horizontal plane than at e.g.  $\phi = 80^\circ$ , especially at high frequencies where a difference can really be seen like on Figure D.11 in Appendix D.

An example of the errors using the different methods at the simulated frequencies using 12 pistons can be seen on Figure 5.5. Additionally, an example of the synthesized radiation patterns can be seen on Figure 5.6 as 'Balloon style' visualizations, where the length of each point on the surface symbolizes the magnitude of the radiation pattern, and the color symbolizes the phase.

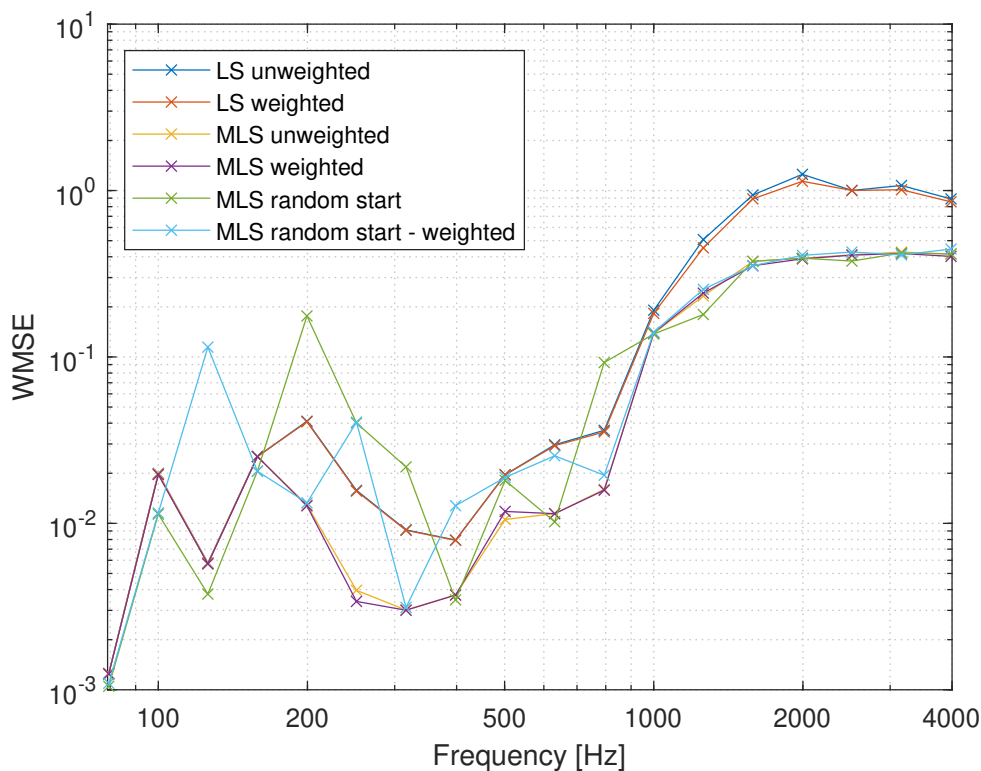


**Figure 5.5:** Weighted Mean squared error of different methods with 12 loudspeakers.

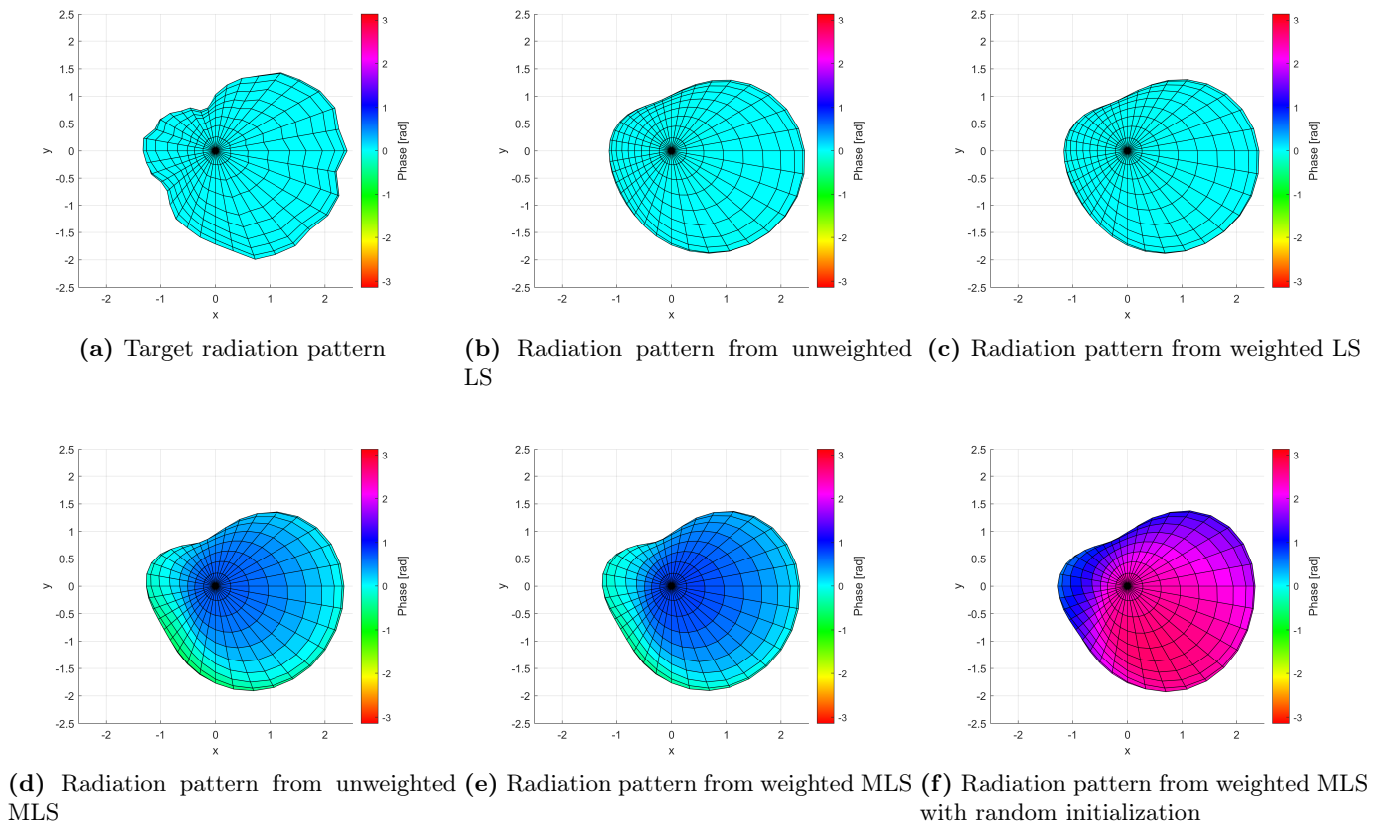


**Figure 5.6:** Radiation patterns at 316 Hz with 12 loudspeakers.

Similar results can be seen for 8 loudspeakers and at many other frequencies in Section D.2.

### 5.4.2 Findings on the Influence of the Number of Loudspeakers

Some investigations into the effect of the number of loudspeakers have also been done. This is described in detail in Appendix E.

The simulations were carried out with a sphere with a radius of 20 cm, with different numbers of pistons placed on the surface, each with a diameter of around 4". For every amount of loudspeakers, 50 random distributions of loudspeakers were simulated to get an idea of the importance of the number of loudspeakers vs. the placement of each loudspeaker.

For a number of loudspeakers corresponding to the number of faces on a platonic solid (6 for a cube, 12 for a dodecahedron, etc.), additional simulations were made with the loudspeakers placed at the midpoints of these faces. Both in the directions found using table values of the normal directions to each faces, e.g.  $(\pm 1, \pm 1, \pm 1)$  for the octahedron, but also with the directions rotated such that one piston was pointed directly in the front direction, i.e.  $(1, 0, 0)$ .

At all the simulated frequencies the results show that the performance of the array generally increases with the number of loudspeakers placed on the body. However, the error varies a lot depending on the specific placement of the loudspeakers. A visualization of how the error varies across different amounts of loudspeakers for one specific frequency, i.e. 1 kHz, can be seen in Figure 5.7 illustrated via boxplots.

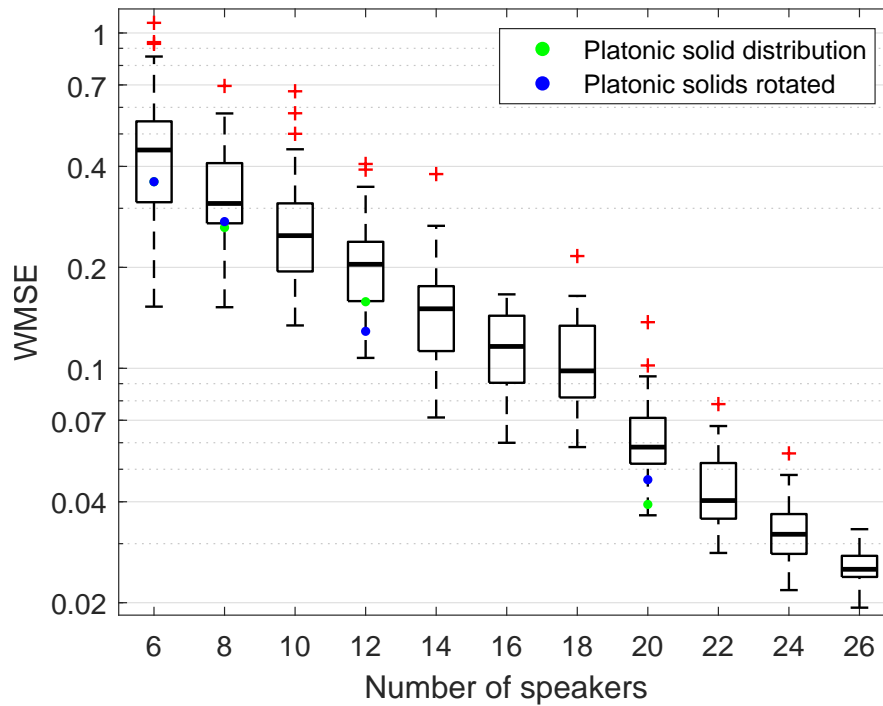


**Figure 5.7:** Weighted MSE at 1000 Hz for 50 realizations of random loudspeaker placements. The boxplots divide the statistical distribution into 4 'quartiles', along with visualizing the minimum, maximum, and median values. The red 'plus' signs signify statistical outliers.

To give a bit of intuition to what the error measure actually means, the radiation pattern resulting from the best loudspeaker placements for 1 kHz are also shown, which can be seen in Figure 5.8.

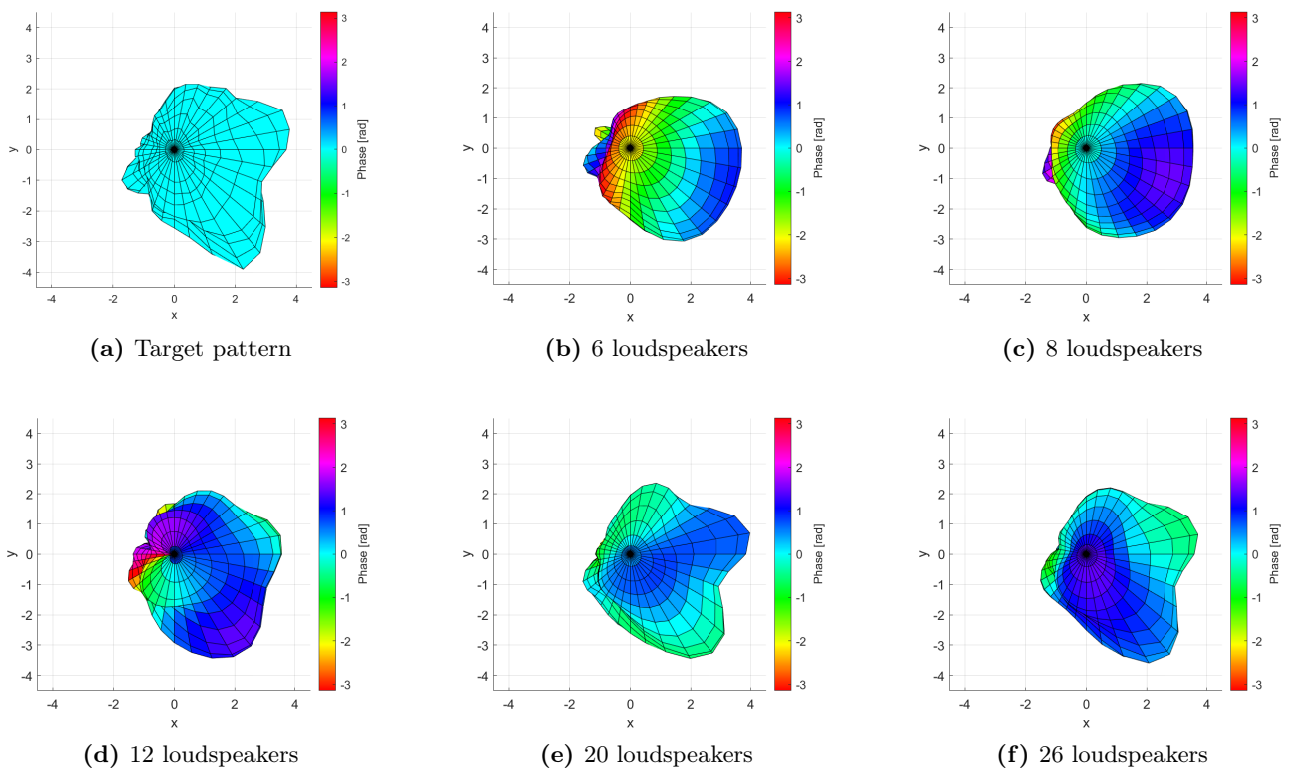


**Figure 5.8:** Lowest error radiation pattern for different number of loudspeakers for 1000Hz.

From the angle shown in the plots in Figure 5.8 it can be seen that the magnitude of the synthesized radiation pattern gets closer to the target as the number of loudspeakers increase, which corresponds well to what can be seen from the error of the best placements in Figure 5.7.

For 6 and 8 loudspeakers, the radiation pattern does not match the target very well visually, but for 12 loudspeakers and upwards, it seems to resemble the target to a decent degree. This can be compared to the boxplots, where it can be seen that with 12 loudspeakers the WMSE can become below 0.1.

One interesting thing to note is that the uniform distributions of loudspeakers based on platonic solids are not necessarily the best way of placing the loudspeakers, although the uniform distributions usually provide a WMSE below the average of the random loudspeaker placements realizations. This suggests that there might be an optimal way, in some sense, to place the loudspeaker for a given radiation pattern.

However, since the directivity of the guitar varies so much with frequency, the optimal loudspeaker placements for one pattern at one frequency might not be the best loudspeaker placements at other frequencies. This can also be seen by comparing the best random loudspeaker placements for different frequencies.

Therefore, some thoughts have to be put into how to place the loudspeakers on the potential loudspeaker array in an optimal way to provide a good overall response across all frequencies.

### 5.4.3 Findings on the Influence of the Shape of the Loudspeaker Array Enclosure

Another parameter that can be changed is the shape of the loudspeaker array enclosure. This is investigated in Appendix F. A few different enclosure shapes were simulated, like a cylinder, dodecahedron, and an icosahedron with loudspeakers placed at sensible positions, i.e. not on the corners. These simulations were then compared to a sphere of a similar size and with loudspeakers placed in the same directions. An example with 18 similar loudspeaker placements can be seen in Figure 5.9.

The error of the different enclosure shapes seems to follow each other pretty well, even for very different shapes such as the octagonal prism and the sphere. At lower frequencies, in particular, there does not seem to be any real difference in the performance, and the error is generally so low that the synthesized radiation pattern matches the target pretty well. At higher frequencies, there generally seems to be a bigger difference between the shapes.

However, it also seems that the variation due to the different placements of loudspeakers is much higher than error due to the shape itself. For example, there seems to be a lot more variation due to the same sphere having different loudspeaker placements as seen in Appendix E than the variation between shapes with similar loudspeaker placements.

Some of the differences between the results from different enclosure shapes at high frequencies might also be due to the slight differences in sizes between the enclosure shapes. For example, the model of an icosahedron is designed to have its vertices located at a radius of 20 cm from the origin, the same as the radius of the sphere. This means that the icosahedron is in fact a bit smaller than the sphere, which might provide it a slight advantage as the loudspeakers are then closer spaced to each other.

But on the other hand, the cylinder is also slightly bigger than the sphere due to the same logic. But it still seems to give a slightly lower error at high frequencies for both the simulated configurations of loudspeakers.

To investigate this last point a bit further, a short simulation has been made to investigate the influence of the loudspeaker array size on the performance. This simulation is explained in more detail in Appendix G

The *WMSE* of three spherical arrays of different sizes can be seen on Figure 5.10.

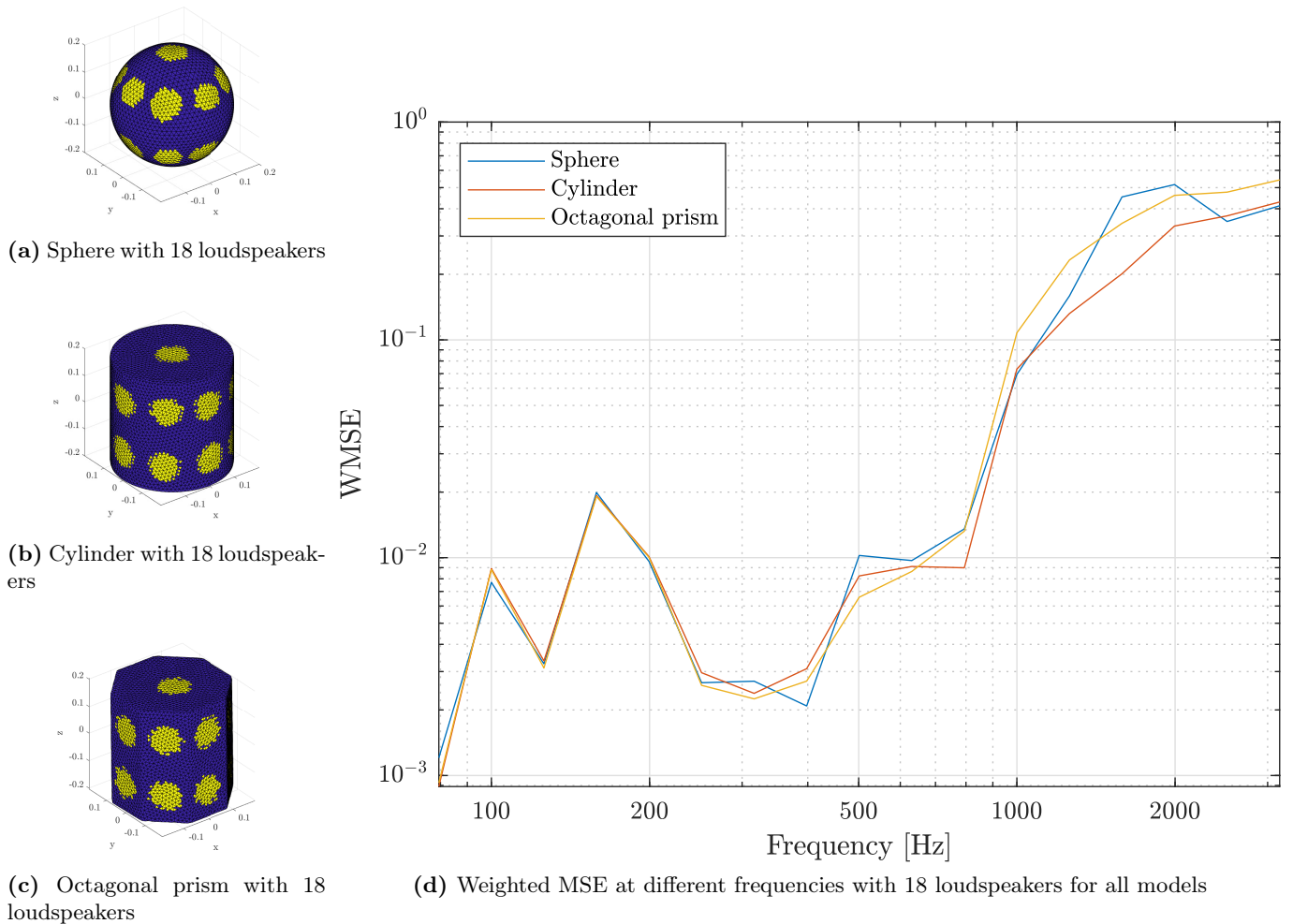


**Figure 5.9:** Comparison of a spherical, a cylinder, and an octagonal prism array shape with similar loudspeaker placements and the weighted MSE of the three shapes.

As it was somewhat expected, the error at high frequencies seems to be lower with a smaller array. At these frequencies, the 3" pistons are probably getting directive and will therefore only be able to influence each other if they are closely spaced.

Another thing of interest is that a really small loudspeaker array seems to provide a worse result at some of the low frequencies, e.g. 316 Hz. It could be because the radiation of each piston is very omnidirectional at these frequencies, with which it will be hard to 'shape' the radiation pattern to a non-omnidirectional shape when the pistons are so spatially close.

### 5.4.4 Discussion

All in all, the BEM-based simulations show that it is possible to approximate the target radiation patterns pretty well with the iterative MLS method up to some frequency. The frequency at which the error gets large is dependant on multiple factors, but the number of loudspeakers and their placement on the surface seems to have the greatest impact on the performance.

The frequency dependant weights for each loudspeaker driver unit are given directly as a 'driver velocity gain', which might not be that intuitive to look at. Be that as it may, these can easily be converted to a voltage gain using the transfer function described in Appendix A, which corresponds well to complex gain, that the filters applied to each driver will need to have at different frequency bins.

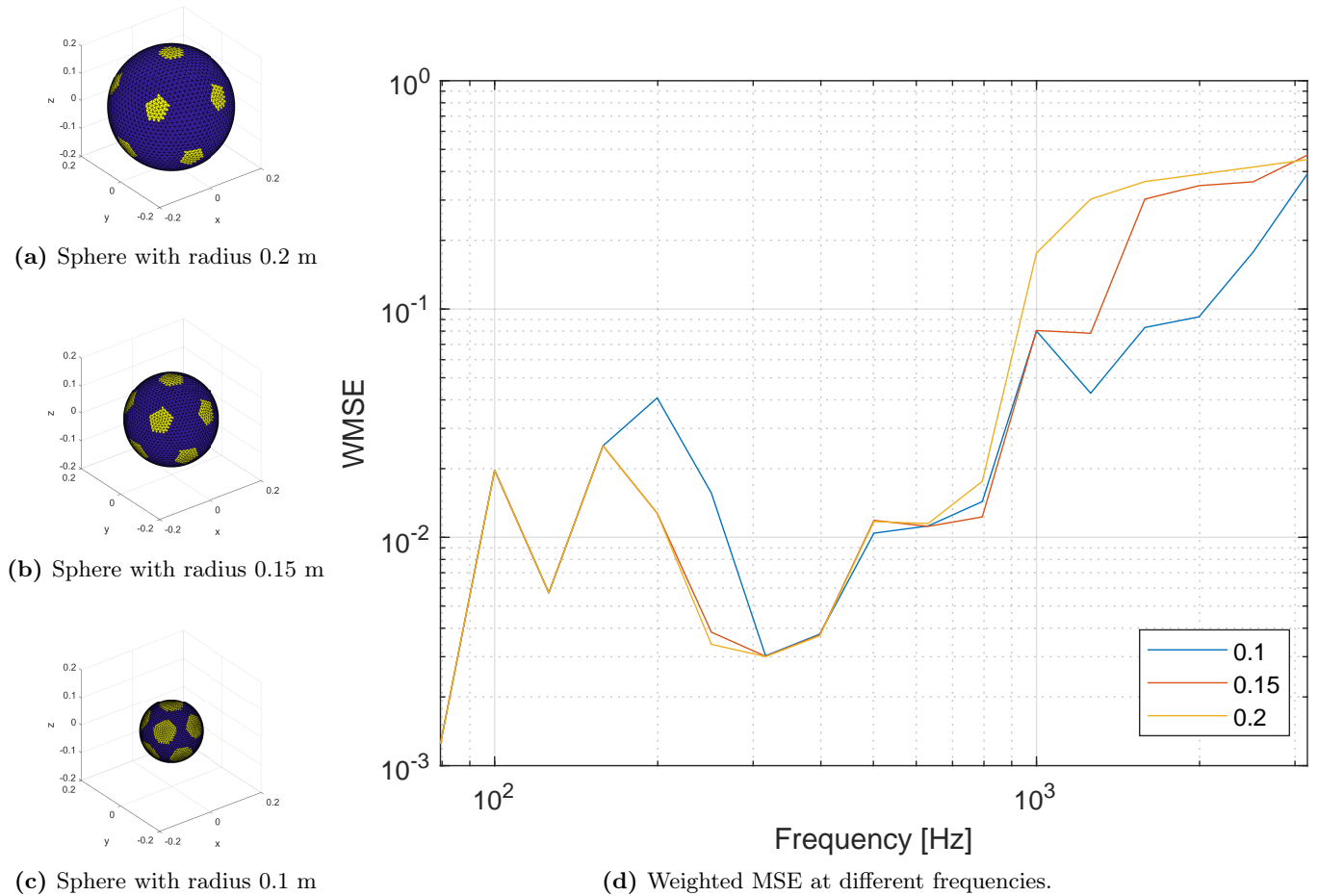


**Figure 5.10:** Comparison of three different sizes of spherical arrays with 12 loudspeakers and a piston diameter of 3" with enclosures of different sizes.

Due to the computational complexity and storage requirements of the BEM-matrices, then the simulations were only performed up to a frequency limit of around 3 kHz. As a consequence, not much can be concluded about the performance above this limit. However, for most of the simulations, the performance seemed to have degraded a lot even before this frequency. It therefore also remains to be seen if it is even realistic to hit the target at this frequency range with a real loudspeaker array.

# Design of Filters 6

From the previous chapter, several ways of synthesizing the radiation pattern based on a complex weighting factor for each loudspeaker unit have been described. This corresponds to prescribing a certain gain and phase shift to the input signals at different frequencies. To someone with even a rudimentary understanding of signal processing, this seems like an obvious problem to solve by applying a filter to each driver signal.

In this chapter, the description of the filter design for synthesizing arbitrary radiation patterns is provided as a multichannel inversion problem. Different algorithms are presented as possible solutions to the problem with different extended features and possible improvements such as regularization and complex interpolation on a logarithmic frequency grid.

## 6.1 Least-Squares Multichannel Inversion

The optimization problem in Chapter 5 is very analogous to a multi-channel inversion problem, i.e. equalizing the frequency response of a sound field at  $M$  reference points using  $L$  loudspeaker. A least-squares multichannel inversion can be used to design a set of digital filters  $\mathbf{w}$  for this purpose.

Since the reference points are placed on a sphere with a fixed radius to the source, then the filters can be seen as a set of beamforming filters[6], which allow reproducing arbitrary radiation patterns with the use of a loudspeaker array. Consider a loudspeaker array consisting of  $L$  loudspeakers and similarly  $M$  microphones acting as observation points of the sound radiation, as illustrated in Figure 6.1.

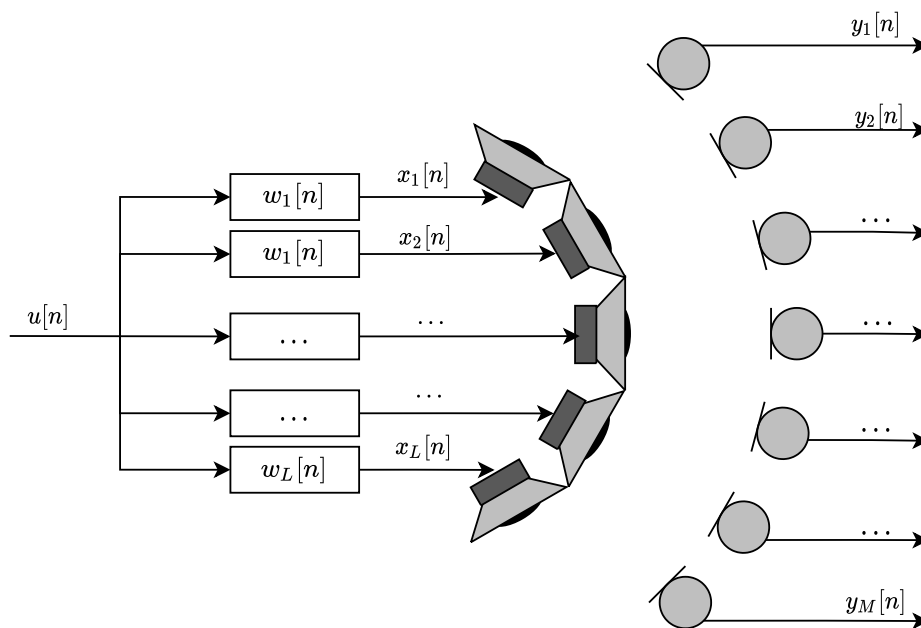


**Figure 6.1:** Block diagram of a multichannel system consisting of a loudspeaker array with  $L$  loudspeakers and a microphone array with  $M$  microphones.

When an input signal  $u[n]$  is sent to the filter set  $\mathbf{w}$  of the  $L$  filters  $w_l[n], l = 1, 2, \dots, L$ , then these filters should ideally produce the  $L$  individual loudspeaker driving signals  $x_l[n], l = 1, 2, \dots, L$  for the loudspeaker array which will reproduce the desired sound field or response at the  $M$  observation points given by the microphone signals  $y_m[n], m = 1, 2, \dots, M$  as accurately as possible[58]. But first these filters need to be found or designed.

The block diagram of Figure 6.1 can be seen as an multiple-input multiple-output (MIMO) system. The loudspeaker driving signals  $x_l[n], l = 1, 2, \dots, L$  can be written as an input signal vector  $\mathbf{x}[n]$  or  $\mathbf{x}(f)$  in the frequency domain, and the microphone outputs  $y_m[n], m = 1, 2, \dots, M$  can be written as output signal vector  $\mathbf{y}[n]$  or  $\mathbf{y}(f)$  in the frequency domain.

$$\mathbf{x}(f) = [x_1(f), x_2(f), \dots, x_L(f)]^T \quad (6.1)$$

$$\mathbf{y}(f) = [y_1(f), y_2(f), \dots, y_M(f)]^T \quad (6.2)$$

The transformation from  $\mathbf{x}(f)$  to  $\mathbf{y}(f)$  is given by

$$\mathbf{y}(f) = \mathbf{H}(f)\mathbf{x}(f) \quad (6.3)$$

where  $\mathbf{H}(f)$  is a  $M \times L$  matrix of plant transfer functions[58] containing the corresponding frequency responses of the impulse responses for each loudspeaker at each observation point, or in other words the sound propagation path effects or transfer functions from each loudspeaker to each microphone.

$$\mathbf{H}(f) = \begin{bmatrix} H_{1,1}(f) & \dots & H_{1,L}(f) \\ \vdots & \ddots & \vdots \\ H_{M,1}(f) & \dots & H_{M,L}(f) \end{bmatrix} \quad (6.4)$$

Given a  $M \times 1$  target frequency response vector  $\mathbf{t}(f)$  for a desired target sound field at the  $M$  observation points

$$\mathbf{t}(f) = [t_1(f), t_2(f), \dots, t_M(f)]^T \quad (6.5)$$

that produces the desired signal vector  $\mathbf{d}(f)$  when fed by the input signal  $u(f)$  (in frequency domain). Then the objective is to minimize the difference between the desired signal vector  $\mathbf{d}(f)$  and the output signal vector  $\mathbf{y}(f)$ , i.e. the error vector  $\mathbf{e}(f)$ . This can be done by finding the set of filters in the frequency domain  $\mathbf{w}(f)$  that when multiplied by  $\mathbf{H}(f)$  match the target frequency response  $\mathbf{t}(f)$  as closely as possible.

This multichannel deconvolution problem[58] can be seen in Figure 6.2, where the component  $e^{-j2\pi f\Delta}$  is a modelling-delay of time  $\Delta$  to ensure the optimal filters to be causal and stable[58].

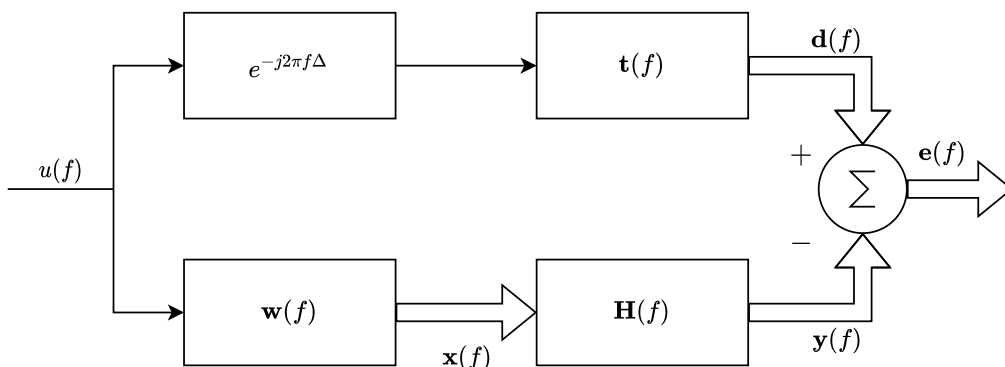


**Figure 6.2:** Block diagram of the multichannel deconvolution problem, Adapted from [58].

The relationship between the signal vectors in Figure 6.2 are given by:

$$\mathbf{x}(f) = \mathbf{w}(f) \cdot u(f) \quad (6.6)$$

$$\mathbf{y}(f) = \mathbf{H}(f) \cdot \mathbf{x}(f) \quad (6.7)$$

$$\mathbf{d}(f) = e^{-j2\pi f\Delta} \cdot \mathbf{t}(f) \cdot u(f) \quad (6.8)$$

$$\mathbf{e}(f) = \mathbf{d}(f) - \mathbf{y}(f) \quad (6.9)$$

where the error vector  $\mathbf{e}(f)$  and the desired signal vector  $\mathbf{d}(f)$  can be written as:

$$\mathbf{d}(f) = [d_1(f), d_2(f), \dots, d_M(f)]^T \quad (6.10)$$

$$\mathbf{e}(f) = [e_1(f), e_2(f), \dots, e_M(f)]^T \quad (6.11)$$

### 6.1.1 Least Squares Solution

The minimization problem of the multichannel deconvolution problem seen in Figure 6.2 can be written as the quadratic cost function

$$J = E + \beta X \quad (6.12)$$

where the  $E$  is an expression of "performance error" defined as the total energy of the error signal  $\mathbf{e}(f)$ , and the  $X$  is an expression of "effort penalty" defined as total energy of the loudspeaker driving signals  $\mathbf{x}(f)$  [58]. This cost function can also be written as<sup>1</sup>:

$$J(f) = \mathbf{e}(f)^H \mathbf{e}(f) + \beta \mathbf{x}(f)^H \mathbf{x}(f) \quad (6.13)$$

where the superscript  $H$  denotes the Hermitian operator that transposes and conjugates the argument.  $\beta$  is a positive regularization factor that determines how much weight the "effort penalty" should have [58]. The factor can be used to control the balance between minimizing the error signal and the amount of energy that may be needed in the loudspeaker driving signals in order to avoid a high gain of certain frequencies.

#### No Regularization

If no regularization is applied, or in other words,  $\beta = 0$ , then the optimal filters can be calculated as the least square solution using the pseudo inverse  $\mathbf{H}^\dagger(f)$  of the plant transfer functions matrix  $\mathbf{H}(f)$ .

$$\mathbf{w}(f) = \left[ \mathbf{H}^H(f) \mathbf{H}(f) \right]^{-1} \mathbf{H}^H(f) \mathbf{t}(f) \cdot e^{-j2\pi f\Delta} \quad (6.14)$$

$$\mathbf{w}(f) = \mathbf{H}^\dagger(f) \mathbf{t}(f) \cdot e^{-j2\pi f\Delta} \quad (6.15)$$

However, this ideal solution is not feasible as it provides no control over the energy that is needed in the loudspeaker driving signals, and can thus result in very high and sharp peaks in the frequency responses of the optimal filters [58] by which it will require excessively large filter gains beyond the practical limitations [59]. The problem occurs often at frequencies where the condition number of the plant transfer functions matrix  $\mathbf{H}(f)$  is large and usually referred to as "ill-conditioned" areas [60, p. 132] [61]

#### Frequency-Independent Regularization

Frequency-independent regularization with  $\beta > 0$  can be used to avoid problems with high filter gains due to the "ill-conditioned" areas of the plant transfer functions matrix  $\mathbf{H}(f)$  by putting more weight to the "effort penalty" at the cost of an increased "performance error". The cost function  $J(f)$  can be minimized

<sup>1</sup>The first term of this expression is mathematically equivalent to the least squares problem outlined in Section 5.3, given since  $\mathbf{e}(f)^H \mathbf{e}(f) = \|\mathbf{e}(f)\|_2^2 = \|\mathbf{d}(f) - \mathbf{H}(f)\mathbf{x}(f)\|_2^2$

as the least-squares solution including the frequency-independent regularization according to the following expression [58][6]:

$$\mathbf{w}(f) = \left[ \mathbf{H}^H(f)\mathbf{H}(f) + \beta\mathbf{I} \right]^{-1} \mathbf{H}^H(f)\mathbf{t}(f) \cdot e^{-j2\pi f\Delta} \quad (6.16)$$

where  $\mathbf{I}$  is an  $L \times L$  identity matrix.

### Frequency-Dependent Regularization

Another approach is frequency-dependent regularization, which can be used to apply at a small amount of regularization inside the optimally conditioned frequency range of the plant transfer functions matrix  $\mathbf{H}(f)$  [6] and a larger amount of regularization in the "ill-conditioned" areas such as in the low and high frequencies to attenuate peaks selectively[62].

Frequency-dependent regularization can be seen as the product of the regularization factor  $\beta > 0$  and a shape factor  $b(f)$ [62]. The shape factor  $b(f)$  is a frequency-dependent function, which when multiplied by  $\beta$  makes the regularization frequency-dependent. It can be designed as a digital filter that amplifies the frequencies that are "ill-conditioned" and need additional regularization in order to avoid the sharp peaks in the frequency responses of the optimal filters.

The least-squares solution including frequency-dependent regularization[62] can be expressed as:

$$\mathbf{w}(f) = \left[ \mathbf{H}^H(f)\mathbf{H}(f) + \beta b^*(f)b(f)\mathbf{I} \right]^{-1} \mathbf{H}^H(f)\mathbf{a}(f) \cdot e^{-j2\pi f\Delta} \quad (6.17)$$

where the superscript  $*$  denotes the complex conjugate of the argument.

## 6.2 The Fast Deconvolution Algorithm

The easiest way to implement Equation 6.17 is by using FFT, so the corresponding frequency responses of the impulse responses for each loudspeaker at each observation point are obtained in the frequency domain in the plant transfer functions matrix  $\mathbf{H}[k]$ .

The modeling delay is initially ignored in the calculation of the optimal filters in the frequency domain  $\mathbf{w}[k]$ . But to ensure causality, the delay is later implemented as a cyclic shift of the filter coefficients in the time domain, usually by  $N/2$  samples[58], where  $N$  is the FFT length typically specified as a power of 2.

The optimal filters  $\mathbf{w}[k]$  can then be found for each frequency bin  $k$  by the following expression[62] (ignoring the modeling delay):

$$\mathbf{w}[k] = \left[ \mathbf{H}^H[k]\mathbf{H}[k] + \beta b^*(k)b[k]\mathbf{I} \right]^{-1} \mathbf{H}^H[k]\mathbf{t}[k] \quad (6.18)$$

The sum-up, the fast deconvolution algorithm can be described in the following steps:

Fast deconvolution algorithm:

1. Obtain the  $L \times M$  plant impulse responses  $h_{l,m}[n]$  and the  $M$  target responses  $t_m[n]$ .
2. (Optional) Design the shape factor  $b[n]$  as a suitable digital filter for frequency dependant regularization, otherwise  $b[n] = \delta[n]$  where  $\delta[n]$  is Kronecker delta function.
3. Calculate  $\mathbf{H}[k]$ ,  $\mathbf{t}[k]$  and  $b[k]$ , by taking  $N$ -point FFTs of the elements of  $\mathbf{H}[n]$ ,  $\mathbf{t}[n]$  and  $b[n]$ , respectively
4. Find the optimal filters  $\mathbf{w}[k]$  for each frequency bin  $k$  from Equation 6.18:
5. Calculate  $\mathbf{w}[n]$ , by taking  $N$ -point IFFTs of the elements of  $\mathbf{w}[k]$ .
6. A modeling delay is implemented as a cyclic shift of the filter coefficients of each element in  $\mathbf{w}[n]$
7. (Optional) Apply a window to each element in  $\mathbf{w}[n]$  with a smooth weighting function (e.g. a Hanning or Tukey window) in order to taper most of the energy in the impulse responses around the modeling delay and ensure that the impulse response of the filters start and stop at a value of 0.
8. The final  $L$  FIR filters for the  $L$  individual loudspeaker driving signal can then be found as the elements in  $\mathbf{w}[n] = [w_1[n], w_2[n], \dots, w_L[n]]^T$

### 6.3 The Iterative Magnitude Fast Deconvolution Algorithm

The fast deconvolution algorithm in Section 6.2, which is finding the 'least squares' (LS) solution, can be expanded to finding the 'magnitude least squares' (MLS) solution in order to provide a better magnitude response where an exact phase response fit of the target response is of less importance. This seems sensible as the exact phase response of the target response is lost during the fractional octave analysis of the 3D guitar measurement.

The MLS solution is often found through an iterative approach because the solution is non-convex as already described in Section 5.3.3. By modifying the fast deconvolution algorithm to include this iterative approach when finding the optimal filter  $\mathbf{w}[k]$ , then an iterative magnitude fast deconvolution algorithm can be defined. This algorithm also allows the use of frequency-independent/dependent regularization of "ill-conditioned" areas.

Iterative magnitude fast deconvolution algorithm:

1. Obtain the  $L \times M$  plant impulse responses  $h_{l,m}[n]$  and the  $M$  target responses  $t_m[n]$ .
2. (Optional) Design the shape factor  $b[n]$  as a suitable digital filter for frequency dependant regularization, otherwise  $b[n] = \delta[n]$  where  $\delta[n]$  is Kronecker delta function.
3. Calculate  $\mathbf{H}[k]$ ,  $\mathbf{t}[k]$  and  $b[k]$ , by taking  $N$ -point FFTs of the elements of  $\mathbf{H}[n]$ ,  $\mathbf{t}[n]$  and  $b[n]$ , respectively
4. Form  $\mathbf{T}[k] = \text{diag}(|\mathbf{t}[k]|)$
5. Choose a convergence tolerance  $\epsilon$  (e.g.  $\epsilon = 10^{-4}$ )
6. For each frequency bin  $k$ :
  - a) Calculate initial guess of the optimal filter  $\mathbf{w}_0[k] = \left[ \mathbf{H}^H[k]\mathbf{H}[k] + \beta b^*(k)b[k]\mathbf{I} \right]^{-1} \mathbf{H}^H[k]\mathbf{t}[k]$
  - b) Calculate initial guess of the phase component  $\mathbf{z}_0[k] = e^{j\arg(\mathbf{t}[k])}$
  - c) Repeat until convergence e.g.  $\epsilon < \frac{\|\mathbf{z}_i[k] - \mathbf{z}_{i-1}[k]\|_2^2}{\|\mathbf{z}_i[k]\|_2^2}$  for the iterations  $i = 1, 2, \dots$ 
    - i.  $\mathbf{z}_i[k] = e^{j\arg(\mathbf{H}[k]\mathbf{w}_{i-1}[k])}$
    - ii.  $\mathbf{w}_i[k] = \left[ \mathbf{H}^H[k]\mathbf{H}[k] + \beta b^*(k)b[k]\mathbf{I} \right]^{-1} \mathbf{H}^H[k]\mathbf{T}[k]\mathbf{z}_i[k]$
  - d) Optimal solution  $\mathbf{w}_*[k] = \mathbf{w}_i[k]$
7. Calculate  $\mathbf{w}[n]$ , by taking  $N$ -point IFFTs of the elements of  $\mathbf{w}[k]$ .
8. A modeling delay is implemented as a cyclic shift of the filter coefficients of each element in  $\mathbf{w}[n]$
9. (Optional) Apply a window to each element in  $\mathbf{w}[n]$  with a smooth weighting function (e.g. a Hanning or Tukey window) in order to taper most of the energy in the impulse responses around the modeling delay and ensure that the impulse response of the filters start and stop at a value of 0.
10. The final  $L$  FIR filters for the  $L$  individual loudspeaker driving signal can then be found as the elements in  $\mathbf{w}[n] = [w_1[n], w_2[n], \dots, w_L[n]]^T$

## 6.4 Target Response Filter

The obtained transfer beam pattern matrix from the 3D measurement of the guitar radiation pattern described in Section 4.2 are used to model the target radiation pattern for the desired loudspeaker array system. The beam pattern matrix contains the set of gains for each of the  $M$  observation points in either 1/3 or 1/6 octave bands.

However, as the fast deconvolution algorithm expects to have a well-defined target vector  $\mathbf{t}[k]$  at every frequency bin, then the guitar radiation patterns need to be transformed to the  $M \times 1$  target frequency response vector  $\mathbf{t}[k]$  for use in the filter design algorithm.

The set of gains for each observation points are used to design a  $N = 4096$  tap long linear phase FIR filter  $t_m[n]$  for each observation points using a frequency sampling-based FIR filter design in MATLAB<sup>2</sup> between 0 Hz and  $f_s/2 = 16$  kHz. This design method basically makes use of linear interpolation to interpolate the magnitude values for each center frequency of the 1/3 or 1/6 octave bands to a discrete frequency response

<sup>2</sup>see <https://www.mathworks.com/help/signal/ref/fir2.html> for more info

grid with  $N$  discrete frequency points, followed by an IFFT and a chosen window (here a rectangular window) to obtain the filter coefficients in the discrete-time domain. As no magnitude values exist at 0 Hz and  $f_s/2 = 16$  kHz, then these are manually set to be 0 gain for the interpolation start and stop frequency point.

This provides a  $M \times 1$  target vector  $\mathbf{t}[n]$  of FIR filters or target impulse responses at each of the  $M$  observation points

$$\mathbf{t}[n] = [t_1[n], t_2[n], \dots, t_M[n]]^T \quad (6.19)$$

which can easily be transformed to the desired  $M \times 1$  target frequency response vector  $\mathbf{t}[k]$  using  $N$ -point FFTs of the elements of  $\mathbf{t}[n]$ .

$$\mathbf{t}[k] = \mathcal{F}\{\mathbf{t}[n]\} = [t_1[k], t_2[k], \dots, t_M[k]]^T \quad (6.20)$$

Since only the magnitude response is preserved in 1/3 or 1/6 octave bands at each observation points, then any phase part (in this case a linear phase, but it could also be a minimum phase, etc. depending on the design method) of the target frequency response vector  $\mathbf{t}[k]$  is discarded for the optimization problem. This is done by taking the absolute value of the target frequency response vector  $\mathbf{t}[k] = |\mathbf{t}[k]|$  leaving back the target frequency response with a fully represented magnitude response and zero-phase.

An example of the target magnitude response for one observation point can be seen below in Figure 6.3.

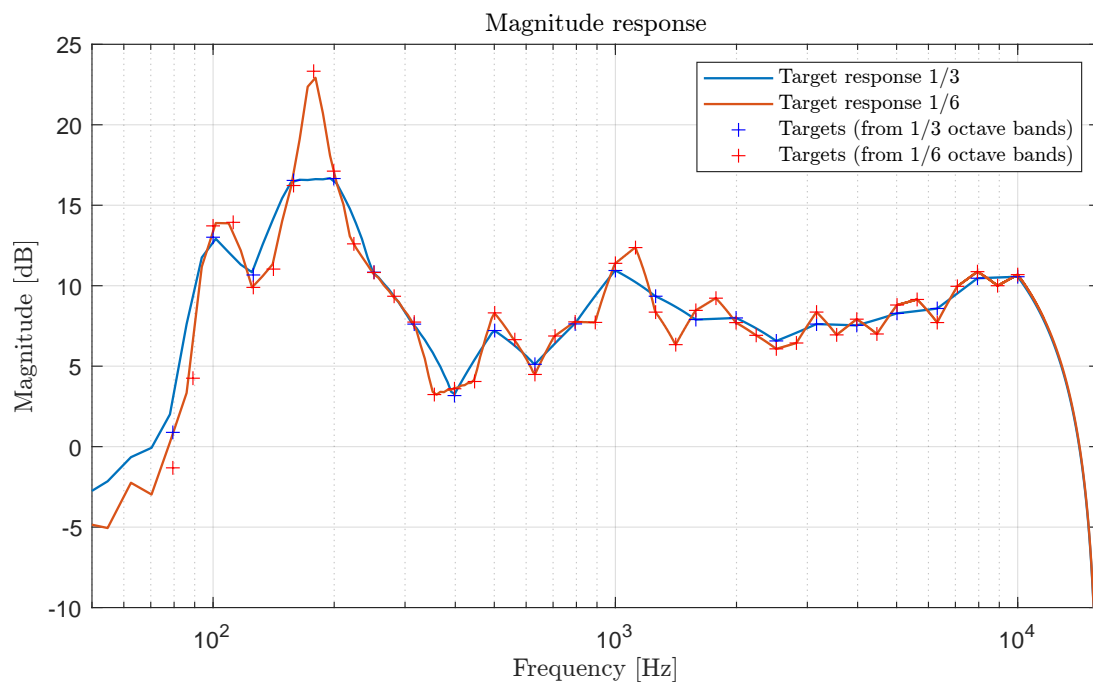


**Figure 6.3:** Target magnitude response of the  $N = 4096$  taps long FIR filter for the observation point in the direction  $\theta = 0^\circ$ ,  $\phi = 0^\circ$ , using the magnitude values for each center frequency in 1/3 and 1/6 octave bands analyses. (25dB/decade)

## 6.5 Solution on Logarithmic Frequency Grid and Complex Interpolation

As mentioned before, finding the optimal FIR filters using the classic fast deconvolution method involves solving an optimization problem at every FFT-bin  $k$ . It potentially means solving the MLS problem several thousands of times, where the iterative MLS-solver may have to go through hundreds of iterations to converge, depending on the value of  $\epsilon$ .

This seems a bit wasteful as the target function is only defined at a logarithmic frequency grid with bins  $\kappa$  at every fraction of an octave. Especially at the higher frequencies, the number of linear frequency bins between two logarithmic frequency bins is very high. When you also take the frequency selectivity of the human auditory system into account [63, chap 3], you can argue that having an exact solution at every linear frequency bin probably does not really matter a lot.

What can instead be done is to solve the MLS problem for the filter transfer function at the logarithmic frequency bins  $\kappa$  using the original target function  $\mathbf{t}[\kappa]$ , and simply interpolating the solution to a linear  $N$ -point frequency grid.

As the filter transfer function data  $w_l[\kappa]$  consists of complex numbers, the frequency bins cannot be interpolated in the same way as real numbers. However, this can easily be circumvented by splitting the complex function into two real functions, interpolating these to the linear frequency grid given by  $k$ , and combine the interpolated functions in the end. For the purposes of this project, a simple linear interpolation scheme should be sufficient.

A simple way is to split  $w_l[\kappa]$  into  $\text{Re}(w_l[\kappa])$  and  $\text{Im}(w_l[\kappa])$ , interpolate each of them, and combine the interpolated functions as  $w_l[k] = \text{Re}(w_l[k]) + j\text{Im}(w_l[k])$ .

Perhaps a more relevant approach when working with transfer functions is to split the transfer function data into a magnitude response  $|w_l[\kappa]|$  and a phase response  $\angle w_l[\kappa]$ .

After interpolation these values can be combined as  $w_l[k] = |w_l[k]| \cdot e^{j\angle w_l[k]}$ . This will result in a frequency response that is piece-wise linear between the original frequency points  $\kappa$  when looking at its bode plot, whereas this will not necessarily be the case when interpolating the real and imaginary part.

While this will result in nice and smooth filter responses in the frequency domain, this might not be the best solution for the sound pressure in the far-field of the filters, at the frequencies in the middle of two logarithmic bins  $\kappa_i$  and  $\kappa_{i+1}$ .

This is because the magnitude and phase response of each individual filter is of minor importance, while the magnitude response in the far-field is of higher concern.

The transfer function to a measurement point  $m$  can be written as

$$G_m(f) = \sum_{l=1}^L H_{l,m}(f)w_l(f) \quad (6.21)$$

where  $H_{l,m}$  is the transfer function from the signal at the  $l$ th speaker to the sound pressure at the  $m$ th measurement point, and  $w_l(f)$  is the transfer function of the  $l$ th filter in frequency domain. Due to linearity, this can be rewritten as

$$G_m(f) = \sum_{l=1}^L H_{l,m}(f)\text{Re}(w_l(f)) + j \sum_{l=1}^L H_{l,m}(f)\text{Im}(w_l(f)) \quad (6.22)$$

This means that the radiation pattern has a well-defined expression in terms of the interpolated variables and that the radiation pattern is expected to behave reasonably well at frequencies in between the discrete logarithmic frequency bins.

The magnitude-phase decomposition does not allow for the magnitudes and phases to be split up in the expression for  $G_m$  in a similar way. Additionally both the magnitude and phase act as non-linear functions as  $\|a+b\| \neq \|a\| + \|b\|$  and  $\angle(a+b) \neq \angle a + \angle b$ . So when the contributions for each loudspeaker are summed

up, there might not be much of an advantage to the fact that the magnitude and phase are piecewise linear between exact solutions.

So, therefore it has been decided to interpolate the real and imaginary parts of the filter transfer function data instead.

However, the bode plot of the transfer function to a measurement point is still not guaranteed to follow a straight line in between the exact solutions. What can instead be done is to upsample the target function with linear interpolation to a finer logarithmic grid, thereby giving the algorithm more frequencies where the target is strictly specified.

In order to be able to interpolate a value at every frequency bin  $k$  from  $f = 0$  to  $f = f_s/2$ , the logarithmic transfer function data is modified by adding a frequency point corresponding to these two frequencies and setting the filter transfer function to zero at these points. This will also band limit the filter to the frequency range in which the original target function is defined.

It is well known, that a purely real impulse response  $g[n]$  will have a DFT that satisfies the following symmetry[64, Chapter 5]

$$G[k] = G^*[N - k] \quad (6.23)$$

around the Nyquist frequency  $f_s/2$ <sup>3</sup>. Thus, the transfer function data on the bins  $k = N/2, \dots, N - 1$  can be found simply by reversing and complex conjugating the already found transfer function data from  $k = 0, \dots, N/2 - 1$ .

With the filter transfer function  $w[k]$  defined at every frequency bin  $k = 0, \dots, N - 1$ , its corresponding impulse response can be calculated by computing its IFFT.

In order to solve the MLS problem on a logarithmic grid, it is also required to have the matrix  $\mathbf{H}$  defined on the logarithmic frequency bins  $\kappa$ . This can also be done by complex interpolation of the  $L \times M$  transfer functions  $\mathbf{H}[k]$ . However, this might introduce some strange things if the plant transfer functions have a large linear phase component from e.g. a propagation delay. This can cause the phase to 'wrap around' from  $-\pi$  to  $\pi$  several times between each logarithmic frequency bin at the high frequencies but not in the low frequencies. This might cause some weird behavior in the time domain, as the linear phase shift may be well estimated at some frequencies but not at others. Luckily an easy way to deal with this is simply to shift all the impulse responses  $h_{l,n}[n]$  by a fixed amount to remove any propagation delay. Of course, one has to be careful to keep every impulse response strictly causal.

This refined version of solving the MLS problem on logarithmic frequency grid followed by complex interpolation will be denoted as the 'magnitude least squares - complex interpolation' (MLS-CI) solution in this project. The algorithm can be summarized by the following steps:

---

<sup>3</sup>This can also be understood by the fact that an FIR-filter with real filter coefficients will have complex conjugated zeros.

Iterative magnitude fast deconvolution algorithm with complex interpolation:

1. (Optional) Up-sample target function  $\mathbf{t}$  to a finer logarithmic frequency grid  $\kappa$
2. Obtain the  $L \times M$  plant impulse responses  $h_{l,m}[n]$  and remove the propagation delay with a circular shift
3. Calculate  $\mathbf{H}[k]$ , and interpolate it to a logarithmic target frequency grid  $\mathbf{H}[\kappa]$
4. (Optional) Define frequency dependant regularization shape factor  $b(\kappa)$ , otherwise  $b[\kappa] = 1$
5. Form  $\mathbf{T}[\kappa] = \text{diag}(|\mathbf{t}[\kappa]|)$
6. Choose a convergence tolerance  $\epsilon$  (e.g.  $\epsilon = 10^{-4}$ )
7. For each logarithmic frequency bin  $\kappa$ :
  - a) Calculate initial guess of the optimal filter  $\mathbf{w}_0[\kappa] = \left[ \mathbf{H}^H[\kappa]\mathbf{H}[\kappa] + \beta b^*(\kappa)b[\kappa]\mathbf{I} \right]^{-1} \mathbf{H}^H[\kappa]\mathbf{t}[\kappa]$
  - b) Calculate initial guess of the phase component  $\mathbf{z}_0[\kappa] = e^{j\text{arg}(\mathbf{t}[\kappa])}$
  - c) Repeat until convergence e.g.  $\epsilon < \frac{\|\mathbf{z}_i[\kappa] - \mathbf{z}_{i-1}[\kappa]\|_2^2}{\|\mathbf{z}_i[\kappa]\|_2^2}$  for the iterations  $i = 1, 2, \dots$ 
    - i.  $\mathbf{z}_i[\kappa] = e^{j\text{arg}(\mathbf{H}[\kappa]\mathbf{w}_{i-1}[\kappa])}$
    - ii.  $\mathbf{w}_i[\kappa] = \left[ \mathbf{H}^H[\kappa]\mathbf{H}[\kappa] + \beta b^*[\kappa]b[\kappa]\mathbf{I} \right]^{-1} \mathbf{H}^H[\kappa]\mathbf{T}[\kappa]\mathbf{z}_i[\kappa]$
  - d) Optimal solution on logarithmic frequency grid  $\mathbf{w}_*[\kappa] = \mathbf{w}_i[\kappa]$
8. Add zeros to the optimal solutions at 0 Hz and Nyquist and interpolate solutions to a  $N/2$  point frequency grid  $\mathbf{w}[\kappa] \rightarrow \mathbf{w}[k]$
9. Form the discrete spectrum from  $N/2$  to  $N - 1$  by reversing and complex conjugating the single sided spectrum.
10. Calculate  $\mathbf{w}[n]$ , by taking  $N$ -point IFFTs of the elements of  $\mathbf{w}[k]$ .
11. A modeling delay is implemented as a cyclic shift of the filter coefficients of each element in  $\mathbf{w}[n]$
12. (Optional) Apply a window to each element in  $\mathbf{w}[n]$  with a smooth weighting function (e.g. a Hanning or Tukey window) in order to taper most of the energy in the impulse responses around the modeling delay and ensure that the impulse response of the filters start and stop at a value of 0.
13. The final  $L$  FIR filters for the  $L$  individual loudspeaker driving signal can then be found as the elements in  $\mathbf{w}[n] = [w_1[n], w_2[n], \dots, w_L[n]]^T$

# Design of the Loudspeaker Array

# 7

To test and validate the theories presented in Chapter 5 and 6, a physical prototype has been made.

The following chapter describes the considerations made in regards to the loudspeaker array characteristics. This includes the choice in the loudspeaker array geometry, size, as well as the material used and the number of driver units required.

The filter design methods presented in Chapter 6 presuppose an acoustic model describing the acoustic transfer functions from the input signal of each loudspeaker to the sound pressures at each measurement point, encapsulated in the frequency dependant matrix  $\mathbf{H}[k]$ . These transfer functions will need to be measured for a given physical loudspeaker array.

In this model, the loudspeaker array can essentially be regarded as a "black box", and the physical processes happening between sending an electric signal to a given driver and the eventual sound pressure being produced at a given measurement point can, more or less, be ignored. For this reason, no effort has been put into issues such as the cross-talk between drivers, as this potential cross-talk will just be a part of the "black box" model in the end.

## 7.1 Physical Design Constraints

While it may sound attractive to design the perfect ideal compact loudspeaker array for synthesizing the radiation pattern of a guitar, it is a pretty pointless exercise to design something that cannot be built in practice.

Instead, a compromise between a prototype that can perform well in recreating the target radiation pattern and a prototype that realistically can be build needs to be found<sup>1</sup>.

### 7.1.1 Considerations about the Loudspeaker Driver Units

The first task of the design is the choice of the loudspeaker driver units for the array. The enclosure of the loudspeaker array must afterward be designed in a way such that these drivers can be physically placed on the array.

These drivers should ideally be small enough so that a good amount of loudspeakers can be placed on the array, but at the same time, they also need to be able to be driven at the frequencies of interest for the guitar signal, which is roughly in a range of 80-5000 Hz.

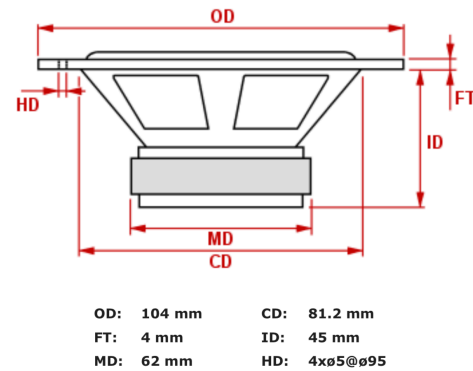
In a more practical sense, it has been preferred to use what was already available at AAU such that a prototype loudspeaker array could be built immediately without waiting for the shipping of a large number of drivers. Luckily, a large amount of 4" midrange drivers of the type 'Vifa M10MD-39-08' was at hand, which seems to be a decent loudspeaker driver unit for this purpose. This driver unit can be seen in Figure 7.1.

---

<sup>1</sup>To paraphrase an old saying: One loudspeaker array in the lab is better than ten loudspeaker arrays in theory.



(a) Picture of the Vifa driver unit next to a 5 Euro Cent



(b) Figure of the Vifa driver unit from datasheet<sup>2</sup>

**Figure 7.1:** Visuals of the midrange loudspeaker driver unit chosen for the loudspeaker array prototype.

Therefore the enclosure need to be designed in such a way that a good amount of these loudspeakaer driver units can be placed on its surface.

### 7.1.2 Considerations about the Geometry of the Loudspeaker Array Prototype

The enclosure of the loudspeaker array can take many shapes. In the previous studies outlined in Section 2.5.2 the shape of the enclosures was limited by the fact that they all used a nearly uniform distribution of loudspeakers on the enclosure. It thus more or less restricted the loudspeaker arrays to use either a spherical enclosure or an enclosure shaped like a platonic solid (such as a cube, dodecahedron, or icosahedron) with the driver units mounted on its faces.

Instead, in this project, the distribution of the loudspeakers does not necessarily have to follow a uniform distribution and could likely follow a non-uniform one instead. This is because the aim is to recreate a specific set of radiation patterns, i.e. the frequency dependant directivity of an acoustic guitar. This differs from a loudspeaker array made to serve as an omnidirectional source or to recreate any arbitrary radiation pattern.

Some examples of different potential enclosure shapes are shown in Figure 7.2.

<sup>1</sup>The datasheet of the units are available online at <http://www.madisound.com/pdf/vifa/m10md-39-08e.pdf>

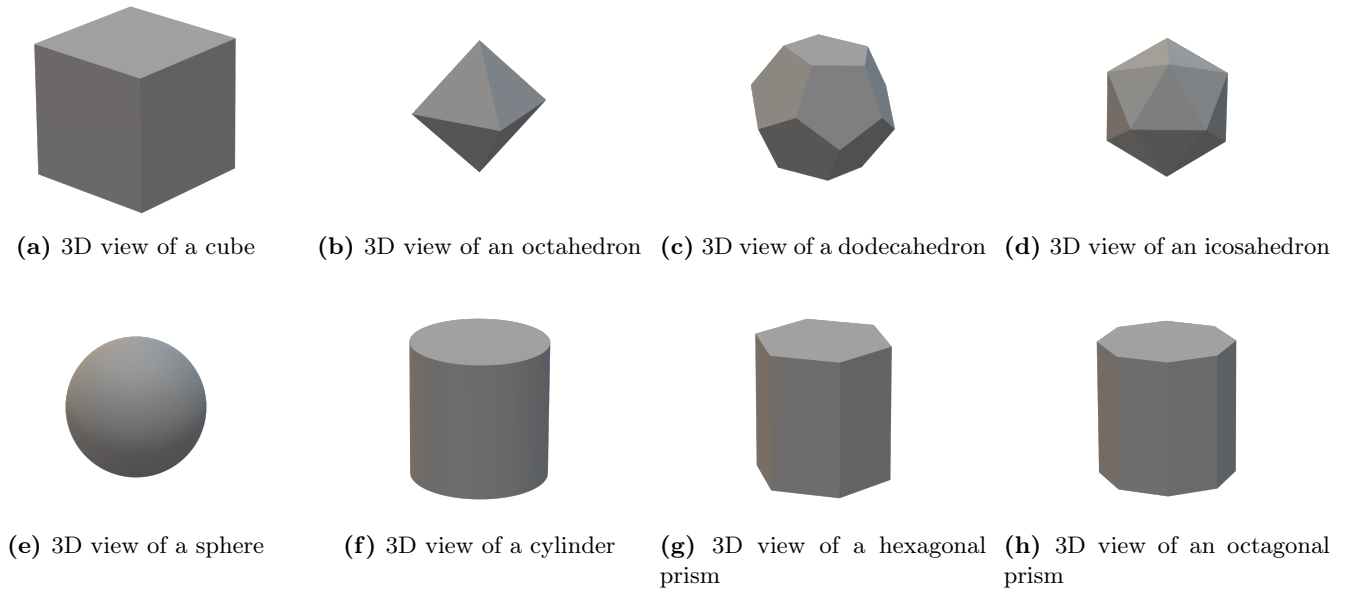


**Figure 7.2:** Illustration of the various geometries available for the design of the loudspeaker array

Many of these shapes have been investigated through simulations in Appendix F. It was generally observed that the shape of the enclosure itself did not have a huge impact on the performance in synthesizing the target radiation patterns compared to the influence of the number of loudspeakers and their placement.

However, there are some practical factors that influence the choice of the enclosure for a prototype. One of the limiting factors is time. As the loudspeaker array will need to be built and measured before the optimal filters can be implemented and tested, then it will be preferred to use an enclosure design, which is not too difficult to construct.

Shapes with curved surfaces, such as a sphere or cylinder, give some apparent issues from the start. First of all, the spots where the loudspeakers should be mounted would need to be flattened in some way to be able to screw the driver unit on tightly with no air leakage. This is much easier on flat surfaces, where the driver units can simply be screwed on a flat edge around each hole. Flat surfaces can also be more easily be constructed from widely available building materials such as wood boards.

So, while there are some very enticing possibilities associated with curved surfaces, namely a continuous set of directions at which the pistons could be facing, it has been chosen to work with the more easily constructible flat-surfaced shapes due to practical reasons.

Concerning the platonic solids, there are also some challenges. The straightforward way of constructing an icosahedron out of wood would be to cut out 20 equilateral triangles with each side cut at a bevel and glue the pieces together with wood glue. This requires the bevel to be cut pretty precisely for all pieces to line up tightly. Additionally, the pieces will need to be held in place while the glue is drying. Similar methods would have to be used for the dodecahedron and octahedron.

Additionally, if there should be enough space to place more than one 4" driver on each face, the faces of each panel will need to be quite large.

Instead, the octagonal prism (or eight-sided cylinder) shown on Figure 7.2h has been chosen as a good compromise between freedom to place the loudspeakers at selected places, and ease of construction.

The octagonal prism has been scaled in dimension to have the possibility of containing 3 of the available

midrange driver units on each of the eight sides and 4 of the midrange driver units mounted on the top and bottom plate of the octagonal prism. This provides an option to have a total of 32 loudspeakers units mounted on the octagonal prism without any driver units touching each other.

A sketch of the loudspeaker array with the chosen outer dimensions being used for planning and construction of the prototype can be seen in Figure 7.3.

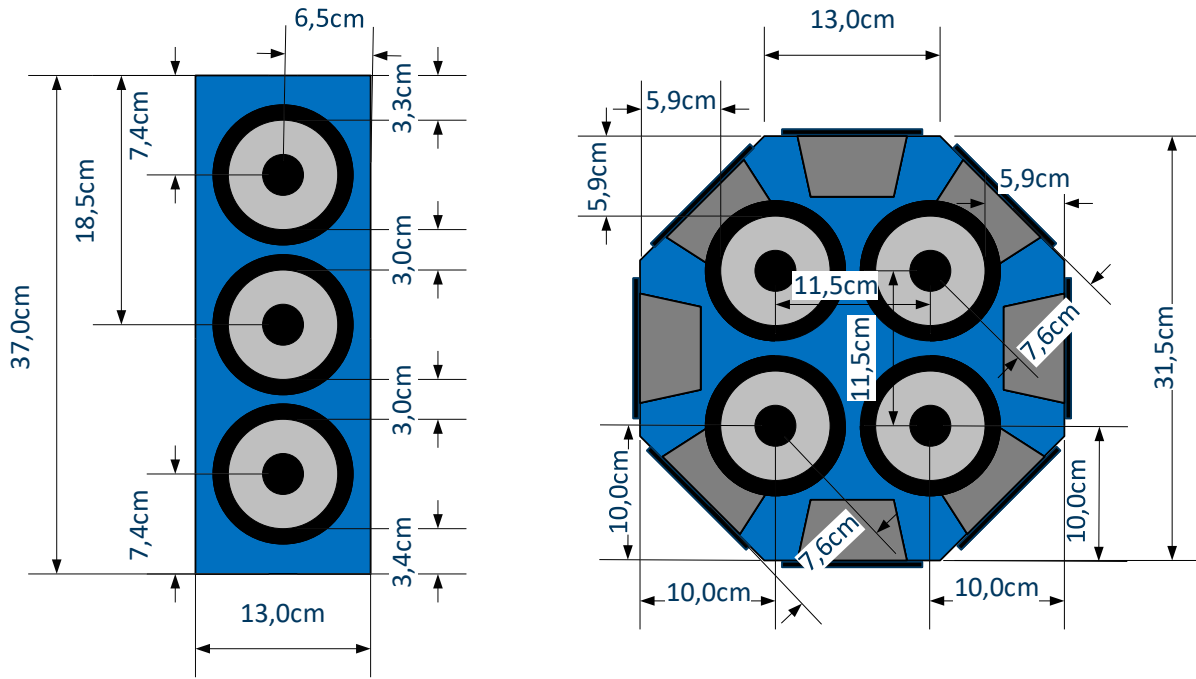


**Figure 7.3:** Construction sketch of the 8 sides plates (left) and the top and bottom plate (right). Measures are rounded to the nearest millimeter.

## 7.2 Strategies for Intelligent Loudspeaker Placement on the Array

As is evident by the simulations in Appendix E, the placement of each loudspeaker unit has a great impact on the radiation synthesis performance.

It is therefore important to place the loudspeakers in a well thought out manner such that a good recreation of the target pattern is possible across all frequencies. Some common-sense principles can initially be outlined.

First of all, it should be noted that a single loudspeaker's influence upon the overall sound field depends upon its own directivity. For instance, a loudspeaker that is barely radiating any sound energy to a point in the far-field will not be able to influence the total sound pressure at this point, which is given by the superposition of the sound pressures radiated by all the loudspeakers.

At low frequencies, every loudspeaker driver should act like an omnidirectional source to some degree due to the principles outlined in Section 2.3.3. Therefore a single loudspeaker should be able to act upon the sound field at every measurement point around the array.

On the contrary, at high frequencies, a single driver is assumed to be very directional, and most of its radiated sound power will be concentrated in a narrow main lobe and a few side lobes. At these frequencies, you can imagine that the placement of each loudspeaker starts to matter a lot.

Finally, it should also be noted that placing an additional loudspeaker can help reduce the error at a point,

no matter if the magnitude of the synthesized pattern overshoots or undershoots the target. If the sound pressure at a single point is too high, an additional loudspeaker can reduce this by producing a pressure contribution out of phase with the existing sound pressure, i.e. destructive interference. Of course, the opposite problem can be solved with constructive interference.

Using these principles together with the target directivity pattern of the guitar described in Section 4.2 you can already get an idea of where the loudspeakers potentially could be placed. For example, at the directivity sonogram on Figure 4.9 it can be seen that most of the sound is radiated between  $\theta = 60^\circ$  and  $\theta = -90^\circ$  at the higher frequencies while the directivity is more omnidirectional at lower frequencies.

Intuitively this tells us that it might be a good idea to place a high amount of loudspeakers in this area, to use the natural directivity of the loudspeakers to produce a good result at high frequencies while the low frequencies are not so dependant on the exact placement due to the loudspeakers themselves being pretty omnidirectional.

However helpful these rules of thumb may be, the question of placing the loudspeakers optimally still stands. Since the target radiation pattern is different at every frequency, this is a very complicated problem, for which an exact solution has not been found in this research.

In any case, a few simple algorithms to choose the "best" loudspeaker placement based on a given target pattern and simulations have been conceived.

### 7.2.1 Additive Approach

This first approach is based on the idea of iterative design (as are the others in fact). The idea is to start by placing a very low number of loudspeakers on a given shape, e.g. at the 3-4 dominant beam directions of the target pattern.

Optimal driver weights for all target frequencies can then be found through simulations<sup>3</sup> with the methods described in Chapter 5, after which the error between the synthesized pattern and the target pattern at each simulated frequency can be computed.

After a full simulation, a new piston can be added to the array in the direction where the error is largest, informed by the principles outlined earlier. The simulation is then repeated for this new array.

The flow chart of the algorithm can be seen in Figure 7.4.

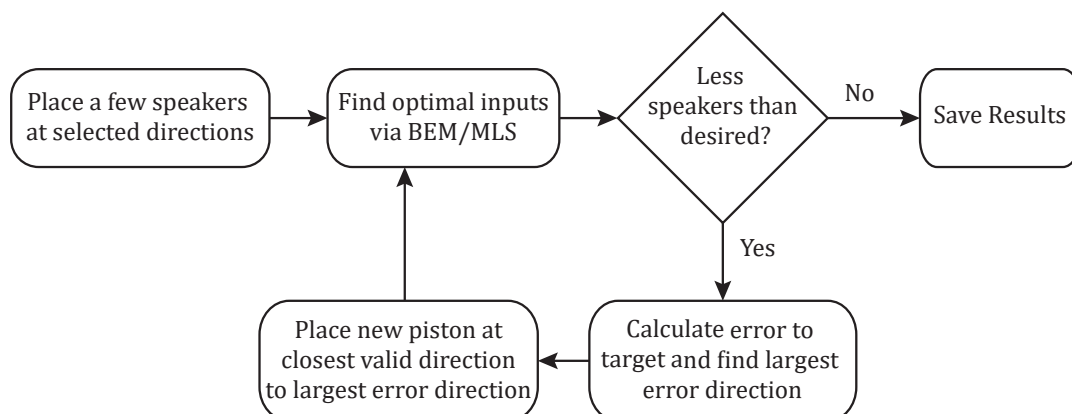


**Figure 7.4:** Flow chart of the additive loudspeaker placement algorithm.

<sup>3</sup>Of course the simulations can be replaced with actual measurements but this is much more time consuming and requires the prototype to be rebuilt multiple times.

After enough loudspeakers have been placed the algorithm can stop. The stopping criteria could either be some threshold for the error to go under or a maximum number of loudspeakers.

While this approach seems intuitive and sensible, the placement of the new loudspeaker needs to be very controlled for enclosure shapes with flat surfaces.

For a spherical enclosure, the algorithm only has to check if the new piston is overlapping with any previous pistons. But for shapes such as the octagonal prism, the number of loudspeaker placements being valid is much lower as a new piston can not overlap with either the previous pistons, edges, or vertices of the enclosure. For example, consider the case where the algorithm finds the largest error at the direction going from the origin to near the corner of the topmost octagon. As a piston cannot be placed here, the new piston would either have to be moved to one of the side plates or somewhere on the top plate, which could be relatively far away from the corner. There is no guarantee that the nearest placement valid to the largest error direction is also a placement with a large error.

Due to the amount of required work in order to handle invalid placement directions robustly, this algorithm has not been implemented for the octagonal prism.

### 7.2.2 Subtractive Approach

A more simple method to implement is to take the opposite approach. That is, filling the shape with as many loudspeakers as is physically possible to start with, and afterward remove the loudspeakers that are the least important. This approach avoids some of the more complicated steps of the additive algorithm since all possible loudspeaker positions are valid from the start.

By starting with a set number  $L_{start}$  of potential loudspeaker positions, the optimization problem now becomes combinatorial by nature:

Given  $L_{start}$  loudspeaker positions on the surface, choose the  $L_{end}$  loudspeaker position that results in the best approximation to the target pattern across frequencies.

A measure of how well a particular loudspeaker combination performs can be found by simulating its synthesized radiation patterns using the methods from Chapter 5, and summing up its WMSE over all the simulated frequencies, say every 1/3 octave frequency, until the frequency limit of the precise BEM-simulation. This total error term is explicitly given as

$$WMSE_{tot} = \sum_{k=1}^K \frac{1}{M} \sum_{m=1}^M w_m (|p_{fp,m,k}| - |t_{m,k}|)^2 \quad (7.1)$$

where  $K$  is the number of frequency points,  $M$  is the number of field points,  $w_m$  is the spatial weighting for the  $m$ th field point,  $p_{fp,m,k}$  is the solution from the simulation at the  $k$ th frequency and  $m$ th field point, and likewise  $t_{m,k}$  is the target function at the  $k$ th frequency and  $m$ th field point<sup>4</sup>.

In theory, an exact solution to this problem can be found by simulating every combination of  $L_{end}$  loudspeakers and picking the combination with the lowest  $WMSE_{tot}$ . However, the problem size can be become massive due to the combinatorial nature of the problem. As an example for the octagonal prism enclosure there is room for  $L_{start} = 32$  loudspeakers. If one wishes to place e.g.  $L_{end} = 25$  loudspeaker i.e. remove the seven least important loudspeakers one would have to simulate  $\binom{32}{25} \approx 3.37 \cdot 10^6$  combinations. This gets even worse for  $L_{end} = 24, 23, \text{etc.}$

<sup>4</sup>Naturally this error measure is biased towards the frequencies at which the error is largest, which has usually been shown to be the high frequencies. To mitigate this, a frequency weighting term could be applied, but this is not done in this project as it might actually be advantageous to give extra care to the frequencies with the largest error.

Instead, an iterative approach is taken where only one piston is removed every iteration. At every iteration  $i$ , there will initially be  $L_i$  loudspeakers left. The piston to remove can then be found by simulating all combinations of  $L_i - 1$  loudspeakers, i.e. each of the  $L_i$  loudspeakers gets turned off one at a time.

With our example number from before, this would mean that at the first step 32 combinations would have to be simulated, then 31, 30, etc. giving a total number of simulations of

$$\#_{simulations} = \sum_{i=0}^I \binom{L_{start} - i}{L_{start} - (1 + i)} \quad (7.2)$$

$$= \sum_{i=0}^I (L_{start} - i) \quad (7.3)$$

where  $I = L_{start} - L_{end} - 1$ . For our previous numbers this would provide a total of  $32 + 31 + \dots + 26 = 203$  combinations that has to be tried which is a huge reduction in the number of computations.

This algorithm is summarised by the flow chart shown on Figure 7.5.

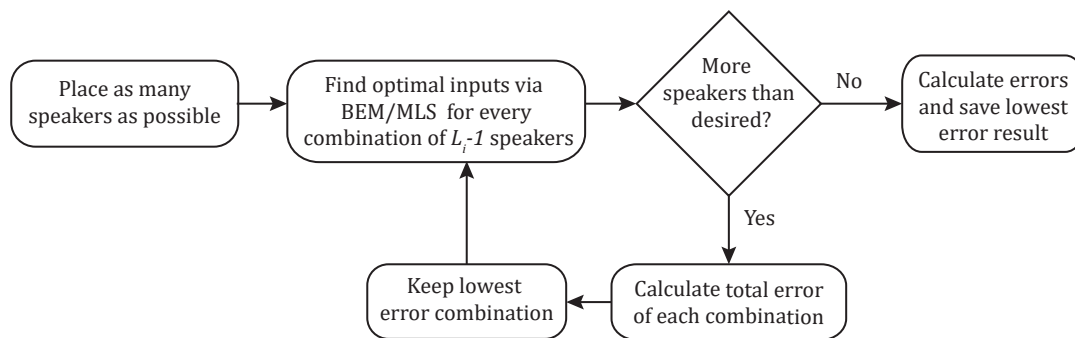


Figure 7.5: Flow chart of the subtractive loudspeaker placement method.

### 7.2.3 Indirect Subtractive Approach

Another variation to the subtractive method has also been implemented. The idea behind this algorithm is to find a way to remove a piston without having to simulate multiple combinations of the same number of loudspeakers.

From a simulation using  $L_i$  loudspeakers, it is easy to compute the resulting error, but it is hard to see which of the  $L_i$  pistons are most important to the performance of the loudspeaker array directly from the error.

Instead, a more indirect approach could be taken, where instead of looking at which pistons contributes the least error when turned off, you look at which piston is contributing the least to the overall sound pressure, assuming that the most important pistons will also be the ones radiating the most sound energy<sup>5</sup>.

A measure of the contribution of each piston can simply be found by summing up the magnitudes of the piston velocity gains at each frequency point.

This measure will, however, be biased towards the frequencies where the velocities are generally higher, i.e. the lower frequencies. But a frequency dependant weighting  $w_k$  could be applied to give a more appropriate

<sup>5</sup>This is due to the rule of thumb that a loudspeaker reduces the error through both constructive and destructive interference with the other loudspeakers.

weighting. A measure of the contribution of the  $l$ th piston can then be found as

$$\text{Contribution}_l = \sum_{k=1}^K w_k |u_{l,k}| \quad (7.4)$$

where  $u_{l,k}$  is the complex velocity gain for the  $l$ th piston found through the MLS-solution in the simulations for the  $k$ th frequency point.

The piston with the lowest contribution score can then be removed. With this method, every amount of loudspeakers only have to be simulated once, which means that e.g. only 7 simulations will have to be run to remove 7 pistons compared to the 203 simulations for our example with the 'Direct' subtractive approach.

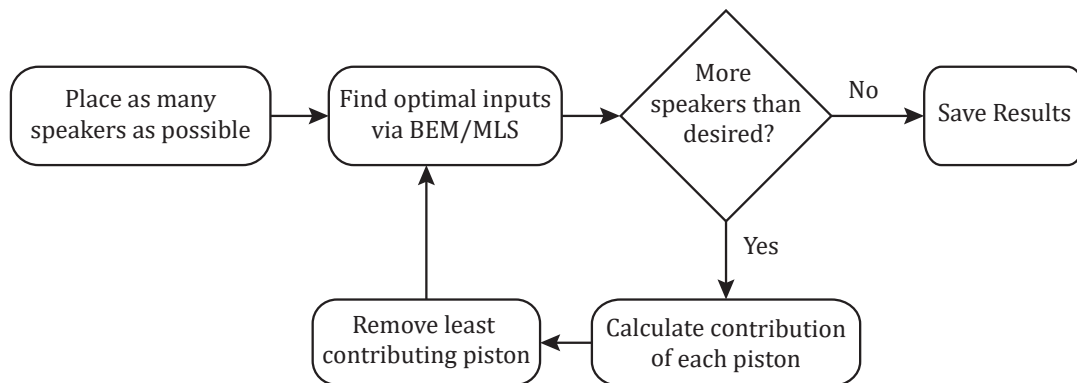


**Figure 7.6:** Flow chart of the indirect subtractive method.

In Appendix H both the indirect and direct subtractive methods are compared through simulations on both the octagonal prism shape lying down and standing up. The direct method was shown to give a better result in terms of  $WMSE$  in most cases.

However, the frequency weights used for the indirect methods were not chosen with a lot of thought put into them. So, perhaps a different weighting system could be thought of, which provides give the indirect method a performance closer to the direct method.

### 7.3 Description of Prototype Loudspeaker Array

Based on simulations of the octagonal prism shown on Figure 7.3 with loudspeakers placed according to the subtractive approach outlined in Section 7.2, a loudspeaker array layout for the octagonal prism has been chosen. These simulations are described in detail in Appendix H.

The loudspeaker placement is shown on a 3D model on Figure 7.7.

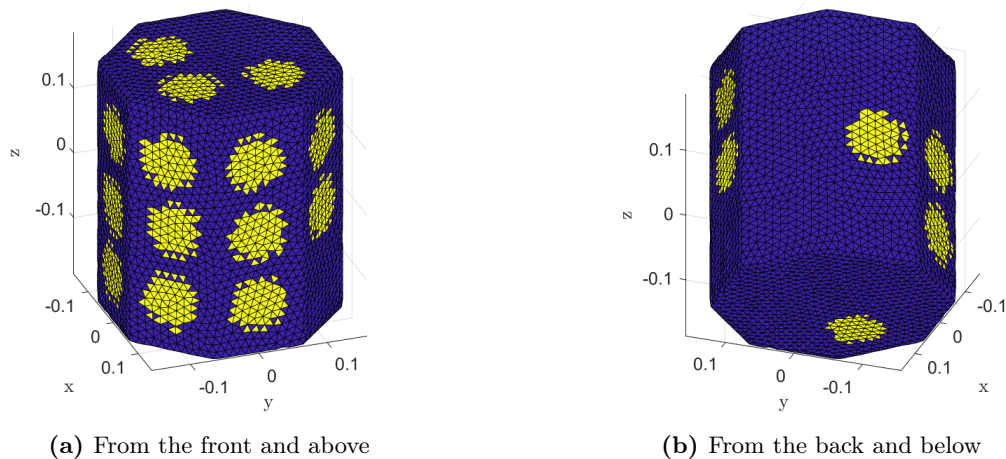


**Figure 7.7:** Loudspeaker placements for the prototype array.

A large number of loudspeakers were placed at the front and to the right side of the array, which fits well with the initial assumptions of where to place the loudspeakers.

The loudspeaker placements were chosen using the "direct" subtractive loudspeaker placement approach since it turned out to have a slightly better performance in terms of  $WMSE$  at the higher frequencies, where the error is generally highest, compared to the indirect method. It is hard to definitely say what is the perfect amount of loudspeakers, as removing a loudspeaker always seems to worsen the performance by a small amount, and vice-versa. How many loudspeakers to put on the array, thus probably depends on the requirements for a specific loudspeaker system<sup>6</sup>.

On this specific prototype, it has been chosen to place 20 loudspeakers on the array because this configuration was shown to have a pretty good performance in the simulations up to around 2 kHz. Around 3 kHz, the performance seems pretty bad, but this was also the case for 24 and 28 loudspeakers in the simulations. To get better performance, then a different enclosure shape and smaller driver units would probably be needed.

Additionally, the same prototype can also be used to test the performance using fewer than 20 drivers by simply turning some of the drivers off and calculating new filters for the remaining loudspeakers.

A complete overview of the loudspeaker placements (and numbering) on the different faces of the octagonal prism can be seen in Figure 7.8.

<sup>6</sup>An obvious approach to determine how many loudspeakers are "enough" is to take a more psycho-acoustical approach and investigate when and how well human subjects can distinguish between the true target radiation pattern and the synthesized radiation patterns. But this is a massive area of research in itself and has therefore not been investigated in this project.

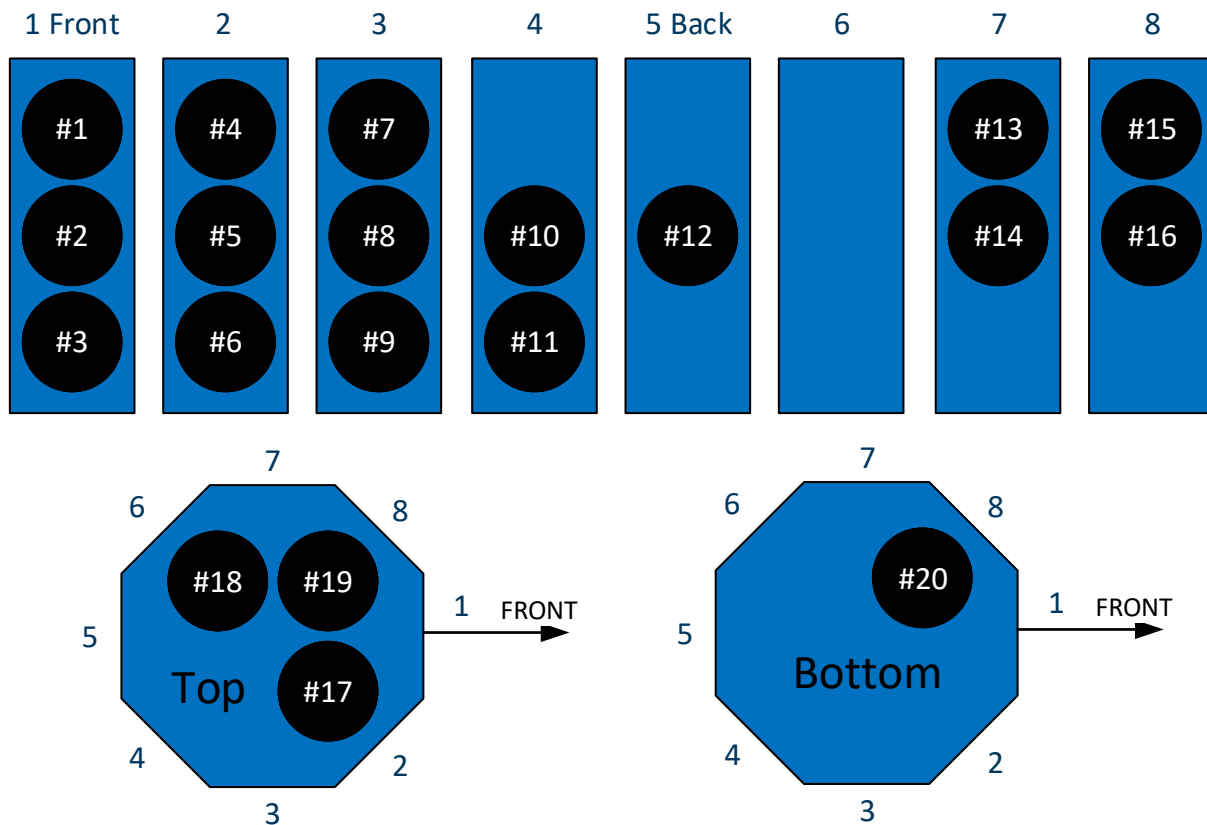


**Figure 7.8:** Overview of the loudspeaker placements on the 8 side plates and the top and bottom plates of the octagonal prism including loudspeaker numeration with "#". The top and bottom plate is seen from the side facing upwards.

Due to a mistake in the construction diagram, the placements on the top and bottom octagons have been flipped along the  $x$ -axis compared to the optimal placement from the simulation shown in Figure 7.7. This means loudspeaker #18 and #20 are out of position, whereas the rest of the loudspeakers are fine where they are. While this means that the placements could be better according to the placement algorithm, the filters found according to the methods in Chapter 6 will still be optimal for the particular array. Since 90% of the loudspeakers are still at the right spots, it has been decided to simply disregard this mistake and use this prototype array anyway.

The physical prototype has been constructed out of wood, more specifically Medium-Density Fibreboard (MDF) sheets. The rectangular side panels were cut from 16 mm sheets. The two octagons were made from a slightly thinner 10 mm sheet in order to be able to cut them precisely with a laser cutter.

The rectangular side pieces were beveled at their sides and glued together with wood glue. The side pieces have been attached to the octagons using both glue and screws. A stand adapter was also screwed onto the bottom side so that the loudspeaker array could be mounted on a loudspeaker stand while performing the acoustic measurements.

Figure 7.9 shows pictures of the array during the construction (left picture), and once the array was finished (right picture), after which some acrylic sealant was used to seal the enclosure air leakage due to the cabling.



(a) The array being assembled.



(b) The finished loudspeaker array from the front right side.

**Figure 7.9:** Prototype loudspeaker array

## 7.4 Measurement of the Prototype Transfer Functions

Once the loudspeaker had been assembled, some measurements were performed on the array to obtain the impulse responses of the 20 driver units needed in the design of the filters from Chapter 6.

The same setup used to measure the 3D sound radiation of the guitar was also used for this purpose. The loudspeaker was placed on a turntable at a distance of 1.7m from the metal arch filled with 17 microphones placed in a range of  $-70^\circ < \phi < 90^\circ$ , and spaced  $\phi = 10^\circ$ . The turntable allowed the array to turn around its central vertical axis with the desired step size of  $\theta = 10^\circ$  within  $0^\circ < \theta < 360^\circ$ . This created a grid of 577 unique measuring points, plus a virtual one at  $\phi = -90^\circ$  (average of all the  $\phi = -70^\circ$  measurements) disposed on a sphere with a radius of 1.53m (every microphone on the arch is supported by 17cm long plastic flat bar). To obtain the impulse responses from each loudspeaker to each observation point, a short Exponential Sine Sweep signal (ESS) of 2 seconds duration and 0.5 seconds pause is send to each driver unit one at a time for each azimuth turntable step. A detailed description of the measurements setup as well as the measurement procedure can be found in Appendix I.

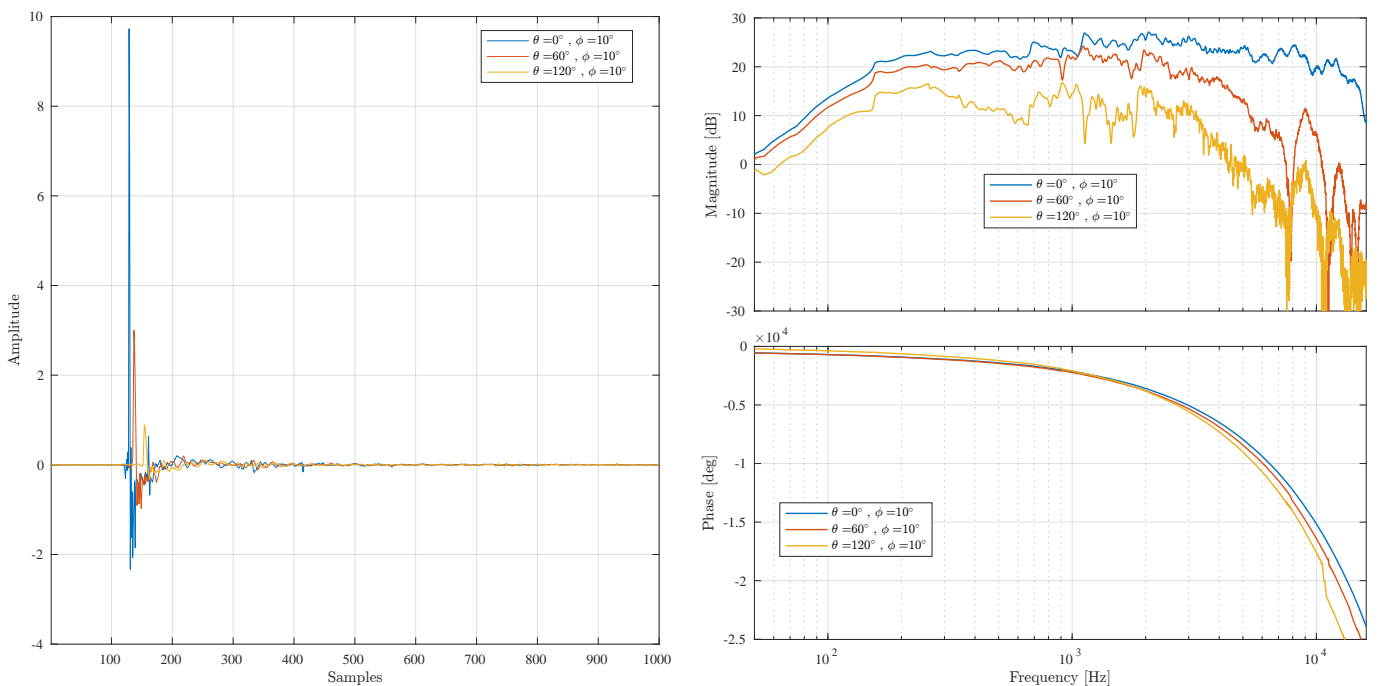
A few impulse responses for one single loudspeaker unit, in this case loudspeaker #2 (front central loudspeaker), are plotted in Figure 7.11 together with the respective magnitude and phase response. The responses are shown for three measuring point placed at the same height (microphone at  $\phi = 10^\circ$ ) but at three different azimuth angles  $\theta = 0^\circ, 60^\circ, 120^\circ$ .

It is easy to see that measuring the loudspeaker at different points on the sphere influences the responses in both the delay/phase and in amplitude/magnitude. In particular, the differences in magnitude responses seem to grow with the frequency, highlighting the directivity properties of the chosen loudspeaker driver



**Figure 7.10:** Picture of the setup for the 3D measurement of the sound radiation loudspeaker array.

units as well the partial shadowing effect of the array enclosure itself. However, some more plots for different measuring points and loudspeaker units can be found in Section I.4.



(a) Impulse responses for the loudspeaker #2 (front center of the array).

(b) Magnitude and phase response for the loudspeaker #2 (front center of the array)

**Figure 7.11:** Impulse response, magnitude response and phase response of loudspeaker #2 (front center of the array) for three different azimuth angles  $\theta = 0^\circ, 60^\circ, 120^\circ$  at the same elevation angle  $\phi = 10^\circ$ .

# Performance of the Loudspeaker

## Array 8

As a result of the preceding chapters, everything needed to synthesize the directivity pattern of a guitar using a loudspeaker array is in place.

### 8.1 Description of Measurements

The loudspeaker array prototype described in Chapter 7 is used in these measurements. The measured impulse responses of this array prototype are then used to design optimal filters. MLS-based filters have been designed using both the iterative magnitude fast deconvolution algorithm described in Section 6.3 (MLS) and using complex interpolation as described in Section 6.5 (MLS-CI). Both sets of filters have been computed using a filter length of 4096 taps. A frequency-independent regularization factor  $\beta = 0.01$  is used in both algorithms in order to limit the effort at frequencies where  $\mathbf{H}[k]$  is ill-conditioned. The iterative MLS-solution is found using a convergence criterion of  $\epsilon = 10^{-4}$ .

The target function for both algorithms is based on the 1/6 octave band filtered RMS-values of the guitar radiation measurements in 3D from Chapter 4, but are slightly different due to how the target is defined in each filter algorithm. In the MLS filters, the target function at each measurement point is interpolated to an FFT-frequency grid as described in Section 6.4.

In the MLS-CI filters, the target function only has to be defined on a logarithmic grid, so the RMS-values at the 1/6 octave band center frequencies from 79 Hz to 10 kHz can be used directly. However, in order to have a little bit more control of what happens in between the logarithmic frequency bins, then the target RMS-values are "upsampled" to the 1/24 octave band center frequencies also using linear interpolation. For the MLS-CI filters, the measured impulse responses were shifted circularly by 115 samples in order to remove most of the propagation delay.

The radiation patterns of the prototype speaker, using each of the sets of filters, are measured in two ways with the same microphone setup as the previous measurements.

Firstly by playing out a filtered version of the pickup signal of an acoustic guitar. The particular signal used is one of the measured pickup signals from the 3D measurements of the guitar radiation from Section 4.2. This allows the recordings at the "sphere" of microphones to be analyzed in the exact same way as the recordings of the guitar, i.e. with fractional octave band filtered RMS-values divided by the RMS value of the fractional octave band filtered pickup signal. The comparison is made particular fair by the fact that the same guitar sequence is used in the comparison, such that it is known that only frequencies at tones produced by the guitar are present in the input signal.

Secondly, the radiation pattern is measured using an exponential sine sweep filtered by the FIR filters. This allows you to deconvolve the microphone recordings with the original sine sweep, using the ESS techniques described in Section I.3, which can give you the impulse response/transfer function from the SIMO-input of

the filters to the sound pressure at the microphone positions. In this way, the magnitude response of the system can be viewed at a much higher frequency resolution compared to fractional octave bands, as well as giving an idea about the time- and phase response of the system.

Both signals are filtered beforehand in MATLAB, and the resulting 20 filtered signals are sent to the speakers using the same setup as used in Appendix I, shown on Figure 8.1.

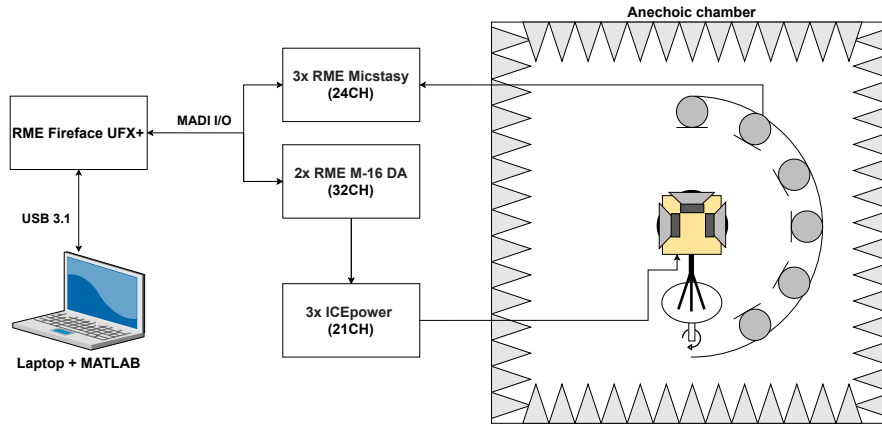


**Figure 8.1:** Overview of measurement setup for measuring the synthesized radiation patterns of the speaker.

The filtered signals are normalized so that the maximum amplitude is -34 dBFS to spare the driver units since the power amplifiers in the setup have a fixed 30 dB gain.

## 8.2 Loudspeaker Sonograms

In this section, an overview of the sound radiation patterns of the loudspeaker array using the MLS and MLS-CI filters for 20 channels are presented as directivity sonograms of the three different planes (the horizontal, frontal, and median plane) using 1/6 octave bands. These can easily be compared to the equivalent directivity sonograms in the horizontal, frontal, and median plane from the 3D measurement of the guitar in Section 4.2, which serve as the desired target radiation patterns.

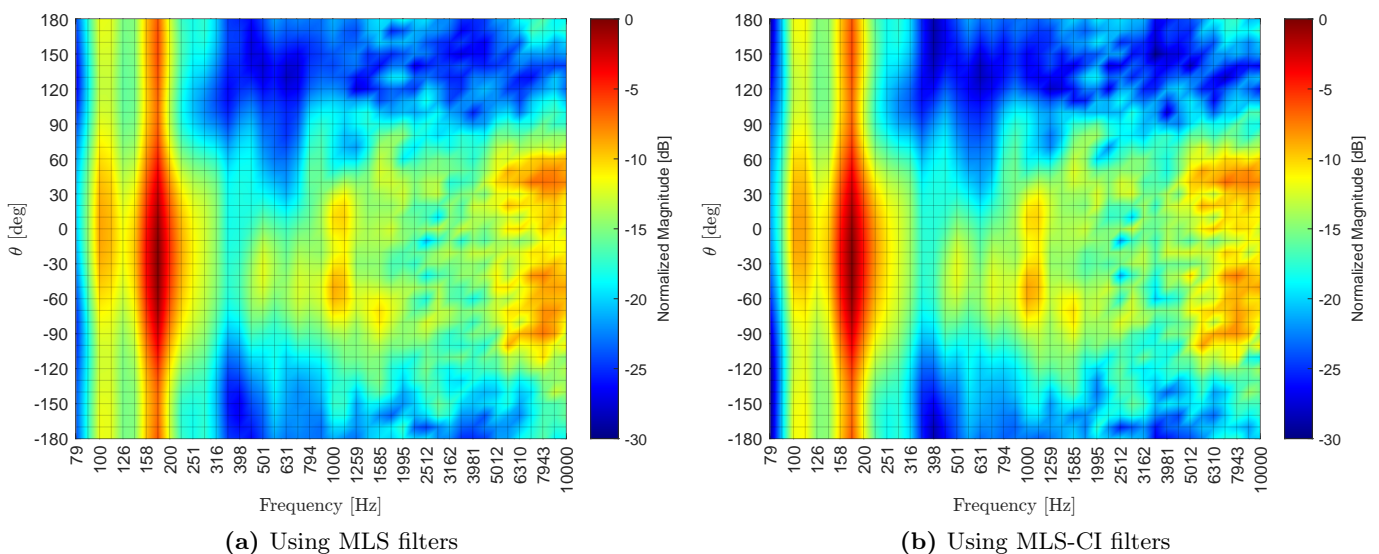


**Figure 8.2:** Directivity sonogram of the loudspeaker array in the full horizontal plane using interpolated 1/6 octave bands to plot frequency vs. azimuth angle  $\theta$ . Front direction is  $\theta = 0^\circ$ . Using  $N = 4096$  taps long FIR filters convolved with an ascending barre chords signal (pre-recorded with the guitar pickup).

From the directivity sonograms of the loudspeaker array in the full horizontal plane of Figure 8.2, it can be seen that both the MLS and MLS-CI filters provide extremely similar synthesized radiation/beam patterns in the horizontal plane. The two different approaches only differ slightly in the radiation pattern in the higher frequencies, making them very difficult to separate.

In general, the two synthesized radiation patterns of the loudspeaker array in the horizontal plane reveal a relatively strong sound radiation of the middle and high frequencies to the front side ( $\theta = 0^\circ$ ) as well as a weaker sound radiation of the middle and high frequencies to the backside ( $\theta = 180^\circ$ ), exactly as desired.

However, the beam patterns of the two filter approaches also resemble the target beam pattern in the full horizontal plane of the 3D guitar measurement (see Figure 4.9) to a very high degree as intended. The overall beam patterns are very comparable, but the two synthesized beam patterns begin to deviate slowly from the target in the horizontal plane from around 2000 Hz and above. In the high frequencies, it can be seen that two synthesized beam patterns of Figure 8.2 radiate the sound with higher gain to a wider range of directions, especially between  $\theta = 20^\circ$  and  $\theta = 60^\circ$  as well between  $\theta = -30^\circ$  and  $\theta = -100^\circ$ , compared to the more narrow beam directions (especially around  $-70^\circ$  azimuth) of the original guitar target in Figure 4.9.

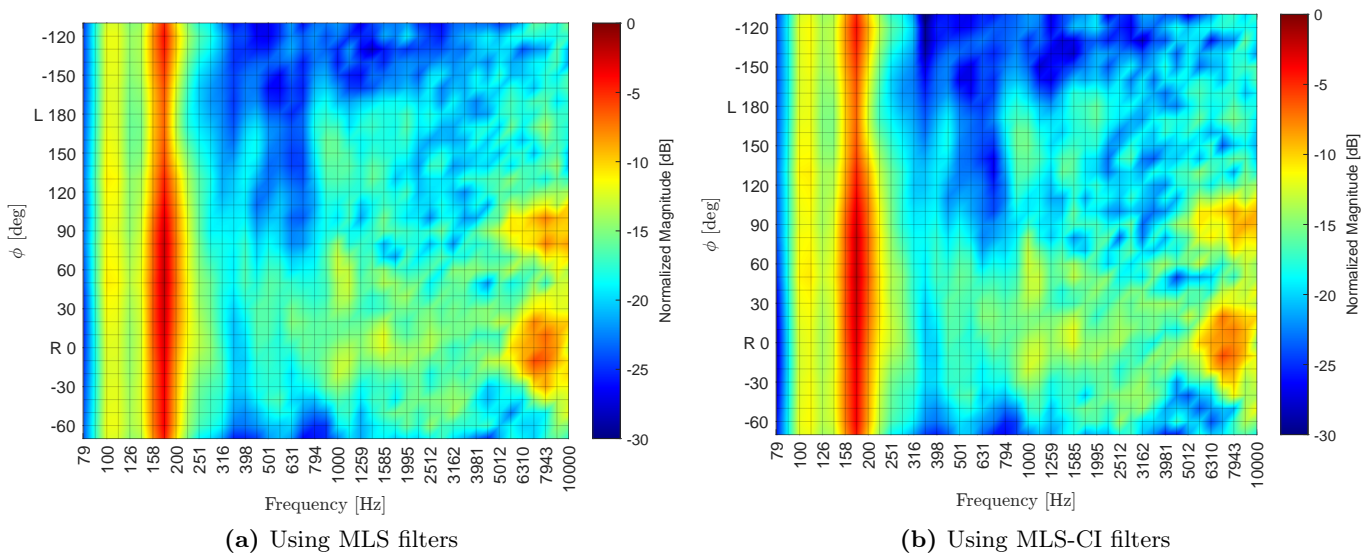


**Figure 8.3:** Directivity sonogram of the loudspeaker array in the frontal plane using interpolated 1/6 octave bands to plot elevation angle  $\phi$  vs. frequency. To get a reference,  $\phi = 0^\circ$  is the right side, while left is  $\phi = 180^\circ$  and top/head is  $\phi = 90^\circ$ . Using  $N = 4096$  taps long FIR filters convolved with an ascending barre chords signal (pre-recorded with the guitar pickup).

Again, the directivity sonograms of the loudspeaker array in the frontal plane seen in Figure 8.3 show almost no visible difference in the beam patterns between using the MLS and MLS-CI filters. The overall sound radiation is concentrated mostly to the right side of the loudspeaker array compared to the left side, which was also the case for the guitar measurements in Chapter 4.

When comparing the two synthesized beam patterns with the guitar target beam pattern in the frontal plane (see Figure 4.10) it becomes clear that the synthesized beam patterns are only a close match up until the middle frequencies, from where the difference in the patterns increases with frequency. However, the general pattern of the target function is overall followed by both approaches.

The two synthesized beam patterns of Figure 8.3 in the frontal plane differ most from the target pattern at high frequencies, where the two synthesized radiation patterns are beaming the sound straight upwards with high gain. The target beam pattern in the frontal plane of Figure 4.10 also radiate some high frequency

(around 7000 Hz) sound with a narrow but strong beam directed to the lower right side ( $\phi = -10^\circ$ ), whereas both of the two synthesized beam patterns radiate the sound at the high frequencies with high gain to a wider range of directions between  $\phi = 30^\circ$  and  $\phi = -30^\circ$ .

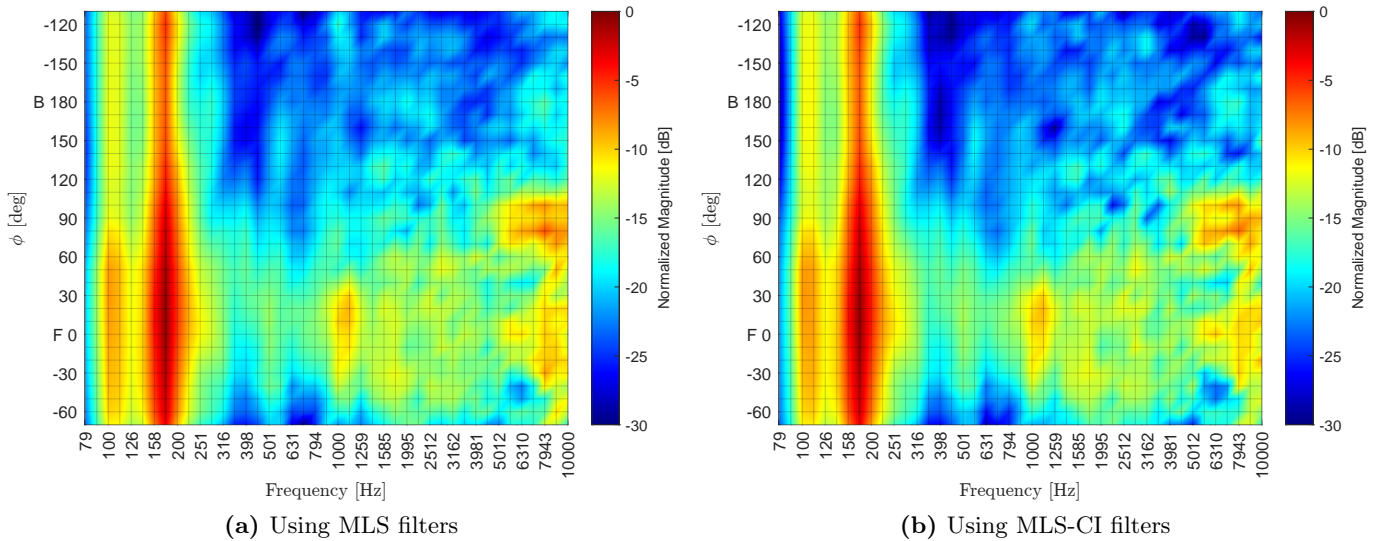


**Figure 8.4:** Directivity sonogram of the loudspeaker array in the median plane from the 3D measurement using interpolated 1/6 octave bands to plot elevation angle  $\phi$  vs. frequency. Front is  $\phi = 0^\circ$ , back is  $\phi = 180^\circ$  and top/head is  $\phi = 90^\circ$  Using  $N = 4096$  taps long FIR filters convolved with an ascending barre chords signal (pre-recorded with the guitar pickup).

When looking at the directivity sonograms of the loudspeaker array in the median plane seen in Figure 8.4, it can again be seen that both the MLS and MLS-CI filters provide very similar overall radiation/beam patterns. Generally, both the two synthesized beam patterns in the median plane reveal a relatively strong sound radiation of the middle and high frequencies to the front side ( $\phi = 0^\circ$ ), whereas only low frequencies are radiated with high gain to the backside ( $\phi = 180^\circ$ ) of the loudspeaker array.

Comparing the two synthesized beam patterns in the median plane of Figure 8.4 to the desired guitar target pattern (Figure 4.11) shows once again great similarity in the overall pattern. Having said that, the target pattern in the median plane radiates the sound around 8000 Hz with a single beam of high gain to an elevation angle around  $\phi = 70^\circ$ , while the two synthesized beam patterns are both struggling with this direction and instead radiate the higher frequencies with a much wider beam of even higher gain going more vertically up between  $\phi = 80^\circ$  and  $\phi = 100^\circ$ .

### 8.3 Loudspeaker Balloon-style Directivity Plots

After having looked at some radiation patterns synthesized by loudspeaker array using either the MLS or MLS-CI filters in the horizontal, frontal, and median plane, it is also possible to evaluate the behavior of the filters under a different perspective.

In the following, the radiation patterns of the loudspeaker array are presented as balloon-style directivity plots using 1/3 octave bands. All the balloon-style directivity plots of the measured loudspeaker array using either the MLS or MLS-CI filters can be found in Appendix J, while the balloon-style directivity plots for a few selected 1/3 octave bands will be presented in this section.

These balloon-style directivity plots are here compared to the equivalent balloon-style directivity plots from the 3D measurement of the guitar (described in Chapter 4 and Appendix C), which serve as the desired

target radiation patterns for each 1/3 octave band.

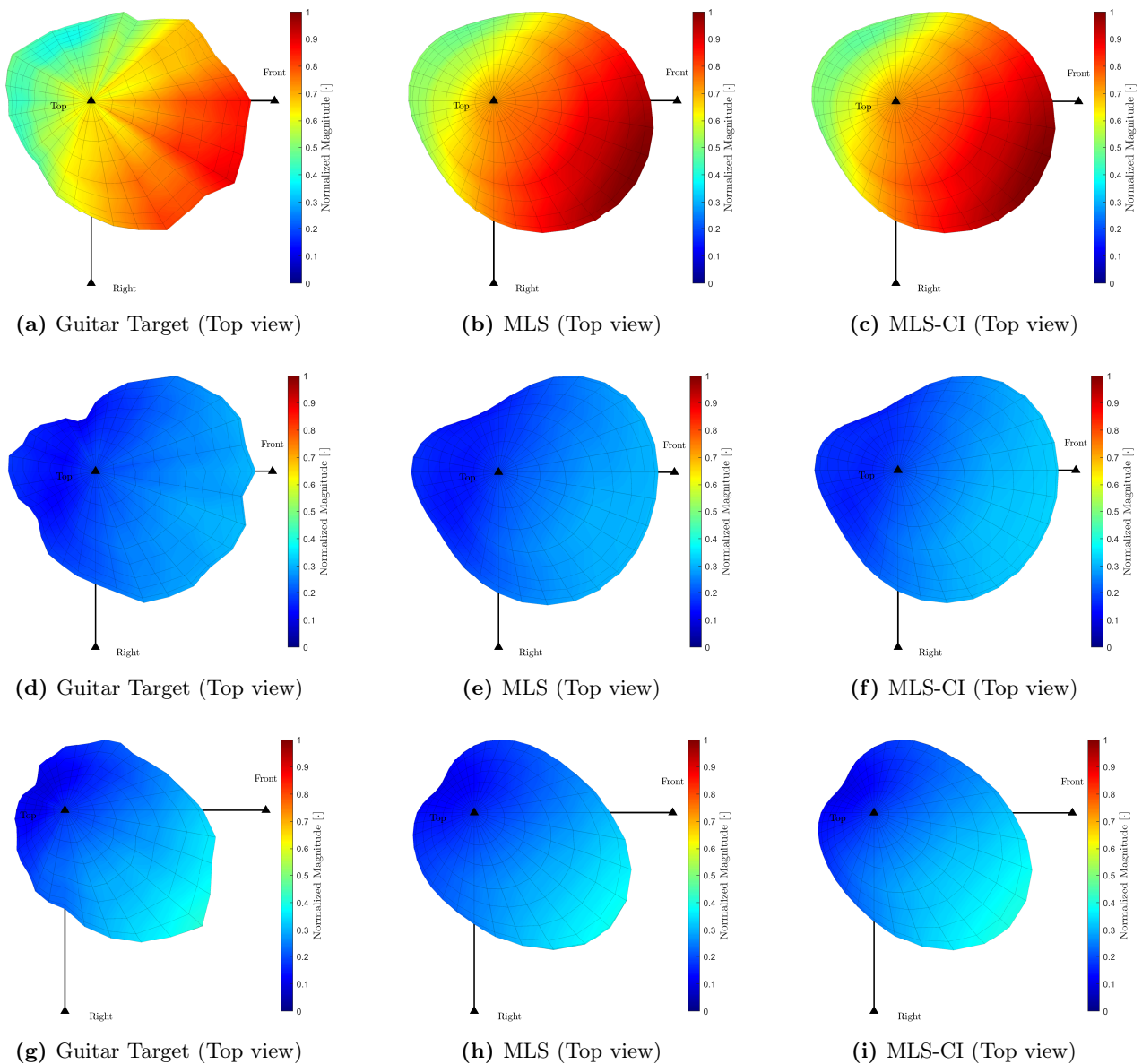


**Figure 8.5:** 3D Balloon-style directivity plots (Top view) in the 1/3 octave bands centered around 158 Hz (top row) 316 Hz (middle row) and 501 Hz (bottom row) for the guitar radiation and the loudspeaker array using either the MLS or MLS-CI filters. The plots are normalized over the maximum magnitude for all 1/3 octave bands in between 79 Hz to 10 kHz.

From Figure 8.5 it can be seen that 3D sound radiation patterns (top view) for the low frequencies of the loudspeaker array using either the MLS or MLS-CI filters resemble the shape of guitar target radiation patterns to a very satisfying degree.

For the three selected 1/3 octave bands in Figure 8.5 the two synthesized radiation patterns are both more smooth than the target pattern between the different directions or measurement points, even though the overall 3D radiation patterns remain almost indistinguishable. However, the overall gain to every direction of the two synthesized radiation patterns seems to differ a bit from the target pattern, especially for the 158 Hz band, where the two synthesized radiation patterns show a little higher gain.

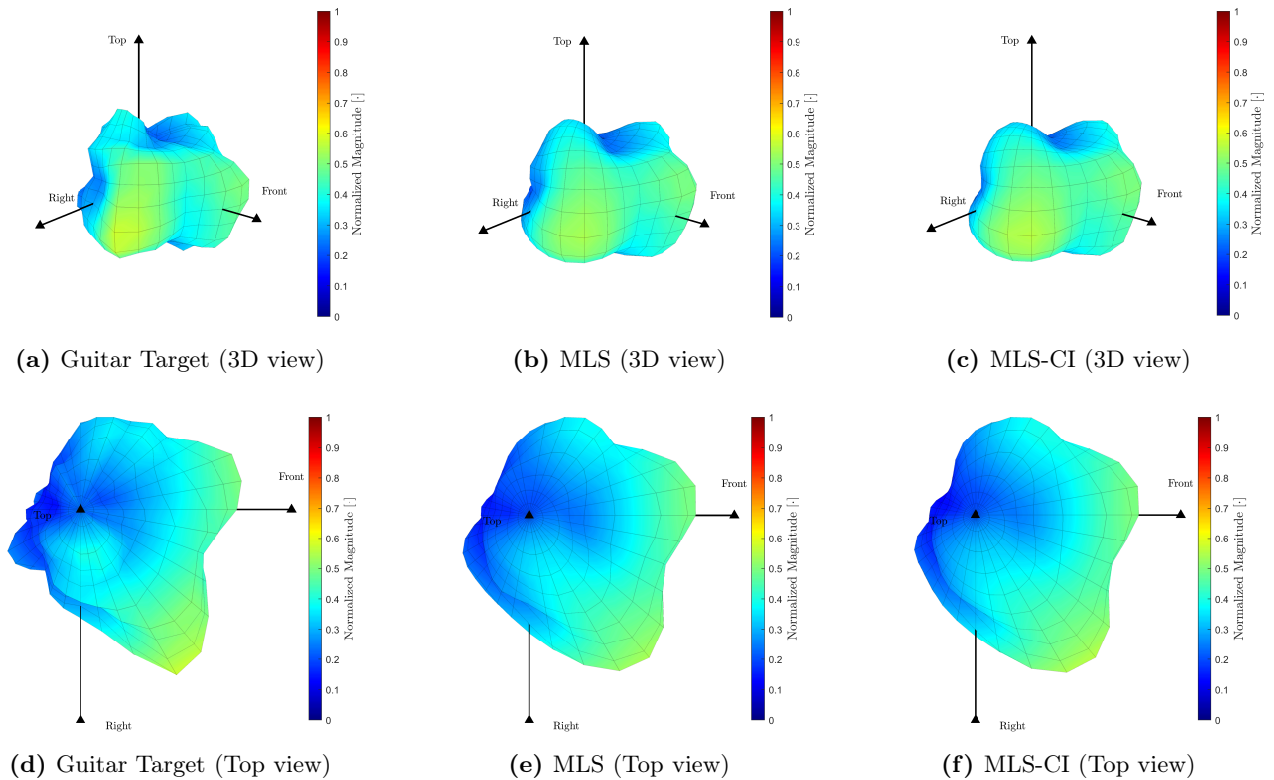


**Figure 8.6:** 3D Balloon-style directivity plots (3D view + Top view) in the 1/3 octave band centered around 1000 Hz for the guitar radiation and the loudspeaker array using either the MLS or MLS-CI filters. The plots are normalized over the maximum magnitude for all 1/3 octave bands in between 79 Hz to 10 kHz.

Looking at the balloon-style directivity plots for 1000 Hz band in Figure 8.6, the overall 3D radiation patterns of the loudspeaker array using either the MLS or MLS-CI filters still approximate to the target pattern with good accuracy, even if with a more smooth transition between the different directions.

It is hard to decide which of the two synthesized radiation patterns is the closest to the target pattern at this frequency band, as the difference between them is at an insignificant level, which one should not be able to distinguish if the only focus is given on the magnitude changes over different directions.

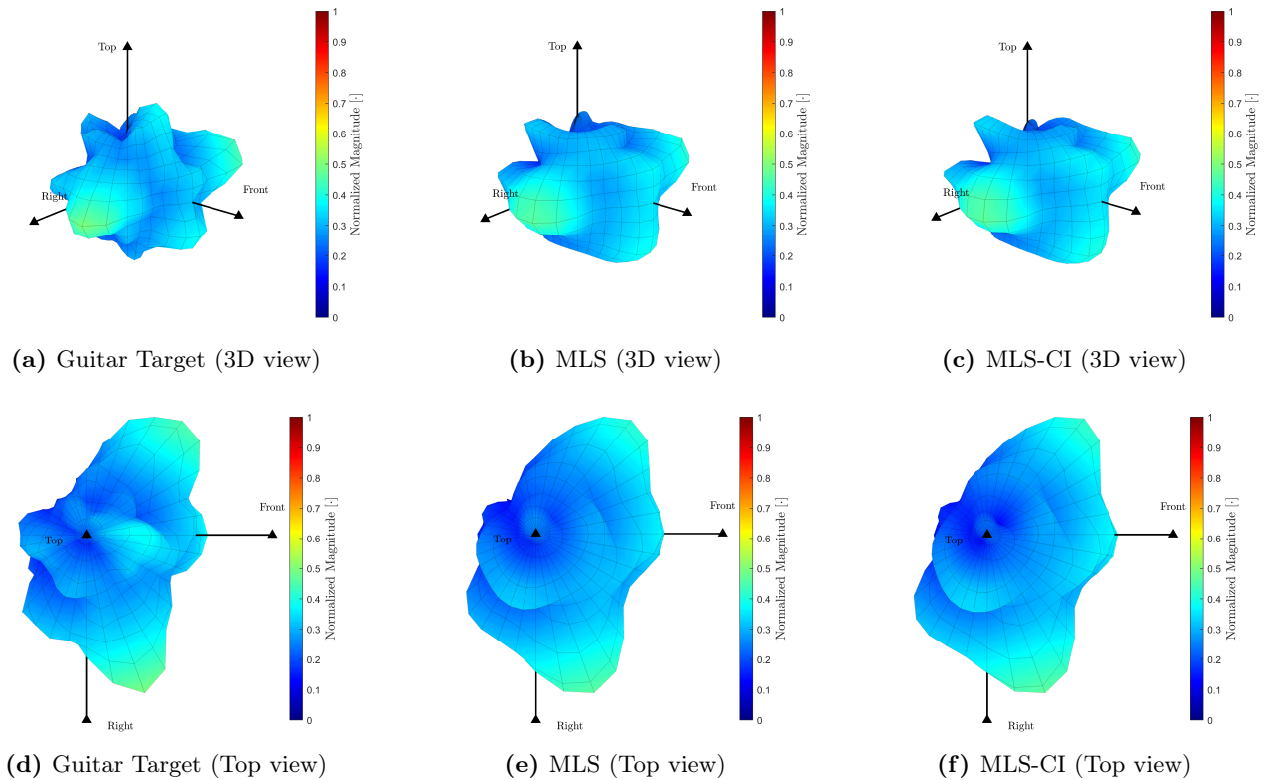


**Figure 8.7:** 3D Balloon-style directivity plots (3D view + Top view) in the 1/3 octave band centered around 1585 Hz for the guitar radiation and the loudspeaker array using either the MLS or MLS-CI filters. The plots are normalized over the maximum magnitude for all 1/3 octave bands in between 79 Hz to 10 kHz.

For the 1/3 octave band centered around 1585 Hz seen in Figure 8.7 the two synthesized radiation patterns now start to differ a bit more from the guitar target radiation pattern. However, it is still clear which radiation pattern that the loudspeaker array using either the MLS or MLS-CI filters is trying to imitate, as both synthesized radiation patterns are reminiscent of the target pattern for the 1585 Hz band.

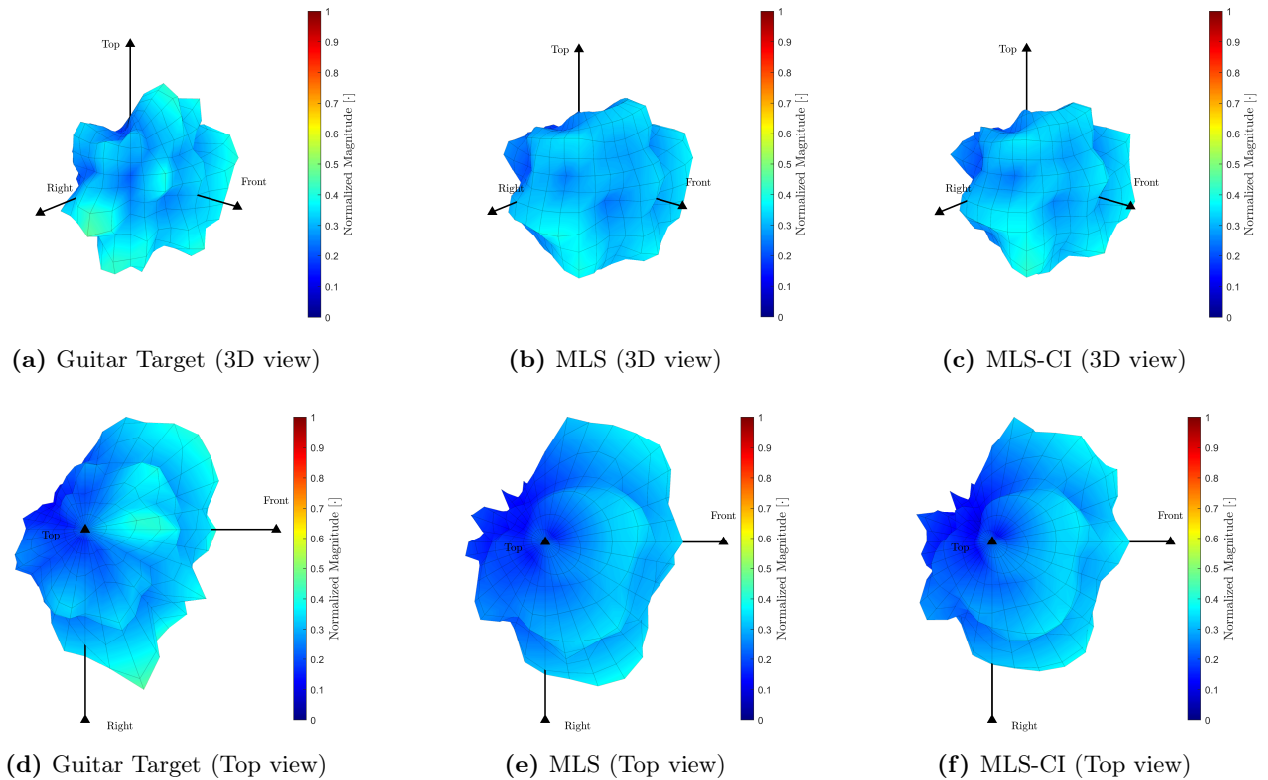


**Figure 8.8:** 3D Balloon-style directivity plots (3D view + Top view) in the 1/3 octave band centered around 1995 Hz for the guitar radiation and the loudspeaker array using either the MLS or MLS-CI filters. The plots are normalized over the maximum magnitude for all 1/3 octave bands in between 79 Hz to 10 kHz.

Going a bit higher in frequency up to the 1/3 octave band centered around 1995 Hz shown Figure 8.8, it becomes clear that the loudspeaker array using either the MLS or MLS-CI filters can only synthesize the guitar target radiation pattern with good accuracy up to around this point in the middle frequencies.

This is proved by the fact that now the two synthesized radiation patterns of the loudspeaker array can not match the fine details of the target radiation pattern (which starts to beam the sound several in specific directions) as good anymore. Instead, the two synthesized patterns become a more smooth approximation of the overall target radiation pattern. However, the approximations are still acceptable but just getting noticeable worse now.

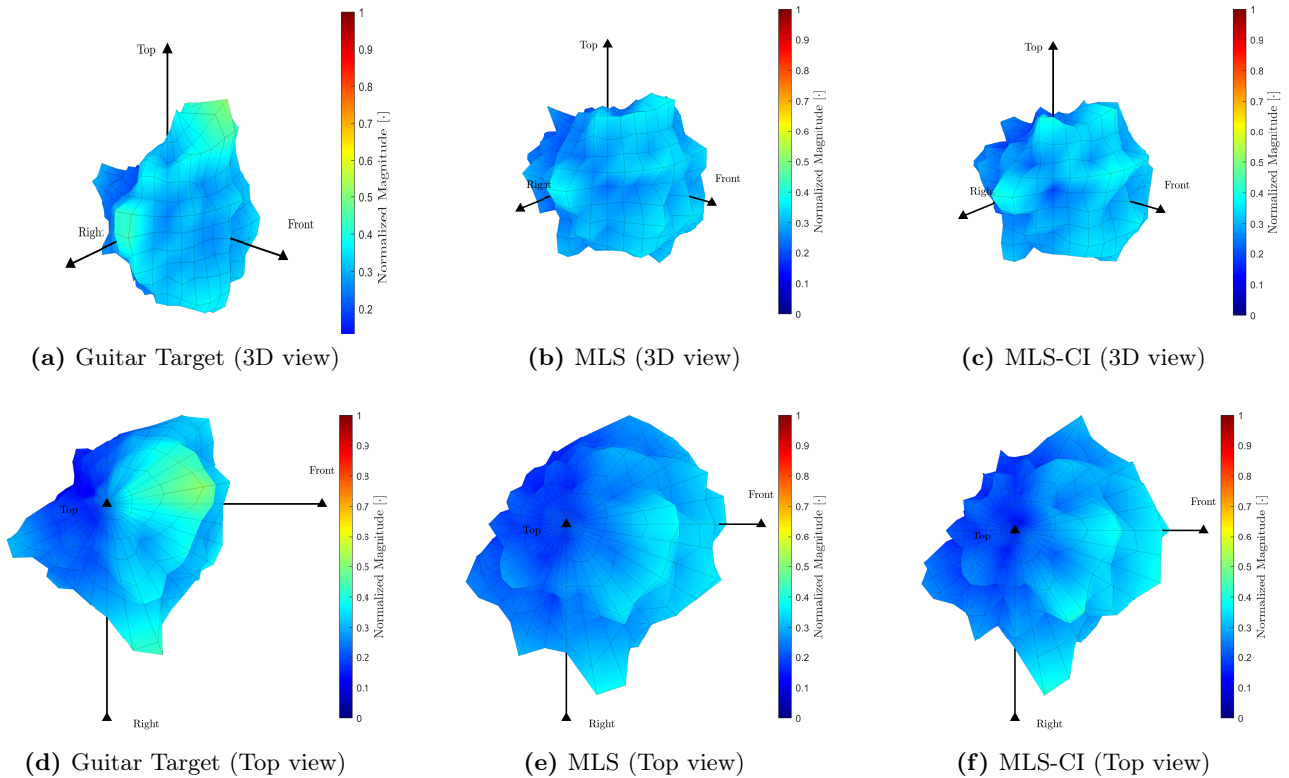


**Figure 8.9:** 3D Balloon-style directivity plots (3D view + Top view) in the 1/3 octave band centered around 3162 Hz for the guitar radiation and the loudspeaker array using either the MLS or MLS-CI filters. The plots are normalized over the maximum magnitude for all 1/3 octave bands in between 79 Hz to 10 kHz.

The accuracy of the two synthesized radiation patterns of the loudspeaker array decreases further with frequency. An example is given by the 1/3 octave band centered around 3162 Hz shown in Figure 8.9, The two synthesized radiation patterns of decent comparability are now noticeable different from the guitar target radiation pattern.

A pronounced beam of high gain concentrated to the direction of around  $\theta = 10^\circ$ ,  $\phi = 60^\circ$  is present in the target radiation pattern of Figure 8.9 but is not nearly as distinct in the two synthesized radiation patterns of the loudspeaker array. This could probably be due to a combination of the now increased directivity of the loudspeaker driver units together with the actual placement of driver units on the array. This combination makes it difficult for the optimization problem in the middle and especially high frequencies to hit the target pattern with good accuracy for all the directions where no loudspeaker units are pointing directly at.

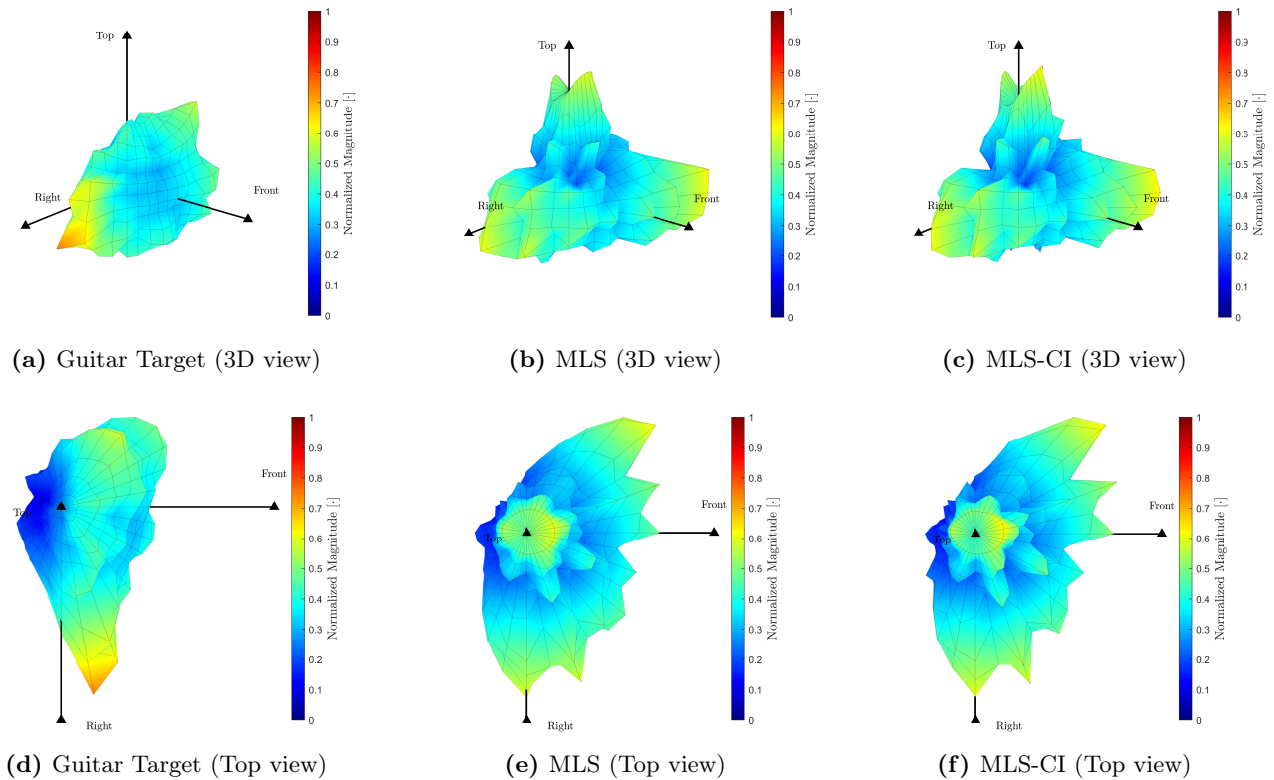


**Figure 8.10:** 3D Balloon-style directivity plots (3D view + Top view) in the 1/3 octave band centered around 6310 Hz for the guitar radiation and the loudspeaker array using either the MLS or MLS-CI filters. The plots are normalized over the maximum magnitude for all 1/3 octave bands in between 79 Hz to 10 kHz.

A further increment in frequency decreases the accuracy of the radiation patterns synthesized by loudspeaker array using either the MLS or MLS-CI filters, resulting in radiation patterns clearly different from the target pattern. This can be seen for the 1/3 octave band centered around 6310 Hz shown in Figure 8.10, where the two synthesized radiation patterns of the loudspeaker array really struggle to hit the target pattern.

Both of the two synthesized radiation patterns of the loudspeaker array include a relatively narrow beam of high gain going towards the z-axis, which does not exist in the target radiation pattern for this 1/3 octave band. Again, this is probably due to the loudspeaker driver units being highly directive in this frequency area, combined with driver unit placements pointing directly upwards. However, the two dominating beam directions of the target radiation pattern are also not synthesized correctly by the loudspeaker array using the MLS or MLS-CI filters compared to the desired radiation pattern of the guitar.

Similar results can be seen for the 1/3 octave band centered around even higher frequencies in Appendix J. However, even though the synthesized radiation patterns at high frequencies do not follow the target radiation pattern very well, the patterns might still be more interesting for guitar playback. This is because the synthesized radiation patterns might be able to excite a room better with high frequencies compared e.g to the sound radiation pattern of a single traditional guitar loudspeaker.

## 8.4 Weighted MSE

In order to get an objective measure to compare the behavior of the two filter design approaches, the *WMSE* between the two synthesized radiation patterns and the target radiation pattern is computed.

Since the overall gain is different for each radiation pattern of the comparison, both the target and synthesized patterns are normalized before the  $WMSE$  is computed.

The  $WMSE$  of the radiation patterns synthesized by loudspeaker array using both the MLS or MLS-CI filters compared to the guitar target radiation pattern can be seen in Figure 8.11, using analysis in 1/3 octave bands and 1/6 octave bands.

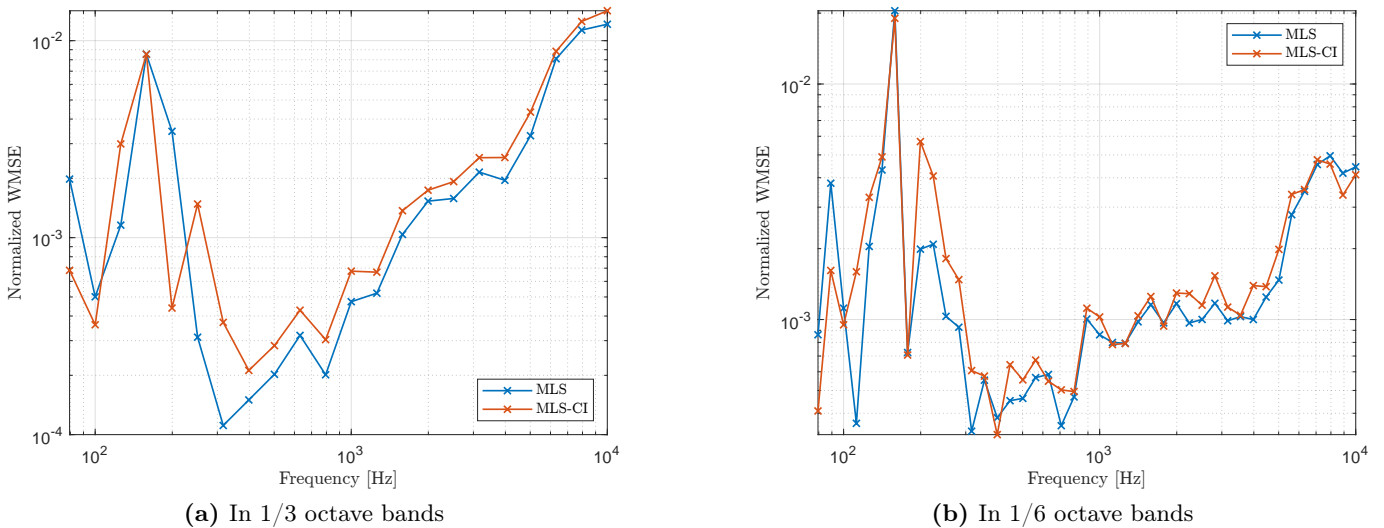


**Figure 8.11:**  $WMSE$  of the radiation patterns normalized over the maximum magnitude for all fractional octave bands in between 79 Hz to 10 kHz.

Compared to what was seen in the simulations, the error in the lower frequencies, between 120 Hz and 200 Hz, seem very high. However, the balloon-style plots in Section 8.3 and the directivity sonograms in Section 8.2, the overall radiation pattern seemed to be recreated quite well with the loudspeaker array using both the MLS or MLS-CI filters when it was compared to the target pattern. Instead, the problem might be due to the overall gain at these frequencies. This is also what can be seen in Figure 8.5(a),(b),(c).

The reason for this problem is simply that the filters are designed to hit the target gain at the center frequency of the fractional octave band, while the fractional octave band calculated radiation patterns consist of not only the energy at the center frequency but everything inside the band. This discrepancy seems to get especially intense in the frequency range where the gain is highest.

Instead, the radiation patterns can be normalized at every fractional octave band to specifically show how well the shape of the target directivity pattern is matched. The  $WMSE$  normalized frequency-wise can be seen in Figure 8.12.

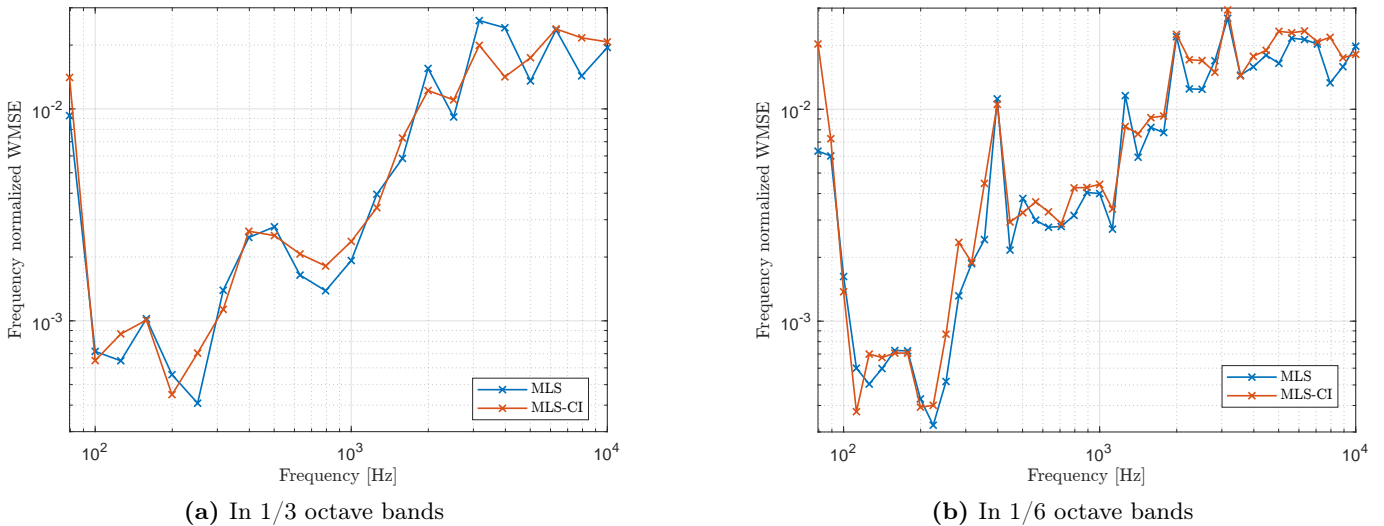


**Figure 8.12:** *WMSE* of the radiation patterns normalized over the maximum magnitude for each individual fractional octave band in between 79 Hz to 10 kHz.

The *WMSE* of the frequency normalized radiation patterns behaves a bit more like expected, namely that the 'shape' of the radiation pattern is generally hit very well at the lower frequencies, while the error gets quite large above 2 kHz.

In the range of 200 Hz to 1.2 kHz, the shape of the synthesized radiation patterns seems to match the target somewhat better in 1/3 octave bands than in 1/6 octave bands. This somewhat supports the perception that the filters are very good at approximating the overall directivity even if they do not get the small details right since the 1/3 octave band targets are more smooth than the 1/6 octave band targets.

At the frequency band centered around 79 Hz, the results seem pretty bad. This could maybe be explained by the fact that the target function in both methods is only well defined down to 79 Hz, which means that the lower half of this band might not follow the target that well.

In the 1/6 octave bands, the MLS filters seem to give a slightly lower *WMSE*, but generally, the error seems to be similar across frequencies.

Of course, the *WMSE* cannot be used to tell everything about the performance since all the spatial information gets reduced to a single number value at each frequency band. However, it does seem to support what was seen earlier through visualizations, i.e. that the shape of the radiation is approximated pretty well up to a certain frequency. The overall gain seems to be the biggest issue in the performance at the low to middle frequencies. But this should in practice be easy to solve by applying a common filter to all 20 speakers, which will change the overall magnitude of the sound pressure at a given frequency without changing the 'shape' of the radiation pattern.

## 8.5 Frequency and Time Response

Some more knowledge of how the speaker is behaving can be seen from the impulse responses and transfer functions calculated using the ESS technique.

The magnitude responses from the system input signal to the sound pressure at the microphones are directly comparable to the target function as it is included in the same manner in the filter design.

The measured magnitude response to one of the microphones is illustrated in Figure 8.13.

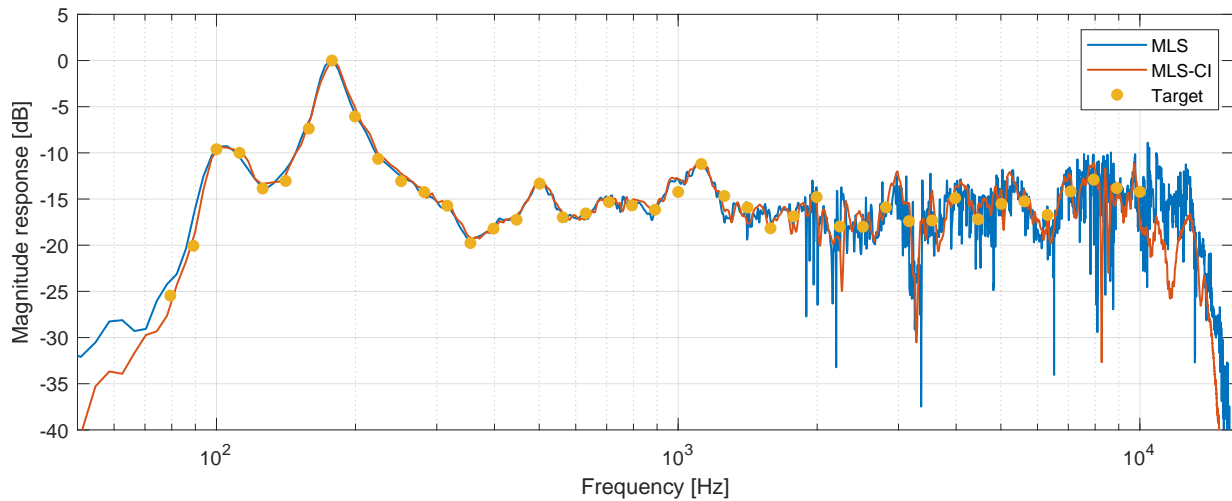


**Figure 8.13:** Magnitude response to the measurement point at  $\theta = -20^\circ, \phi = 10^\circ$ , along with 1/6 octave target points.

In the lower frequencies below 1 kHz, both filter design approaches seem to follow the target points very nicely. As the frequency increases, the magnitude responses seem to go through the points less smoothly than in the lower frequencies, especially for MLS.

Above 2 kHz, the magnitude response for the MLS filters gets a large number of narrow peaks and dips in between the target frequencies. In comparison, the MLS-CI result is way more smooth, even though it isn't perfect either. So it makes sense that the target is not approximated that well when the synthesized radiation pattern is measured in fractional octave bands since the magnitude response of many of the frequencies inside a fractional octave band in the high frequencies differ from the target by a large amount.

By instead looking at the impulse responses, some differences between the two approaches of filter generation start to appear. An example of the impulse responses from the system input to the microphone can be seen in Figure 8.14.

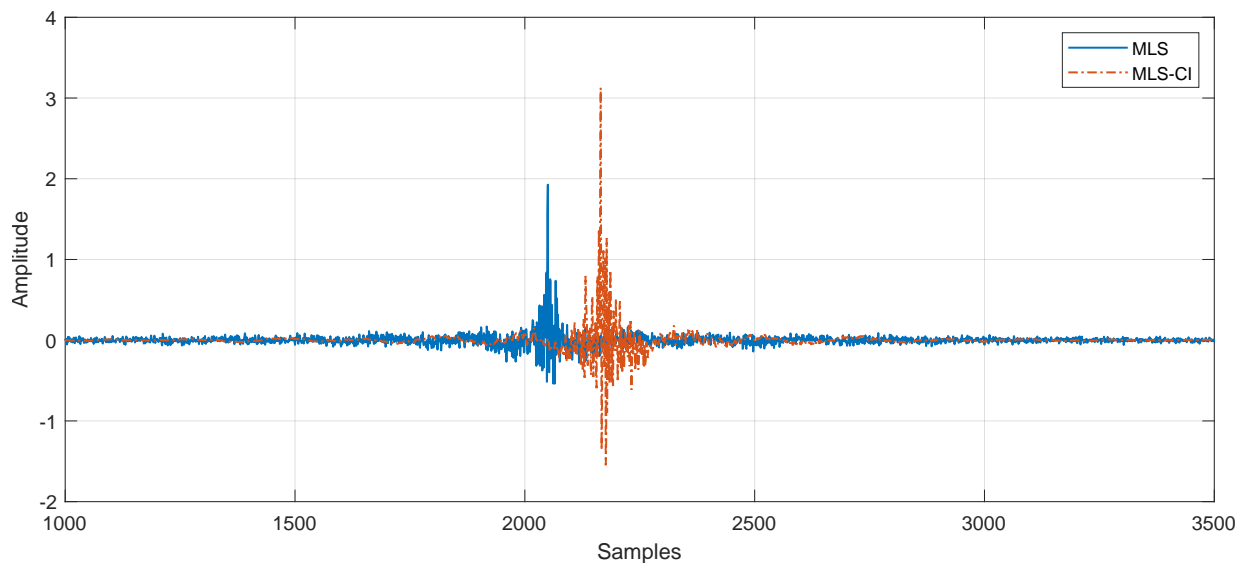


**Figure 8.14:** Impulse response to the measurement point at  $\theta = -20^\circ, \phi = 10^\circ$ .

The FIR filters themselves show similar behavior as can be seen in Figure 8.15.

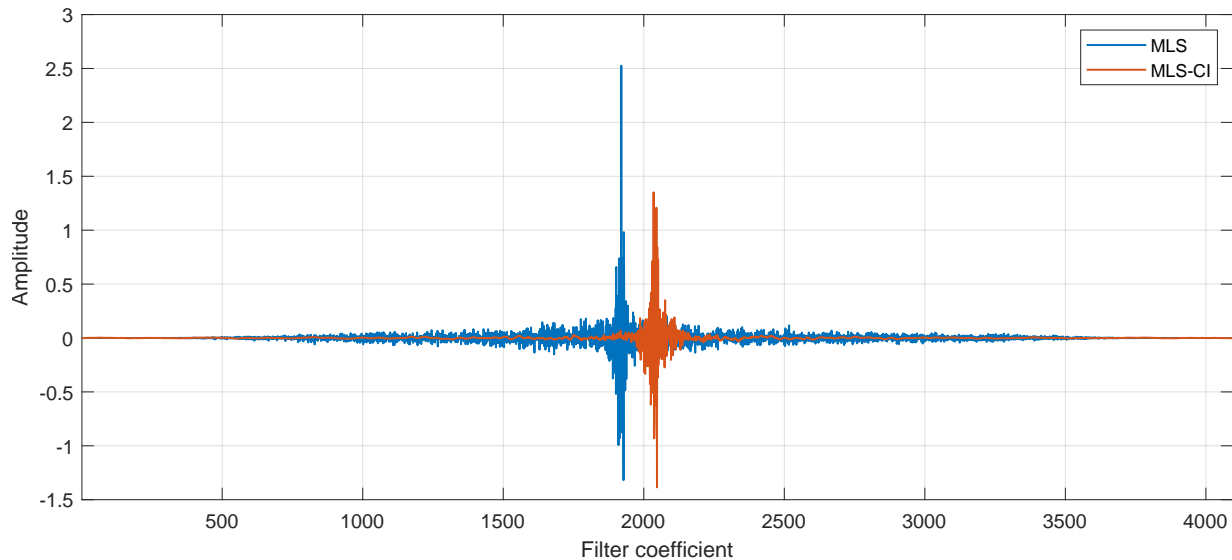


**Figure 8.15:** Filter impulse response for speaker #2.

While it has not been the main focus of the project to design the filters for a specific phase response or time-domain characteristic, there are still a few things worth commenting on when comparing the two methods.

The impulse response from the MLS approach has a much longer pre- and post-ringing, even though a Tukey window has been applied to the filters to reduce the energy outside of the main peak. The MLS-CI has its energy way more concentrated in time, with much less ringing.

The pre-ringing is especially something one should at least be careful about since it might affect some of the transient sounds being played by the guitar. However, no audible artifacts were noticed by the authors doing testing by playing pickup signals through the loudspeaker array.

The reason for this time-domain behavior is most likely due to the fact that the MLS filter algorithm finds an optimal solution at every single frequency bin. In particular, at the high frequencies, this causes the filters to have a high degree of 'noise' on the magnitude response compared to the more smoothed out MLS-CI filters<sup>1</sup>.

## 8.6 Results with a Reduced Number of Loudspeaker Driver Units

An additional set of filters have been made similarly to before, but this time using only 12 of the 20 loudspeakers driver units, i.e. using 12 out of 20 channels. The 12 remaining loudspeakers were chosen with the subtractive algorithm described in Section 7.2, from the same starting layout as before. The resulting 12 loudspeakers can be seen in Figure 8.16<sup>2</sup>.

<sup>1</sup>This effect is perhaps easiest visualized by looking at it in the opposite way. It is a well-known fact in signal processing that zero-padding an impulse response and taking its FFT will result in an increased frequency resolution where the magnitude response goes smoothly through the increased number of frequency bins. Logically, this means that in order to have a magnitude that is non-smooth over a small number of bins, there must be some non-zero amplitude components in the impulse response away from the main peak.

<sup>2</sup>The speaker on the bottom of the physical array is slightly different located from the speaker suggested by the algorithm due to the mistake discussed in Section 7.3, but again this probably does not have a huge impact.

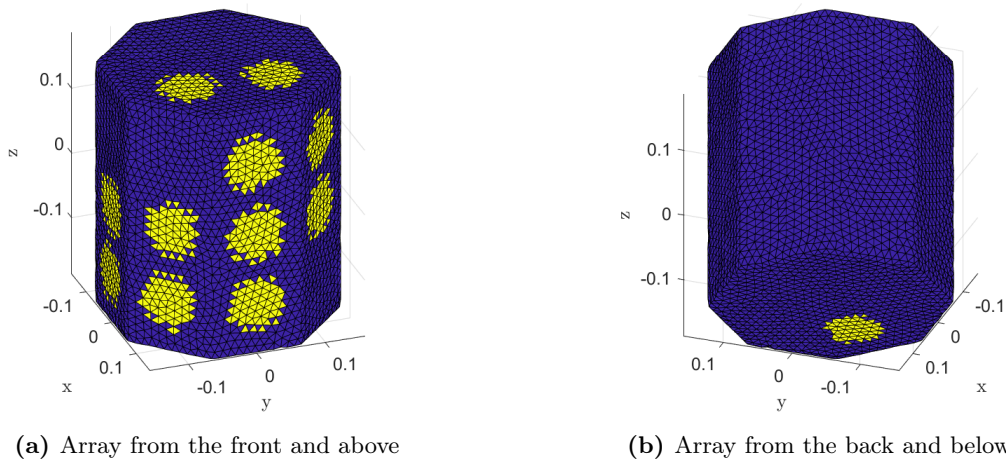


**Figure 8.16:** Loudspeaker array with 12 speakers found using the subtractive placement algorithm.

The subtractive placement algorithm definitely still prefers to have many speakers on the front side of the loudspeaker array as all the loudspeakers at the back of the 20 loudspeakers array have been removed.

12 filters have been designed with the same parameters as in Section 8.1 with both MLS and MLS-CI except that only the transfer functions corresponding to the 12 remaining loudspeakers are used from the  $\mathbf{H}$  matrix. The filters were convolved with the same guitar pickup as used before. The resulting signals were sent out to the 12 loudspeakers.

During the measurements, the other 8 loudspeakers stayed connected to the PA, in order to keep them still but active, so they would not act as passive slaves. The corresponding microphone recordings were again analyzed in fractional octave bands in the same way as before.

As it turned out in the analysis that the loudspeaker array using the MLS and MLS-CI filters for 12 channels again provided almost indistinguishable results, only the results of the loudspeaker array using the MLS-CI filters will be presented here.

### 8.6.1 Loudspeaker Sonograms using 12 Loudspeakers

An overview of the sound radiation patterns of the loudspeaker array using the MLS-CI filters for only 12 channels can again be seen from directivity sonograms in the horizontal, frontal, and median plane using  $1/6$  octave bands. These can be seen in Figure 8.17a, Figure 8.18a and Figure 8.19a, respectively.

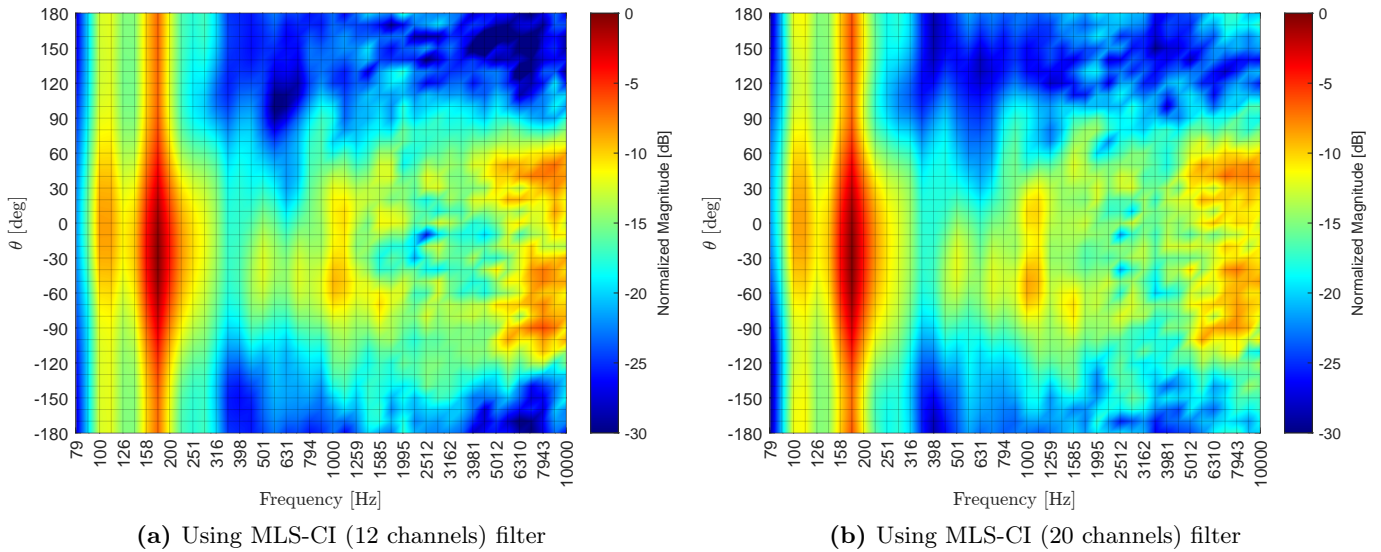


**Figure 8.17:** Directivity sonogram of the loudspeaker array (12 and 20 channels) in the full horizontal plane using interpolated 1/6 octave bands to plot frequency vs. azimuth angle  $\theta$ . Front direction is  $\theta = 0^\circ$ . Using  $N = 4096$  taps long FIR filters convolved with an ascending barre chords signal (pre-recorded with the guitar pickup).

The directivity sonogram in the horizontal plane using 12 loudspeakers seen in Figure 8.17a exhibits a striking resemblance to the equivalent directivity sonograms for 20 loudspeakers shown in Figure 8.17b. The only area where the differences are really noticeable is the area outside of the main beam, i.e. to the backside. But in general, not a lot of degradation of the directivity pattern is seen from going down to 12 loudspeakers from 20 loudspeakers, when looking at the sonogram. Similar results can be seen for the frontal plane in Figure 8.18 and for the median plane in Figure 8.19.

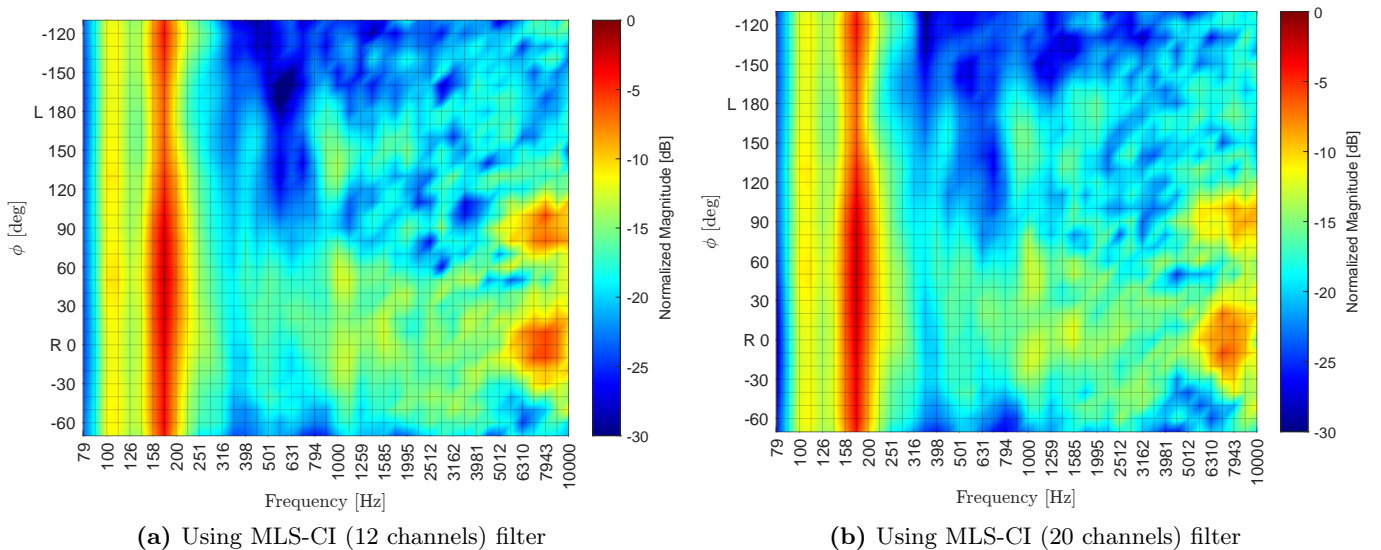


**Figure 8.18:** Directivity sonogram of the loudspeaker array (12 and 20 channels) in the frontal plane using interpolated 1/6 octave bands to plot elevation angle  $\phi$  vs. frequency. To get a reference,  $\phi = 0^\circ$  is the right side, while left is  $\phi = 180^\circ$  and top/head is  $\phi = 90^\circ$ . Using  $N = 4096$  taps long FIR filters convolved with an ascending barre chords signal (pre-recorded with the guitar pickup).

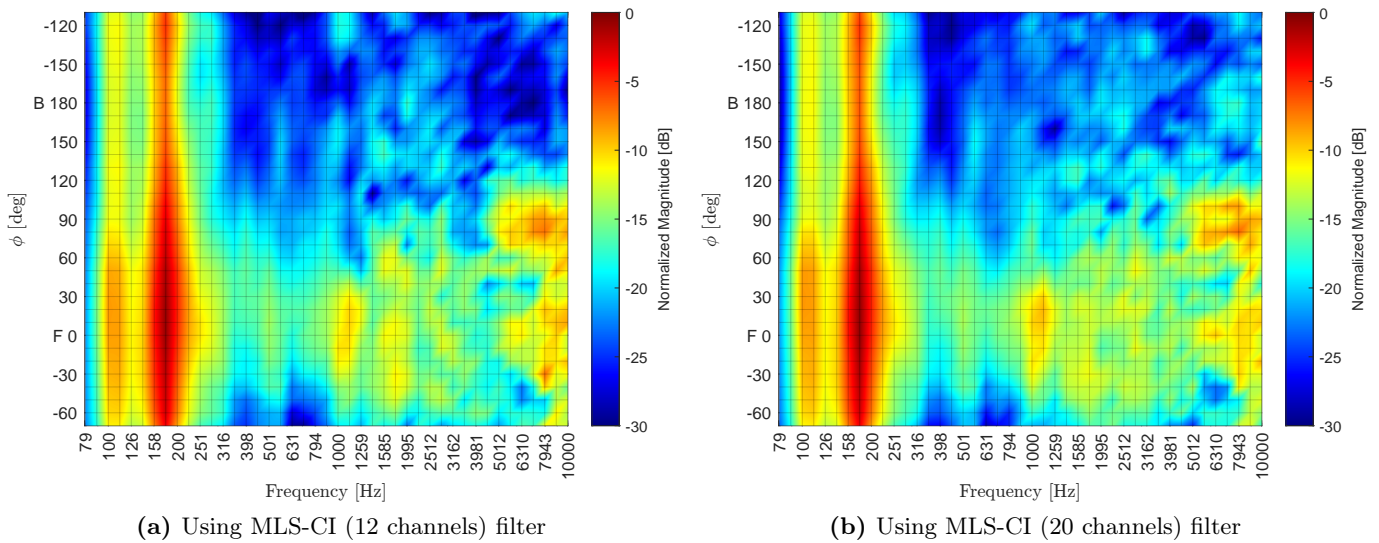


**Figure 8.19:** Directivity sonogram of the loudspeaker array (12 and 20 channels) in the median plane from the 3D measurement using interpolated 1/6 octave bands to plot elevation angle  $\phi$  vs. frequency. Front is  $\phi = 0^\circ$ , back is  $\phi = 180^\circ$  and top/head is  $\phi = 90^\circ$  Using  $N = 4096$  taps long FIR filters convolved with an ascending barre chords signal (pre-recorded with the guitar pickup).

### 8.6.2 Balloon-style Directivity Plots using 12 Loudspeakers

The differences between 12 and 20 loudspeakers can perhaps better be seen when looking at the balloon-style plots. At the lower frequencies, the difference between 12 and 20 loudspeakers are very slight as can be seen in Figure 8.20 for 1/3 octave band centered around 631 Hz.

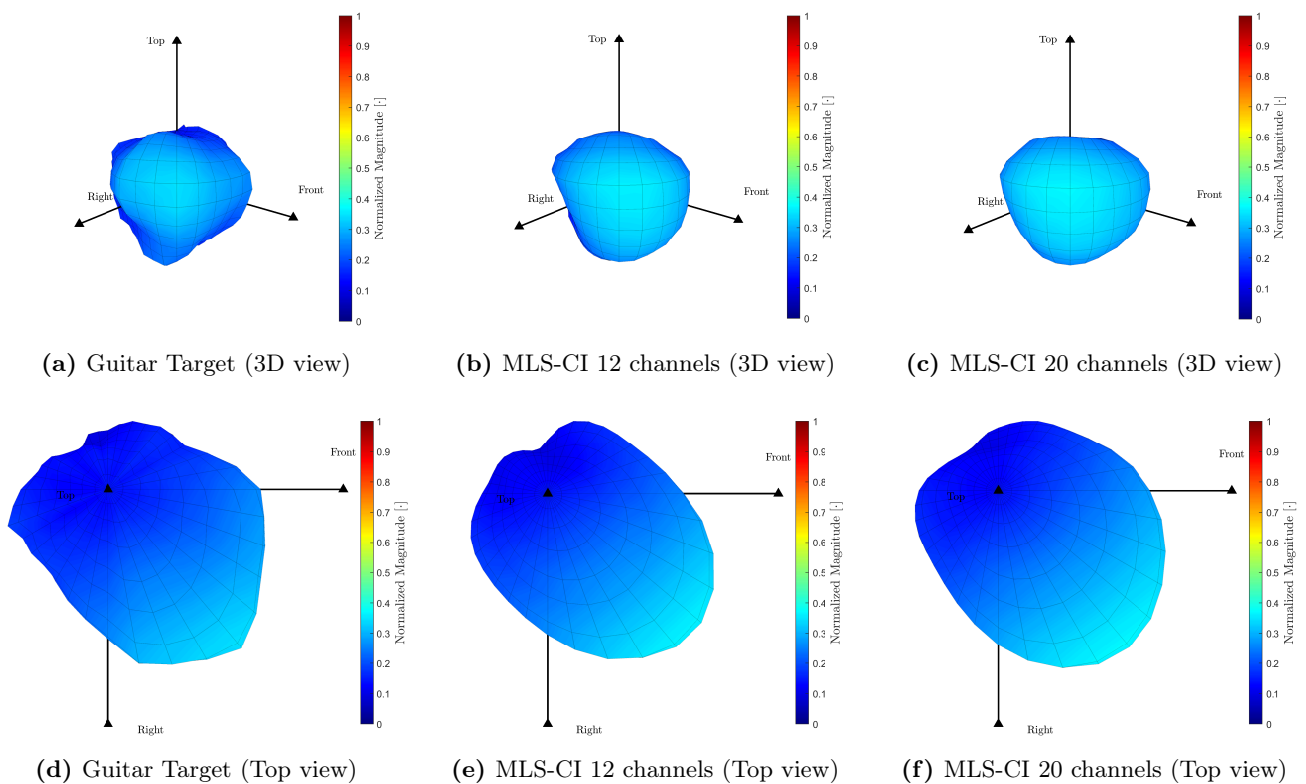


**Figure 8.20:** 3D Balloon-style directivity plots (3D view + Top view) in the 1/3 octave band centered around 631 Hz for the guitar radiation and the loudspeaker array using the MLS-CI filters. The plots are normalized over the maximum magnitude for all 1/3 octave bands in between 79 Hz to 10 kHz.

The target is very well approximated for both 20 and 12 loudspeakers according to the balloon-style plot, so it is hard to conclude that the pattern with 20 loudspeakers should be better from visualizations alone.

However, in middle frequencies, the differences become more apparent. An example for the 1/3 octave band centered around 1000 Hz is shown in Figure 8.21.

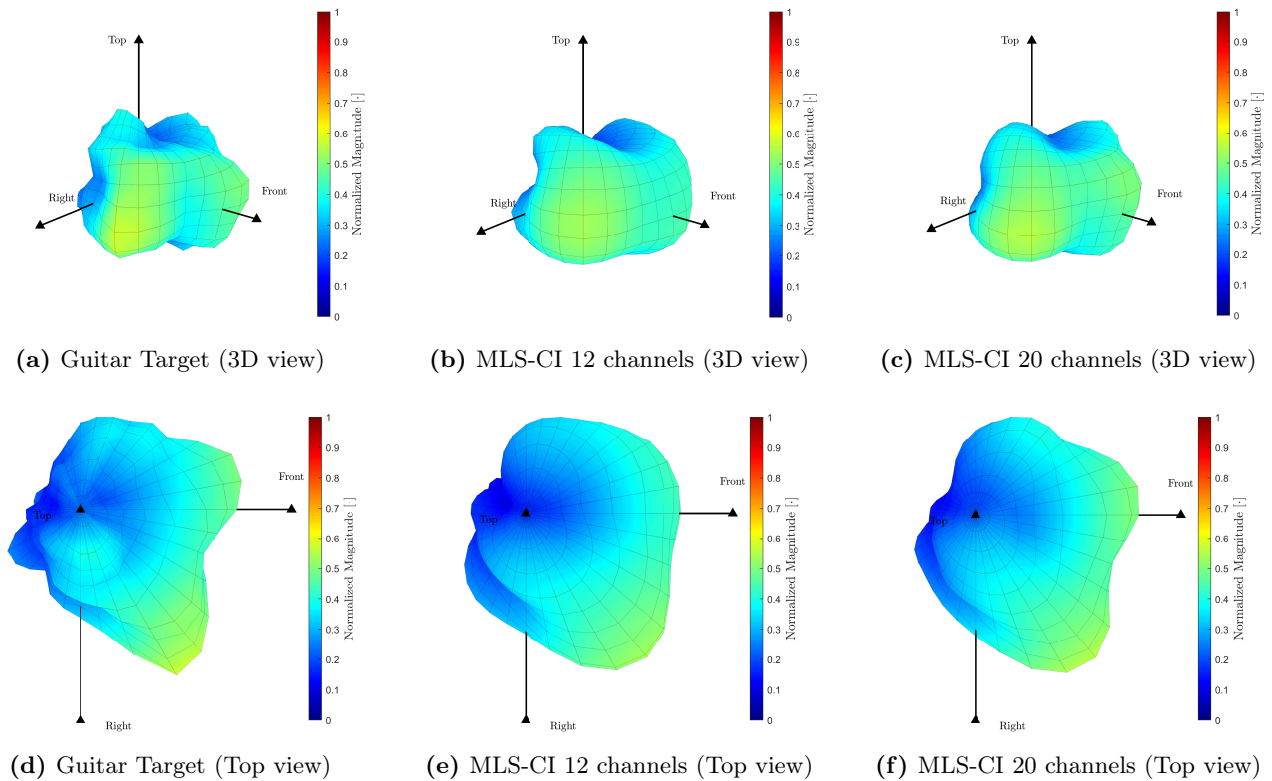


**Figure 8.21:** 3D Balloon-style directivity plots (3D view + Top view) in the 1/3 octave band centered around 1000 Hz for the guitar radiation and the loudspeaker array using the MLS-CI filters. The plots are normalized over the maximum magnitude for all 1/3 octave bands in between 79 Hz to 10 kHz.

The directivity with 12 loudspeakers seems to give a much more smoothed-out result. The guitar target pattern for this 1/3 octave band clearly has two main lobes directed to angles around  $\theta = -60^\circ$  (right side) and  $\theta = 10^\circ$  (left side) when looking from a top view. In the directivity pattern with 12 loudspeakers, it is much harder to distinguish these two lobes since the radiation pattern with 12 loudspeakers seems to act more like a subcardioid to the front side. With 20 loudspeakers, the target is slightly better approximated. The directivity pattern with 20 loudspeakers also seems to better approximate the sound radiation going upwards along the z-axis.

Similar results can be seen for 1/3 octave band centered around 1585 Hz in Figure 8.22.

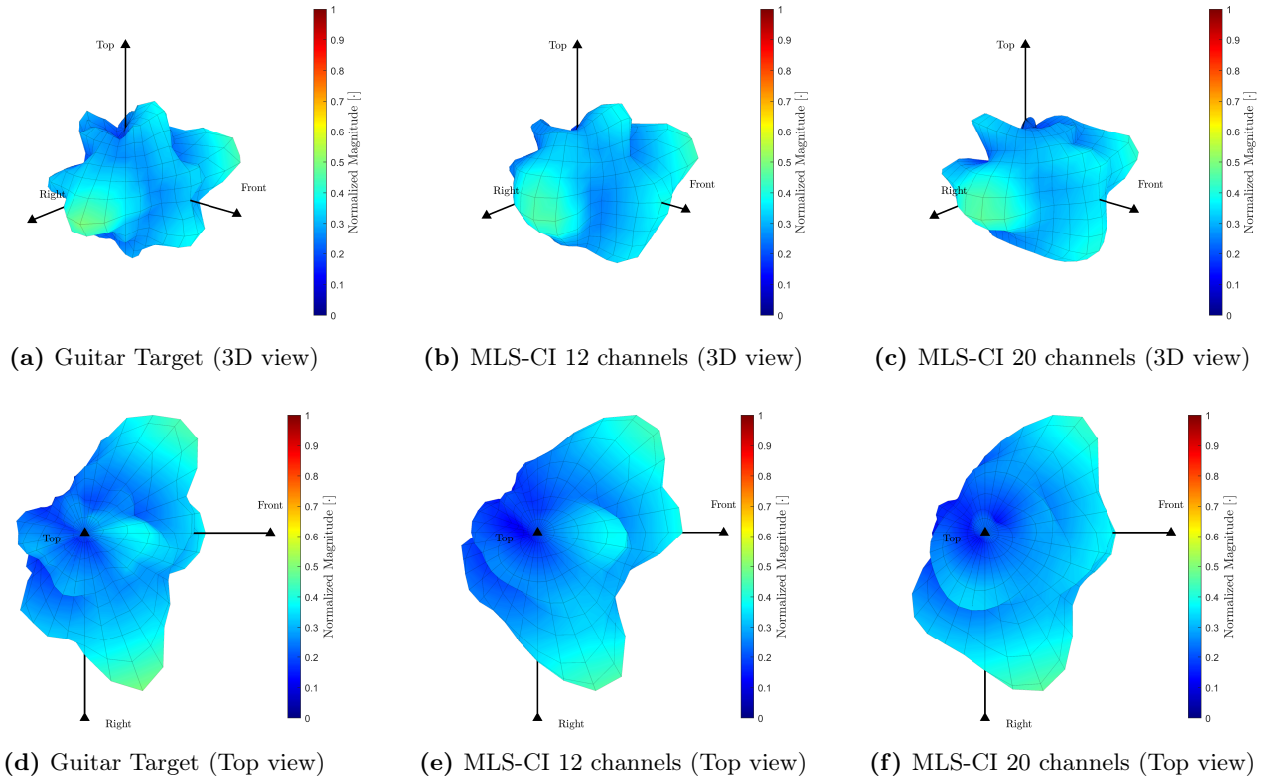


**Figure 8.22:** 3D Balloon-style directivity plots (3D view + Top view) in the 1/3 octave band centered around 1585 Hz for the guitar radiation and the loudspeaker array using the MLS-CI filters. The plots are normalized over the maximum magnitude for all 1/3 octave bands in between 79 Hz to 10 kHz.

Again, the overall pattern seems to be reasonably preserved using 12 loudspeakers, but there are few mistakes. Examples include how much sound is radiated to the backside at  $\theta = 180^\circ$  and to the front side at  $\theta = 0^\circ$ .

For even higher frequencies, the radiation patterns do not change too much using either 12 and 20 loudspeakers, since both arrays consist of mostly the same highly directive driver units with equivalent placements on the front side of the loudspeaker array. This results in very similar sound radiation on the front side of the loudspeaker arrays, where most of the sound energy is radiated. However, some difference can be found in the sound radiation on the backside of the loudspeaker array, due to the loss of degrees of freedom.

One can also look at the *WMSE* to get an objective measure as to how well the target radiation pattern is hit. This is shown in Figure 8.23. The radiation patterns are again normalized over each frequency band in order to focus on how well the 'shape' of the pattern is preserved.

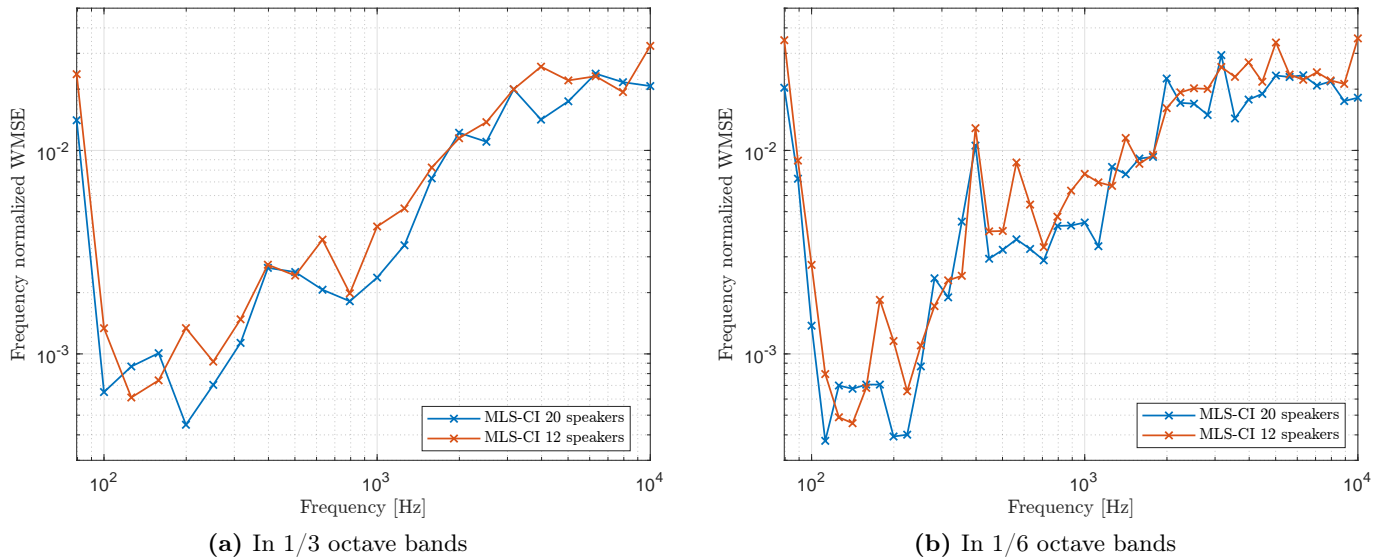


**Figure 8.23:**  $WMSE$  of the radiation patterns (20 vs. 12 loudspeakers) normalized over the maximum magnitude for each individual fractional octave band in between 79 Hz to 10 kHz.

The error with 12 speakers seems to be a little bit higher in most frequency bands, but generally, the error seems to grow with frequency at a similar rate for both 20 and 12 speakers. Curiously, at some frequencies, the layout with 12 speakers actually has a lower  $WMSE$ .

An explanation for this might be due to the fact that the MLS-CI filters are made by interpolating the exact MLS solutions between frequency bands. If the exact solutions at adjacent center frequencies are very different, then this means that the radiation pattern will change a lot between center frequencies. This will probably cause some artifacts in the fractional octave band filtered radiation patterns as they do not exclusively depend on the radiation at the center frequency, but the average radiation pattern in the whole band.

In the case where the array has fewer speakers, the exact solutions at the center frequencies are probably worse due to a reduced number of degrees of freedom. But sometimes it may provide an added benefit of reducing the effect of the previously mentioned artifacts since the radiation patterns will change less between center frequencies. However, this will probably not outweigh the cost of having worse results in the exact solutions from the start, which will probably provide an overall worse result. For example, at 150 Hz in the Figure 8.23a, the error with 12 speakers is lower than the error with 20 speakers, whereas the error at 200 Hz with 12 speakers becomes much larger.

However, all in all, the loudspeaker array with 12 loudspeakers actually seems to find a decent result even with a greatly reduced number of loudspeaker driver units, and might in many cases be sufficient to provide an acceptable radiation pattern.

# Discussion 9

---

Based on the preceding chapters, it is now possible to review the different choices made in the project and discuss their validity.

## 9.1 Uncertainties from the Measurement Setup

The actions taken in the preceding chapters were heavily based on three stages of acoustic measurements, using a similar measurement setup based on a 'sphere' of microphones, realized with a half-circle arch of microphones and a turning table to rotate the source.

First, a target radiation pattern in 3D was measured from a guitarist playing on an acoustic guitar. Later the plant impulse responses of the prototype loudspeaker array were measured in order to calculate the optimal filters, and afterward, the resulting radiation patterns from using these filters were measured as well.

Both the target, plant, and resulting radiation pattern were assumed to be in the far-field of the source, such that the shape of the synthesized directivity patterns will not be dependent on the distance to the sound source. For this to be the case, the arch of microphones would have to be sufficiently far away for every measurement point. The arch had a radius of 1.7 m, but in order to minimize the reflections from the metal arch bar, the microphones were extended out by 17 cm, resulting in the microphones being around 1.53 m away from the center of the source. This is probably far enough away to be considered the far-field for both the guitar and the loudspeaker array, but not by a huge amount. It was not possible to validate this assumption by measuring with a larger arch, due to practical limitations.

Some of the equipment used in the setup may have caused some inaccuracies in the measurements due to reflections. This mainly concerns the ADC's, DAC's and amplifiers, as well as the turning table. While all these elements were covered in acoustic foam to reduce reflections, some of the measurements might still have been impacted by non-anechoic conditions. This is of most concern in the measurements of the driver impulse responses where the reflections probably could have a significant effect when a loudspeaker was pointing away from a microphone or specifically for the loudspeaker pointing down towards the turning table.

Another source of error is the fact that the turning table caused the loudspeaker array to tilt, mostly towards the  $x$ -direction, by a differing amount based on the weight distribution of the loudspeaker turned to some angle. As a consequence of this tilting effect and the coordinate system being defined in relation to the center of the sound source, then the measurement points will not be located perfectly on a sphere anymore, but be shifted by a few cm in space instead. However, as this spatial error is likely somewhat smaller than the distance between each measurement point but much smaller than the total distance between the source and microphones, the effect on the final results was probably insignificant. Especially given that the problem of synthesizing the correct radiation pattern is so over-determined with over 500 target points and 20 or 12 degrees of freedom to the solution, an exact solution will probably never be found in the first place.

## 9.2 Measured Guitar Radiation as Target Function

Early on, it was decided to base all of the design decisions for the loudspeaker array on a specific radiation characteristic, namely the radiation pattern of an acoustic guitar. This includes both the simulations of different loudspeaker array parameters and optimization methods in Chapter 5, the design of the physical loudspeaker in Chapter 7 and the eventual design of the filters used for radiation pattern synthesis.

A useful representation of a frequency-dependent radiation pattern for a directive loudspeaker is to represent the radiation pattern as a spatial response given as the ratio between the relative sound pressure at a point in the far-field and an input signal level.

In this representation, the radiation pattern of the instrument corresponds directly to the directivity of the loudspeaker given as a transfer function from its electric input signal to the sound pressure in some direction.

However, the guitar can hardly be described as an LTI-system with an electric input and an acoustic output signal, and treating it as such would probably not yield very useful results. This can be explained by the fact that the piezoelectric pickup on the guitar converts the vibration of the bridge to an electric signal, while the radiated sounds consist of many contributions from the front plate, bridge, strings, etc. Thus the pickup and microphone signals will probably be correlated a lot but not be completely coherent<sup>1</sup>.

Instead, the radiation pattern of the guitar was approximated by calculating the RMS sound pressure at each direction in fractional octave bands and dividing it by the corresponding fractional octave band filtered RMS-value of the pickup signals. In this way, only a 'gain' from the input to the sound pressure is specified, and this gain is only an average over some frequency bands.

An added bonus to this representation is that the target can be measured by playing the guitar somewhat normally. This might give a more realistic estimate of the radiation compared to if the guitar would have to be excited by some test signal.

This way of describing the radiation of the guitar will of course oversimplify the sound radiation of a guitar by quite a bit. But, it can probably be justified by psychophysical principles such as the perceptibility of absolute phase and the logarithmic frequency selectivity of the human auditory system. Based on similar psychophysical arguments, it is considered sufficient to look at the frequency-dependent radiation patterns in 1/6 octave bands<sup>2</sup>.

From the initial measurements in 2D in Section 4.1, it was seen that the calculated radiation pattern estimates changed somewhat when the guitar was played with different styles or by different guitarists. In a very broad sense, the radiation pattern was similar, but many small details in the radiation pattern seemed to have changed outside of the low frequencies. One could take this to mean that the measurements are not very good at approximating the radiation of the guitar. But another interpretation is that it is simply impossible to prescribe a singular exact 'Radiation Characteristic' to the guitar depending only on frequency. The latter explanations sound plausible since one would expect the radiation to change somewhat due to the body of the guitarist, the way the guitar is being held, which guitar strings and how many are being excited, etc.

Therefore it is probably most sensible to describe the radiation pattern of the guitar in a very averaged way, as it is not known if the small details in the radiation pattern will be the same for a different model of guitar, a different playing style, and so on.

---

<sup>1</sup>It was tried to deconvolve the microphone signals with the pickup signals, and it did not yield a "nice" impulse response. However, the more refined methods presented in [15] were not tried.

<sup>2</sup>A typical guitar will be able to produce complex tones with fundamentals at intervals of 1/12 of an octave, so there does not seem to be any reason to go above a resolution of 1/12 octave bands. However, it also seems a bit overkill to describe a specific radiation pattern at every single note.

A simple alternative measurement that might have provided a more "complete" description of the radiation pattern, could have been to play the guitar at different dynamic levels, which might have changed the timbre of the sound. However, this also means that the measurement would have been more time consuming and more effort would be needed to make sure the guitar was being excited the same way every time.

Because of the particular microphone setup used to measure the sound radiation of the guitar in 3D, a measurement had to be performed for every azimuth angle in order to complete the sphere of measurement points. This resulted in some large variations between each azimuth angle, but this was somewhat mitigated by averaging over the azimuth angles with a window of 10 degrees. The variations between the measurements are simply assumed to be due to the slight differences in playing style or small movements by the guitarist in between different measurements. Of course, this averaging will have a profound effect on features in the true radiation pattern, if the feature is more narrow than this smoothing window. However, these narrow features would also not have been well represented if the radiation pattern had simply been measured with a fixed  $10^\circ$  resolution.

Even after applying this smoothing, the measured radiation patterns still seem to vary by a suspicious amount in the low frequencies, e.g. for 100 Hz or 158 Hz in Figure C.7, compared to what one would expect for a sound source radiating sound at these wavelengths, so the exact radiation patterns should probably be taken with a grain of salt. Therefore, it is probably also not critical that the loudspeaker prototype does not match the target 100% as there is a very significant degree of uncertainty in the measured target radiation patterns.

However, the overall radiation patterns used as a target function are still very distinct between  $1/3$  or  $1/6$  octave bands, even though they have effectively both been averaged over frequencies and azimuth angles.

All in all, the measurements are probably a decent enough approximation of a radiation pattern of an acoustic guitar to be used as a target function, as the fine details lost in the measurement process probably would not have been possible to recreate anyway with a practical loudspeaker array<sup>3</sup>.

### 9.3 The use of BEM - Simulations

Numerical simulations were used heavily in order to determine how a loudspeaker array should be made for synthesizing the specific target radiation pattern.

A scheme for simulating the radiation of a given loudspeaker array, given by the  $L \times M$  matrix  $\mathbf{H}$  were developed using the Boundary Element Method. This method allows for a great deal of versatility for simulating many different shapes, compared to an analytical method like the spherical cap model[22]. This proved to be very useful in determining the loudspeaker layout of the prototype loudspeaker using the subtractive methods in Section 7.2.

However, the computational complexity and memory requirements for the direct BEM resulted in a lot of compromises being made. First of all, the simulations were in most cases only done up to a frequency of 3.16 kHz due to the requirements of the edges in the 3D meshes being small compared to the lowest wavelength in the simulations. Halving the length of the elements in the mesh will approximately result in the number of elements  $N$  being quadrupled and the number of vertices  $Q$  being doubled as seen in Figure 9.1.

---

<sup>3</sup>The non-linear response of a guitar and the change in radiation due to small movements cannot be recreated with a single filter for each channel anyway.

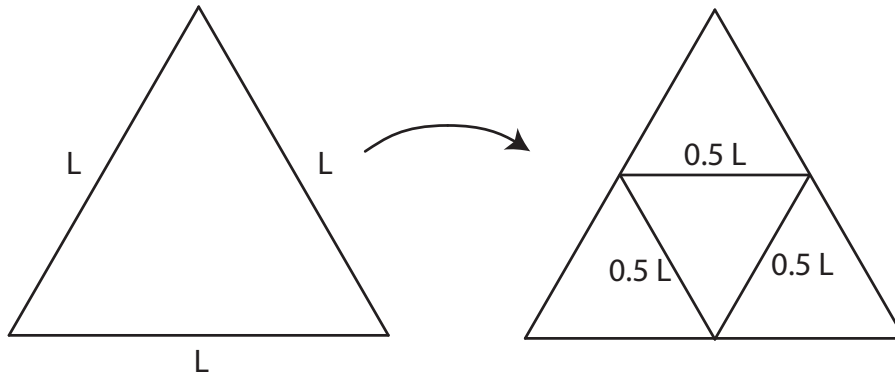


**Figure 9.1:** Triangle being divided into 4 similar triangles with half-length of the original triangle.

Likewise, doubling the number of vertices  $Q$  in the mesh quadruples the number of entries in the BEM matrices in openBEM  $\mathbf{A}$  and  $\mathbf{B}$  as they are both  $Q \times Q$ . This means that increasing the frequency limit for accurate BEM simulations gets very expensive, especially in terms of memory when the BEM-matrices are pre-computed and stored<sup>4</sup>.

For example, the mesh used for the octagonal prism consists of 4000 vertices, which means its BEM matrices consists of  $4000^2 = 16 \cdot 10^6$  entries of complex doubles, which means storing the  $\mathbf{A}$  and  $\mathbf{B}$  matrices for one frequency takes  $\approx \frac{1}{2}$  GB of data. On the desktop computer used for computing the BEM-matrices, the computations of the  $\mathbf{A}$  and  $\mathbf{B}$  matrices took around 11 min per frequency.

It might have been possible to increase the resolution of the meshes to cover more a larger frequency range, but this would come at the expense of much longer computation times<sup>5</sup> and larger storage requirements.

In modern times, the computations of BEM-simulations has been greatly optimized through the inclusion of the 'Fast Multipole method' (FMM) in the calculations[65]<sup>6</sup>. While the mathematics of the FMM-BEM is too complicated to get into at this point, it should be noted that the full coefficient matrices  $\mathbf{A}$  and  $\mathbf{B}$  do not need to be explicitly computed with this method to find the solution on the boundary. In this project, it is quite nice to have these matrices when computing the simulated  $\mathbf{H}$  matrix as the matrices can be reused for all  $L$  loudspeakers, but also sometimes the same coefficient matrices need to be reused a huge amount of times, i.e. in the simulations with randomized loudspeaker placements in Appendix E and the direct subtractive placement simulation in Appendix H. In these cases, the pre-computation of the BEM-matrices probably saved computation time in the long run.

However, the results from more or less all the simulations showed that the target radiation pattern was not approximated very well at high frequencies with the types of loudspeaker arrays simulated. This was also seen in the measurements of the prototype loudspeaker.

One area where the frequency limitation of the simulations affected the prototype was in the choice of loudspeaker positions. The final 20 loudspeaker positions were chosen based on simulations at 1/3 octave bands from 79 Hz to 3.16 kHz. This means that the algorithm completely disregarded the target pattern above 3.16 kHz in choosing the loudspeaker positions. However, this choice is also somewhat justified, since most of the sound power radiated from the guitar is below 3 kHz anyway, and in fact, the largest amount

<sup>4</sup>This would be even worse if the collocation points were given for every element instead of every vertex as is done in openBEM.

<sup>5</sup>The computation of the BEM matrices is  $O(N^2)$  where  $N$  is the number of elements in the mesh, the program will have to go through every  $N$  element and calculate the contribution from each  $N$  element to it,

<sup>6</sup>In this method the mesh is divided into several 'clusters', and the contribution from elements that are far away are approximated by the multipole expansion of the contribution of all the elements in their corresponding cluster.

of energy seems to be concentrated from 100-500 Hz according to Figure 4.2. Therefore it is probably not beneficial in the long run trying to improve the performance above 3 kHz if it comes at the expense of the performance below 1kHz.

## 9.4 On the Prototype Loudspeaker Array

Probably the most significant difference between this study and the previous work outlined in Section 2.5.2, is the use of a non-uniform loudspeaker placement on the array. Since the loudspeakers could be placed more freely, then the shape of the loudspeaker array did not necessarily need to be a sphere or platonic solid.

The prototype loudspeaker array was designed in a way, which made it easy to construct and made it possible to place a large number of loudspeakers at specific areas of the surface.

For this reason, the loudspeaker array was made in the shape of an octagonal prism, dimensioned such that three 4" drivers could be placed on a single side.

Using the loudspeaker placement algorithms from Section 7.2, a layout of 20 loudspeakers was chosen and subsequently built.

In the chosen layout, the locations of the loudspeakers were very biased towards the front and right sides of the loudspeaker array, which is also where the guitar radiates the most sound. This was even more apparent when reducing the number of loudspeakers to 12.

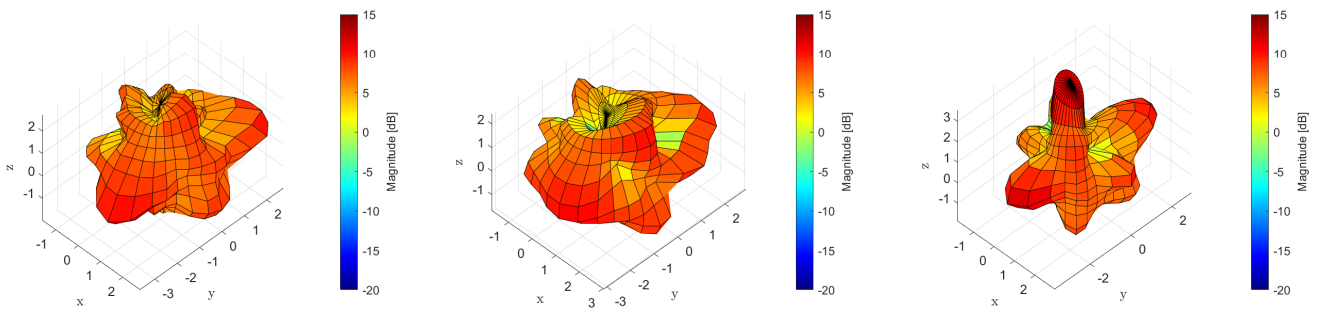
With both 20 and 12 loudspeakers, the overall directivity was decently approximated up to some frequency. At the frequencies where the guitar is radiating the most sound power, both layouts find really good results. In that sense, both seem to be suitable loudspeaker arrays for synthesizing the directivity pattern of a guitar, but of course, the prototype has not been compared to loudspeaker arrays of different shapes. Thus, it would not be surprising if there exists some loudspeaker array shape, that can perform similar or better with the same or a lower amount of driver units.

However, it can be seen through simulations that the prototype loudspeaker performs better than a similar array with a uniform distribution of loudspeakers, especially if only 12 loudspeakers are used, as seen in Figure 9.2. Similar results were found for 1 kHz and 1.2 kHz, so there is strong evidence to suggest that the placement of the loudspeakers does play an important role in synthesizing a specific radiation pattern.



(a) Octagonal prism array with 12 non-uniformly placed loudspeakers

(b) Sphere with radius 15 cm with 12 uniformly placed loudspeakers



(c) Target radiation pattern

(d) Synthesized pattern with octagonal prisms loudspeaker array

(e) Synthesized pattern with spherical loudspeaker array

**Figure 9.2:** Simulation of synthesized radiation patterns with two different array shapes with 12 loudspeakers at 1.58 kHz.

One problem that does seem to occur with the octagonal prism, is that the number of flat surfaces is only 10 (8 sides, a top, and a bottom). This starts to affect the radiation at frequencies when each driver starts getting very directive as  $ka$  increases. The effect can be seen in the balloon plots for 6.3 kHz in Figure 8.10, where the most sound is radiated straight up at  $\phi = 90^\circ$  and to  $\theta = -90^\circ$  and  $45^\circ$ , which are all normal directions to the flat panels of the enclosure.

If it is desired to use similar mid-range drivers as the Vifa loudspeakers in the prototype, it might be an advantage at higher frequencies to make better use of the natural directivity of the loudspeakers by putting them all at slightly different angles. But as this effect only seems to show up at very high frequencies, where the guitar is not radiating much sound, this might not be that critical.

### 9.5 On the Different Filter Design Algorithms

From the results of Chapter 8 the loudspeaker array using either the MLS or MLS-CI filters showed very similar performance regarding the accuracy in the synthesized radiation patterns, which makes sense since they solve the optimization problem with a very similar approach and were of course implemented on the same loudspeaker system. Having said that, the MLS-CI filters provided a more smooth magnitude response in the middle and high frequencies at each observation point and in the filter magnitude response itself.

This might provide the MLS-CI filters an advantage over MLS filters as the impulse response in the time domain, seen in Figure 8.14 for one observation point and Figure 8.15 for one driver unit filter, contains way

less pre- vs post-ringing compared to the corresponding results using MLS filters. In theory, it should create less audible artifacts for the audience or listener, but this claim needs further evaluation or confirmation in real life during listening tests, as the amount of pre- vs. post-ringing in the time domain, as well as ripples in the magnitude response using the MLS filter, might already be on an inaudible level. In addition, it can be added, that the authors themselves could not hear any obvious artifacts when playing pickup signals through the loudspeaker array using any of the two filter approaches with which the difference might seem insignificant.

Additionally, the MLS-CI provided a huge improvement in computation time, since it did not solve the optimization problem at every FFT-bin but only at the 1/24 octave band center frequencies, of which there are 169 in between 79 Hz and 10 kHz, which is much lower than the 4096 frequency bins at which the basic MLS algorithm have to be solved. The post-processing of the logarithmic solution is almost free in terms of computation time compared to running the iterative MLS solver.

On paper, when calculating the weighted MSE, the loudspeaker array using the MLS filters turned out to provide a slightly lower overall error compared to the corresponding implementation using the MLS-CI filters. Nonetheless, the difference between the two filter approaches is negligible compared to the changes in the target radiation pattern (see Section 4.1) when using different playing styles or for different musicians playing the same guitar.

Therefore it might not be necessary to try to match the radiation pattern of a guitar as exactly as was done in this project since only the overall target radiation pattern seems to be preserved regardless of playing style or musician, even for the same guitar. For that reason, it might also be sufficient to use much shorter FIR filters and still get a decent result. With shorter filters, the computation time of the MLS-filters will be improved somewhat, but MLS-CI filters might still be preferable simply for their response in the time domain.

A solution using LS filters was discarded at an early stage due to simulations showing poor performance in terms of magnitude accuracy compared to the MLS filters. However, a loudspeaker array using LS filters might have been a reasonable solution if a specific phase is desired at the measurement point, such as e.g. a minimum or linear phase, which are something the MLS filters cannot guarantee. This would, of course, come with a trade-off of a worse synthesis of the magnitude response, but this might be a reasonable consideration for a real system, also depending on how good of an approximation to the magnitude response is really needed. Nevertheless, because any phase information of the guitar target was discarded during the radiation pattern analysis of the guitar, then the seemingly zero-phase of the target was not regarded as being an important objective in the synthesized radiation patterns.

That being said, the iterative MLS solver was observed to often find a solution, where the resulting radiation pattern had a phase pretty similar to the initial target phase (i.e. zero-phase in our case) at low frequencies, since the iterative algorithm only finds a local minimum near the initial guess, e.g. the LS-solution. Assuming this is always the case, a specific phase at the microphone positions might be somewhat approximated even with the MLS approach by simply specifying an initial phase to the target. This has however not been further investigated in this work.

## 9.6 Perceptual Considerations

A subject to debate is also how accurate a synthesized radiation pattern necessarily needs to be in order to get the impression of a real guitar playing. Perhaps even a less accurate approximation of guitar radiation pattern is good enough to provide a satisfying spatial sound impression of the instrument to feel it lively and present in the environments in which the loudspeaker array is operating. Even a very rough approximation

of the directivity of an acoustic guitar is probably much more similar to the real deal than a conventional loudspeaker.

A less accurate approximation of guitar radiation pattern would be easier to achieve and reduce the overall cost as the amount of necessary loudspeaker driver units (and thereby also amplifier and DAC channels) could be reduced. But, also the amount of necessary computer power could be reduced, as both fewer and perhaps shorter optimal filters are needed to be implemented on e.g. a DSP in a final product.

In this project, an approximation to the radiation pattern of a guitar was achieved with both 20 and 12 loudspeakers, with a varying but still a quite good degree of accuracy.

However, no clear answer to the perceptual aspects regarding the radiation pattern accuracy for compact sound sources exists to the best of the authors' knowledge, for which quite extensively subjective listening experiments are needed in order to reveal how accurate the synthesized radiation pattern actually needs to be.

A little different aspect worth considering is also the interaction with a room or an acoustic environment. Even though the results of Chapter 8 showed quite an accurate synthesized radiation pattern compared to the guitar target radiation pattern in the low and middle frequencies, notable differences or errors were present for the higher frequencies. These results were obtained in (almost) anechoic conditions, but the errors of the synthesized radiation pattern in the high frequencies might influence the impression of the instrument illusion when the loudspeaker array is located in a different acoustic environment.

In a reflective acoustic environment such as a room or a church, the loudspeaker array might not excite the room exactly as a real guitar will do, because of these differences in the radiation patterns, especially at higher frequencies. However, the big question is if it really matters for the loudspeaker array to excite the room identically to the guitar for all frequencies in order to create a perceptual impression of a guitar playing in the room. A room will naturally introduce some narrowband sound coloration originating from all the reflections present, and one might accept the differences in the radiation patterns as being a part of the room effects, and thus not the instrument illusion if no clear reference of a guitar playing in the same room at the same position is known.

# Conclusion 10

---

In this thesis, methods for synthesizing the directivity pattern of an acoustic guitar with a compact loudspeaker array have been investigated. Through acoustic measurements of the sound radiation pattern from a guitarist to a surrounding sphere of observation points, it was shown that the directivity of the acoustic guitar is very frequency-dependent and directional in the middle and high frequencies.

This frequency-dependent radiation pattern was described as a discrete set of gain factors between the effective level of the electric pickup signal on a guitar and the effective sound pressure in fractional octave bands at each observation point in the sphere.

A mathematical acoustic model of a compact loudspeaker array was set up, which made it possible to investigate how different parameters of the loudspeaker array affect the synthesis of the specific radiation pattern through simulations. Based on these simulations it was shown that the radiation pattern at a specific frequency could be well approximated by applying optimal complex weights to each driver found as the solution to a magnitude least-squares problem. It was also shown that the positioning of the drivers on a given shape had a significant impact on the performance.

Using these principles, a prototype loudspeaker array with 20 speakers was designed based on an algorithm to choose the best loudspeaker driver positions out of several candidates.

A modified fast deconvolution algorithm was used to obtain FIR-filters for the prototype that were optimal in a magnitude least-squares sense. The computation times of these filters were greatly reduced by using complex interpolation since an exact solution was not needed at every FFT-bin.

Measurements of the sound radiation of the prototype loudspeaker array showed that the radiation pattern of the guitar was well approximated up to around 2 kHz. At higher frequencies, a rough approximation to the target was still seen, but most of the details in the target radiation pattern were lost or misplaced.

Results using both all 20 but also only 12 of the loudspeaker drivers on the array were obtained and evaluated primarily through visual comparison to the measured radiation pattern of the guitar, which showed slightly superior results with 20 speakers.

The question of how accurate the recreation of the radiation pattern of the guitar needs to be in order to create a spatial sound impression of a real guitar playing in front of an audience in an acoustic environment remains to be explored.

However, the findings of this work clearly show that the measured sound radiation characteristics of the guitar can be recreated to a satisfying degree at the most prominent frequencies of the guitar using a specifically designed loudspeaker array.

As the main results of the research have been analysed and discussed, now it is time to talk about some side or alternative works that could have been added to the project if time and possibilities allowed for that. Thus in this section, ideas for future work are presented as a possible continuation of the project or as possible expansions to this study.

These ideas vary from possible modification of the actual loudspeaker array prototype, as in Section 11.1, or some interesting alternative filter implementations aimed for a real-time implementation, Section 11.2. In addition to that, some concepts for a more flexible loudspeaker array able to synthesize the radiation pattern of other instruments are expressed in Section 11.3, together with some ideas in Section 11.4 for a possibly listening test in order to achieve a subjective evaluation.

## 11.1 Multi-way System

One approach which might improve the synthesized radiation pattern in the middle and high frequencies could be with the use of a multi-way loudspeaker array system. One simple approach could be a two-way loudspeaker system where a few midrange or low-frequency drivers are responsible for synthesizing the desired radiation pattern in the low and middle frequencies, which seem to be the easiest patterns to match. In addition, a greater amount of tweeters are responsible for synthesizing the desired radiation pattern in the middle and high frequencies by taking advantage of the smaller physical dimension of tweeters compared to midrange and woofer drivers.

This should allow for a more accurate radiation pattern in the middle and high frequencies since more individual and less directive driver units (tweeters) can be located on the loudspeaker array and thereby provide additional degrees of freedom in the filter design while extending the frequency range where beamforming is possible due to the directivity of the drivers.

An alternative approach also exploiting a two-way system could be a loudspeaker array of smaller physical dimension but with a similar amount of individual channels, where several of the current midrange driver units are replaced with tweeters pointing at the dominating beam directions of the guitar. This should also increase the accuracy of the synthesized radiation pattern at the higher frequencies because the loudspeaker array geometry dimension is reduced, just as it was shown in Appendix G. A related advantage of a smaller array is probably also that the spatial aliasing frequency gets increased. This could result in the reproduced sound field being less impacted by distortion due to spatial aliasing.

## 11.2 Real Time Filter Implementation Issues

The FIR filters found at the moment with the MLS and MLS-CI algorithms have a length of  $N = 4096$  taps and include a modelling delay of  $N/2$  samples at  $f_s = 32\text{kHz}$ . This will result in a delay of 64 ms only due to the modelling delay in the filters to ensure causality, but this relatively large delay will be a huge problem for real-time applications.

An example of a musician performing in front of a small audience with an acoustic guitar connected to the loudspeaker array for application will result in audible artefacts such as an echo effect (especially for the musician) caused by the time delay between the sound coming from the guitar naturally and the sound coming from the loudspeaker array minimum 64 ms later.

In order to make the current loudspeaker array using either MLS or MLS-CI filter more usable for real-time applications, then the delay in the filters have to be removed drastically. An easy fix would be to reduce the filter length to maybe  $N = 1024$  taps resulting in a modelling delay of about 16 ms, which are on a more acceptable level but not perfect. Unfortunately, a shorter FIR filter length will decrease the low-frequency performance of the loudspeaker array as the synthesized radiation pattern at low frequencies will deviate more from the guitar target radiation pattern due to a worse frequency resolution of the filters.

Another strategy to reduce the delay in the filters could be to implement the modelling delay as a shorter circular time shift of e.g.  $N/4$ ,  $N/8$ ,  $N/16$  samples or just enough samples to ensure that the filters are casual and stable in time. However, this might also be a trade-off between the amount of the modelling delay allowed and the performance of the filters, as a shorter circular time shift will sacrifice the symmetry in the filter impulse response and require a proper window function to be applied. Therefore, the optimal amount of modelling delay might be difficult to decide.

If using the more traditional LS filter design method then a specific phase component could have been included in the target radiation pattern such as e.g. a minimum phase or a mixed phase. This might not require as long a modelling to make the filters casual if e.g. the target is a mixed-phase system with a propagation delay similarly to the actual propagation delay between the loudspeaker array centre and the different observation points.

An entirely different solution could be an IIR filter implementation, which requires a different approach to the optimization problem and in the general filter design. Nevertheless, it might provide a more computationally efficient real-time implementation that approximates a minimum phase implementation more efficiently.

### 11.3 Synthesis of Other Instruments

An interesting addition to the research could be the possibility of using the loudspeaker array assembled in this project to synthesize other similar radiation patterns. In this section, this possibility is analysed together with the strategies needed to accomplish that.

The radiation patterns of many similar instruments such as a classical guitar, a resonator guitar or an acoustical bass etc. could possibly be reproduced in addition the guitar on the same loudspeaker array. In order to exploit the same distribution of the loudspeaker driver units located on the loudspeaker array, the different instruments should ideally possess a similar radiation pattern.

Hence, first, some measurements of the different musical instruments should be performed with the same criteria used for the measurements of the acoustic guitar. An analysis and comparison of the results obtained can then be used to define which of the instruments provide a close match with the radiation pattern of the acoustic guitar and thus be properly reproduced on the loudspeaker array.

However, it could also be the case that some of the measured instruments have a similar radiation pattern to the acoustic guitar except for some mismatch e.g. to the left part or to the back part in the radiation pattern, where the guitar seems to radiate less and whereas a consequence the number of loudspeaker driver units on the loudspeaker array, therefore, is lower. In those circumstances, some little adjustments of the loudspeaker array, perhaps by adding a few more loudspeaker units where needed, could lead to a good solution compromise.

Afterwards, filter banks can be designed, and the prototype can be modified to be able to switch in between different filters depending on the instrument, whose radiation pattern is desired to be recreated.

## 11.4 Listening Tests

Another interesting aspect could be to evaluate the performance of the loudspeaker array in synthesizing the target radiation pattern in a more subjective context, e.g through listening experiments. In order to do that, some subjective listening tests need to be performed on the loudspeaker array.

An objective for this type of test is to find a way to compare the sound radiation of an acoustic guitar in a room with the performance of the loudspeaker array trying to reproduce the exact same radiation pattern in the same testing room (e.g. standard listening room). In addition to that, it could also be interesting to have a comparison in between the loudspeaker array and a standard guitar amp/loudspeaker system, perhaps a stereo system, fed with the same pickup signal from the guitar.

However, the aforementioned test presents some unavoidable physical issues in its realization as the three systems, i.e. the guitarist playing the guitar, the loudspeaker array and the standard guitar amp, cannot play and cannot occupy the same spot in the room at the same time or at least it would result unfeasible to quickly switch in between one and the other if they have to occupy the exact same position in the room.

Thus, some other solutions like binaural recordings using a dummy head or mannequin could fit the purpose. Ideally, the mannequin could be moved by a trolley around the room while recording the source from different angles and heights for the whole duration of a test pickup signal (perhaps 30 to 60 seconds). The process could be repeated for the same mannequin "journey" in the same way for all the three sources needed to be tested.

Afterward, some test subjects could listen to the binaural recording through a pair of headphones. At this point, some terms of evaluation such as AB or ABC tests can be adopted. For example, the recording of a real musician playing the guitar could be presented to the subjects first. The subjects could afterward be asked, which of the other two recordings (A or B), that was able to resemble the guitar playback the most. Subsequently, the subjects could also be asked about the audibility of artifacts such as ringing, distortion, or sound coloration, possibly defining them in a scale from 1 to 10, where 1 could perhaps mean no audible artifacts at all, whereas 10 means very audible and disturbing artifacts in the reproduction.

Another approach could simply be to present the listeners with the three signals in a random order, and ask which of the signals resembles the spaciousness and the naturalness of an acoustic guitar playing live the most.

These hypothetical tests could be repeated for a certain number of test subjects which could be chosen to be a mix of experienced listeners and average listeners. Obviously, the number of people in the cluster to be tested will impact the reliability of the subjective results as a higher number of tests naturally leads to more trustworthy results. In any case, a minimum of 20-30 candidates should be included to form a basis for statically significant results.

# Bibliography

---

- [1] O. Warusfel, P. Derogis, and R. Causse, “Radiation synthesis with digitally controlled loudspeakers,” in *Audio Engineering Society Convention 103*, Audio Engineering Society, 1997.
- [2] O. Warusfel and N. Misdariis, “Directivity synthesis with a 3d array of loudspeakers: application for stage performance,” in *Proceedings of the COST G-6 Conference on Digital Audio Effects (DAFX-01)*, Limerick, Ireland, pp. 1–5, 2001.
- [3] P. Kassakian and D. Wessel, “Design of low-order filters for radiation synthesis,” in *Audio Engineering Society Convention 115*, Audio Engineering Society, 2003.
- [4] A. M. Pasqual, *Sound directivity control in a 3-D space by a compact spherical loudspeaker array*. PhD thesis, Universidade Estadual de Campinas, 2010.
- [5] T. Ziemer, *Implementation of the radiation characteristics of musical instruments in wave field synthesis applications*. PhD thesis, Institute of Systematic Musicology, University of Hamburg, 2014.
- [6] A. Farina and L. Chiesi, “A novel 32-speakers spherical source,” in *Audio Engineering Society Convention 140*, Audio Engineering Society, 2016.
- [7] L. E. Kinsler, A. R. Frey, A. B. Coppens, and J. V. Sanders, *Fundamentals of acoustics*. John Wiley & sons, 1999.
- [8] R. M. French, *Engineering the guitar: theory and practice*. Springer Science & Business Media, 2008.
- [9] International Organization for Standardization (ISO), *Acoustics – Standard tuning frequency (Standard musical pitch)*. ISO 16:1975, Geneva, Switzerland, 1975.
- [10] T. D. Rossing *et al.*, *The science of string instruments*. Springer, 2010.
- [11] A. Chaigne and J. Kergomard, *Acoustics of musical instruments*. Springer, 2016.
- [12] M. Elejabarrieta, A. Ezcurra, and C. Santamaria, “Evolution of the vibrational behavior of a guitar soundboard along successive construction phases by means of the modal analysis technique,” *The Journal of the Acoustical Society of America*, vol. 108, no. 1, pp. 369–378, 2000.
- [13] I. Perry, *Sound radiation measurements on guitars and other stringed musical instruments*. PhD thesis, Cardiff University, 2014.
- [14] J. Pätynen and T. Lokki, “Directivities of symphony orchestra instruments,” *Acta Acustica united with Acustica*, vol. 96, no. 1, pp. 138–167, 2010.
- [15] A. Pérez Carrillo, J. Bonada, J. Pätynen, and V. Välimäki, “Method for measuring violin sound radiation based on bowed glissandi and its application to sound synthesis,” *The Journal of the Acoustical Society of America*, vol. 130, no. 2, pp. 1020–1029, 2011.
- [16] D. L. Brosnac, *Guitar Electronics: A Workbook*. DB Music Company, 1980.
- [17] G. Ballou, *Handbook for Sound Engineers*. Taylor & Francis, 4 ed., 2008.

- [18] M. Colloms, *High Performance Loudspeakers: Optimising High Fidelity Loudspeaker Systems*. John Wiley & Sons, 7 ed., 2018.
- [19] J. Borwick, *Loudspeaker and Headphone Handbook*. Focal Press, 3 ed., 2001.
- [20] E. G. Williams, *Fourier acoustics: sound radiation and nearfield acoustical holography*. Academic press, 1999.
- [21] F. Zotter and M. Frank, *Ambisonics: A practical 3D audio theory for recording, studio production, sound reinforcement, and virtual reality*. Springer Nature, 2019.
- [22] F. Zotter, A. Sontacchi, and R. Holdrich, “Modeling a spherical loudspeaker system as multipole source,” *Fortschritte der Akustik*, vol. 33, no. 1, p. 221, 2007.
- [23] M. T. Neal and M. C. Vigeant, “A compact spherical loudspeaker array for efficiently recreating instrument directivities,” *Journal of the Audio Engineering Society*, vol. 68, no. 11, pp. 796–809, 2020.
- [24] M. Otani, H. Watabe, T. Tsuchiya, and Y. Iwaya, “Effects of spatial aliasing in sound field reproduction: Reproducibility of binaural signals,” *Acoustical Science and Technology*, vol. 38, no. 3, pp. 147–153, 2017.
- [25] A. Roginska and P. Geluso, *Immersive sound: The art and science of binaural and multi-channel audio*. Taylor & Francis, 2017.
- [26] F. Zotter and M. Noisternig, “Near-and farfield beamforming using spherical loudspeaker arrays,” in *3rd Congress of the Alps Adria Acoustics Association*, 2007.
- [27] R. Rabenstein and S. Spors, “Spatial aliasing artifacts produced by linear and circular loudspeaker arrays used for wave field synthesis,” in *Audio Engineering Society Convention 120*, Audio Engineering Society, 2006.
- [28] J. Meyer, “Directivity of the bowed stringed instruments and its effect on orchestral sound in concert halls,” *The Journal of the Acoustical Society of America*, vol. 51, no. 6B, pp. 1994–2009, 1972.
- [29] M. Pollow, G. Behler, and B. Masiero, “Measuring directivities of natural sound sources with a spherical microphone array,” in *Proceedings of the 1st Ambisonics Symposium Graz*, vol. 7, pp. 36–37, 2009.
- [30] R. Bader, “Radiation characteristics of multiple and single sound hole vihuelas and a classical guitar,” *The Journal of the Acoustical Society of America*, vol. 131, no. 1, pp. 819–828, 2012.
- [31] T. Ziemer and R. Bader, “Implementing the radiation characteristics of musical instruments in a psychoacoustic sound field synthesis system,” in *Audio Engineering Society Convention 139*, Audio Engineering Society, 2015.
- [32] N. R. Shabtai, G. Behler, and M. Vorländer, “Generation of a reference radiation pattern of string instruments using automatic excitation and acoustic centering,” *The Journal of the Acoustical Society of America*, vol. 138, no. 5, pp. EL480–EL486, 2015.
- [33] N. R. Shabtai, G. Behler, M. Vorländer, and S. Weinzierl, “Generation and analysis of an acoustic radiation pattern database for forty-one musical instruments,” *The Journal of the Acoustical Society of America*, vol. 141, no. 2, pp. 1246–1256, 2017.
- [34] R. Caussé, J.-F. Bresciani, and O. Warusfel, “Radiation of musical instruments and control of reproduction with loudspeakers,” in *ISMA: International Symposium of Music Acoustics*, pp. 67–70, 1992.

- [35] P. Derogis, R. Causse, and O. Warusfel, “On the reproduction of directivity patterns using multi-loudspeaker sources,” in *Proceedings of the International Symposium on Musical Acoustics*, pp. 387–392, 1995.
- [36] R. Avizienis, A. Freed, P. Kassakian, and D. Wessel, “A compact 120 independent element spherical loudspeaker array with programable radiation patterns,” in *Audio Engineering Society Convention 120*, Audio Engineering Society, 2006.
- [37] F. Zotter and A. Sontacchi, “Iem report 39/27: Icosahedral loudspeaker array,” tech. rep., Graz, Tech. Rep, 2007.
- [38] F. Zotter, H. Pomberger, and A. Schmeder, “Efficient directivity pattern control for spherical loudspeaker arrays,” *Journal of the Acoustical Society of America*, vol. 123, no. 5, p. 3643, 2008.
- [39] F. Schultz, M. Zaunschirm, and F. Zotter, “Directivity and electro-acoustic measurements of the iko,” in *Audio Engineering Society Convention 144*, Audio Engineering Society, 2018.
- [40] F. Zotter, *Analysis and synthesis of sound-radiation with spherical arrays*. PhD thesis, University of Music and Performing Arts, Austria, 2009.
- [41] A. Pasqual, “Spherical harmonic analysis of the sound radiation from omnidirectional loudspeaker arrays,” *Journal of Sound and Vibration*, vol. 333, no. 20, pp. 4930–4941, 2014.
- [42] “Icosahedral 120-element loudspeaker array being assembled.” <https://cnmat.berkeley.edu/content/icosahedral-120-element-loudspeaker-array-being-assembled>. Accessed: 2021-03-01.
- [43] L. F. Cóser, “Simulation of a spherical loudspeaker array using a flexible membrane model,” Master’s thesis, Universidade Estadual de Campinas, 2010.
- [44] A. D. Pierce, *Acoustics: an introduction to its physical principles and applications*. Springer, 2019.
- [45] S. Kirkup, “The boundary element method in acoustics: A survey,” *Applied Sciences*, vol. 9, no. 8, p. 1642, 2019.
- [46] P. M. Juhl, *The boundary element method for sound field calculations*. Doctoral thesis, Department of Acoustic Technology, Technical University of Denmark, August 1993.
- [47] S. Marburg and B. Nolte, *Computational acoustics of noise propagation in fluids: finite and boundary element methods*, vol. 578. Springer, 2008.
- [48] S. M. Kirkup, *The boundary element method in acoustics*. Integrated sound software, 2007.
- [49] H. A. Schenck, “Improved integral formulation for acoustic radiation problems,” *The journal of the acoustical society of America*, vol. 44, no. 1, pp. 41–58, 1968.
- [50] G. Diwan, J. Trevelyan, and G. Coates, “Comparison of chief and burton-miller approaches in collocation partition of unity bem for helmholtz problems.,” in *9th UK Conference on Boundary Integral Methods*, 2013.
- [51] A. Burton and G. Miller, “The application of integral equation methods to the numerical solution of some exterior boundary-value problems,” *Proceedings of the Royal Society of London. A. Mathematical and Physical Sciences*, vol. 323, no. 1553, pp. 201–210, 1971.
- [52] W. Meyer, W. Bell, B. Zinn, and M. Stallybrass, “Boundary integral solutions of three dimensional acoustic radiation problems,” *Journal of sound and vibration*, vol. 59, no. 2, pp. 245–262, 1978.

- [53] V. C. Henriquez and P. M. Juhl, “Openbem—an open source boundary element method software in acoustics,” *Internoise 2010*, vol. 7, pp. 13–16, 2010.
- [54] V. C. Henriquez, *Numerical Transducer Modeling*. PhD thesis, Technical University of Denmark, 2002.
- [55] S. Boyd and L. Vandenberghe, *Convex optimization*. Cambridge university press, 2004.
- [56] P. W. Kassakian, *Convex approximation and optimization with applications in magnitude filter design and radiation pattern synthesis*. PhD thesis, University of California, Berkeley Berkeley, CA, 2006.
- [57] S. Valette and J.-M. Chassery, “Approximated centroidal voronoi diagrams for uniform polygonal mesh coarsening,” in *Computer Graphics Forum*, vol. 23, pp. 381–389, Wiley Online Library, 2004.
- [58] O. Kirkeby, P. A. Nelson, H. Hamada, and F. Orduna-Bustamante, “Fast deconvolution of multichannel systems using regularization,” *IEEE Transactions on Speech and Audio Processing*, vol. 6, no. 2, pp. 189–194, 1998.
- [59] M. Kolundzija, C. Faller, and M. Vetterli, “Designing practical filters for sound field reconstruction,” in *Audio Engineering Society Convention 127*, Audio Engineering Society, 2009.
- [60] D. C. Lay, S. R. Lay, and J. McDonald, *Linear algebra and its applications*. Harlow: Pearson Education Limited, 5. edition, global ed., 2016.
- [61] O. Kirkeby and P. A. Nelson, “Digital filter design for inversion problems in sound reproduction,” *Journal of the Audio Engineering Society*, vol. 47, no. 7/8, pp. 583–595, 1999.
- [62] O. Kirkeby, P. Rubak, P. A. Nelson, and A. Farina, “Design of cross-talk cancellation networks by using fast deconvolution,” in *Audio Engineering Society Convention 106*, Audio Engineering Society, 1999.
- [63] B. C. Moore, *An introduction to the psychology of hearing*. Brill, 2012.
- [64] A. Oppenheim and R. Schaffer, *Discrete-time Signal Processing*. Prentice-Hall signal processing series, Pearson, 3rd. ed., 2010.
- [65] Z.-S. Chen, H. Waubke, and W. Kreuzer, “A formulation of the fast multipole boundary element method (fmbem) for acoustic radiation and scattering from three-dimensional structures,” *Journal of Computational Acoustics*, vol. 16, no. 02, pp. 303–320, 2008.
- [66] S. Jønsson, “Accurate determination of loudspeaker parameters using audio analyzer type 2012 and laser velocity transducer type 3544,” *Brüel and Kjær Application Note BO*, pp. 0384–12, 1996.
- [67] R. Bortoni, S. Noceti Filho, and R. Seara, “Comparative analysis of moving-coil loudspeakers driven by voltage and current sources,” in *Audio Engineering Society Convention 115*, Audio Engineering Society, 2003.
- [68] C. J. Struck, K. Thorborg, and A. D. Unruh, “An improved electrical equivalent circuit model for dynamic moving coil transducers,” in *Audio Engineering Society Convention 122*, Audio Engineering Society, 2007.
- [69] R. Bortoni and H. Sette Silva, “Loudspeakers’ electric models for study of the efforts in audio power amplifiers,” in *Audio Engineering Society Convention 115*, Audio Engineering Society, 2003.
- [70] A. Farina, “Advancements in impulse response measurements by sine sweeps,” in *Audio Engineering Society Convention 122*, Audio Engineering Society, 2007.

- [71] S. Müller and P. Massarani, “Transfer-function measurements with sweeps, director’s cut including previously unreleased material and some corrections’ previously published in journal of the audio engineering society vol. 49,” *J. Audio Eng. Soc*, pp. 443–471, 2001.

# Glossary

---

- 3D Mesh** A collection of vertices, edges, and faces, that combined together establish a three-dimensional structure.
- AAU** Aalborg University
- ADC** Analog-to-Digital Converter. A circuit that converts an analog signal to a digital signal.
- ASIO** Audio Stream Input/Output. A low latency multi-channel digital audio transfer protocol for computer sound cards, which can access external hardware directly.
- Balloon-style directivity plots** A visualization of a radiation pattern for sound source in 3D for a single frequency using a 3D mesh. This provides a 'balloon' surface where the distance of every point on surface to the origin corresponds to the directivity gain. The color of the balloon can be used to visualize either the magnitude or phase value of each direction.
- BEM** Boundary Element Method. A numerical method for solving integral equations such as the Kirchhoff-Helmholtz integral equation.
- BIE** Boundary Integral Equation. A type of equation where a usually unknown functions is expressed inside a integral over some boundary. An example is the Kirchhoff-Helmholtz integral equation.
- CHIEF** Combined Helmholtz Integral Equation Formulation. A method that adds some extra points in the interior space of some vibrating body in order to provide a over-determined system that can be solved in a least squares sense with the BEM
- DAC** Digital-to-Analog Converter. A circuit that converts a digital signal to an analog signal.
- Directivity sonogram** Visualization of the directivity of a sound source, like a guitar or a loudspeaker, as a function of angle and frequency. The color of the plot can be used to visualize the magnitude at each angle and frequency.
- DSP** Digital Signal Processor. A microprocessor specially developed and optimized for signal processing.
- EMF** ElectroMotive Force. A electric potential produced by e.g. a loudspeaker acting as a generator when it coverts mechanical energy into electrical energy according to Faraday's induction law. EMF is the voltage, which counteracts the applied current originally responsible for inducing the voltage.
- ESS** Exponential Sine Sweep. An excitation signal used for measuring impulse responses. It uses a sine wave that increases in frequency with an exponential rate over time.
- FFT** Fast Fourier Transformation. A faster and more efficient method of the Discrete Fourier Transform.
- FIR** Finite-duration impulse response. A FIR filter is a digital filter of a finite impulse response type.
- IEEE** Institute of Electrical and Electronics Engineers. A professional association for electronic engineering and electrical engineering.
- IFFT** Inversed Fast Fourier Transform. Computes the Inverse Discrete Fourier Transform using the Fast Fourier Transform algorithm the other way around.
- IIR** Infinite-duration impulse response. A IIR filter is a digital filter of a infinite impulse response type.
- Linear phase** A linear phase system is a system with a phase as a linear function of frequency. This results in a equal time shift/delay of all frequency components defined by the negative slope of the linear function, also known as the group delay. The coefficients of linear phase filter will be symmetrical around this constant group delay.

- LS** Least Squares. A minimization problem often used for finding an optimal solution to an over-determined system of linear equations by minimizing the residuals between a set of fixed values and the values predicted by a model.
- LS filters** A set of filters designed by solving LS problem on a linear frequency grid.
- MADI** Multichannel Audio Digital Interface. A professional multi-channel digital audio transfer protocol and interface for serial digital transmission over coaxial cable or fibre-optic lines.
- MATLAB** MATrix LABoratory. A mathematics computer program/programming language used for signal processing, vector and matrix calculations as well as visualization of results and measurements.
- Minimum phase** A minimum phase system is a system where both the system and its inverse system are causal and stable, meaning that all zeros and poles of the system are located within the unit circle in the z-domain. The minimum phase part of a causal and stable system contains all the possible magnitude information as well as the minimum phase information of the system. A minimum phase system is known to provide the response with the lowest group delay, which can be seen in the coefficients of minimum phase filter being maximally concentrated toward time 0.
- Mixed phase** A mixed phase system is a system with zeros located both inside and outside the unit circle in the z-domain (for the system to be stable its poles must of course also be inside the unit circle). The inverse system of a mixed phase will be unstable by nature since the zeros outside the unit circle of a stable mixed phase system will turn into poles by inversion. The zeros outside the unit circle of a mixed phase system also add some excess phase to the system with which the group delay and phase response will become non-minimum.
- MLS** Magnitude Least Squares. A non-linear least squares problems concerned with minimizing the differences between the magnitudes of complex valued data and the the magnitudes complex valued solution.
- MLS-CI filters** Magnitude Least Squares - Complex Interpolation filters. A set of filters designed by an alternative and fast approach, which solves MLS problem on a logarithmic frequency grid followed by complex interpolation of the solution to a linear frequency grid comparable to the MLS filters.
- MLS filters** Magnitude Least Squares filters. A set of filters designed by solving MLS problem on a linear frequency grid.
- MSE** Mean Squared Error. A measure of error defined as the average of the squared errors. In this project the error is often defined as the difference between the guitar target response and synthesized response at each observation point in space.
- OpenBEM** An open source MATLAB implementation of the boundary element method for acoustics.
- Pickup** A transducer responsible for capturing mechanical vibrations produced by the guitar/instrument and converting those into an electric signal.
- Platonic Solid** A set of regular convex 3D shapes given by a set of regular polyhedral faces (triangles, pentagons, etc). Examples include the Cube, Icosahedron and Dodecahedron.
- Radiation Pattern** A representation of how the radiated sound energy is distributed in terms of directions.
- RMS** Root Mean Square. The effective value of a signal.
- SH** Spherical Harmonics. A set of elemental complex functions on a sphere, which can be used to approximate any radiation pattern in 3D.
- SNR** Signal to Noise Ratio. The ratio between the power of a desired signal and the power of an undesired noise signal, often given in dB.
- Spatial aliasing** Distortion of a sound field due limited spatial resolution when spatially discretizing a continuous sound field.

**SPL** Sound Pressure Level. The sound pressure expressed in dB relative to a standard reference sound pressure, often  $20 \mu\text{Pa}$ .

**USB** Universal Serial Bus. An external serial bus interface standard for communication between devices and a host controller such as a computer.

**WMSE** Weighted Mean Squared Error. The mean squared error using a weighting function to put less or more weight on some errors. In this project a spatial density weighting is often applied to each observation point in space in order to favour densely sampled points less.

**Zero phase** A special case of a linear phase system where the phase slope is zero, creating phase shift of zero for all frequencies. The coefficients of zero phase filter will be symmetrical around time 0 making it acausal by nature, unless it works as simple gain factor (a Kronecker delta function times a constant gain).

# Loudspeaker Model



In this appendix, a model of the electro-dynamic loudspeaker is presented as an equivalent circuit. It can be used for the analysis of the loudspeaker dynamics and behavior, as the model makes it possible to establish transfer functions to describe parameters and signals in both the electrical, mechanical and acoustic reference system.

## A.1 Loudspeaker Model

Overall the loudspeaker is a transducer that converts energy between the electrical, mechanical, and acoustic systems. The link between the system's boundaries can be described by the force factor  $Bl$  between the electro-mechanical interface and by the diaphragm surface area  $S_d$  between the mechanical-acoustic interface.

Due to the close coupling between the systems, the electrical impedance will reflect the conditions in the mechanical system as well as in the acoustic system, and similar can be said about the mechanical or acoustic impedance. It is thus possible to specify the system behavior of all three subsystems solely from the electrical, mechanical or acoustic side based on the information from the important unit parameters of the loudspeaker. The loudspeaker unit parameters are listed in the datasheet as the "Thiele-Small" parameters, where the physical parameters used for the equivalent electrical circuit model can be seen in Table A.1.

Thiele-Small parameter	Symbol	Unit	Example: Vifa M10MD-39-08
Voice coil DC resistance	$R_e$	$\Omega$	5.4 $\Omega$
Voice coil inductance	$L_e$	H	$\approx 0.13$ mH
Moving mass	$M_{ms}$	kg	2.9 g
Compliance of suspension	$C_{ms}$	m/N	$\approx 1.13$ mm/N
Mechanical resistance	$R_{ms}$	N · s/m	$\approx 0.45$ Ns/m
Force factor	$Bl$	T · m	4.1 Tm
Elective radiating area	$S_d$	m <sup>2</sup>	37 cm <sup>2</sup>

**Table A.1:** Thiele-Small electromechanical parameters (also called fundamental parameters) and example values for Vifa M10MD-39-08 (discontinued). The approximately example values of  $L_e$ ,  $C_{ms}$  and  $R_{ms}$  are taken from the datasheet of a known replacement speaker (Scan-Speak Discovery 10F/8424G) as these values are not listed in the old datasheet of Vifa M10MD-39-08

Based on these parameters and the close coupling between the electrical, mechanical and acoustic system of the loudspeaker, it is possible to model the loudspeaker as an equivalent circuit that combines the electrical, the mechanical, and the acoustic system through the interfaces previously mentioned. This equivalent circuit provides an overview of the model and can be seen in Figure A.1

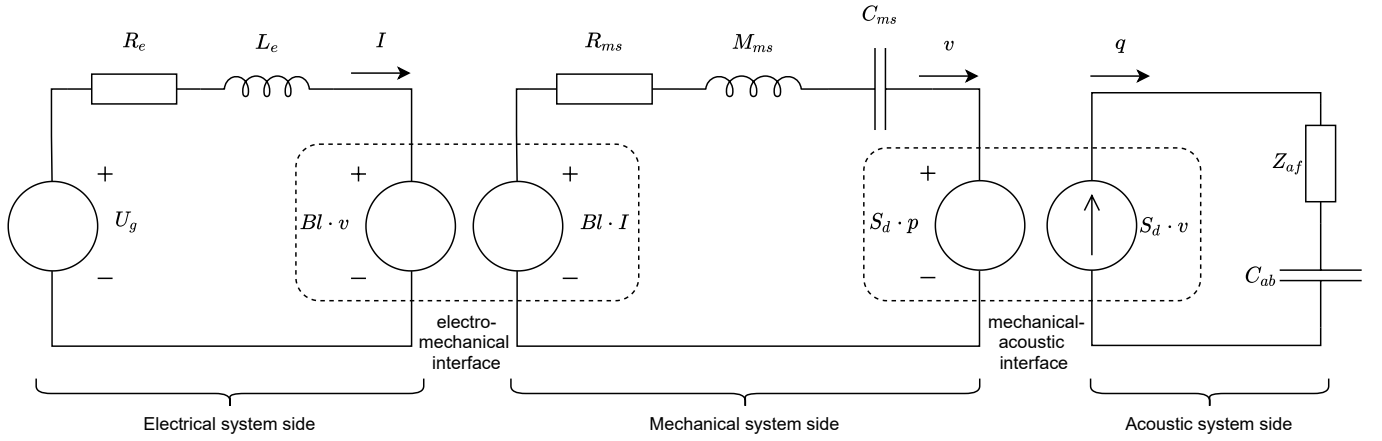


**Figure A.1:** Equivalent circuit of a loudspeaker mounted in a closed enclosure. Signals are represented by a voltage source  $U_g$ , the electric current  $I$ , the voice coil velocity  $v$ , the sound pressure  $p$  working on the diaphragm, and a volume velocity  $q$

As can be seen in the electro-mechanical interface of Figure A.1, the voice coil of the loudspeaker will affect the diaphragm by the Lorentz force  $F = Bl \cdot I$  [18, Ch. 4.7] when immersed in the magnetic field with an applied current  $I$ . However, a voltage  $U = Bl \cdot v$ , which counteracts the applied current, will also be induced in the voice coil according to Faraday's induction law when the voice coil moves with the velocity  $v$  in the magnetic field.

In the mechanical-acoustic interface, the diaphragm moves a volume of air at a velocity that can be expressed as the volume velocity  $q = S_d \cdot v$ . Conversely, the sound pressure of the air  $p$  across the diaphragm will affect the diaphragm with a force  $F = S_d \cdot p$ , which will again counteract the velocity  $v$  of the diaphragm.

The acoustic radiation impedance  $Z_a$  is a complicated function of frequency and consists of two parts,  $Z_{af}$  and  $Z_{ab}$ , the radiation impedances acting on the front and back of the diaphragm respectively. The back radiation impedance  $Z_{ab}$  will be dominated by the air compliances (and vent masses in a bass reflex system) [19, sec. 7.2.3], and can thereby be replaced by the air compliance introduced by the back enclosure  $C_{ab}$  given by:

$$C_{ab} = \frac{V_b}{\rho_0 \cdot c^2} \quad [\text{m}^3/\text{Pa}] \quad (\text{A.1})$$

where  $V_b$  is the internal box volume of the enclosure,  $\rho_0$  is the density of air, and  $c$  is the speed of sound. Acoustic losses in the enclosure due to e.g. absorption are disregarded in this model, but may be included as a loss component  $R_{ab}$  in parallel with  $C_{ab}$ .

The front radiation impedance  $Z_{af}$  consists of the radiation resistance  $R_{af}$  and a radiation reactance  $X_{af}$  so  $Z_{af} = R_{af} + jX_{af}$ . The magnitude of radiation resistance (air resistance) is very small compared to the other impedances of the total system and can be neglected without loss of accuracy in the model [66][67][68]. The radiation reactance  $X_{af}$  can be seen as an addition to the moving mass of the system coming from the volume of air in contact with the diaphragm, and thus be included as part of the moving mass  $M_{ms}$  (air load) [66][68], which is how it is often stated in loudspeaker datasheets. Otherwise, the air load will add around 10% to the total moving mass [18, sec. 3.2.2][66]. The radiation impedance of the front  $Z_{af}$  can therefore be replaced by a short circuit ( $Z_{af} = 0$ ).

### A.1.1 Transformation to the Mechanical Equivalent Circuit

In order to obtain a foundation for analysis that can provide information about the movement and dynamic of the loudspeaker, such as the diaphragm velocity  $v$ , it is advantageous to transform the whole system of

Figure A.1 to the mechanical side for easy analysis.

First, the acoustic system is transferred to the mechanical system side based on the impedance relation  $Z_m = S_d^2 \cdot Z_a$  [69]. The front radiation impedance  $Z_{af}$  is again replaced by a short circuit, with which it does not need to be transferred. The enclosure compliance  $C_{ab}$  will then on the mechanical side be a compliance given by:

$$C_{mb} = \frac{C_{ab}}{S_d^2} = \frac{V_b}{\rho_0 \cdot c^2 \cdot S_d^2} \quad [\text{m/N}] \quad (\text{A.2})$$

since the impedance on mechanical side of the acoustic compliance (modelled as a capacitor) is given by:

$$Z_m(C_{ab}) = S_d^2 \cdot Z_a = S_d^2 \cdot \frac{1}{j\omega C_{ab}} = \frac{S_d^2}{j\omega C_{ab}} = \frac{1}{j\omega C_{mb}} \quad (\text{A.3})$$

The electrical system is transferred to the mechanical system side based on the impedance relation  $Z_m = \frac{(Bl)^2}{Z_e}$  [69] where the impedances connected in series become admittances connected in parallel and the voltage source becomes a velocity source (current source) from the relation  $U = Bl \cdot v$ . However, the Thevenin-Norton equivalent allows the current source to be written up as a force source (voltage source) in series with the admittances connected in parallel. This gives the following expressions:

$$Z_m(R_e) = \frac{(Bl)^2}{Z_e} = \frac{(Bl)^2}{R_e} \quad (\text{A.4})$$

$$Z_m(L_e) = \frac{(Bl)^2}{Z_e} = \frac{(Bl)^2}{j\omega L_e} = \frac{1}{j\omega \frac{L_e}{(Bl)^2}} \quad (\text{A.5})$$

$$v_g = \frac{U_g}{Bl} \xrightarrow{\text{Thevenin-Norton}} F = \frac{U_g}{Bl} \cdot \left( \frac{1}{\frac{(Bl)^2}{R_e}} + \frac{1}{j\omega \frac{L_e}{(Bl)^2}} \right)^{-1} = \frac{U_g \cdot Bl}{R_e + j\omega L_e} \quad (\text{A.6})$$

A new mechanical equivalent circuit of a loudspeaker mounted in a closed enclosure using the found expressions for the impedances and sources can be seen in Figure A.2

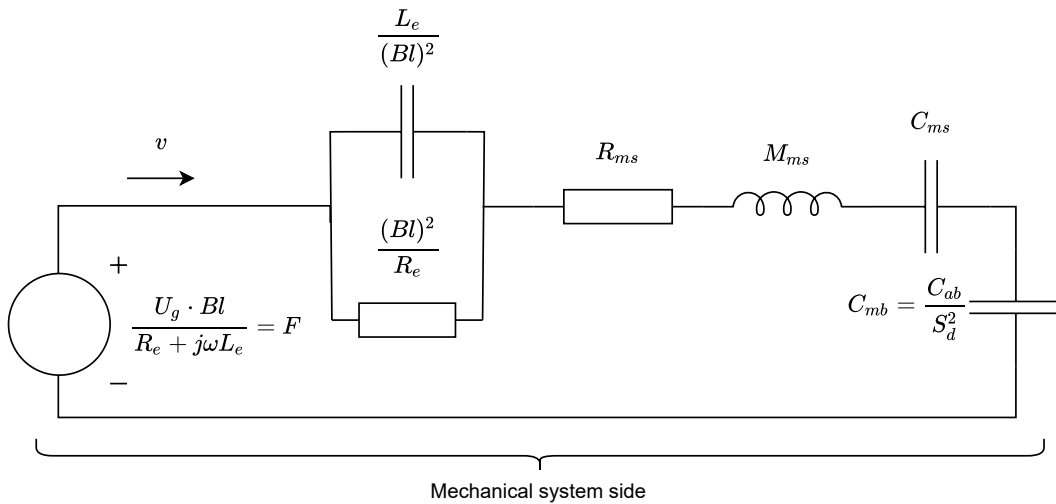


**Figure A.2:** Mechanical equivalent circuit of a loudspeaker mounted in a closed enclosure, where  $F$  denotes the resulting force in the mechanical system

From here it is easier to analyze the movement and dynamic of the loudspeaker. The voice coil velocity  $v$  can for example be found using Ohms-law in the mechanical domain, but first, the total mechanical impedance

must be found as:

$$\begin{aligned} Z_{mres} &= \left( \frac{1}{\frac{(Bl)^2}{R_e}} + \frac{1}{j\omega \frac{L_e}{(Bl)^2}} \right)^{-1} + R_{ms} + j\omega M_{ms} + \frac{1}{j\omega C_{ms}} + \frac{1}{j\omega C_{mb}} \\ &= R_{ms} + j\omega M_{ms} + \frac{1}{j\omega C_{ms}} + \frac{1}{j\omega C_{mb}} + \frac{(Bl)^2}{R_e + j\omega L_e} \end{aligned} \quad (\text{A.7})$$

Afterwards the voice coil velocity  $v$  can simply be found from the following relation:

$$v = \frac{F}{Z_{mres}} = \frac{\frac{Bl}{R_e + j\omega L_e}}{R_{ms} + j\omega M_{ms} + \frac{1}{j\omega C_{ms}} + \frac{1}{j\omega C_{mb}} + \frac{(Bl)^2}{R_e + j\omega L_e}} \cdot U_g \quad [\text{m/s}] \quad (\text{A.8})$$

Where  $C_{mb}$  again is the compliance of the confined air in the cabinet on the mechanical side given in Equation A.2,  $U_g$  is the applied voltage to loudspeaker terminals, and the rest is the Thiele-Small electromechanical parameters listed in Table A.1.

Conversely, the required voltage to loudspeaker terminals  $U_g$  to provide a certain diaphragm velocity  $v$  can be determined from:

$$U_g = \frac{R_{ms} + j\omega M_{ms} + \frac{1}{j\omega C_{ms}} + \frac{1}{j\omega C_{mb}} + \frac{(Bl)^2}{R_e + j\omega L_e}}{\frac{Bl}{R_e + j\omega L_e}} \cdot v \quad [\text{V}] \quad (\text{A.9})$$

An example of the velocity response for a given loudspeaker (Vifa M10MD-39-08) can be seen in Figure A.3.

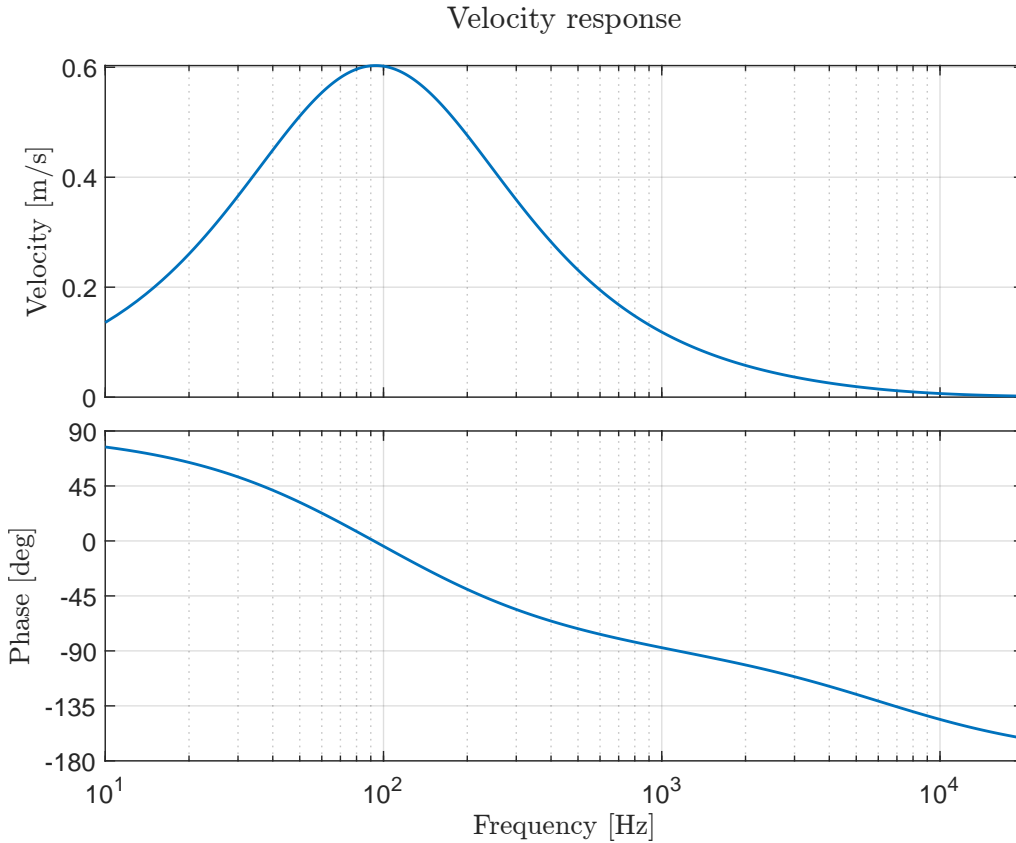


**Figure A.3:** Velocity response for the loudspeaker example (Vifa M10MD-39-08) of Table A.1 mounted in a 20L cabinet when 2.83V<sub>rms</sub> is applied to the loudspeaker terminals (1 Watt into an 8 ohm loudspeaker)

# 2D Guitar Measurement

## Description

# B

In this appendix, a description for the 2D measurement of the radiation pattern of an acoustic guitar is presented. The measurements were conducted in the acoustics labs at Aalborg University, Fredrik Bajers Vej 7B, 9220 Aalborg, Denmark in the anechoic chamber B4-111, and controlled from the adjacent control room B4-113 of the aforementioned labs.

The 2D measurements served as a base for future work as the measurements gave a first glance at the radiation pattern of a guitar on the horizontal plane and a part of the frontal plane.

The description of the equipment list, measurement setup and procedure are reported in Section B.1, Section B.2 and Section B.3 respectively while the results of the measurement are grouped and presented in Section B.4.

### B.1 Equipment List

The equipment used to perform the measurements is following listed:

- 1x Arch of 1.7 m radius
- 2x Speaker stands
- 31x G.R.A.S. 40AZ 1/2" prepolarized free-field microphone
- 31x G.R.A.S. 26CC 1/4" CCP standard preamplifier with SMB connector
- 1x G.R.A.S. 40AD pressure microphone
- 1x DPA-4037AAU microphone preamplifier with XLR connector (AAU-modified)
- 1x Røde NT2000 condenser microphone
- 1x Microphone stand
- 1x B&K Type 4231 sound calibrator
- 4x RME Micstasy 8-channel full range pre-amp
- 1x RME Fireface UFX+
- 1x High chair
- 1x Fender CD-60 CE acoustic guitar
- 1x Laptop with MATLAB
- 1x STANLEY CL-E laser
- 1x Point laser

### B.2 Setup

The setup used for measuring the radiation pattern of the guitar is made up of two parts, one inside the anechoic chamber and one inside the control room.

A semicircle arch of 1.7 meters in radius was installed horizontally inside the anechoic chamber. Two speaker stands together with a metallic wire hanging from the ceiling were used to keep it still at a distance of 1.1

meters from the floor. The origin of the arch was thought of as the acoustic center to be measured. The arch was distributed with 31 microphones spaced at every  $\theta = 6^\circ$  from each other in order to be disposed in a range  $-90^\circ < \theta < 90^\circ$ .

A sketch of the microphone positions (and channel names) on the semicircle arch can be seen in Figure B.1a while an overview of the measurement setup for the measurement of the guitar radiation pattern can be seen in Figure B.1b

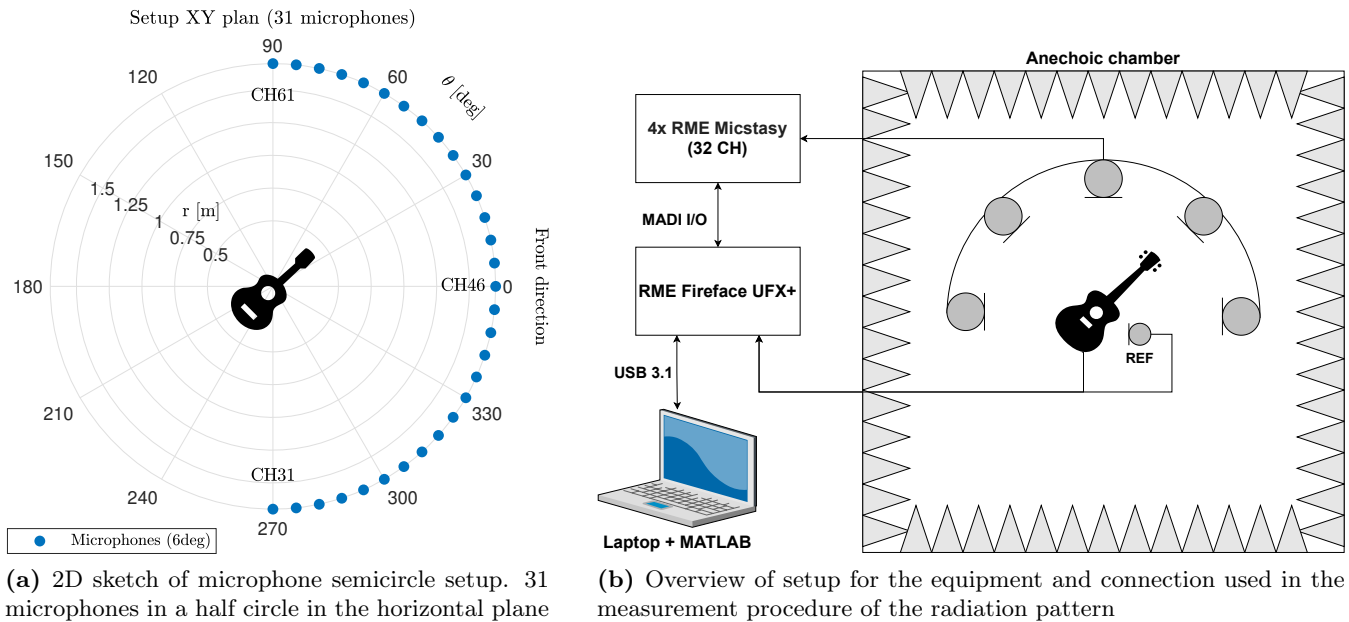


**Figure B.1:** Overview of the 2D measurement setup

All signals from the microphone on the semicircle arch were amplified and sampled by four 8 channel microphone preamps and AD converters (RME Micstasy), which were daisy-chained using the MADI protocol, so the microphone signals could be sent digitally to the soundcard placed inside the control room (RME Fireface UFX+) through the MADI interface (Coaxial). Conversely, the soundcard was also able to communicate and control the Micstasys from the control room via MIDI over MADI. This created an easy way to control the 31 channels remotely without the use of a lot of additional cabling. Moreover, all the microphones were calibrated with a sound calibrator (B&K Type 4231), even though the difference between the 31 microphones was found to be at a maximum of 1.8 dB.

A guitarist was seated on a high chair<sup>1</sup> holding a guitar with the soundhole placed in the center of the half-circle. The guitar was equipped with a built-in pickup (piezo-electric) and with a reference microphone placed at the head of the guitar to not modify the radiation characteristics of the instrument. The head of the guitar was considered to be the least sensitive point on the guitar, as it does not contribute much to the radiation of sound. The pickup signal of the guitar, as well as the reference microphone(s), were captured directly by the built-in mic/inst. input channels of the soundcard. The pickup signal and the reference microphone were used to create a level reference for all the measurements that did not vary with e.g. unwanted different orientations of the guitar.

The RME Fireface UFX+ soundcard located in the control room was connected through USB to a laptop running MATLAB, where the measurement could be written into a multichannel .wav file in frames of 2048 samples per channel. The recorded signals in the .wav file could then be post-analyzed to obtain information about the radiation pattern.

<sup>1</sup>A high chair similar to the stools usually found in bars.

To increase the accuracy, a combination of lasers was used to point to the center of the guitar soundhole. All the parts of the arch not covered by microphones as well as the stands and the Micstasys were covered with absorbing material so to avoid any unwanted reflections. The measurement setup in the anechoic chamber is shown in Figure B.2.



(a) Guitarist playing the guitar inside a ring of microphones seated on a chair with a soundhole at 1.1 m distant from the floor



(b) Guitarist playing inside a ring of microphones with reference studio microphone in front of the guitar's soundhole

**Figure B.2:** 2D measurement setup in the anechoic chamber with the musicians seated on a chair

### B.3 Procedure

In order to obtain the radiation pattern of the guitar, the instrument needs to be excited. In Section 2.5.1 many different studies which made use of disparate excitation techniques are presented. For the scope of the project, a musician playing the instrument was preferred over the other excitation techniques.

In these particular measurements, two guitarists were employed to play different styles, in different positions and with different body orientations in order to investigate which way of exciting the guitar is most sensible for these measurements.

The procedure went as follow: First, the musicians were asked to seat on a high chair as it is shown in Figure B.2a. Both the musicians alternated to play 20 seconds of open chords. Subsequently, only one guitarist played 20 seconds of ascending barre chords, 20 seconds of fingerstyle notes, and 20 seconds of sweep using a steel guitar slide.

All these measurements carried out while seating on the chair were repeated with the presence of a reference studio condenser microphone placed in front of the guitar within 10 cm to 20 cm from the soundhole. The setup can be seen in Figure B.2b

Then, one guitarist was asked to stand up and play 20 seconds of ascending barre chords<sup>2</sup> while facing at  $\theta = 0^\circ$  of the arch. The soundhole of the guitar was carefully placed at the center of the array of microphones with the help of the lasers at a distance of 1.1 m from the floor. The procedure was repeated with the guitarist facing the imaginary  $\theta = 180^\circ$  of the arch (his back faced the  $\theta = 0^\circ$ ) as it can be seen in Figure B.3a.

<sup>2</sup>In particular the 'E'-shaped major barre chord starting on the low E, then F, F#, etc.



(a) Guitarist playing the guitar inside a ring of microphones standing up and facing the arch at  $\theta = 180^\circ$



(b) Guitarist playing inside a ring of microphones lying down on the floor and facing the arch with  $\theta = 0^\circ$

**Figure B.3:** 2D measurement setup in the anechoic chamber with the musician playing in different body orientation

In the last procedure, the radiation of the guitar was measured from the frontal plane (with an offset of around 1 meter in the guitar front direction). To do that, the musician was lying down on the floor, with the acoustic center of the guitar being at a distance of approximately 30 cm from the supporting panel. Initially, the upper part of the frontal plane was measured. The musician lying on the floor was asked to turn the body so that the head could be faced below the arch. Then, the lower part of the plane was measured by turning the body so that the feet could be faced below the arch as shown in Figure B.3b. In both cases, the guitarist played 20 seconds of ascending barre chords.

## B.4 Polar Plots Results

In this section, the polar plots resulted from the analysis of the measurements are presented.

In the analysis, the multichannel .wav files containing the measurement are passed through either a 1/3 or a 1/6 octave filter bank which performs the 1/3 or 1/6 octave band analysis. The 1/3 octave filter bank consists of 22 band-pass filter bands from 79 Hz-10 kHz, while the 1/6 octave filter bank consists of 43 band-pass filter bands from 79 Hz - 10 kHz. The filter banks can be seen as a parallel structure of either 1/3 octave filters or 1/6 octave filters and are implemented in MATLAB as a system object<sup>3</sup>.

Afterwards, the Root Mean Square (RMS) value is calculated for each frequency band of each channel (including the pickup signal). The output signals of all the microphone channels are scaled with the input signal (the pickup signal) by dividing the RMS value of each frequency band for all channels with the corresponding RMS values of the pickup signal. This provides a transfer beam pattern matrix, which contains the relation between input and output levels for all frequency bands of each microphone channel. It also means that the transfer beam pattern matrix (and beam patterns) can be seen as a set of transfer gains for all frequency bands of the sound going from the guitar to each microphone position.

High gains to some directions at e.g high frequencies do not necessarily mean that the guitar can produce high frequencies with high sound pressure levels at these directions, but rather that high frequencies producing a small pickup signal will be amplified more to this direction compared to other frequencies that naturally radiate more energy and thereby also produce larger pickup signals.

The transfer beam pattern matrix is normalized to the maximum RMS value of all frequency bands for one recording at a time. The beam patterns can afterwards be extracted from the normalized transfer beam pattern matrix and plotted as e.g. polar plots for a single frequency band as level vs direction (microphone channel) or used to plot a directivity sonogram where the horizontal axis represents the frequency bands and the vertical axis represents the beam direction (microphone channel).

The first part of the results compares the guitar radiation pattern of the guitar for different playing styles in the half horizontal plane, in order to evaluate the impact of the excitation techniques on the radiation pattern. The second and third parts of the results provide a better overview of the sound radiation pattern in the full horizontal plane and in the full-frontal plane when the guitar is excited with ascending barre chords.

### B.4.1 Different Playing Styles in the Half Horizontal Plane (sitting on chair)

In Figure B.4 the 2D polar plots show the beam pattern in the half horizontal plane using different playing styles, while the musician is sitting on a chair facing the guitar front at  $\theta = 0^\circ$ .

---

<sup>3</sup>see <https://se.mathworks.com/help/audio/ref/octavefilterbank-system-object.html> for more info

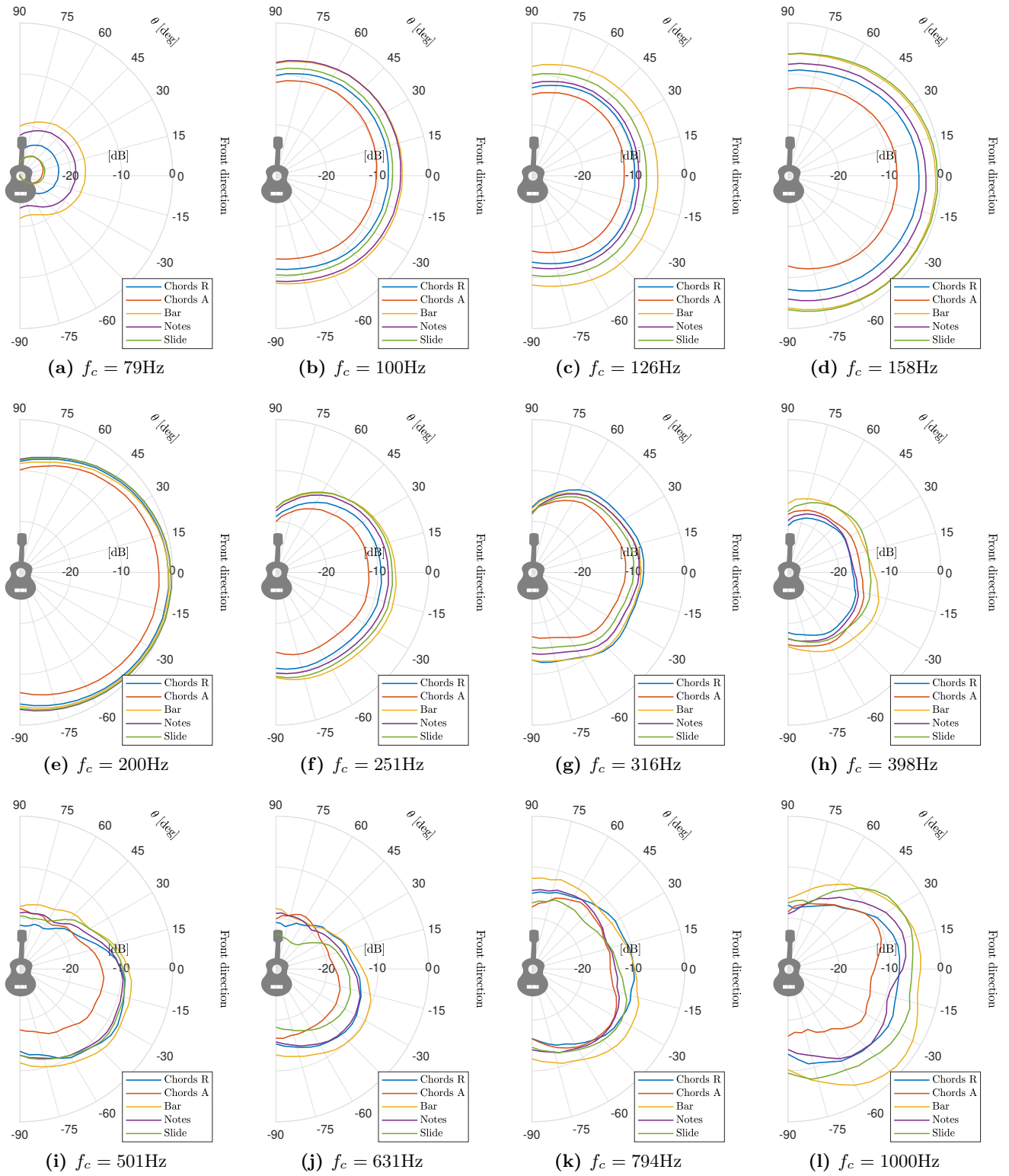


**Figure B.4:** Beam pattern  $b(\theta)$  for the guitar in the half horizontal plane with different playing styles as excitation plotted in 1/3 octave bands with  $\theta = 6^\circ$  spatial resolution. The polar plots are normalized over the maximum magnitude of each playing style for all 1/3 octave bands within 79 Hz to 10 kHz (Part 1)

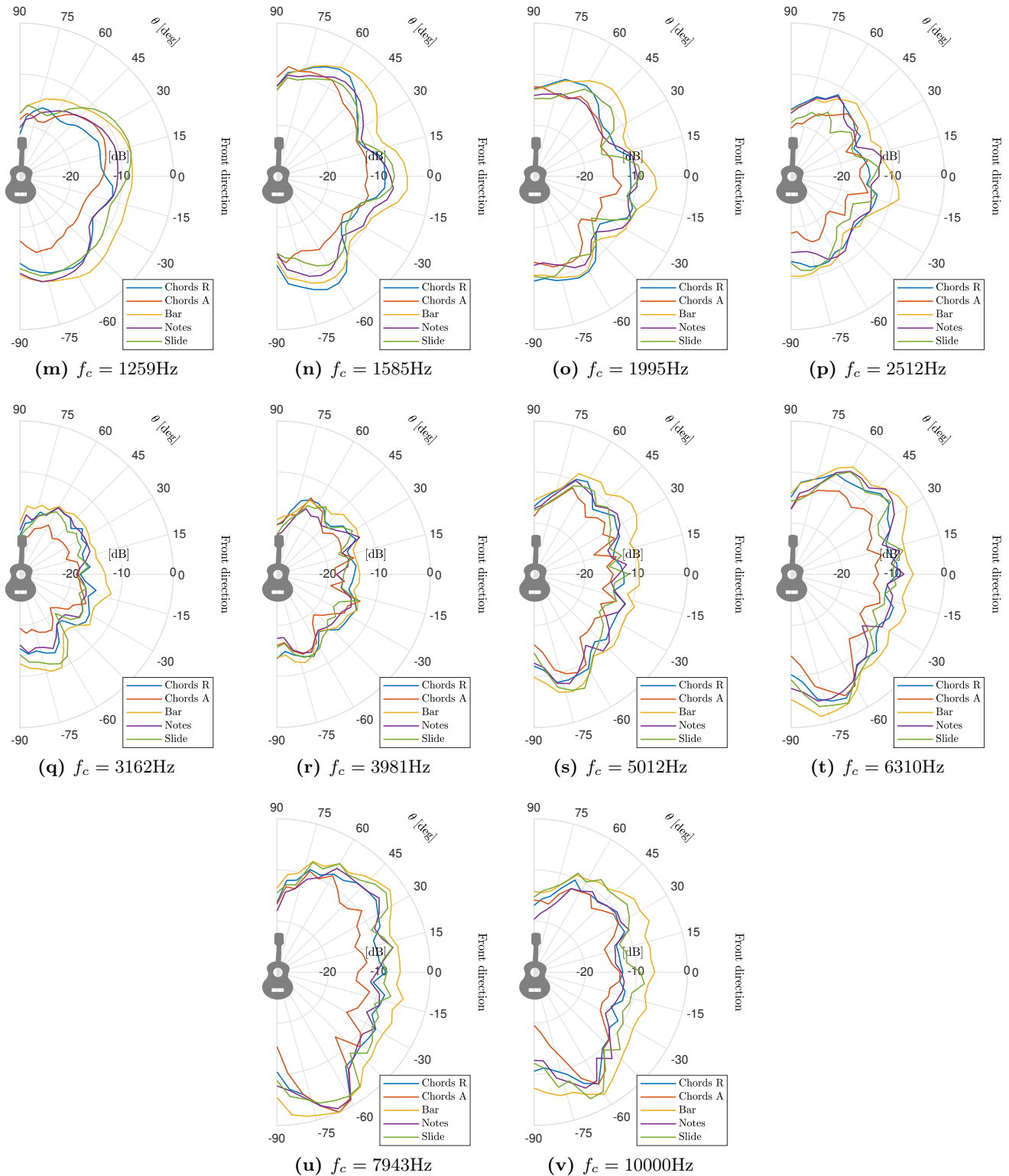


**Figure B.4:** Beam pattern  $b(\theta)$  for the guitar in the half horizontal plane with different playing styles as excitation plotted in 1/3 octave bands with  $\theta = 6^\circ$  spatial resolution. The polar plots are normalized over the maximum magnitude of each playing style for all 1/3 octave bands within 79 Hz to 10 kHz (Part 2)

### B.4.2 Guitar Full Horizontal Plane (standing up)

In Figure B.5 the 2D polar plots show the beam pattern in the full horizontal plane while the musician is standing up. The full horizontal plane is obtained by combining two measurements performed when facing the guitar front at  $\theta = 0^\circ$  (front pattern) and  $\theta = 180^\circ$  (back pattern).

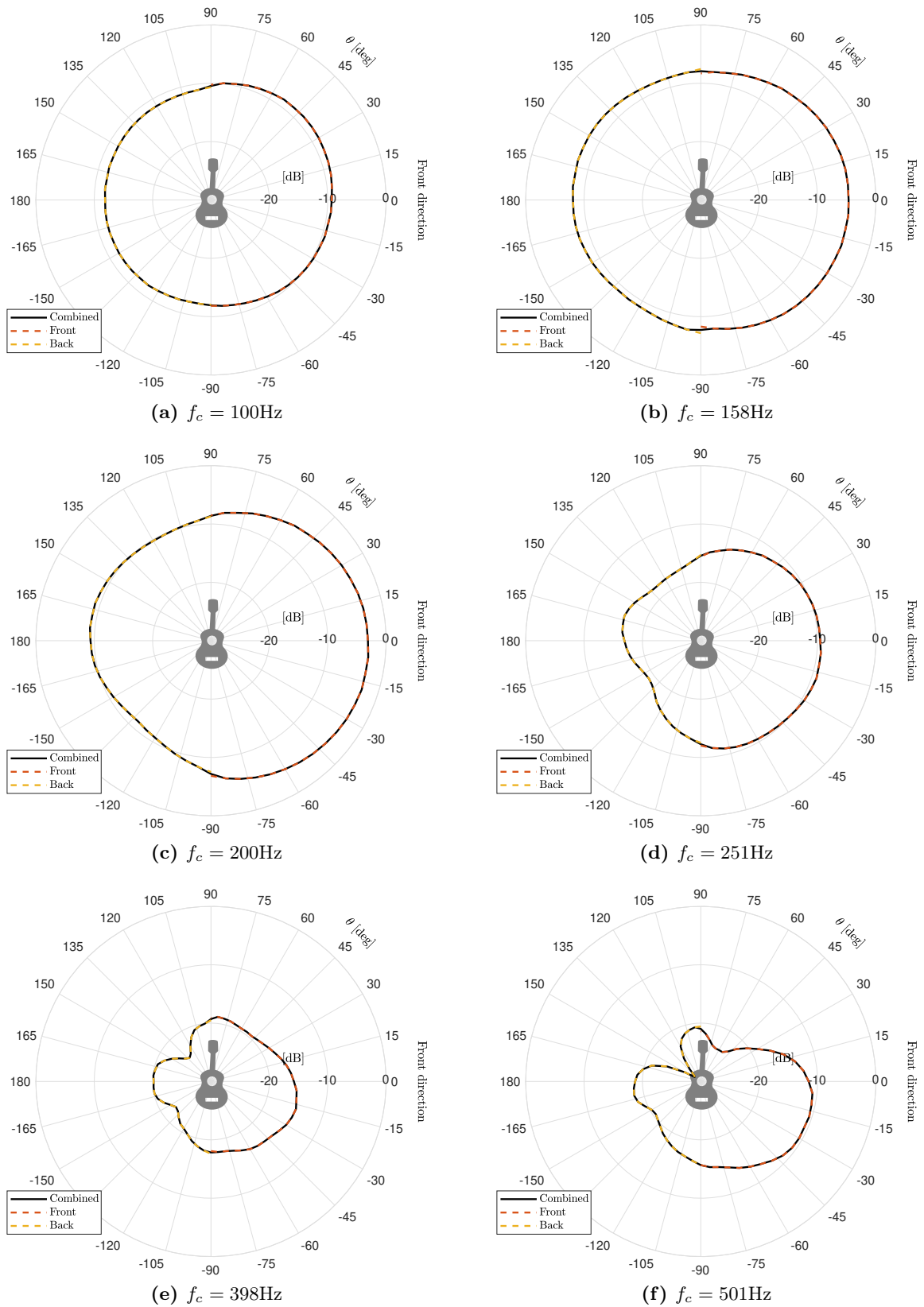


**Figure B.5:** Beam pattern  $b(\theta)$  for the guitar in the full horizontal plane plotted for some of the 1/3 octave bands with  $\theta = 6^\circ$  spatial resolution. The guitar is excited with ascending barre chords. The polar plots are normalized over the maximum magnitude for all 1/3 octave bands within 79 Hz to 10 kHz (Part 1)

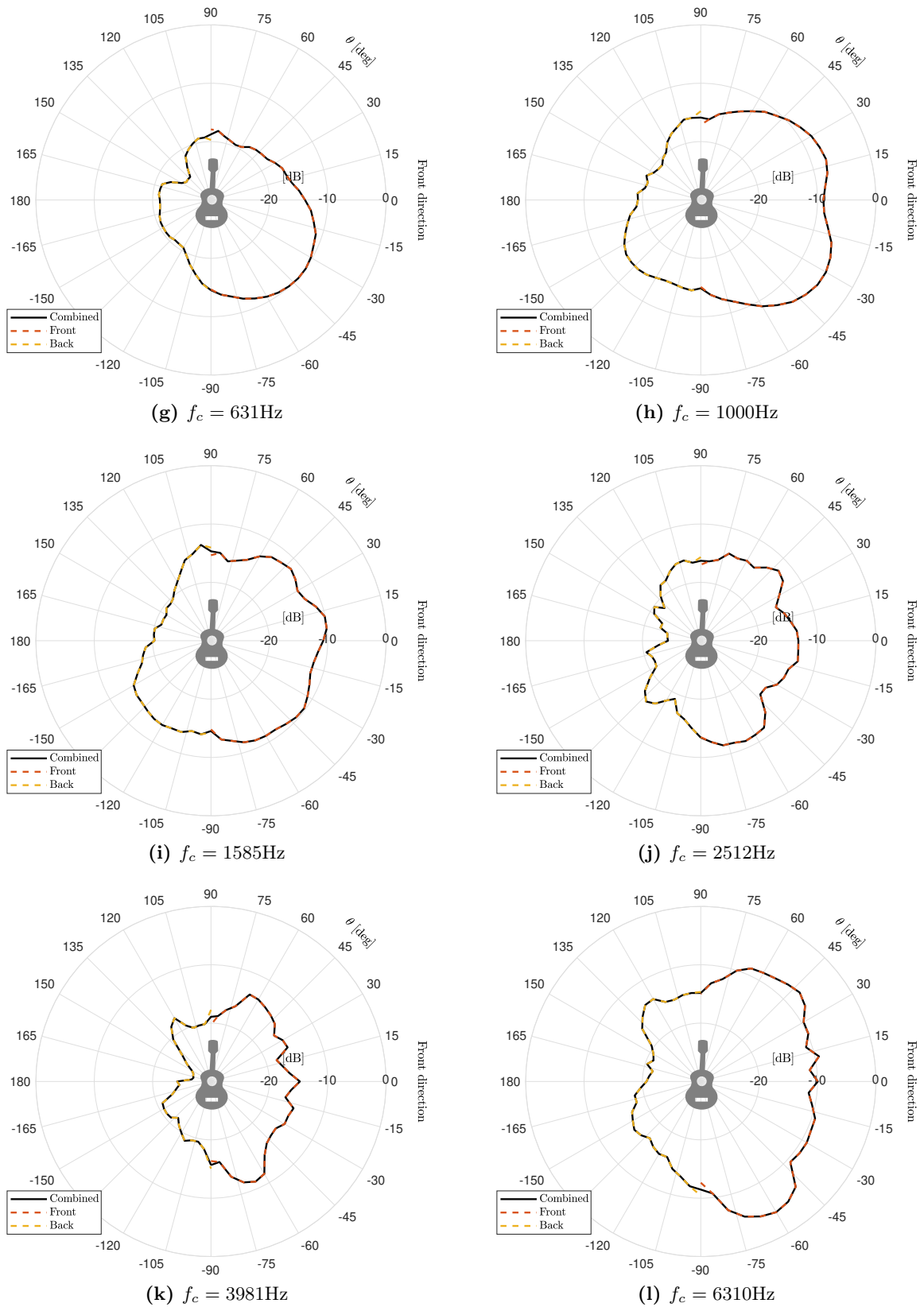


**Figure B.5:** Beam pattern  $b(\theta)$  for the guitar in the full horizontal plane plotted for some of the 1/3 octave bands with  $\theta = 6^\circ$  spatial resolution. The guitar is excited with ascending barre chords. The polar plots are normalized over the maximum magnitude for all 1/3 octave bands within 79Hz to 10kHz (Part 2)

### B.4.3 Guitar Full Frontal Plane (lying down)

In Figure B.6 the 2D polar plots show the beam pattern in the full-frontal plane (with an offset of around 1 meter in the guitar front direction) while the musician was lying down on the floor. These results are obtained by combining the top part of the frontal plane with the bottom part of the frontal plane.

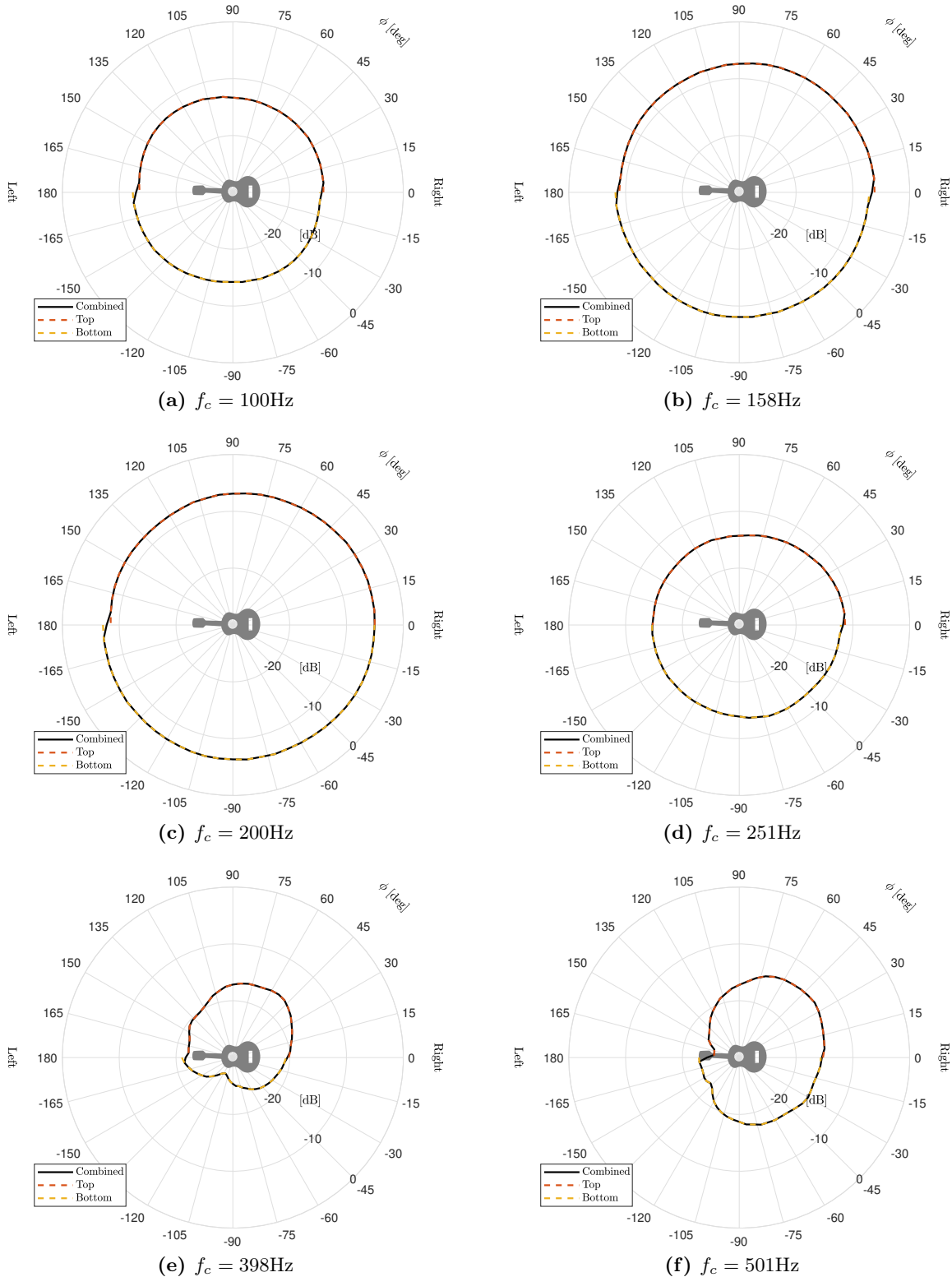


**Figure B.6:** Beam pattern  $b(\phi)$  for the guitar in the full-frontal plane plotted for some of the 1/3 octave bands with  $\phi = 6^\circ$  spatial resolution. The guitar is excited with ascending barre chords. The polar plots are normalized over the maximum magnitude for all 1/3 octave bands within 79 Hz to 10 kHz (Part 1)

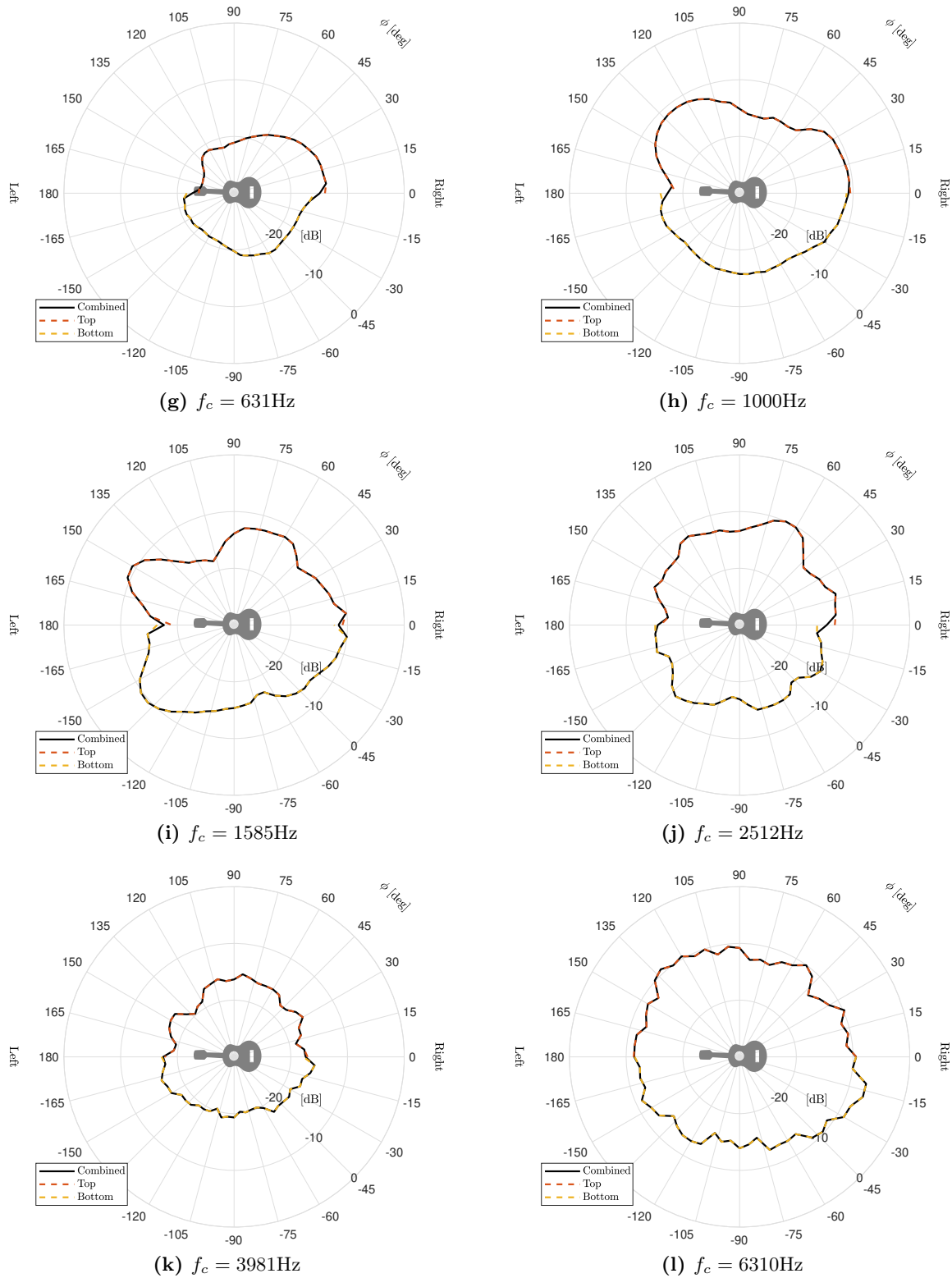


**Figure B.6:** Beam pattern  $b(\phi)$  for the guitar in the full-frontal plane plotted for some of the 1/3 octave bands with  $\phi = 6^\circ$  spatial resolution. The guitar is excited with ascending barre chords. The polar plots are normalized over the maximum magnitude for all 1/3 octave bands within 79 Hz to 10 kHz (Part 2)

# 3D Guitar Measurement

## Description



This appendix describes, in detail, the 3D measurements of the radiation pattern of an acoustic guitar carried on at the anechoic chamber B4-111 in the Acoustic Labs at Aalborg University, at Frederik Bajers Vej 7B, 9220 Aalborg Denmark while controlled from the control room B4-113 of the previously mentioned labs. This research was conducted after the trial measurement in 2D described in Appendix B.

The description of the equipment list, measurement setup and procedure are reported in Section C.1, Section C.2 and Section C.3 respectively while the results of the measurement are grouped and presented in Section C.4.

### C.1 Equipment List

The equipment used to carry on the measurement is following listed:

- 1x Arch of 1.7 m radius
- 17x G.R.A.S 40AZ 1/2" prepolarized free-field microphone
- 17x G.R.A.S 26CC 1/4" CCP standard preamplifier with SMB connector
- 1x B&K Type 4231 sound calibrator
- 3x RME Micstasy 8-channel full range pre-amp
- 1x RME Fireface UFX+
- 1x Outilne ET 250-3D turning table
- 1x Mechanical turning table linked switcher
- 1x High chair
- 1x Fender CD-60 CE acoustic guitar
- 1x Laptop with MATLAB
- 1x Electro-Voice N/D267 dynamic microphone
- 1x Sound Devices MixPre
- 1x beyerdynamic DT990 headphones
- 1x beyerdynamic DT770 headphones
- 2x STANLEY CL-E laser

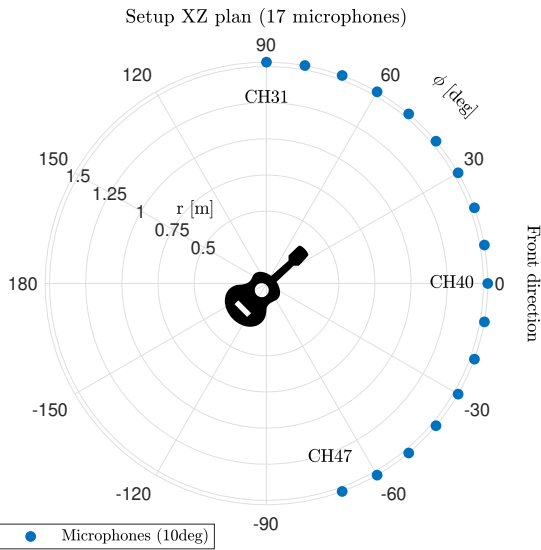
### C.2 Setup

The anechoic chamber was set up with an arch of 1.7 m radii, disposed in a vertical direction orthogonal to the floor. The arch was fixed on to two metal bars that were hanging from the ceiling and kept still by fitting it in a channel made of wood fixed on the floor of the chamber.

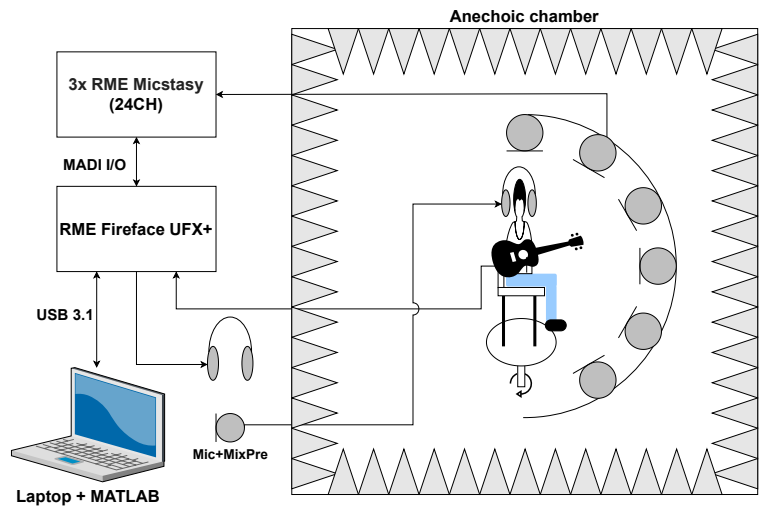
The arch was filled with 17 1/2" free-field microphones placed at a distance of  $\phi = 10^\circ$  from each other, in a range of  $-70^\circ < \phi < 90^\circ$ . This angle of separation was found as a good compromise between complexity and resolution. The minimum elevation angle was chosen to be  $\phi = -70^\circ$  as every microphone with a lower

angle on the arch would have been shadowed by the turning table used to hold up the musician at the center of the sphere.

A sketch of the microphone positions (and channel names) on the semicircle arch can be seen in Figure C.1a while an overview of the measurement setup for the measurement of the guitar radiation pattern can be seen in Figure C.1b. A visualization of the setup is shown in Figure C.2



(a) 2D sketch of microphone semicircle setup. 17 microphones in a semicircle in the vertical plane



(b) Overview of setup for the equipment and connection used in the measurement procedure of the radiation pattern

**Figure C.1:** Overview of the 3D measurement setup



(a) Picture of the arch from an angle view.



(b) Picture of the arch from the side.

**Figure C.2:** Pictures of the setup in the anechoic chamber. The arch is mounted together with the turning table and the chair placed in the middle of it

All the microphones on the arch were attached to flat plastic bars which were fixed perpendicularly to the arch. This was done to avoid a close contact of the microphones with the arch that could cause an unwanted pick up of either the reflection from the arch or a resonance induced on the metal arch. In any case, they helped to establish a better free-field condition. However, it also reduced the microphone distance by 17cm to the origin of the metal arch creating a free-field microphone semicircle with a radius of 1.53 m.

The microphones were calibrated with a B&K Type 4231 sound calibrator so to reduce any inequalities in between the microphones even though the difference in between the 17 microphones again was found to be at a maximum of 1.8 dB. The arch was wrapped with isolating foam which further reduced any unwanted reflections. Figure C.3 shows the process of the build-up of the arch.



(a) The preparation of all the plastic flat bars used to mount the microphones on the arch

(b) The arch filled with the microphones on top of plastic flat bars

**Figure C.3:** The build up of measurement arch with precise angle spaced microphones

A platform was created in the middle of the sphere, at 1.7 m from the metal arch or 1.53 m from each microphone. A high chair on which the musician was asked to sit was placed on the turning table, in such a way that the guitar held by the musician could face towards the  $\phi = 0^\circ$  microphone.

The turntable was able to move with the desired step size which was directly controlled from a switcher situated in the adjacent control room. Since every azimuthal angle needed to be recorded separately, the step size was set to  $\theta = 5^\circ$ , so that the radiation pattern at every  $10^\circ$  can be approximated with averaging.

The results in Section C.4 are plotted with a azimuth step size of  $\theta = 10^\circ$ , and exploit the  $\theta = 5^\circ$  sampling, to give a more accurate representation of the radiation pattern of the guitar by averaging in between adjacent azimuth angles. For example a measurement point at  $\phi = 0^\circ$ ,  $\theta = 30^\circ$  will be given by an average in between  $\phi = 0^\circ$ ,  $\theta = 25^\circ$  and  $\phi = 0^\circ$ ,  $\theta = 30^\circ$  and  $\phi = 0^\circ$ ,  $\theta = 35^\circ$ .

This results in a grid of measurement points on a sphere sampled at  $10^\circ$  in both azimuth and elevation, where every point has been averaged in azimuth by a window of  $\pm 5^\circ$ .

A sketch of this sampling of measurement points the 3D measurement grid (after averaging in between adjacent azimuth angles) can be seen in Figure C.4

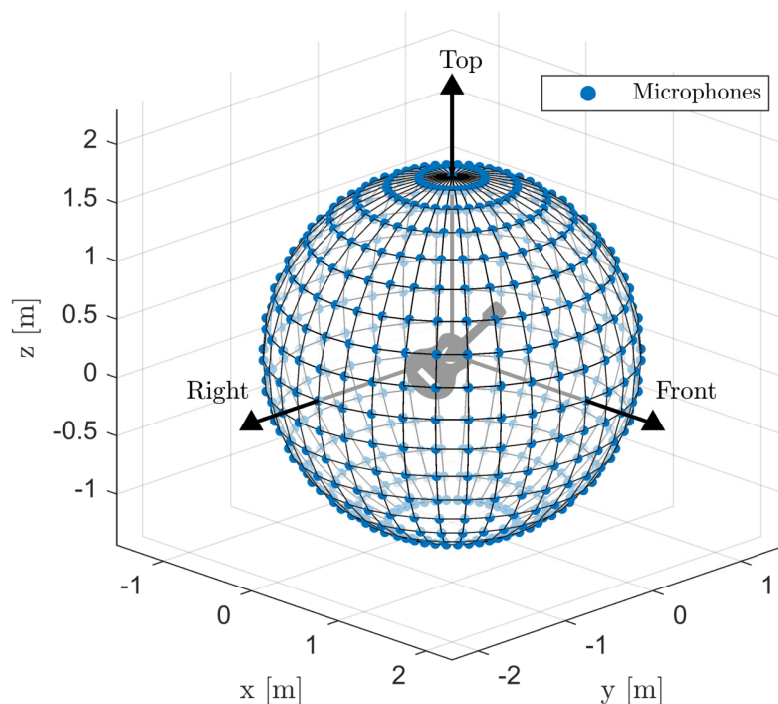


**Figure C.4:** 3D sketch of microphone sphere grid (17 microphones in a semicircle in the vertical plane, sampling every  $10^\circ$  of azimuth angle)

The signals from the microphones were sent to three 8 channel RME Micstasy, microphone preamp, and AD converter, which were daisy-chained with the MADI protocol. In this way, the signals could be sent digitally to the RME Fireface UFX+ soundcard situated in the control room through coaxial cables (MADI Interface). On the other hand, the soundcard could control the Micstasy settings from remote via MIDI over MADI. Everything was controlled by a laptop running MATLAB in the control room connected to the soundcard through USB, where the measurement could be written into a multichannel .wav file in frames of 2048 samples per channel. The recorded signals in the .wav file could then be post-analyzed to obtain information about the 3D radiation pattern.

A link for communication was created between the musician in the anechoic chamber and the operator sitting in the adjacent control room. In order to do that, a microphone was placed inside the control room for the use of the operator, which could be heard by the musician inside the anechoic chamber through a set of closed headphones. Conversely, the operator was able to hear the musician talking by just picking up the signals from one of the microphones placed on the arch inside the anechoic chamber to be played over another set of headphones in the control room.

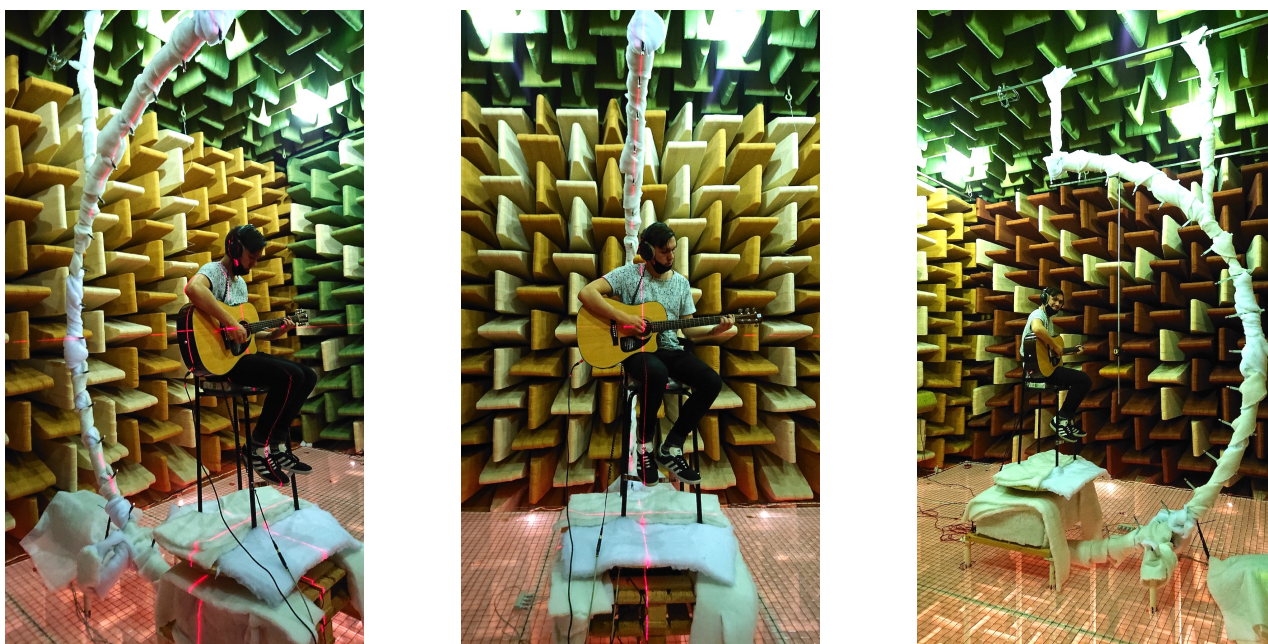
### C.3 Procedure

The scope of this measurement setup is to acquire the radiation pattern of an acoustic guitar in 3D at the points of a sphere with a specific radius, which is defined as the distance of the sphere's points from the acoustic center of the instrument. The procedure described here differs from the measuring technique used in Appendix B, as the number of measuring points is way larger than in the 2D situation.

The musician was asked to seat on a high chair placed over a turntable in the middle of a sphere at 1.7 m

distance from the arch. The turntable, which was able to move around with the desired step size, allowed the musician with the guitar to turn for  $\theta = 360^\circ$  around its center axis.

Particular care was taken in fitting the acoustic center of the instrument, found as the point inside the guitar's body, halfway through the soundhole and the middle of the guitar sides on the axis passing through the center of the turning table. This was done with help of a combination of lasers pointing at the guitar's center and at the turning table center simultaneously. In this way, for every turn, the acoustic center coincided with the center of the measuring sphere. Figure C.5 shows pictures from the measurement procedure. The starting situation is shown in Figure C.5c where the musician holds the guitar facing the arch at  $\theta = 0^\circ$ . Figure C.5a and Figure C.5b instead show the musician turned at  $\theta = 180^\circ$  with the lasers pointed on him. It is shown how the acoustic center was kept intact, as it appears perfectly centered halfway through the soundhole and the guitar's side while it is also perfectly aligned with the microphones on the arch.



(a) Guitarist playing the guitar inside the setup station and facing the arch at  $\theta = 180^\circ$  (b) Guitarist playing the guitar inside the setup station and facing the arch at  $\theta = 180^\circ$  (c) Guitarist playing the guitar inside the setup station and facing the arch at  $\theta = 0^\circ$

**Figure C.5:** Illustration from the different angles of the measurement setup with the musician playing the guitar over the turning platform.

At this point, the musician is asked to play to excite the guitar in the center of the arch. The signal chosen in this measurement session was a 20 seconds of ascending barre chords as it was found as the most effective in between all the excitation signals tried in the measurements described in Appendix B. The musician was also asked to try to play as similar as possible (both in style and in amplitude) at every turn of the rotating table. This was required so to acquire a signal homogeneous for every step angle.

The procedure was controlled by an operator in the control room who was guiding the musician in the recording session by advising him to start to play every time the recording was initialized as well as to stop when the recording was ended. This was done using the communication link previously described.

## C.4 Balloon-style Directivity Plots Results

In this section, the balloon-style directivity plot results from the analysis of the measurements previously described are presented as the guitar radiation pattern in 3D.

In the analysis, the multichannel .wav files containing the measurement for each turntable step recording are passed through a 1/3 octave filter bank which performs the 1/3 octave band analysis. The 1/3 octave filter bank consists of 22 band-pass filter bands from 79 Hz-10 kHz. The filter banks can be seen as a parallel structure of 1/3 octave band filters and are implemented in MATLAB as a system object<sup>1</sup>.

Afterwards, the Root Mean Square (RMS) value is calculated for each frequency band of each channel (including the pickup signal) for all turning table step recordings. The output signals of all the microphone channels are scaled with the input signal (the pickup signal) by dividing the RMS value of each frequency band for all channels with the corresponding RMS values of the pickup signal within the same turntable step recording. This provides a transfer beam pattern matrix, which contains the relation between input and output level for all frequency bands of each microphone channel for all the turntable step recordings. It also means that the transfer beam pattern matrix can be seen as a set of transfer gains for all frequency bands of the sound going from the guitar to each microphone position.

High gains to some directions at e.g high frequencies do not necessarily mean that the guitar can produce high frequencies with high sound pressure levels at these directions, but rather that high frequencies producing a small pickup signal will be amplified more to this direction compared to other frequencies that naturally radiate more energy and thereby also produce larger pickup signals.

As the measurements are obtained at multiple turntable steps of  $\theta = 5^\circ$  so the guitar front is facing at  $\theta = 0^\circ, 5^\circ, \dots, 360^\circ$ , then some indices/directions gains in the transfer beam pattern matrix will overlap or repeat from different recordings. Therefore, to avoid any discontinuity that might be present due to the different recordings, the gains at  $\theta = 0^\circ$  and  $\theta = 360^\circ$  need to be averaged for each elevation angle  $\phi$ . Similarly, all the turntable step recordings containing a microphone at  $\phi = 90^\circ$  require to be averaged to avoid discontinuity from different recordings. Lastly, the transfer beam pattern matrix is transformed into a new smaller matrix with  $10^\circ$  spatial resolution in both azimuth and elevation by averaging every azimuth step size of  $\theta = 10^\circ$  with  $\pm 5^\circ$  of the transfer beam pattern matrix. This is done in order to provide an even more accurate or realistic representation of the radiation pattern of the guitar by averaging out e.g. guitar movement uncertainties and variations in different play sections of ascending barre chords.

The new smaller transfer beam pattern matrix is normalized to the maximum RMS value of all frequency bands over all the turning table step recordings. The beam patterns can then be extracted from the normalized transfer beam pattern matrix and plotted in a 3D mesh as a balloon-style directivity plot for every single frequency band.

In Figure C.6 and Figure C.7, the guitar sound radiation pattern while the musician is sitting on a chair mounted on the turning table setup can be seen as the balloon-style directivity in a 3D view and in a top-view (XY plane) respectively.

---

<sup>1</sup>see <https://se.mathworks.com/help/audio/ref/octavefilterbank-system-object.html> for more info

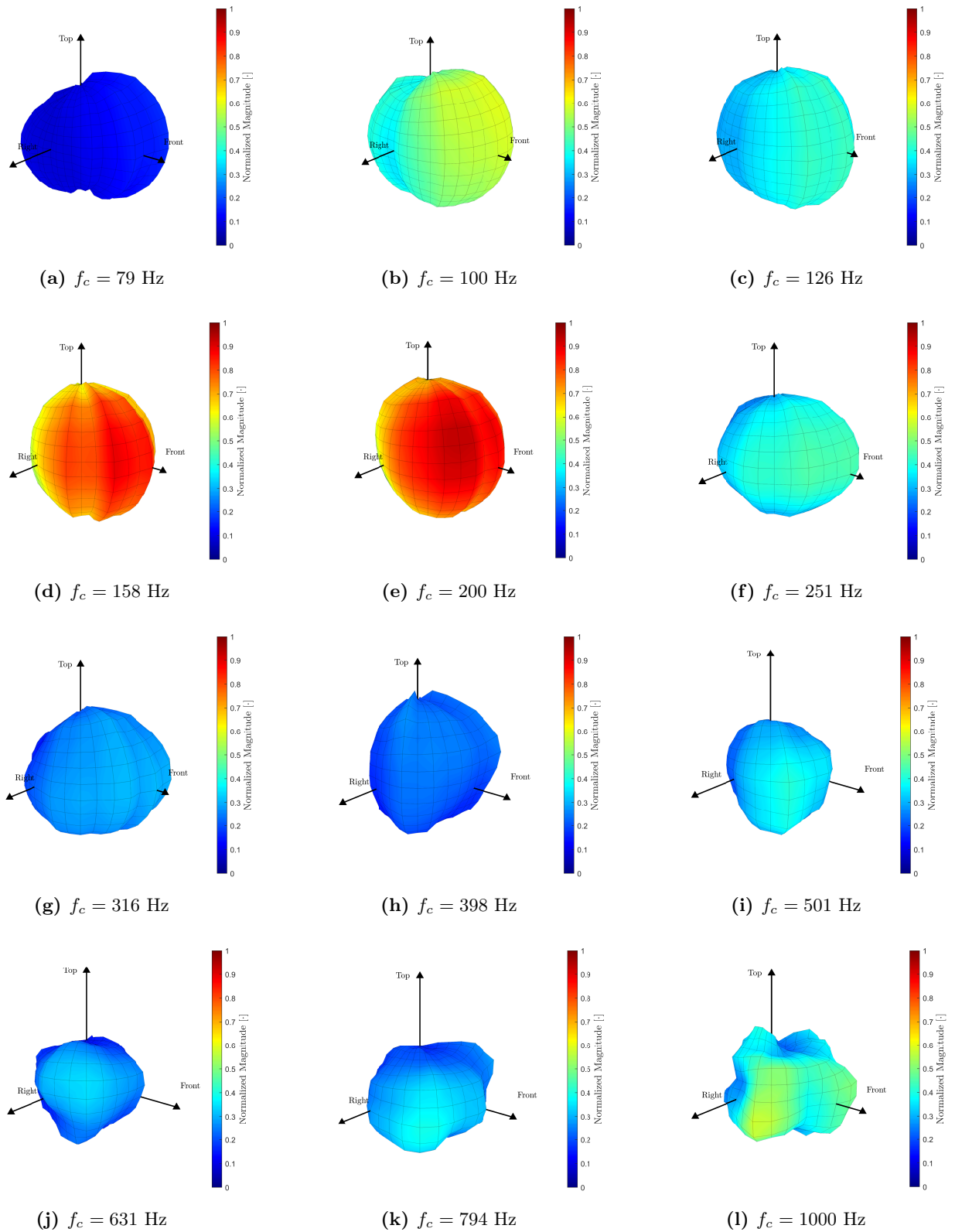


**Figure C.6:** 3D Balloon-style directivity plots (3D view) for the guitar radiation in the 1/3 octave bands with  $10^\circ$  spatial resolution ( $\theta = 10^\circ \pm 5^\circ$  average). The plots are normalized over the maximum magnitude for all 1/3 octave bands within 79 Hz to 10 kHz (Part 1)

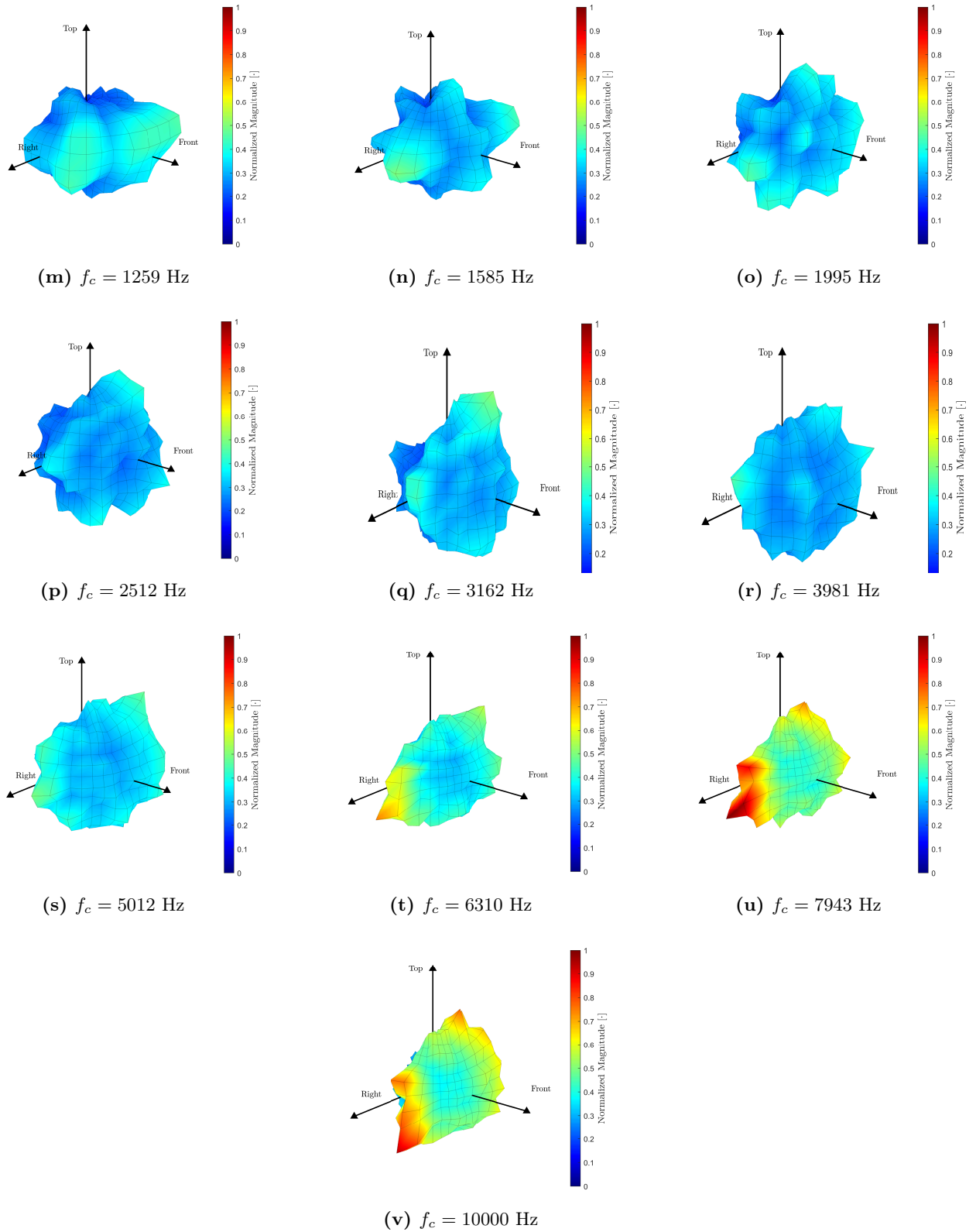


**Figure C.6:** 3D Balloon-style directivity plots (3D view) for the guitar radiation in the 1/3 octave bands with  $10^\circ$  spatial resolution ( $\theta = 10^\circ \pm 5^\circ$  average). The plots are normalized over the maximum magnitude for all 1/3 octave bands within 79 Hz to 10 kHz (Part 2)

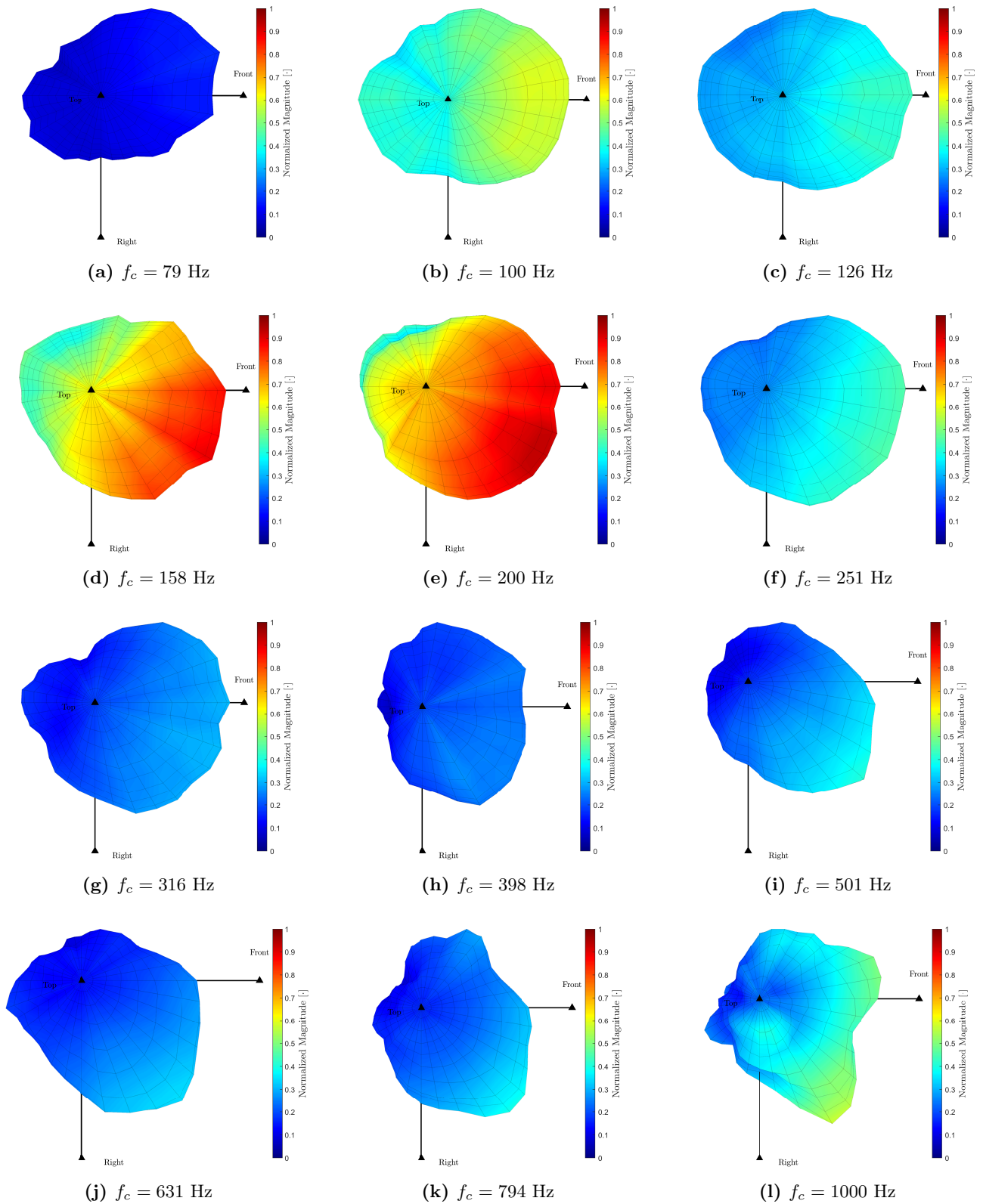


**Figure C.7:** 3D Balloon-style directivity plots (Top-view) for the guitar radiation in the 1/3 octave bands with  $10^\circ$  spatial resolution ( $\theta = 10^\circ \pm 5^\circ$  average). The plots are normalized over the maximum magnitude for all 1/3 octave bands within 79 Hz to 10 kHz (Part 1)

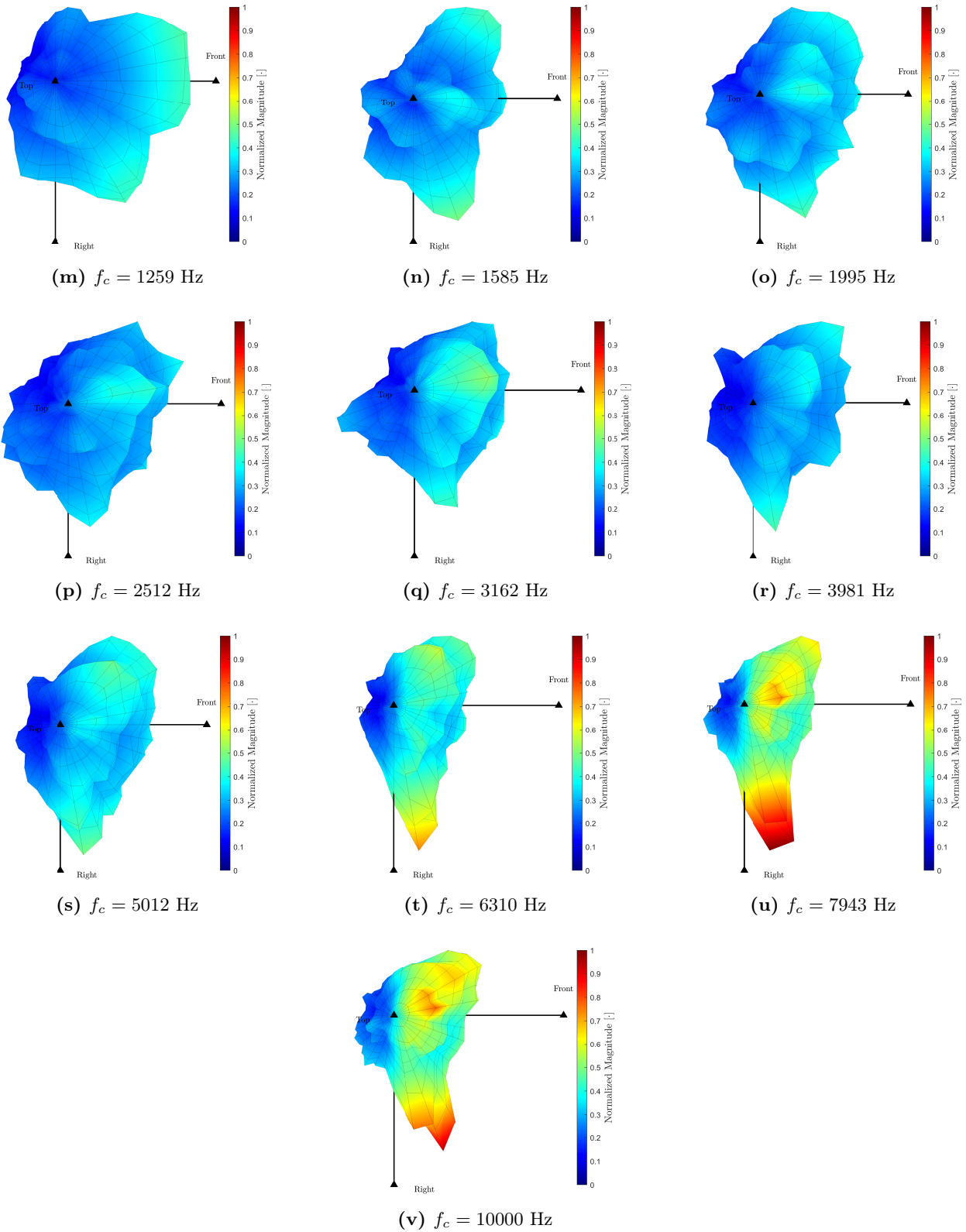


**Figure C.7:** 3D Balloon-style directivity plots (Top-view) for the guitar radiation in the 1/3 octave bands with  $10^\circ$  spatial resolution ( $\theta = 10^\circ \pm 5^\circ$  average). The plots are normalized over the maximum magnitude for all 1/3 octave bands within 79 Hz to 10 kHz (Part 2)

# Comparison of Optimization Methods with Simulations

# D

Several methods of finding the optimal speaker velocities for a given radiation pattern have been investigated in Section 5.3. In this appendix, a few simulations will be carried out to identify how they compare to each other with a real target function through simulations. This is done so that it is easier to see which methods are worth implementing on the actual loudspeaker system.

## D.1 Simulation Parameters

A 3D model of a sphere consisting of 5120 equilateral triangles of the same size is used as a model for the loudspeaker array.

The BEM matrices for this sphere, scaled to a radius of  $R = 0.2$  m, have been pre-computed for all 1/3 octave bands from 79 Hz to the upper limit for precise BEM-calculations where the edge lengths of each triangle are larger than 1/6 of the wavelength.

With a maximum edge length of  $l_{max} = 16.5$  mm, this upper limit corresponds to:

$$f_{lim} = \frac{1}{6} \cdot \frac{c}{l_{max}} \approx 3.46 \text{ kHz} \quad (\text{D.1})$$

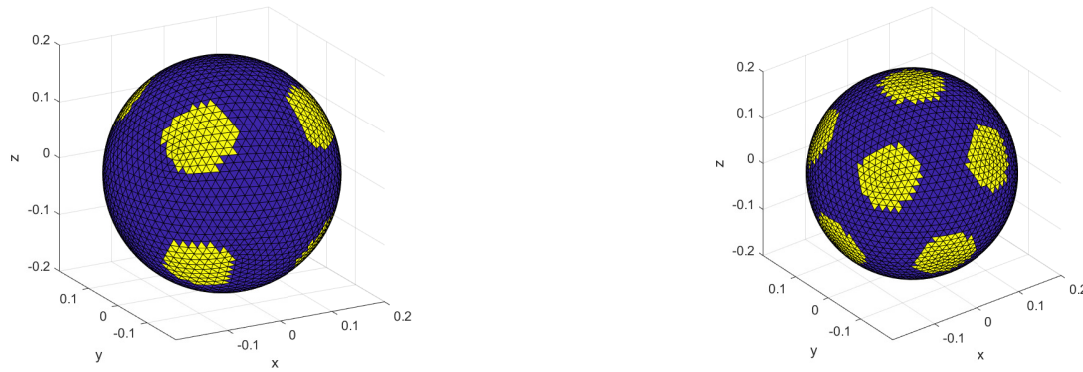
for  $c = 343$  m/s.

This means that the model can cover the 1/3 octave band center frequencies up to 3.16 kHz with good accuracy. In order to get a bit more of the frequency area of interest covered in the simulation the next center frequency at 3.98 kHz is included as well although the result must be taken with a bit of caution.

Speakers are placed on the sphere in two different configurations: one with 8 speaker directions given by the vectors  $(\pm 1, \pm 1, \pm 1)^T$  corresponding to the faces of an octahedron, and one with 12 speaker directions given by  $(\pm 1, \pm \Phi, 0)^T$ ,  $(0, \pm 1, \pm \Phi)^T$ ,  $(\pm \Phi, 0, \pm 1)^T$  where  $\Phi = \frac{1+\sqrt{5}}{2}$  is the golden ratio, corresponding to the faces of a dodecahedron.

A speaker size of 5" has been chosen, which corresponds to a speaker angle of  $18.27^\circ$  on the sphere.

The speaker placements on the models can be seen on Figure D.1.



(a) Model with 8 uniformly distributed speakers

(b) Model with 12 uniformly distributed speakers

**Figure D.1:** Illustration of the speaker models used in this simulation. The blue areas denote the area of the sphere not part of a piston, whereas the yellows denote the area of the sphere part of the pistons

Using these models, the optimal driver velocities are calculated using the methods described in Section 5.3 with both LS and MLS optimization and both with and without the spatial density weighting applied.

An error measure is calculated at each frequency for each method in order to get an objective sense of how the methods compare with each other. A weighted mean squared error across the field points is found as

$$WMSE = \frac{1}{M} \sum_{m=1}^M w_m (|p_{fp,m}| - |t_m|)^2 \quad (\text{D.2})$$

where  $M$  is the number of field points,  $w_m$  is the weighting for the  $m$ th field point,  $p_{fp,m}$  is the complex pressure at the  $m$ th field point and  $t_m$  is the target, defined as the 3D measurement of the guitar at the  $m$ th field point.

The weighting is used so that the error measure is not biased towards densely sampled areas of the acoustic field.

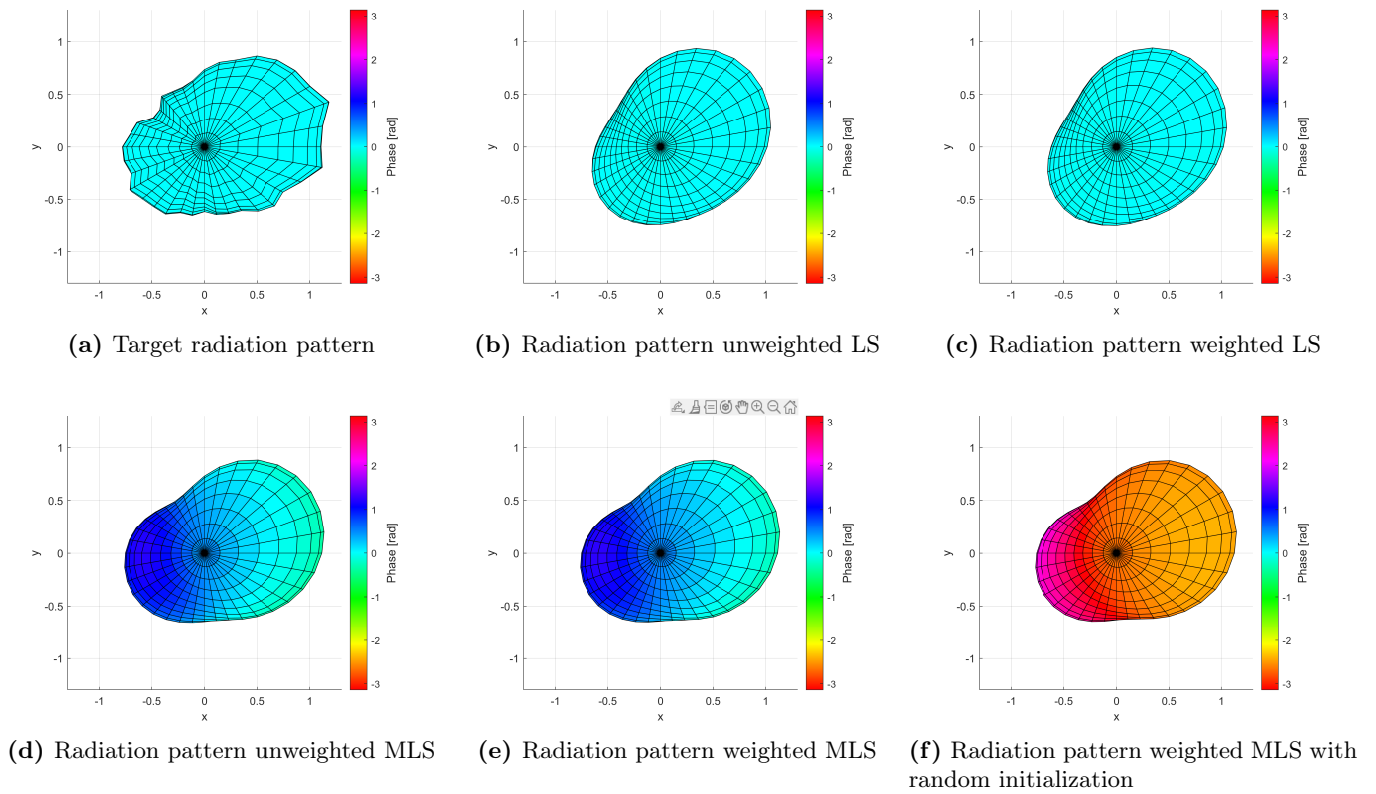
## D.2 Results

The resulting radiation patterns using the different optimization methods are shown in following figures. The simulations are plotted for both the weighted and unweighted LS and MLS and initialised with LS solution. Additionally a simulation using the MLS optimization with a random starting vector has been made to see how well the result converges.

The radiation patterns are plotted as balloon-style directivity plots (Top-view) with the length from the origin denoting its magnitude at each observation point and the color indicating the phase at each observation point..

### D.2.1 Results with 8 Speakers

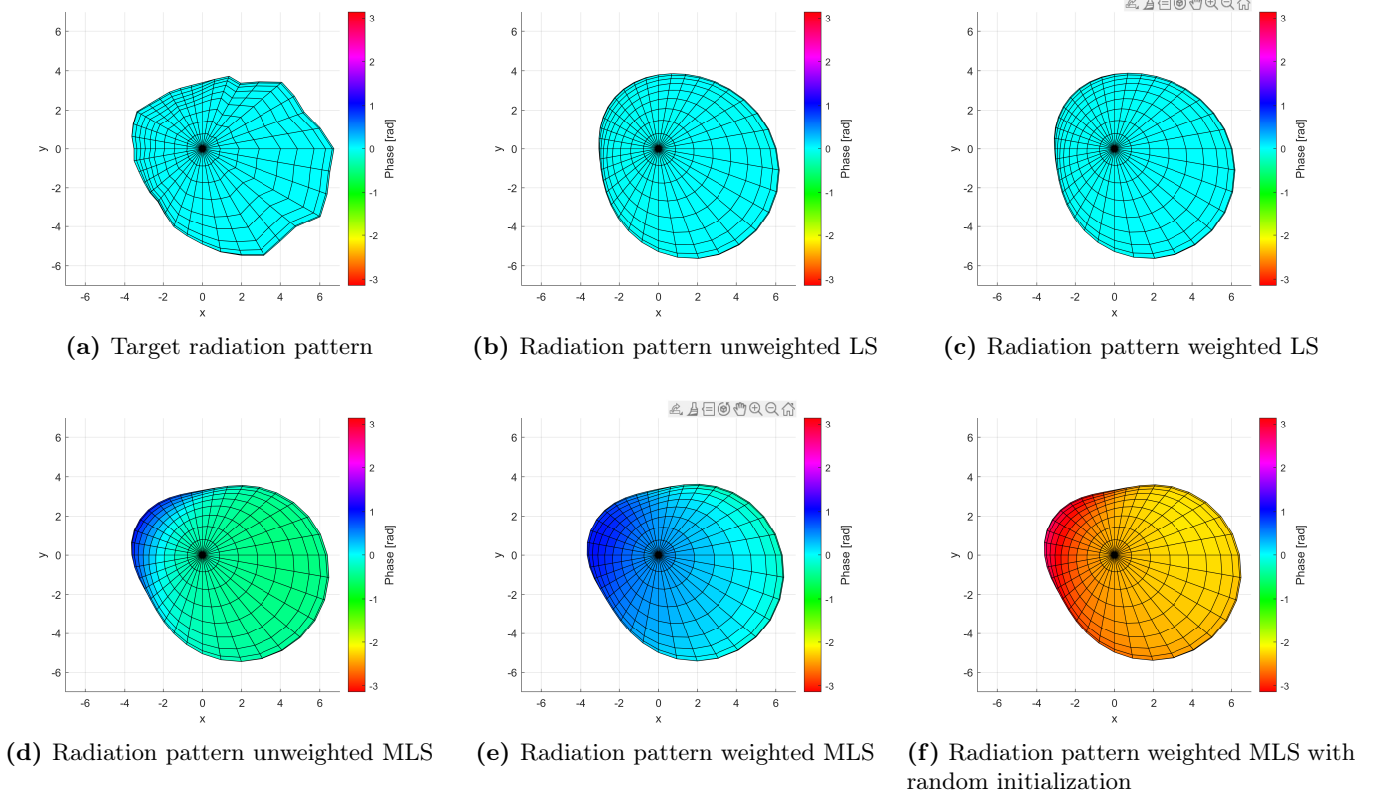
The resulting radiation patterns for few selected frequencies can be seen below.



**Figure D.2:** Radiation patterns at 79 Hz with 8 speaker units

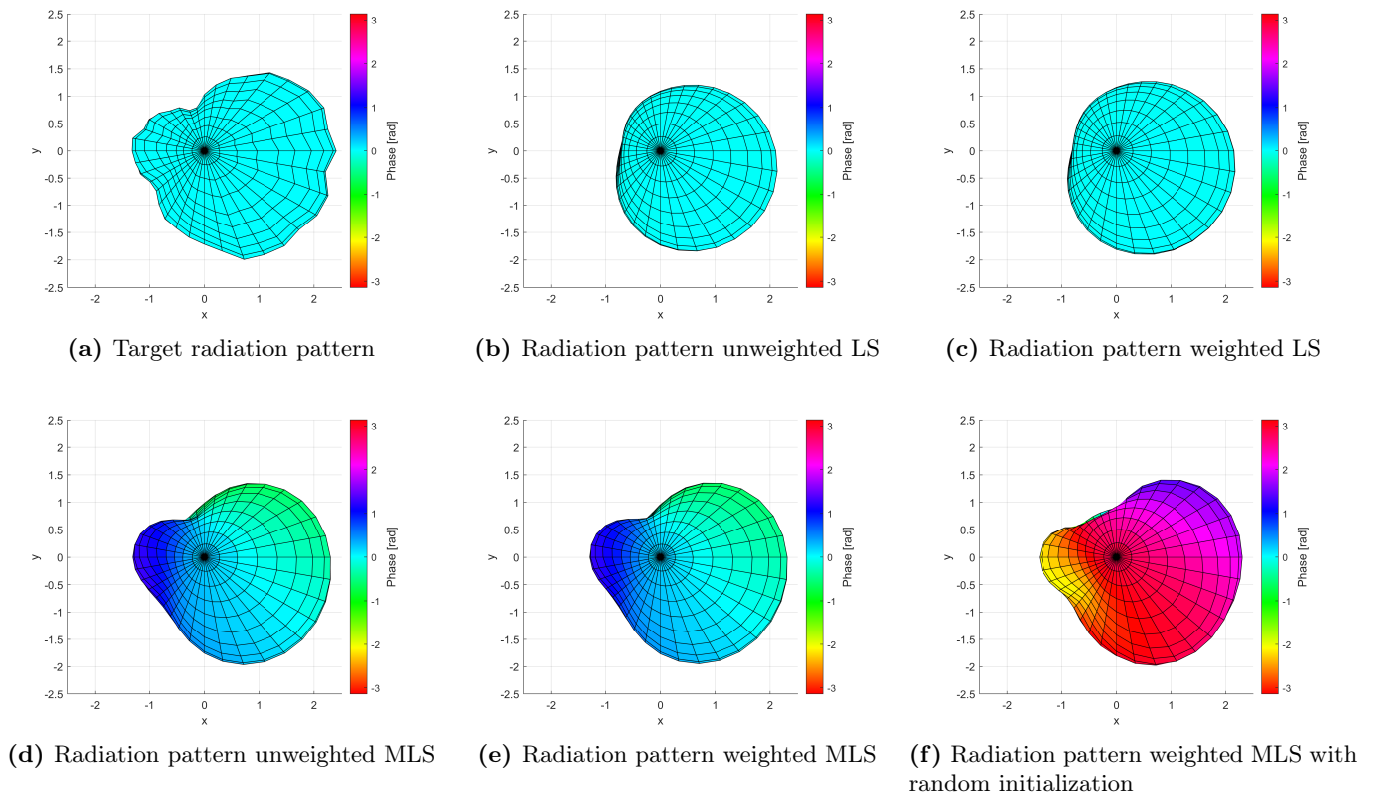
For 79 Hz both the weighted and the unweighted LS methods seem to find pretty much the same pattern. Both weighted MLS methods find a pretty good approximation to the desired pattern in the horizontal plane. However, it seems that to achieve this a phase shift between the front and back part is necessary, both with and without a random initialization.

It can also be seen that the MLS solution with the LS-solution as an initial guess finds a pretty good solution without having to change the phase too much over a short distance, keeping almost zero phase in the front part of the synthesized pattern.



**Figure D.3:** Radiation patterns at 158 Hz with 8 speaker units

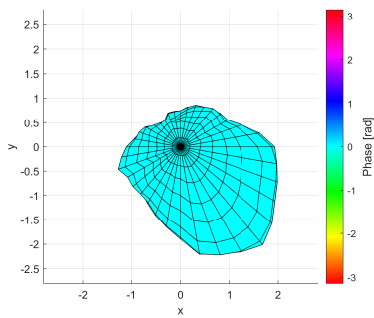
Again for 158 Hz, similar results can be seen, except now the unweighted MLS looks better than both LS solutions. It is hard to distinguish between the 3 MLS except that they show some differences in the phase. While the LS solutions are beaming the sound forwards and to the right similarly to the target, the overall shape of the target function is generally not preserved to a very high degree.



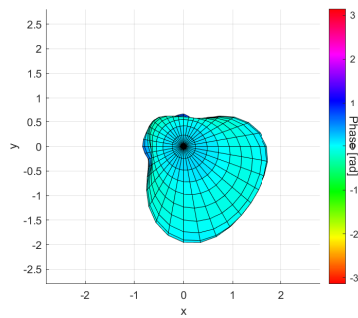
**Figure D.4:** Radiation patterns at 316 Hz with 8 speaker units

Figure D.4 shows some first interesting results. Here some differences between the LS and MLS solutions clearly appear from the plots, as well as in between the MLS with a random start and the ones without, suggesting that different local minimums can be hit depending on the starting point as was mentioned in [56].

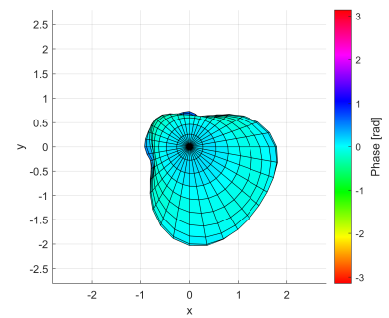
Again we see that some beaming of the sound field is done in the LS solutions, but it can be clearly seen that the LS-solutions struggle compared to the MLS solutions. As seen before the LS solutions are very successful in making sure that the synthesized pattern has the same phase as the target pattern, however not much importance can be placed on this since the phase of the target function does not necessarily have anything to do with the actual phase of the sound radiated from an acoustic guitar. It can additionally be seen that the MLS solutions achieve a pretty good approximation of the target function by allowing the phase of the synthesized pattern to vary slightly.



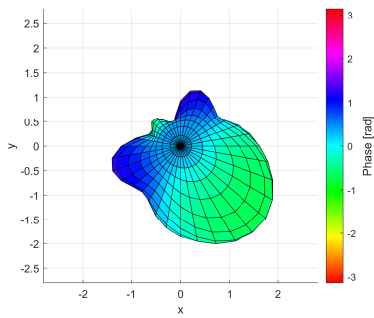
(a) Target radiation pattern



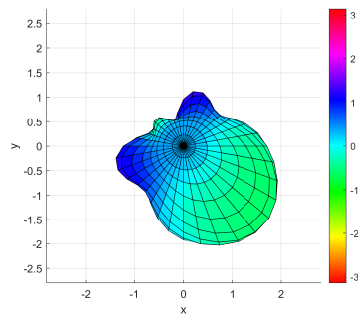
(b) Radiation pattern unweighted LS



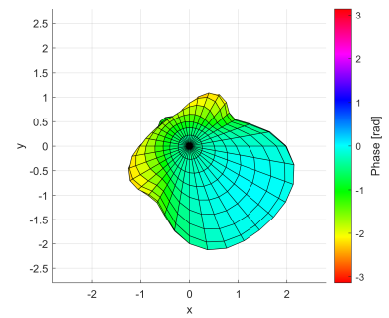
(c) Radiation pattern weighted LS



(d) Radiation pattern unweighted MLS



(e) Radiation pattern weighted MLS



(f) Radiation pattern weighted MLS with random initialization

**Figure D.5:** Radiation patterns at 631 Hz with 8 speaker units

In the plots of Figure D.5, the radiation patterns at 631 Hz are shown. The MLS-based methods still look to outperform the LS methods. At this point, even the LS solutions struggle to keep everything exactly in phase, whereas the MLS methods find solutions that vary in phase by a decent amount. It can also be seen that some sidelobes appear for the MLS methods, even though they seem to be less pronounced in the MLS solution with random initialization applied.

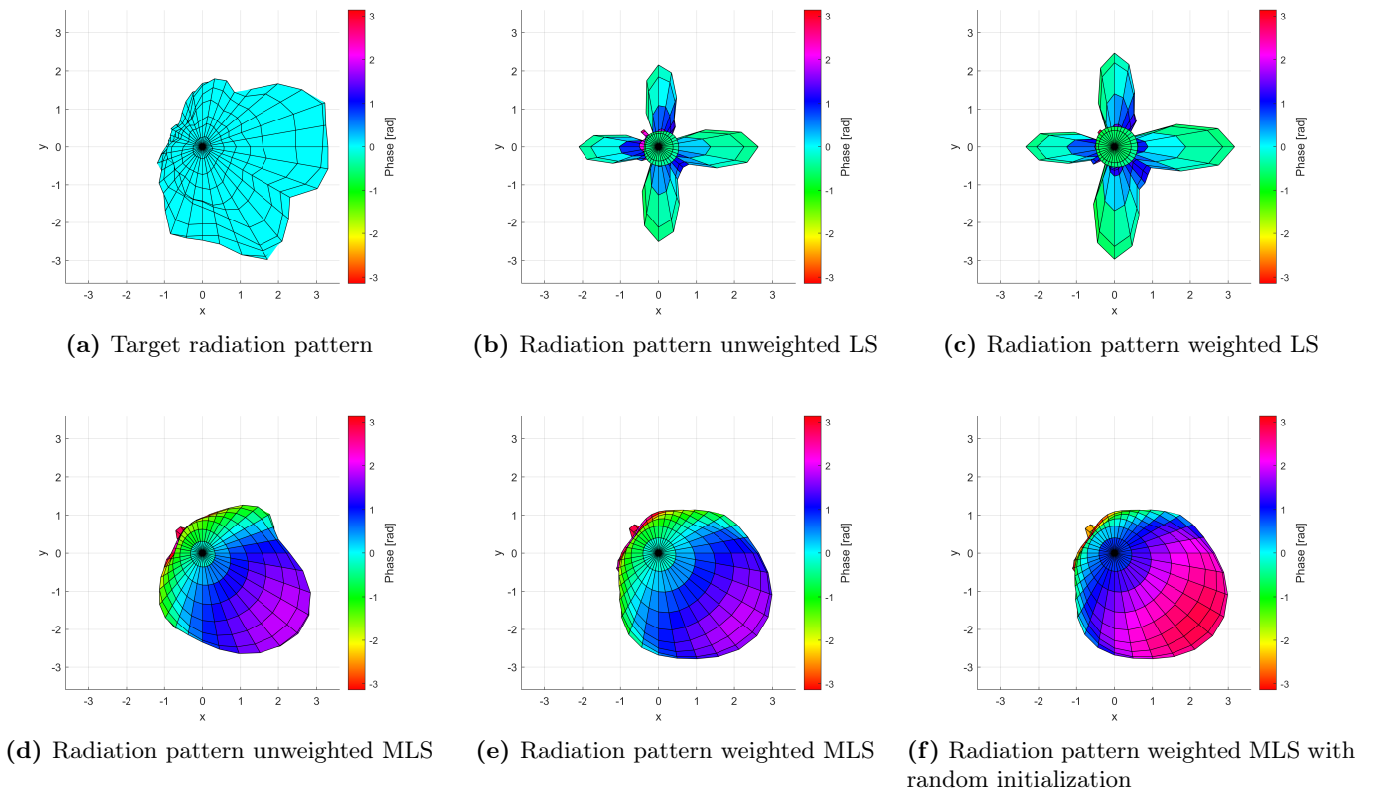
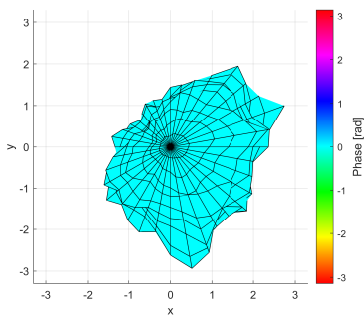


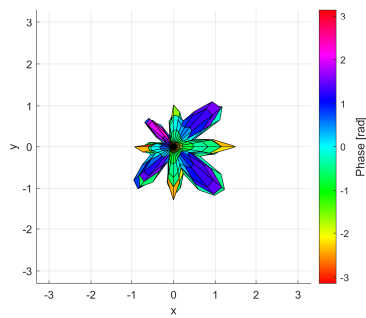
**Figure D.6:** Radiation patterns at 1259 Hz with 8 speaker units

The results in Figure D.6 show the limits of the LS solution with only 8 speakers as they do not hit the target at all. Instead, some very narrow beams are produced in the  $\pm x, \pm y, \pm z$  directions, which corresponds well to the midpoint between four of the speakers in this layout.

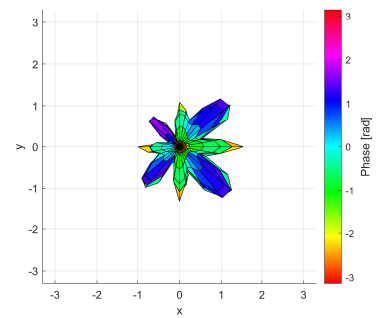
The MLS solutions this time seem to vary the pattern in some little details from weighted to unweighted version as well as from the weighted MLS with random initialization. However, MLS methods find a more "nice" looking pattern even though they still do not match the target pattern that well.



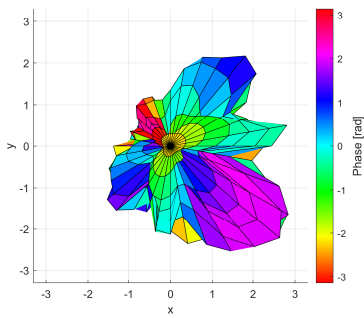
(a) Target radiation pattern



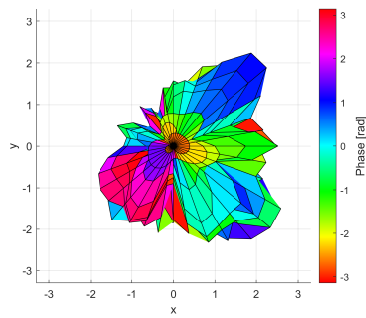
(b) Radiation pattern unweighted LS



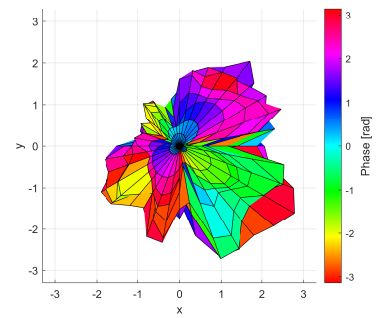
(c) Radiation pattern weighted LS



(d) Radiation pattern unweighted MLS



(e) Radiation pattern weighted MLS



(f) Radiation pattern weighted MLS with random initialization

**Figure D.7:** Radiation patterns at 2512 Hz with 8 speaker units

At 2512 Hz both methods continue to struggle to reproduce the target pattern. The LS-solutions seem to only be able to beam the sound out in the direction of the drivers. The MLS solutions still try to produce some pattern even if the phase varies a lot in all of them. Anyway, the patterns produced by all the three MLS methods do not seem to do much more than slightly beam the sound forward and to the sides, at least when looking from above. The radiation of the target does not seem to be properly recreated by any of the methods at these high frequencies.

The WMSE of all the different methods have been computed and is shown in Figure D.8.

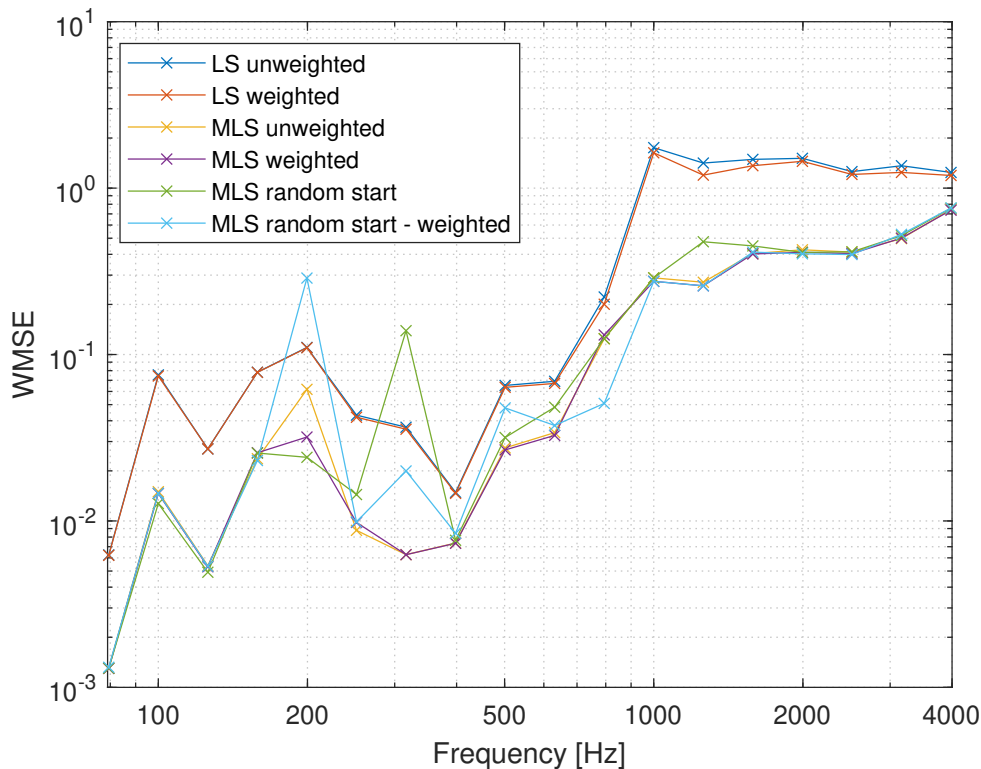


**Figure D.8:** Weighted Mean squared error of different methods with 8 speakers.

The calculated errors seem to agree with what we could intuit from the illustrations of the radiation patterns. First of all, it can be seen that the error increases massively as the frequency increases, especially in the frequency range between around 600-1000 Hz.

Clearly, the MLS-solutions with the chosen starting points outperform the LS-solutions. With a random start, it seems to follow the other MLS solutions, but at some specific frequencies, it gets even significantly worse like at 158 and 199 Hz. However, at 794 Hz the weighted MLS with random start manages to find a solution that is significantly better than all the others, so it seems that sometimes a better minimum can be found around a different starting point.

As was also seen before, there does not seem to be a big difference whether or not you apply the weighting function described in Section 5.3.4 except for at 79 and 200 Hz where it seems to provide a better result.

### D.2.2 Results with 12 Speakers

It is now possible to similarly look at the resulting radiation patterns using 12 speakers. For the purpose of not having too much repetition, a smaller number of plots will be shown for this layout.

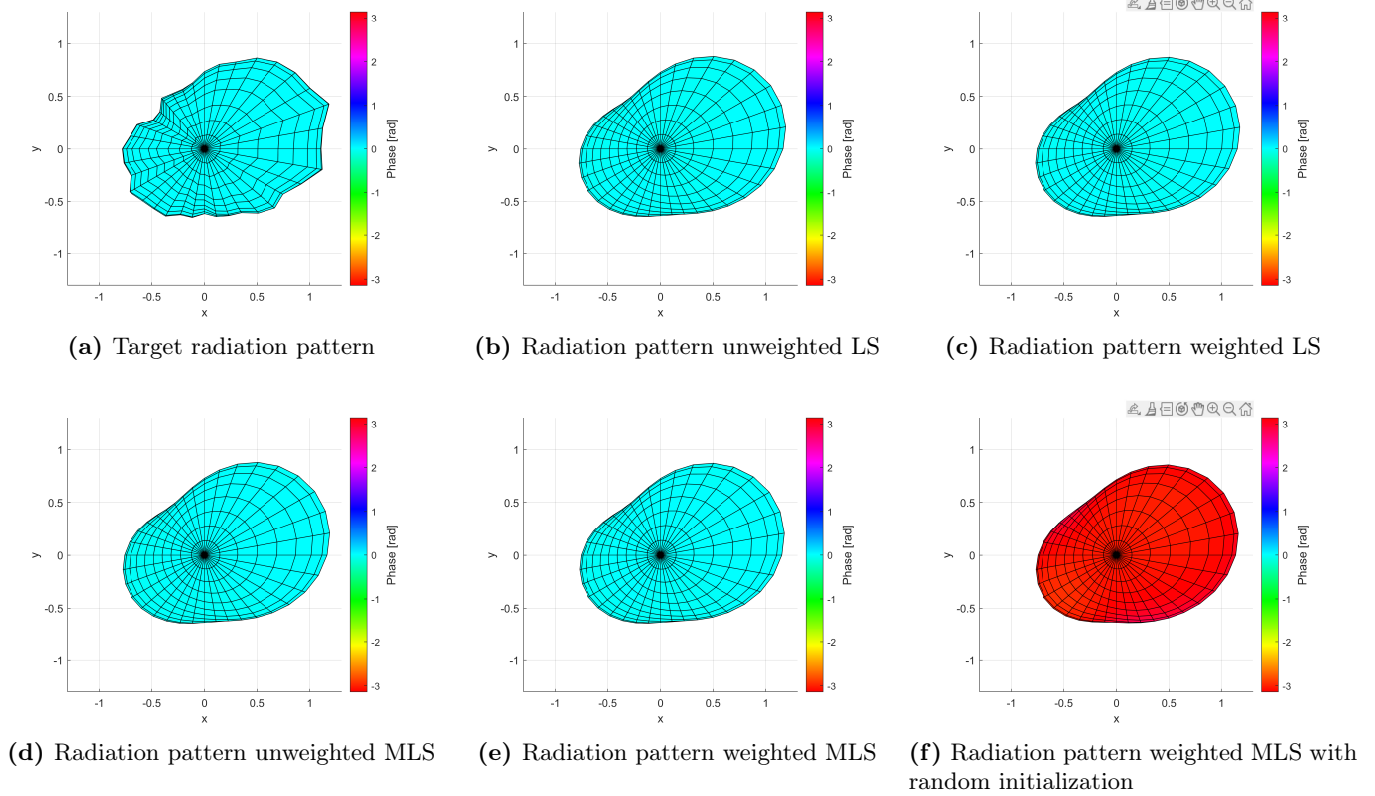
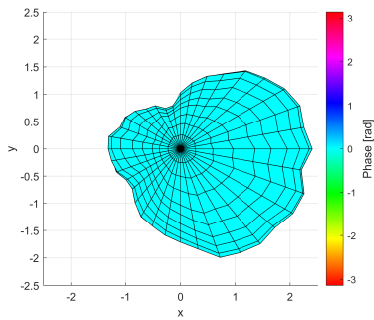
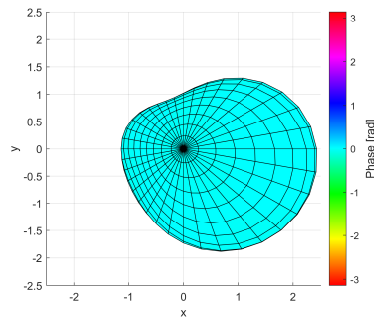


**Figure D.9:** Radiation patterns at 79 Hz with 12 speakers.

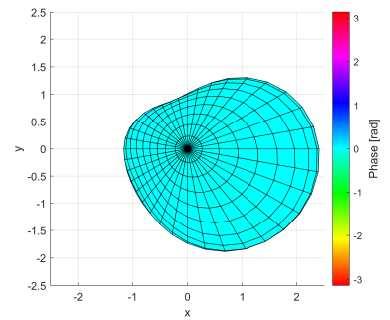
On Figure D.9 the radiation pattern at the lowest simulated frequency with 12 speakers can be seen. In contrast to Figure D.2 all methods pretty much find the same radiation pattern, at least when looking from above. Still, some of the fine details of the target pattern are missing, but these details are likely due to measurement uncertainty anyway since it is doubtful that the guitar varies that much over just 10 degrees at this low of a frequency.



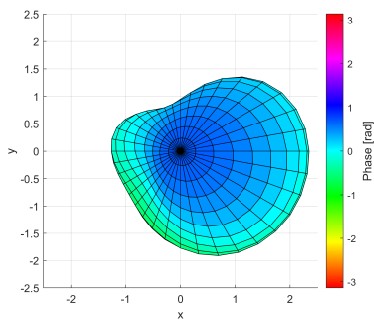
(a) Target radiation pattern



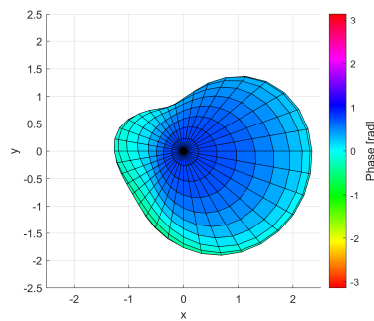
(b) Radiation pattern unweighted LS



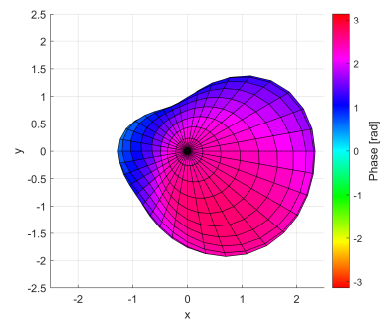
(c) Radiation pattern weighted LS



(d) Radiation pattern unweighted MLS



(e) Radiation pattern weighted MLS



(f) Radiation pattern weighted MLS with random initialization

**Figure D.10:** Radiation patterns at 316 Hz with 12 speakers

Going a bit higher up in frequency shows a clear improvement of the LS solution on Figure D.10 compared to the layout of Figure D.4 with 8 speakers. For MLS solutions it is hard to tell if the solution using 12 speakers is actually better than the ones with 8 on Figure D.4. This could suggest that it is not only the number of speakers that determine how well the radiation pattern is reproduced but perhaps also other factors such as the placement of the speakers in relation to the target pattern.

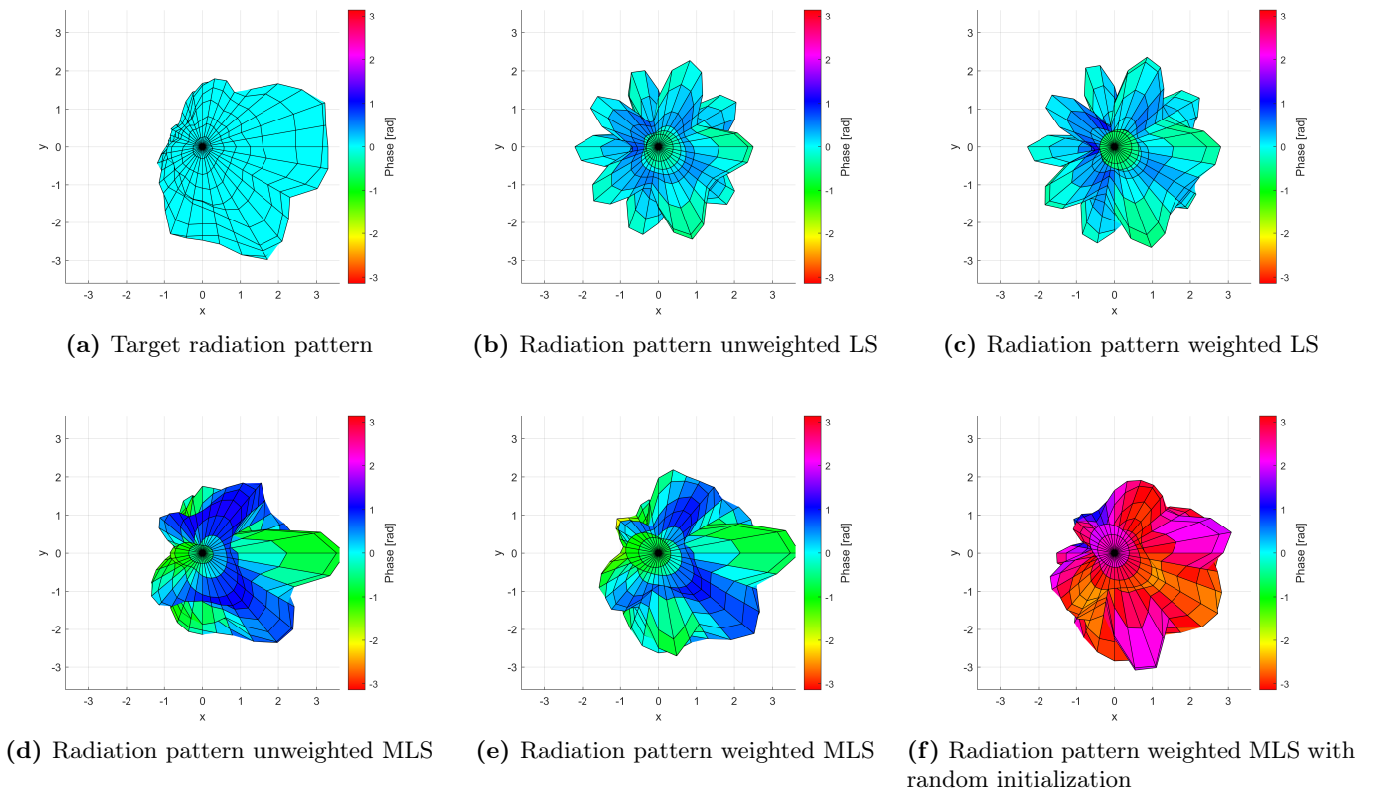


**Figure D.11:** Radiation patterns at 1259 Hz with 12 speakers

At high frequencies, the LS solutions still seem to have some problems, as it seems like the only improvement comes from having more speakers and therefore more directions towards which the sound can be beamed directly.

The MLS solutions also struggle a bit but look immediately somewhat better than the same results with 8 speakers.

Once again the WMSE is following shown in Figure D.12.

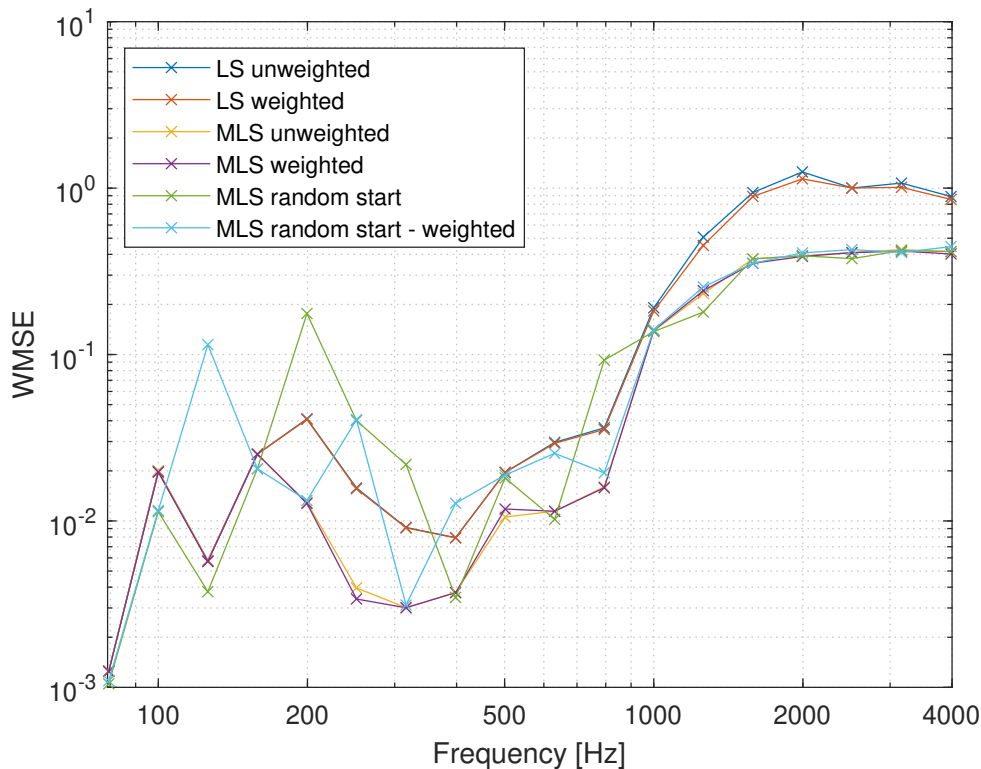


**Figure D.12:** Weighted Mean squared error of different methods with 12 speakers.

At a first glance of Figure D.12, it looks like the error increases with the frequency. This time decent results are found up to around 800 Hz whereafter the error increases by an order of magnitude for all methods.

Like before the MLS-based methods seem to generally outperform the LS-based methods at least above 158 Hz.

Using a random start again seems to find a similar result for the most part, but there are still a few frequencies where it finds a much worse result.

### D.3 Discussion

The results from these simulations clearly show that the MLS optimization finds a better approximation of the target magnitude. It also seems to allow the array to produce somewhat usable radiation patterns to a higher frequency than when using LS-based methods.

While it was known that the MLS methods can produce radiation patterns with a different phase than the target function, it was also shown that the MLS solutions do not have particularly "harsh" relative phases in the synthesized radiation pattern until the optimization begins to struggle in the high frequencies.

# Effect of the Number of Speakers on Radiation Synthesis Performance



It is common knowledge that a greater number of speakers will lead to a better synthesis of a given radiation pattern. However, it is not known how many speakers are necessary for recreating the radiation pattern of an acoustic guitar, or where the speakers should be placed.

In this appendix, Monte Carlo simulations of different speaker layouts with the same number of speakers will be described. These simulations will be done for multiple numbers of speakers so to get a statistical idea of the effect of the number of speakers.

Additionally, when applicable, the results will be compared to the results that can be obtained with a perfectly uniform distribution of loudspeakers, e.g. when the loudspeaker locations correspond to the face-centers of platonic solids.

## E.1 Simulation Parameters

The model of a spherical enclosure used in Appendix D is also used in this simulation.

Random piston directions can be found by picking a point given by  $(\theta, h)$  in cylindrical coordinates on the unit cylinder and projecting it down to the unit sphere as

$$\begin{pmatrix} x \\ y \\ z \end{pmatrix} = \begin{pmatrix} \sqrt{1-h^2} \cos(\theta) \\ \sqrt{1-h^2} \sin(\theta) \\ h \end{pmatrix} \quad (\text{E.1})$$

If  $\theta, h$  are picked from a uniform random distribution between  $[0, 2\pi)$  and  $[-1, 1]$  respectively, the resulting directions will be uniformly distributed on the sphere<sup>1</sup>

The pistons are given a radius of  $14.6^\circ$  which corresponds to 4" drivers on a sphere with a radius of 0.2 m, which should be small enough to allow a good number of speakers on the sphere.

For each realization, a piston is placed on a random point on the sphere one at a time. After each placement, a check is performed to see if the new piston is close to overlapping with a previous piston and if so the newer piston is discarded. This process is repeated until the desired number of pistons has been placed.

After a random piston layout has been selected, the optimal velocities are found using the weighted MLS-optimization method from Section 5.3.

For each realization the resulting radiation pattern and its WMSE, as described in Appendix D, is computed and saved.

---

<sup>1</sup><https://mathworld.wolfram.com/SpherePointPicking.html>

To compare the results with the strictly uniform distributions of speakers, often used in previous studies[4, 40, 23], these have also been simulated at the amounts where speakers can be placed on the faces of platonic solids, i.e. 6 at the faces cube, 8 with an octahedron, 12 with a dodecahedron and 20 with an icosahedron.

This has both been done by placing the speakers at the normal directions to the faces found with table values for these directions, e.g.  $[\pm 1, \pm 1, \pm 1]^T$  for the octahedron, but also in such a way that one of the pistons is pointing directly to the front i.e.  $[1, 0, 0]^T$ .

This rotated layout is found by finding the rotation matrix to  $[1, 0, 0]^T$  using Rodriguez rotation formula <sup>2</sup> and applying it to all piston directions.

## E.2 Results

In this section simulated results and error statistics for multiple numbers of loudspeakers are presented to get an overview of the impact on the number of speakers at different frequencies. The comparison is made by looking at two different kinds of plots.

The first kind shows the *WMSE*, plotted on a logarithmic scale on the y-axis, for the diverse numbers of speakers, which are plotted on the x-axis. The charts are obtained from 50 random configurations for each number of speakers plus one platonic solid distribution and one platonic solid distribution rotated so to have one piston on the front of the array. In the plots are also reported some outlier results, marked as red crosses.

The second kind reports the lowest error radiation pattern for the different number of speakers in balloon-style directivity plots. Here the analysis is mostly a visual comparison of the diverse results with the target function (the radiation pattern of the acoustic guitar).

Some conclusions can be achieved by analysing the plots for the different frequencies, from Section E.2.1 to Section E.2.5.

Increasing the number of speakers always improves the performance by reducing the *WMSE* i.e. the difference from the target function. In addition to that, it also seems like going up in frequencies increases the impact of having different numbers of speakers. Indeed, by both looking at the *WMSE* and by visual interpretation of the radiation patterns, it appears like having more speakers affects the results more at higher frequencies than it does at low-mid, which comes in agreement with many considerations made throughout the project regarding the directivity of the speaker units.

Another interesting thing to notice in the plots is the placement platonic solid distribution and platonic solid distribution rotated, marked respectively as the green and blue dots in the Figure E.1, E.3, E.5, E.7, E.9. It seems like the completely uniform distribution on the faces of a platonic solid does not necessarily provide better results. Although they often lead to an above-average result, the green and blue dots are never found to be below the minimum error for all the frequencies. This could mean that other configurations, perhaps at 20 speakers could work better than the platonic solid distribution.

---

<sup>2</sup>[https://handwiki.org/wiki/Rodrigues%27\\_rotation\\_formula](https://handwiki.org/wiki/Rodrigues%27_rotation_formula)

E.2.1 Results for 100 Hz

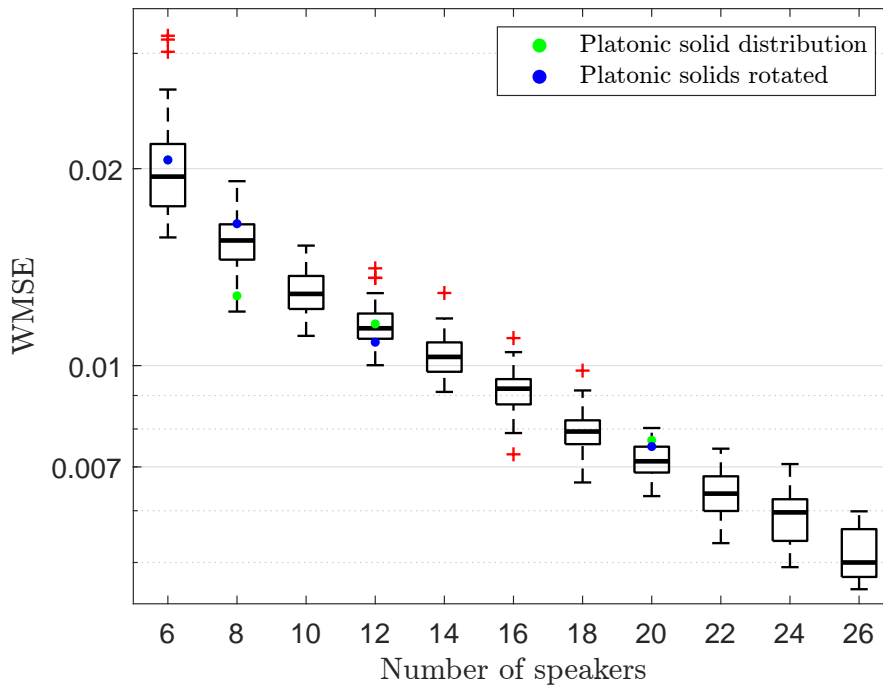


Figure E.1: Box plot to illustrate the error statistics for multiple number of speaker at 100Hz

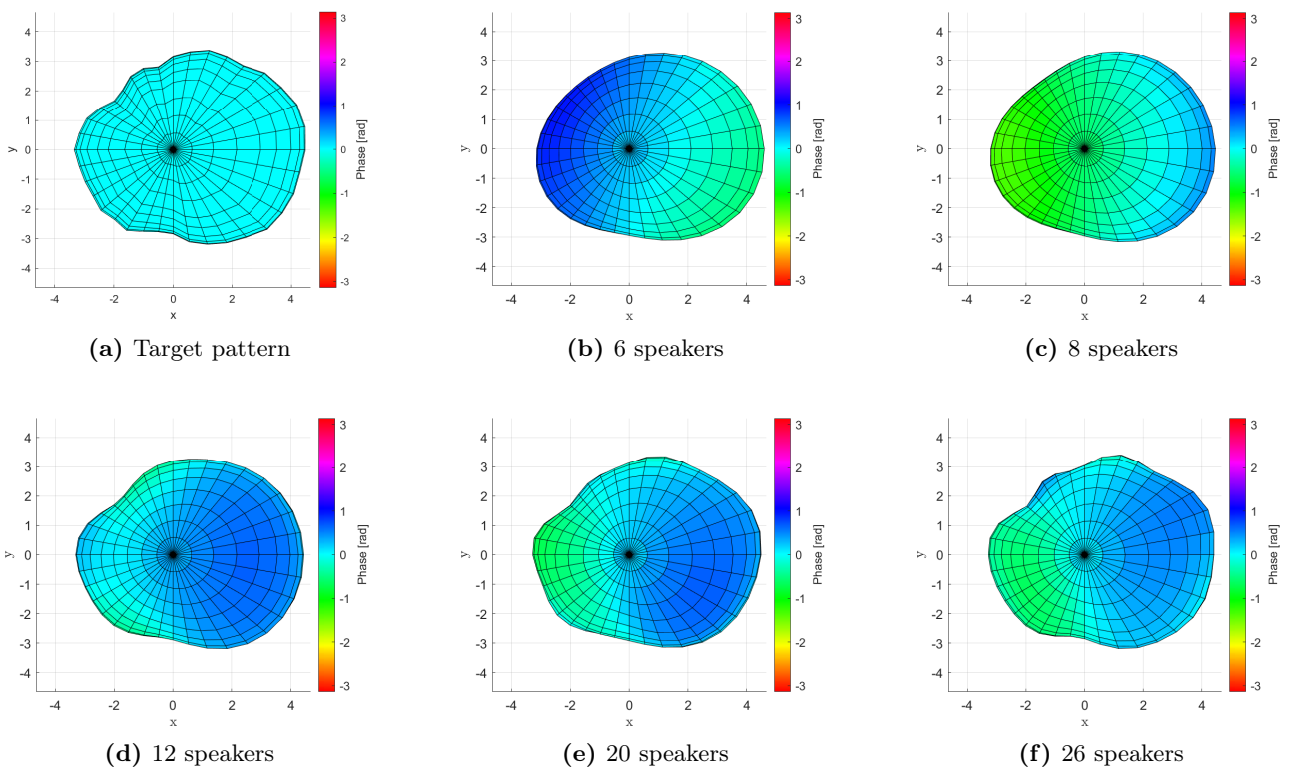


Figure E.2: Balloon-style directivity plot (topview) of the lowest error radiation pattern for different number of speakers for 100 Hz

E.2.2 Results for 200 Hz

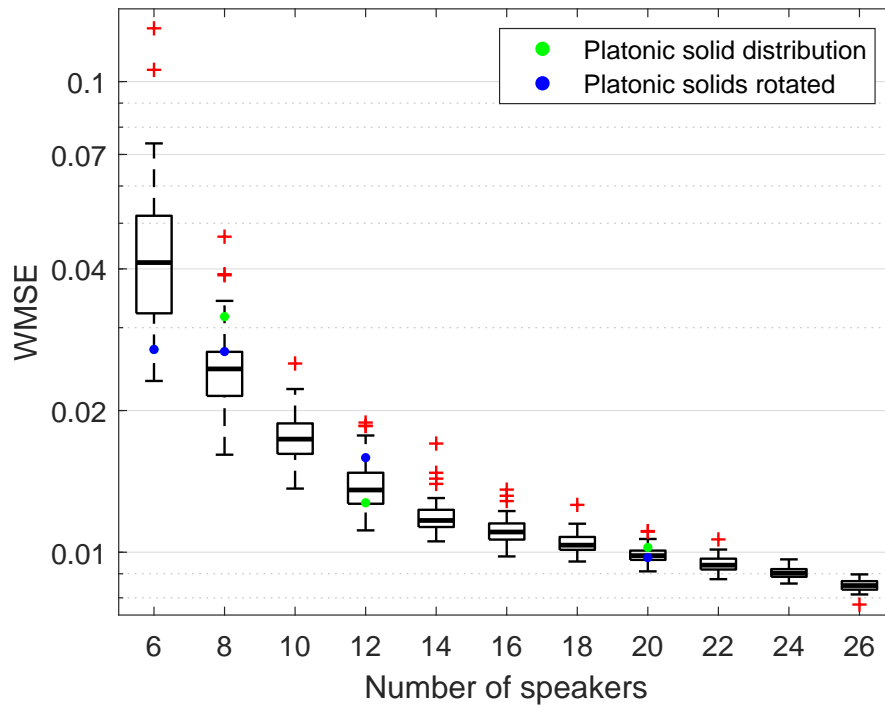


Figure E.3: Box plot to illustrate the error statistics for multiple number of speaker at 200Hz

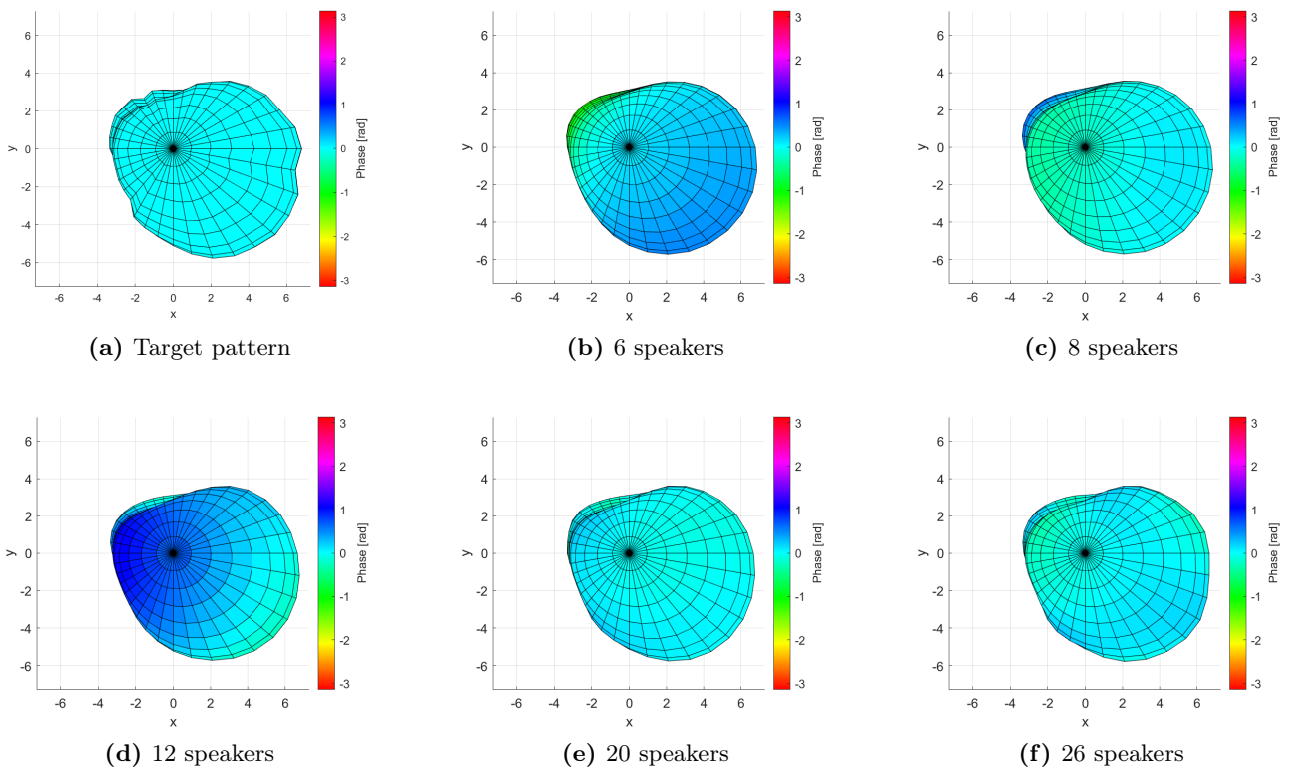


Figure E.4: Balloon-style directivity plot (topview) of lowest error radiation pattern for different number of speakers for 200 Hz

E.2.3 Results for 500 Hz

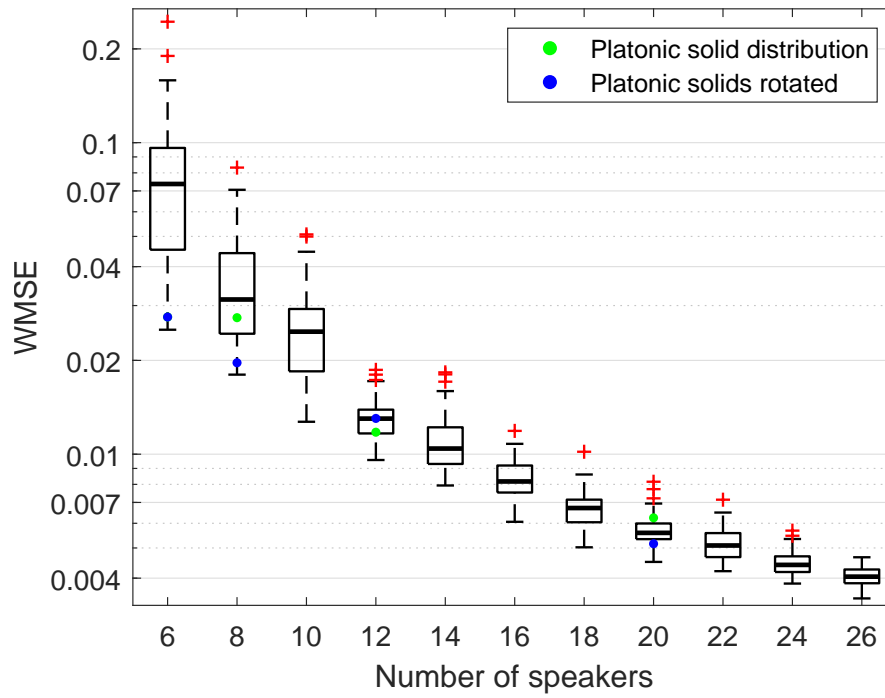


Figure E.5: Box plot to illustrate the error statistics for multiple number of speaker at 500 Hz

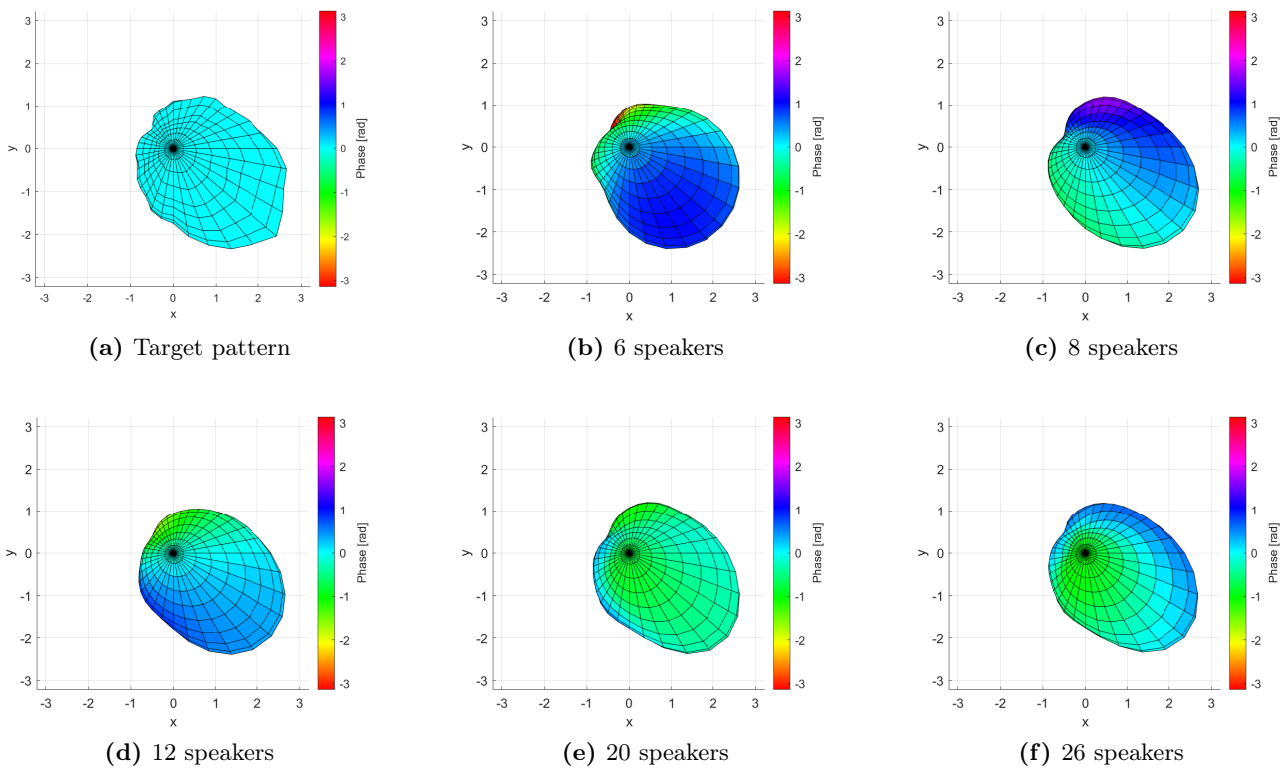


Figure E.6: Balloon-style directivity plot (topview) of lowest error radiation pattern for different number of speakers for 500 Hz

E.2.4 Results for 1000 Hz

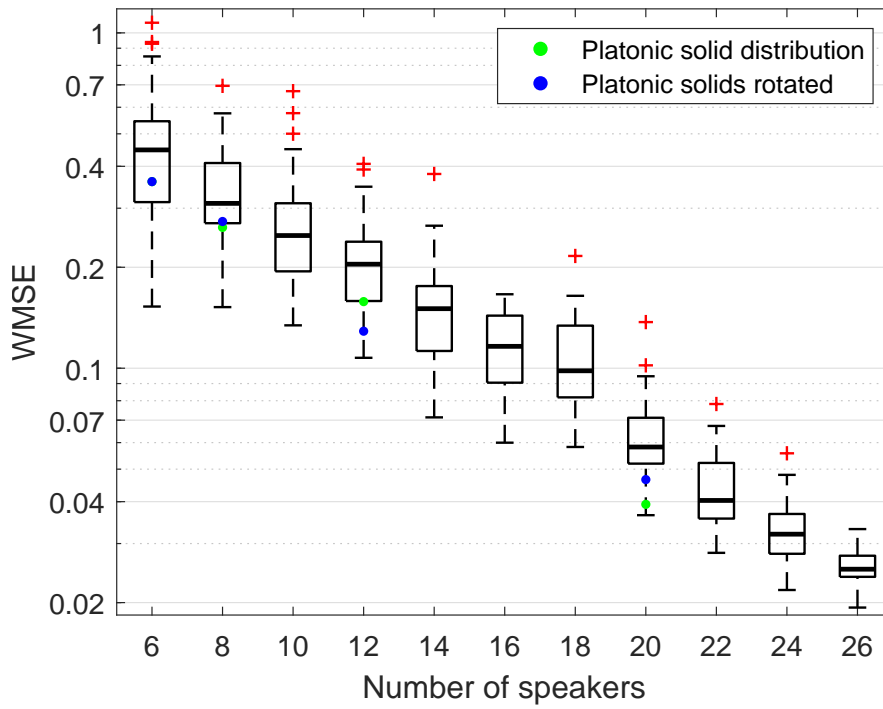


Figure E.7: Box plot to illustrate the error statistics for multiple number of speaker at 1000Hz

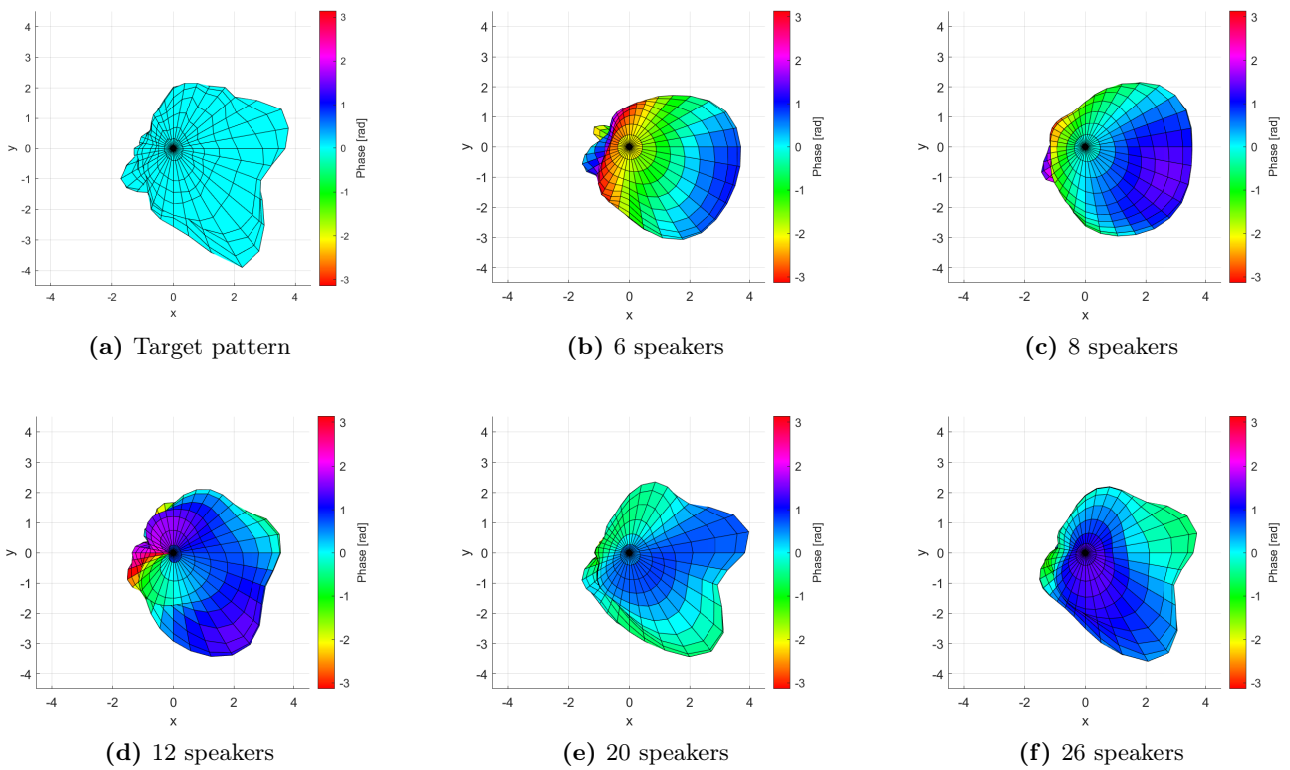


Figure E.8: Balloon-style directivity plot (topview) of lowest error radiation pattern for different number of speakers for 1000Hz

E.2.5 Results for 2000 Hz

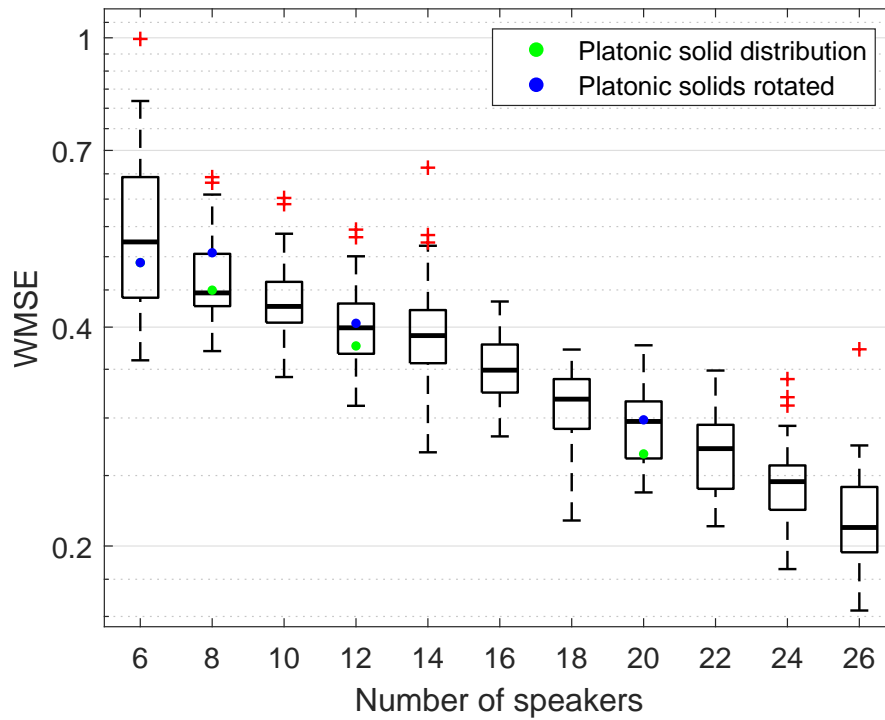


Figure E.9: Box plot to illustrate the error statistics for multiple number of speaker at 2000Hz

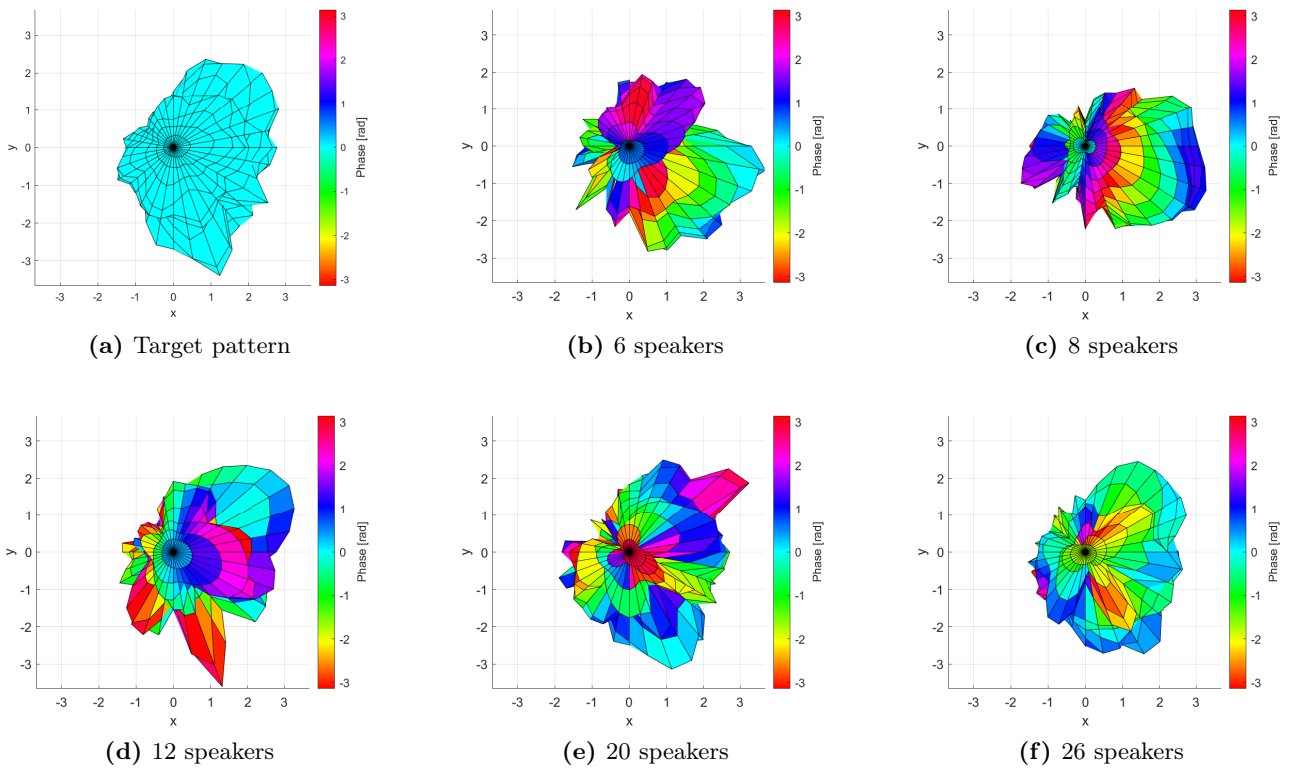


Figure E.10: Balloon-style directivity plot (topview) of lowest error radiation pattern for different number of speakers for 2000Hz

### E.3 Discussion

After having analyzed the results, it becomes clear that a higher number of speakers results in a better performance of the array, lowering the *WMSE* from the target function, especially at high frequencies.

However, it is still to be defined the criteria to choose the best configuration for a specific number of speakers. The first thought that comes to mind is to obviously take the speaker configuration that shows to commit the least error. As a matter of fact, this strategy cannot work effectively as a configuration that results as the best at one frequency, does not result to be the best at the other frequencies.

A visual example of this concept can be found in Figure E.11. Here three different frequencies are analyzed, and for each of them, the distribution of speaker with the least error from the target function is plotted, together with the respective target. The three configurations appear to be pretty different from each other, confirming what was just discussed.

Thus, the best distribution of speaker units could be the one that overall shows the least error for all the frequencies.

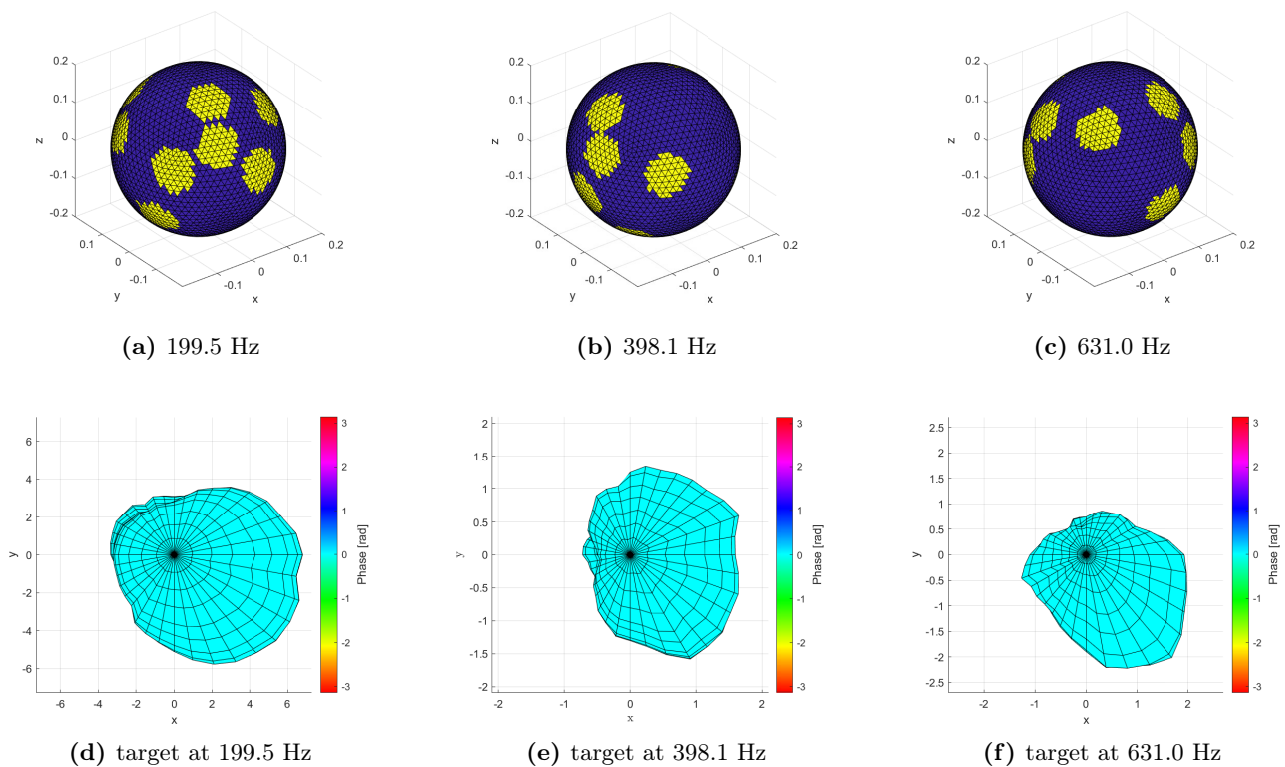
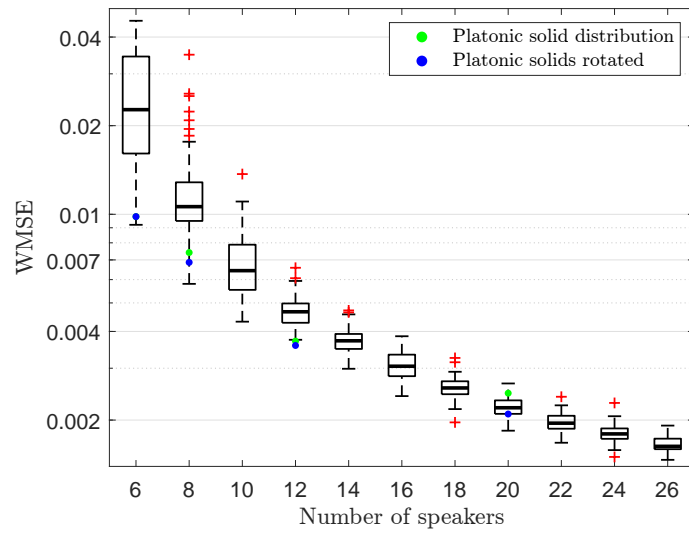


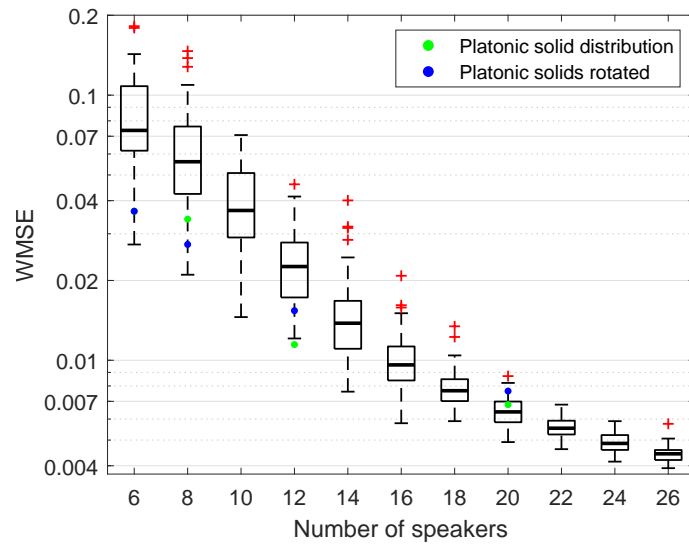
**Figure E.11:** Best found speaker placements and their corresponding target patterns

Some additional *WMSE* plots are instead shown in Figure E.12. Again it can be noticed how the platonic solid distribution, i.e a perfectly uniform placement, does not always lead to the best results, or if it does for some specific number of speakers, it cannot be the best placement at all the frequencies.

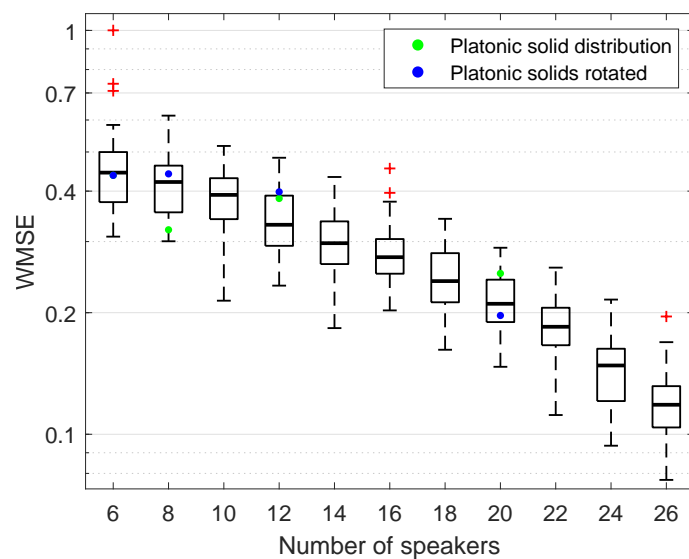
As an example by looking at Figure E.12, the platonic configuration for 12 speaker results as the minimum *WMSE* for 398.1 Hz, as well as for the 631 Hz, but it does not for 1584.9 Hz, where instead seems to commit even more error than other random distributions.



(a) 398.1 Hz



(b) 631.0 Hz



(c) 1584.9 Hz

**Figure E.12:** Additional box plots, to illustrate the error statistics for multiple number of speaker at three different frequencies

# Simulation of the Effect of the Shape of the Enclosure

# F

Another parameter that is worth to be investigated for the aim of this research is the influence that the shape of the array has on the final results, i.e. in trying to recreate the target function.

Thus, in this appendix, a comparison between the sphere and different enclosure shapes is presented so to get an idea of the importance of this aspect in the design of the loudspeaker array prototype.

The simulated shapes can be seen in Figure F.1.

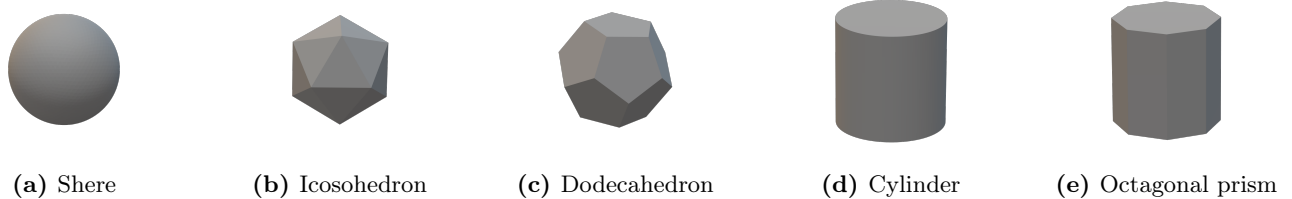


**Figure F.1:** 3D shapes used as an enclosure

## F.1 Simulation Parameters

For all the different shapes investigated, the radiation patterns for each 1/3 octave band were synthesized using the MLS-method as described in Section 5.3.3, using a  $\mathbf{H}$  matrix computed via BEM-simulations.

The convergence criteria  $\epsilon$  was set to  $10^{-4}$  in all cases.

In the simulations, the  $WMSE$  is used as the main term of comparison in between the sphere, which is always kept as a reference shape, and the different interesting shapes that are taken into account.

The simulations are done at all 1/3 octave band center frequencies between 79 Hz and 3.16 kHz, in order to show the differences across frequencies as well.

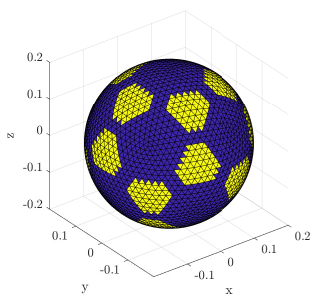
Like in Appendix E, the pistons are given a radius of 4". When possible the direction dependant aperture function is given by Equation 5.19. However, in the case of the octagonal prism and the cylinder, this can not be done, and therefore all simulations with this shape use the alternative aperture function from Equation 5.22.

## F.2 Results

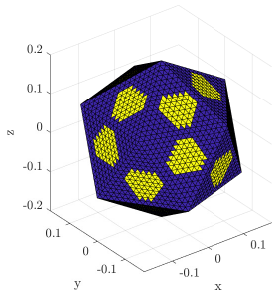
In the following sections, the impact of the shape of the enclosure is analyzed for the same number of speaker units, with approximately the same placements on the array.

### F.2.1 Icosahedron

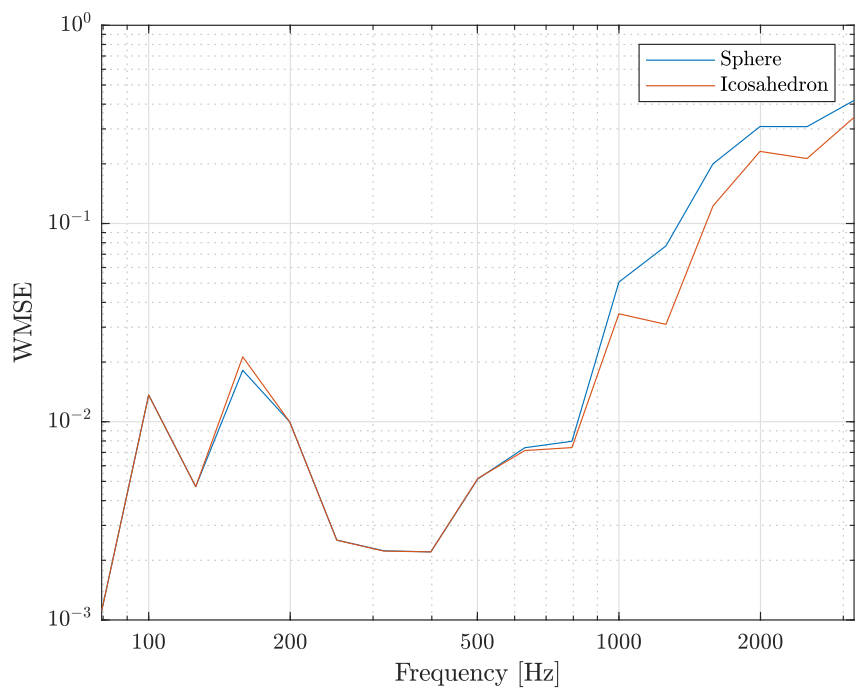
The first shape investigated is the icosahedron, a platonic solid with 20 driver units on its 20 faces, Section F.2.1. From the plots of Figure F.2, it is easy to get an idea of the behavior of the two enclosures, and the difference between them. At low frequencies, until around 600 Hz it seems like the icosahedron almost shows the same exact *WMSE* of the sphere, while it starts to deviate a bit the more growing up in frequency. However, overall the icosahedron seems to perform even better than the sphere, especially at high frequencies.



(a) Sphere with 20 speakers



(b) Icosahedron with 20 speakers

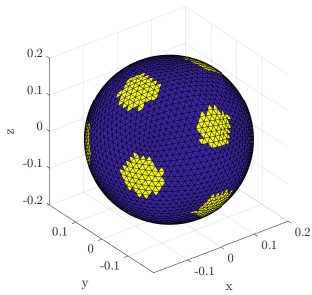


(c) Weighted MSE at different frequencies with 20 speakers for both models

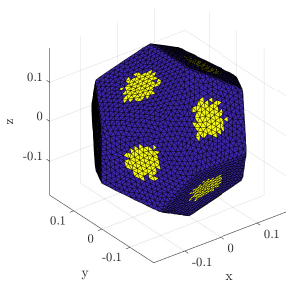
**Figure F.2:** Comparison of a spherical and an icosahedral array shape with similar speaker placements and the weighted MSE of the two shapes

### F.2.2 Dodecahedron

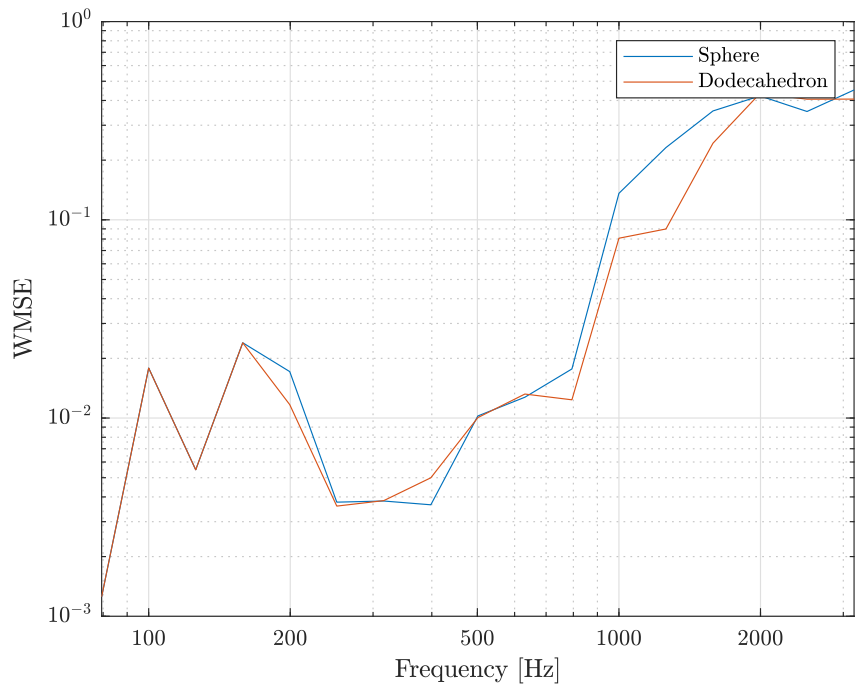
A little different result is instead achieved by comparing the sphere with the dodecahedron, a platonic solid with 12 drivers on its 12 faces, Section F.2.2. In this case, the *WMSE* lines of the two shapes start to deviate from each other at lower frequencies, from around 160 Hz, as it can be seen from Figure F.3. Above that, it becomes hard to define which of the two configurations presents the smallest error, as the two lines alternate each other. Initially, the sphere seems to present a little less error, while above around 800 Hz the dodecahedron shows a lower *WMSE*. Overall, the dodecahedron seems to resemble the target function a little bit better than the sphere.



(a) Sphere with 12 speakers



(b) Dodecahedron with 12 speakers



(c) Weighted MSE at different frequencies with 12 speakers for both models

**Figure F.3:** Comparison of a spherical and an dodecahedral array shape with similar speaker placements and the weighted MSE of the two shapes

Generally, the reason why in both cases the two platonic solids seem to behave a bit better than the sphere could possibly be due to their smaller size. The driver units are indeed placed closer to each other as the faces of the solids have a smaller distance from the center than the radius of the same sized sphere.

### F.2.3 Cylinder and Octagonal Prism - 10 Speakers

When investigating for a number of speakers that can not perfectly fit in the number of faces of platonic solids, then other enclosures can be taken into account.

In this section, the sphere is compared to a cylinder and to an octagonal prism, when mounting 10 speaker, again, on the same<sup>1</sup> placements along the surface.

By looking at Figure F.4 it is possible to conduct the same analysis on *WMSE* done in the previous sections. Here, the situation seems a bit more complicated, as the different error lines alternate between each other a lot. However, it is possible to define a trend. For the low frequencies, until around 440 Hz the octagonal prism seems to overcome the other two shapes, which more or less resemble each other. Above 500 Hz the trend is inverted. The octagonal prism commits the biggest *WMSE*, while the cylinder and the sphere start to follow each other, even though the cylinder seems to outperform at higher frequencies.

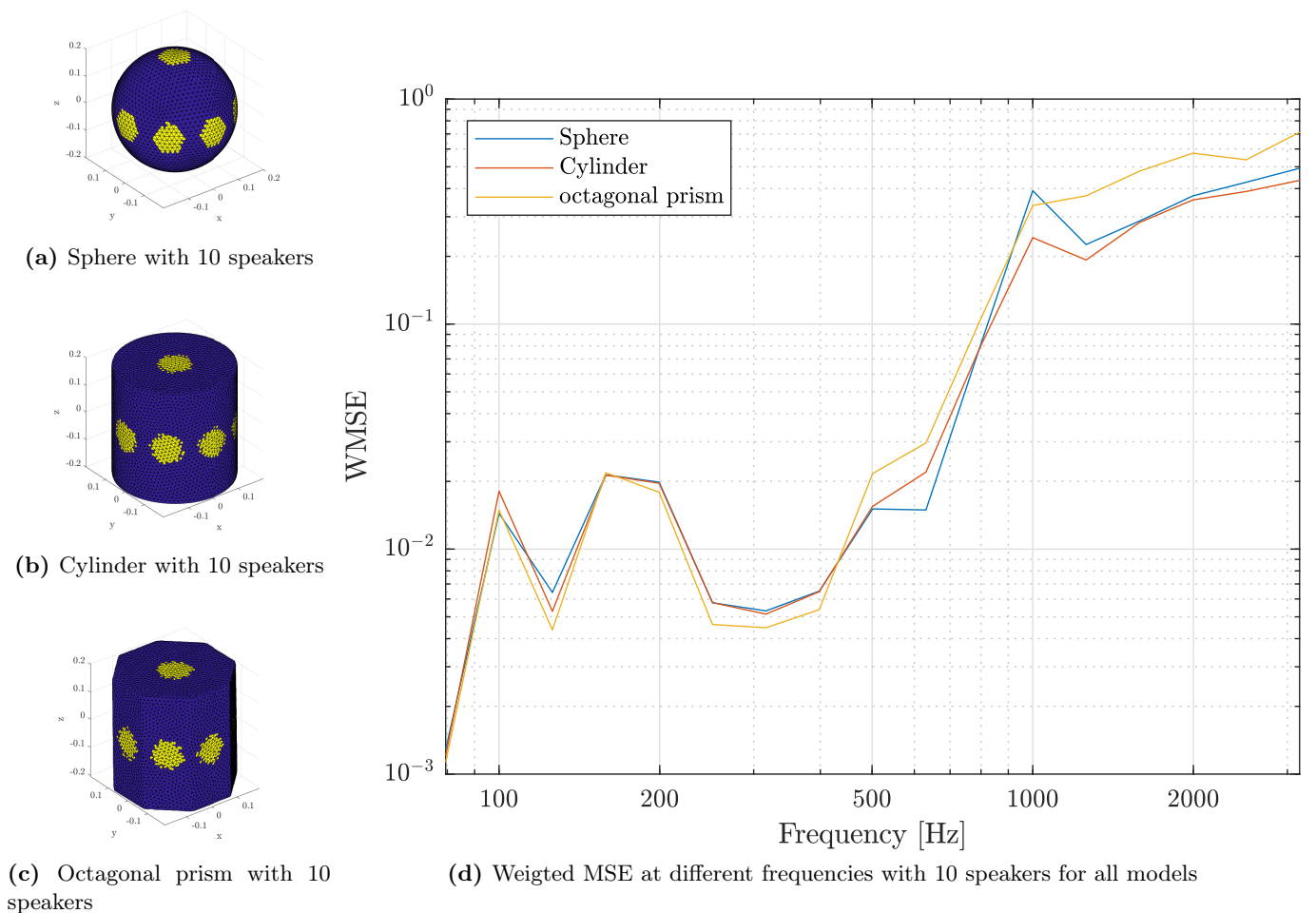


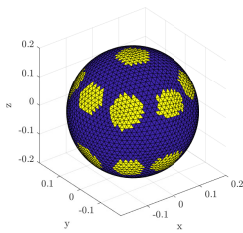
**Figure F.4:** Comparison of a spherical, a cylinder, and an octagonal prism array shape with similar speaker placements and the weighted MSE of the three shapes

<sup>1</sup>Same has to be taken with a pinch of salt, as it is not possible to achieve the same exact placement on different enclosure's shapes.

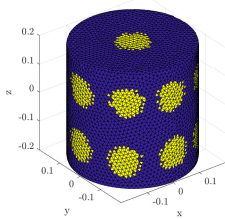
### F.2.4 Cylinder and Octagonal Prism - 18 Speakers

In Figure F.5 the *WMSE* is this time plotted for the sphere, the cylinder, and the octagonal prism in a configuration with 18 driver units, mounted in an as similar placement as possible over the three solids' surfaces.

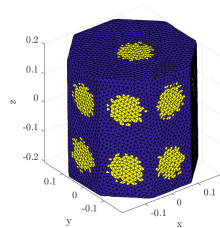
Once more by looking at the *WMSE* it is possible to get an idea of the impact different shapes have on the performance of the array. It is clear again how the low frequencies are not really affected by the different enclosures, at least until around 300 Hz. As seen before, by increasing the frequency, diversities start to appear. It is really difficult to define a trend this time, as it seems that the error committed by the different configurations is overall very similar. Still, the cylinder seems generally to outperform the other two shapes.



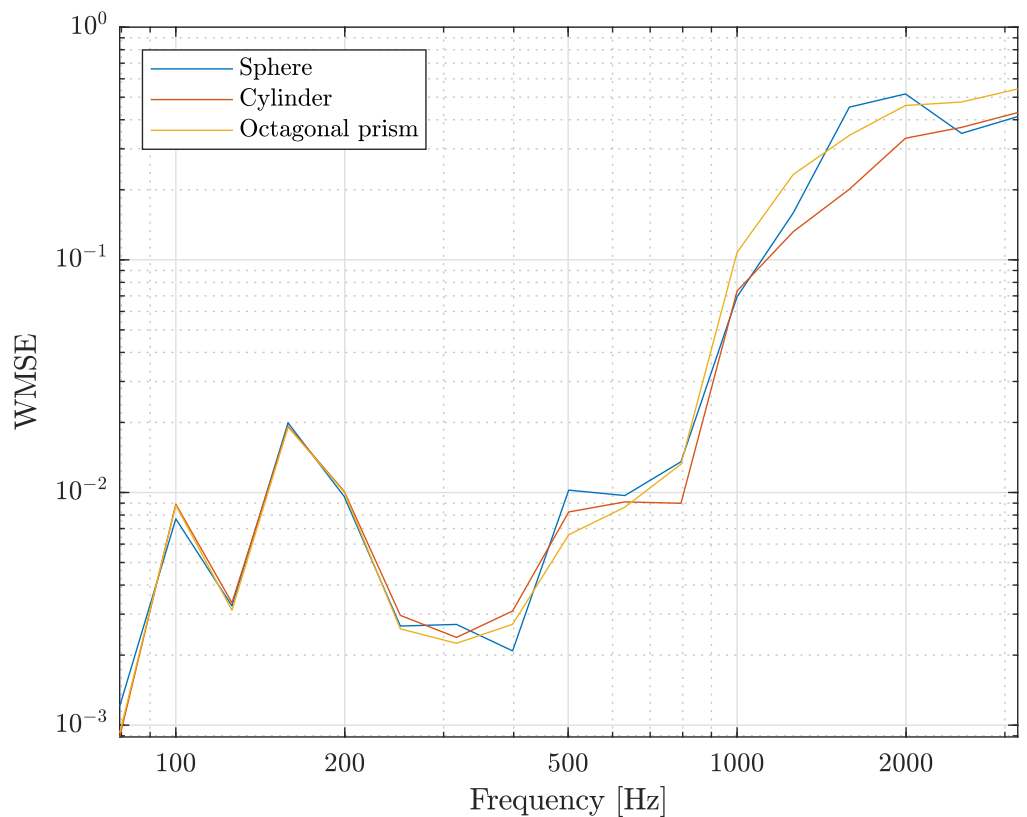
(a) Sphere with 18 speakers



(b) Cylinder with 18 speakers



(c) Octagonal prism with 18 speakers



(d) Weighted MSE at different frequencies with 18 speakers for all models

**Figure F.5:** Comparison of a spherical, a cylinder, and an octagonal prism array shape with similar speaker placements and the weighted MSE of the three shapes

# Simulation of the Effect of the Enclosure Size on Radiation Synthesis Performance



Another potentially important factor to investigate is how the overall size of the array affects its ability to synthesize a given radiation pattern. This is investigated in this appendix through BEM-simulations similarly to Appendix D, E and F.

## G.1 Simulation Parameters

Three differently sized arrays are used, all based on the spherical model used in earlier simulations. The model is scaled such that it has a radius of  $R = 0.2$  m,  $0.15$  m, and  $0.1$  m.

13 pistons of diameter  $3'' = 7.62$  cm have been placed on the surface, in a dodecahedral pattern. This size was chosen such that it would fit all the sizes.

The models used can be seen in Figure G.1

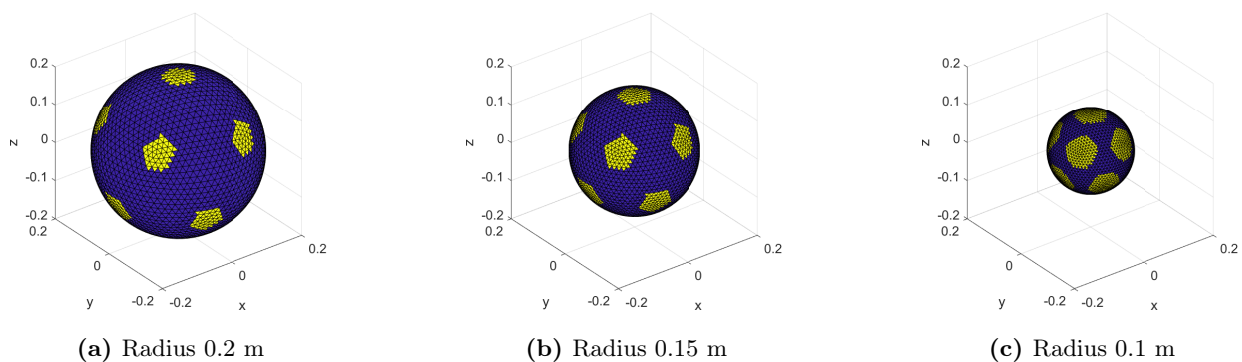


**Figure G.1:** 3D model of spherical loudspeaker arrays with 12 speakers with different enclosure sizes but the same piston diameter.

Additionally, a simulation where the 'relative' size of the piston compared to the enclosure is kept constant given as a constant angle of  $20^\circ$ . The models for that simulation is shown in Figure G.2.

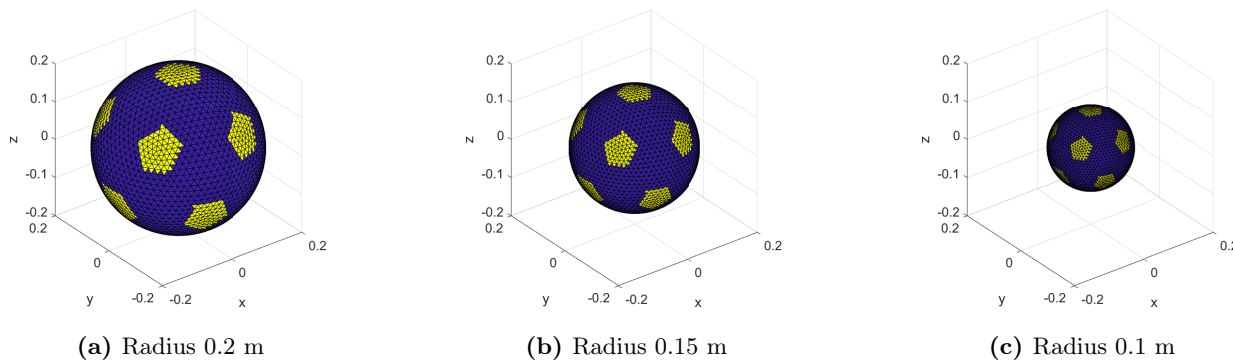


**Figure G.2:** 3D model of spherical loudspeaker arrays with 12 speakers with different enclosure sizes and the same relative piston sizes.

In all cases, the radiation synthesis is simulated via the BEM-methods from Chapter 5 and the optimal piston velocities are found via the iterative MLS algorithm, with a convergence criteria  $\epsilon = 10^{-4}$ . The simulations are done at every 1/3 octave band center frequency from 79 Hz to 3.16 kHz, and the results are compared to the target patterns at these frequencies by computing the *WMSE*.

## G.2 Results

The computed *WMSE* can be seen in Figure G.3.

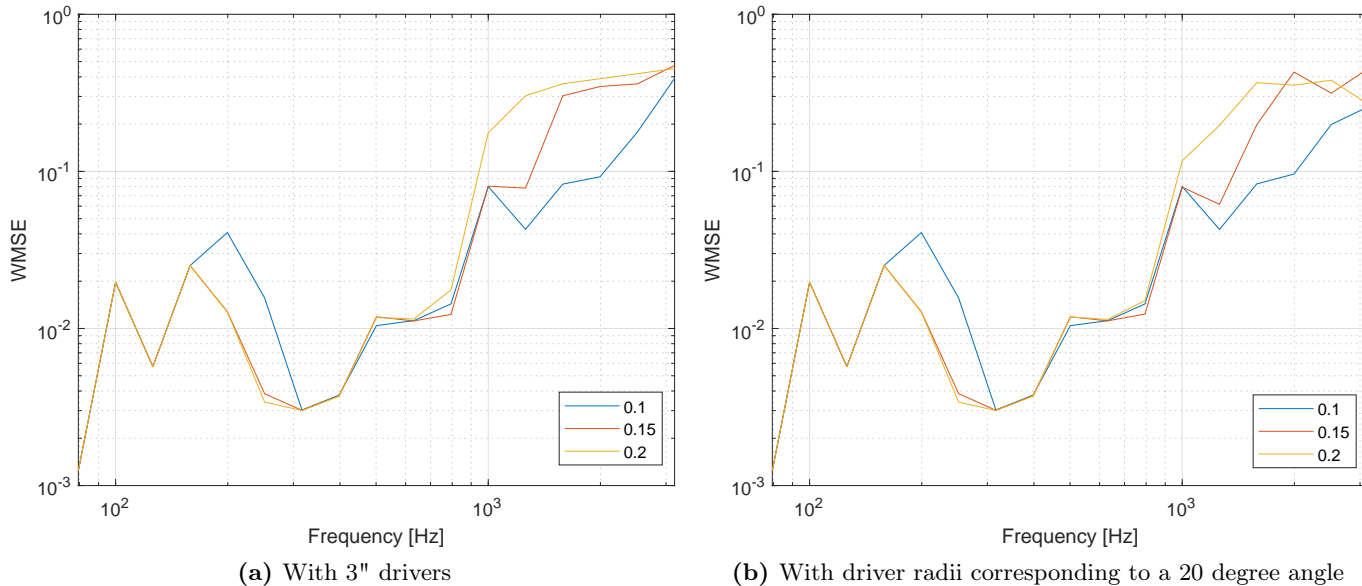


**Figure G.3:** Weighted MSE for spherical arrays of different sizes

It can clearly be seen that having a small enclosure is a benefit in the higher frequencies, seemingly invariant of the driver size. This suggests that just having the center of each array being closer together allows for the array to perform better in the higher frequencies where the speakers are very directional.

# Simulations of Different Placement Strategies on Octagonal Prism



In this appendix, the simulation results used for determining the final speaker placement on the prototype are described.

Additionally, these simulations will be used to get an idea of how the placement strategies differ.

Only the subtractive placement methods have been implemented in this study, and thus only these algorithms will be tested in this appendix.

## H.1 Simulation Parameters

The octagonal prism enclosure design described in Section 7.1.2 is used. A model of the shape has been drawn in `blender` with the same measures as is given by the sketch of Figure 7.3. The enclosure is oriented in two different ways: one standing up with the octagons (meant as the octagon faces of the prism) pointing up and down and another with the octagons pointing to the left and right as shown in Figure H.1.

The models are filled up with 3 pistons on each "side" and 4 on each octagon giving a total of 32 speakers. The piston radius has been chosen as 40.5 mm which corresponds to the radius of the cone on the VIFA M10MD drivers available for the prototype.

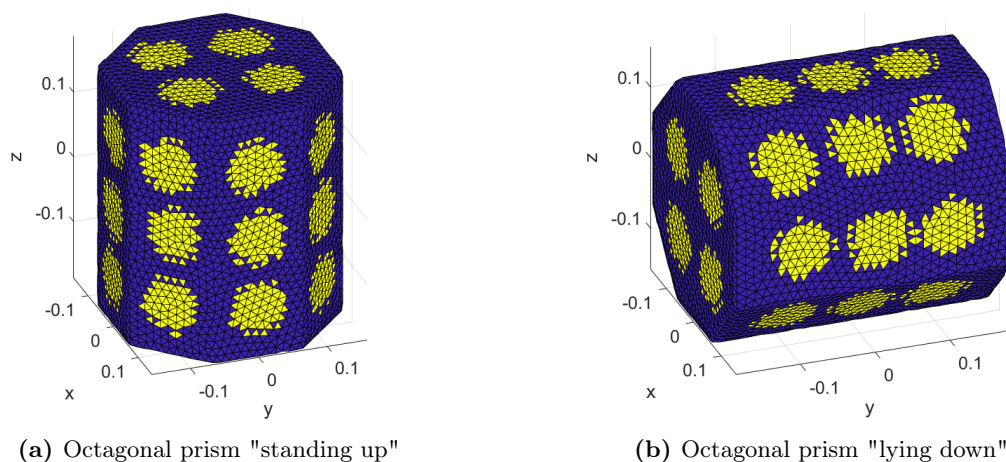


**Figure H.1:** Potential models for the prototype filled up with 32 pistons. Yellow areas denote the pistons and blue areas the enclosure.

The "Direct" subtractive method is implemented similarly to Figure 7.5, with the optimal inputs being found using the MLS optimization as described in Section 5.3.3.

The indirect subtractive method is implemented in two ways, an unweighted and a weighted version, where the frequency dependant weighting of the piston contribution is found simply as the *WMSE* of that frequency.

All methods have been computed until only 12 speakers are left, and every immediate result is saved.

In order to make the simulations a bit more "realistic", a frequency-independent regularization factor  $\beta = 5 \cdot 10^{-3}$  has been added, just so that no piston is allowed to have an insanely high-velocity gain.

## H.2 Results

In this section, the results of the simulations of different placement of the driver units among the surface of the octagonal prism are exposed and analyzed. Different strategies are taken into consideration, like "standing up" or "lying down" the array. In the end, some comparisons with platonic solids are also evaluated.

### H.2.1 Enclosure "Standing Up"

The *WMSE* can be computed for each frequency point like in the other simulations.

For 20 speakers the *WMSE* of the 3 algorithms are shown in Figure H.2.

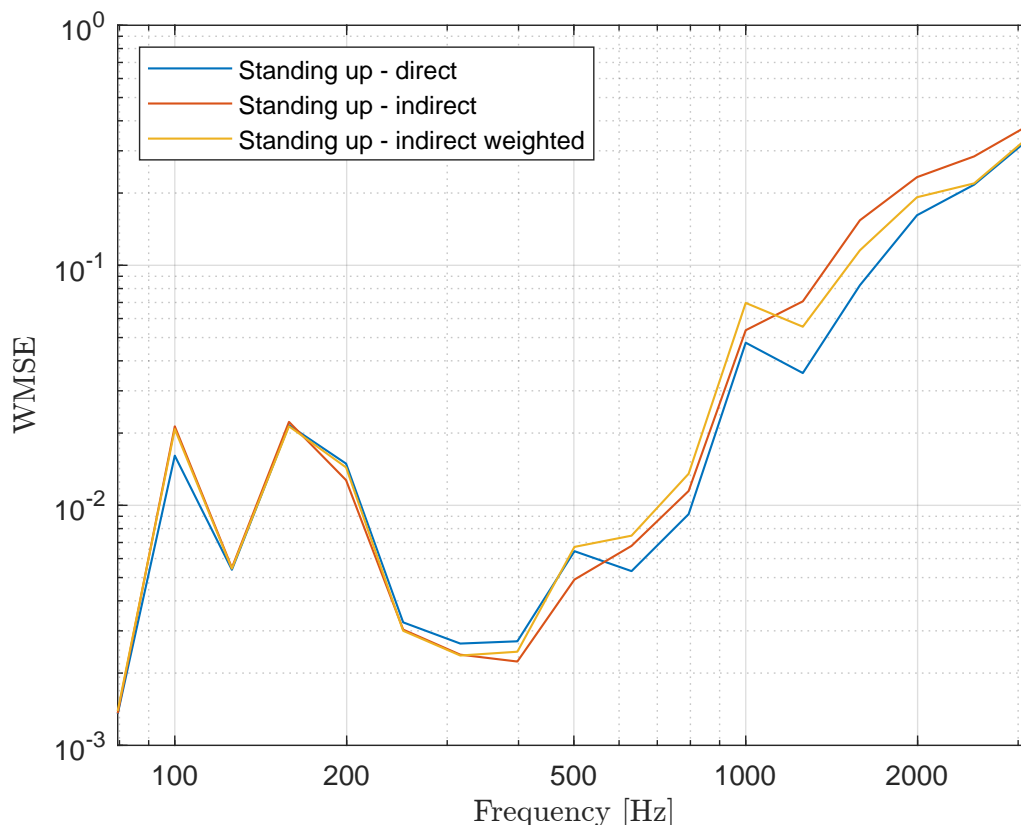


**Figure H.2:** *WMSE* for 20 speakers on the "standing" enclosure

At the higher frequencies from around 600 - 2500 Hz the direct placement strategy ends up with the best result, especially from around 1 - 2 kHz.

Similar results can be seen for 16 and 24 speakers respectively on Figure H.3.

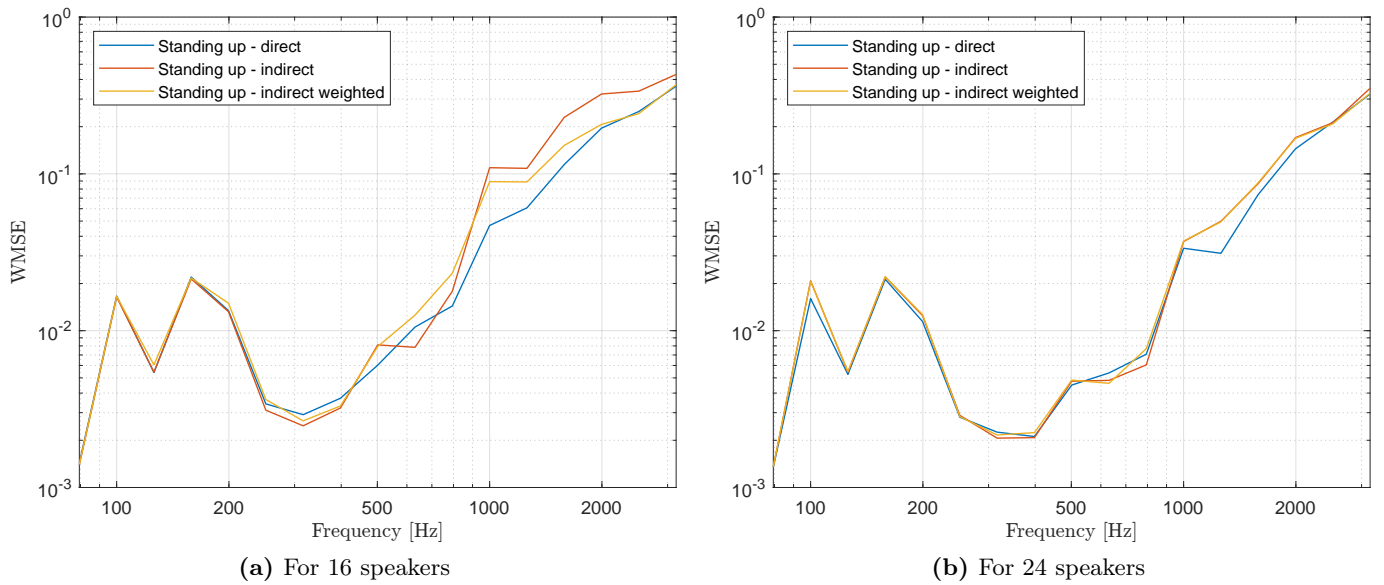
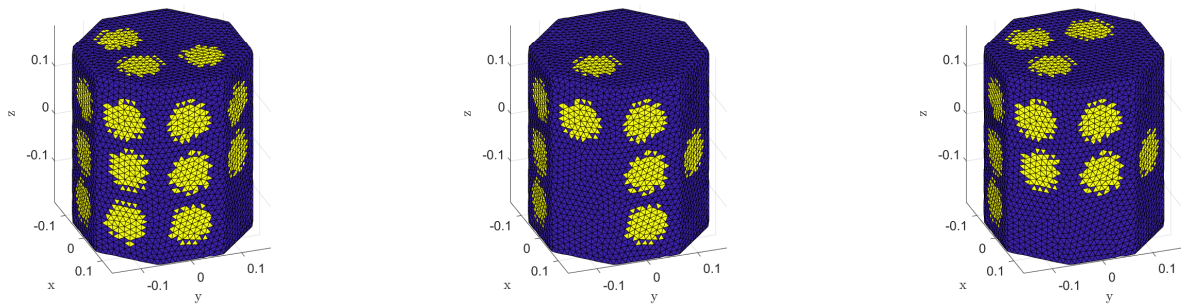


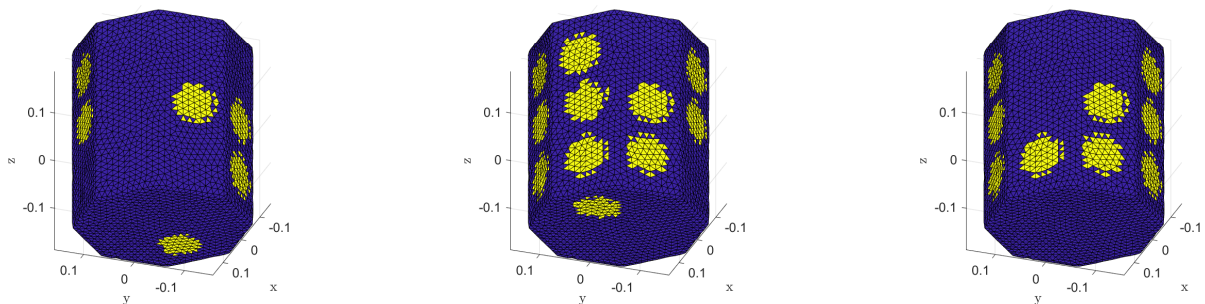
**Figure H.3:** *WMSE* for 16 and 24 speakers of the "standing" enclosure

Generally, the only points where the direct method gives a slightly worse result are at points where the error is so small anyway that it probably doesn't make a big difference.

On Figure H.4 the 20 speaker positions that remain for all algorithms can be seen.



(a) Direct method above and to the front (b) Indirect method above and to the front (c) Weighted indirect method above and to the front



(d) Direct method below and at the back (e) Indirect method below and at the back (f) Weighted indirect method below and at the back

**Figure H.4:** Speaker placement resulting from the three subtractive algorithms

The direct method especially seems to prefer to put many speakers at the front right part of the enclosure which matches our expectations of where a lot of speakers are necessary.

The indirect approach seems to place a lot more on the back especially when no weighting is applied.

One interesting thing to note is that only 4 speaker position has been removed by all the three algorithms even though 12 speakers have been removed. The methods do not seem to agree with each other very much. This means that the indirect method may not be that good an estimate of which piston is best to remove, but it could also be that a better frequency weighting function is needed.

We can also look at the direct method by itself to see how the error gets larger by removing the speakers. This is shown for every 4 speakers removed between 28 and 12 on Figure H.5.

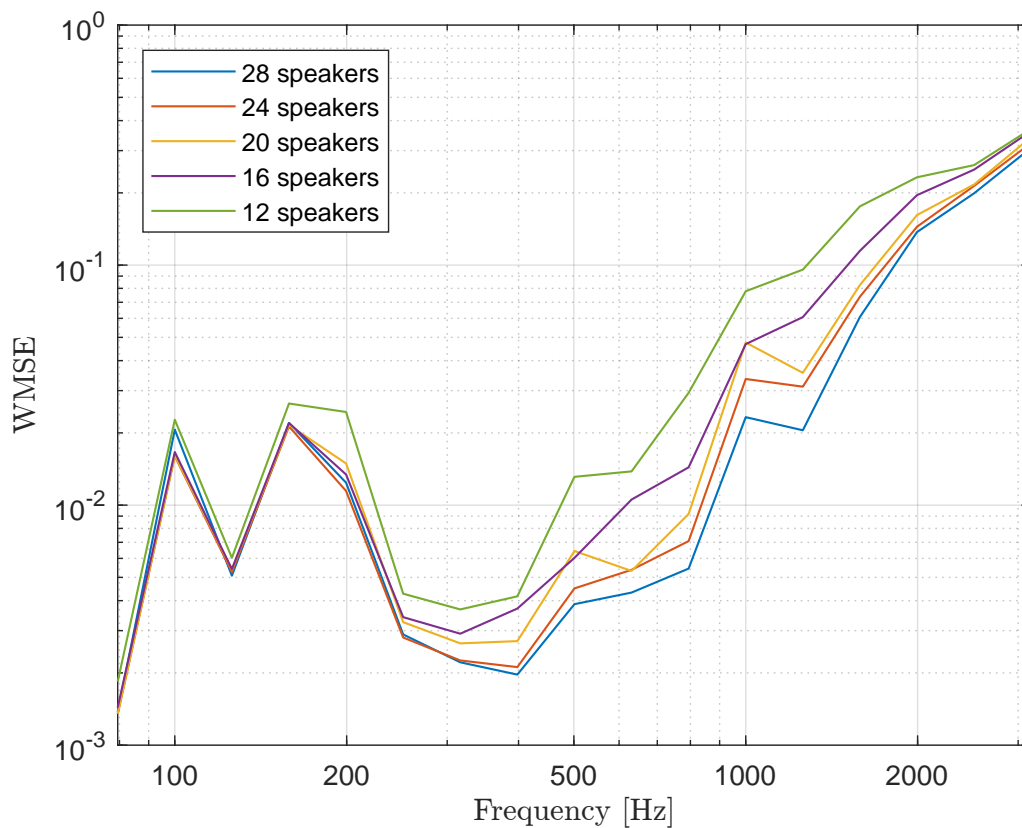


**Figure H.5:** *WMSE* of the direct subtractive method with different number of speakers

It seems that the error increases more between 20 and 16 speakers than it does between 24 and 20 speakers at the high frequencies where the error is high.

### H.2.2 Enclosure "Lying Down"

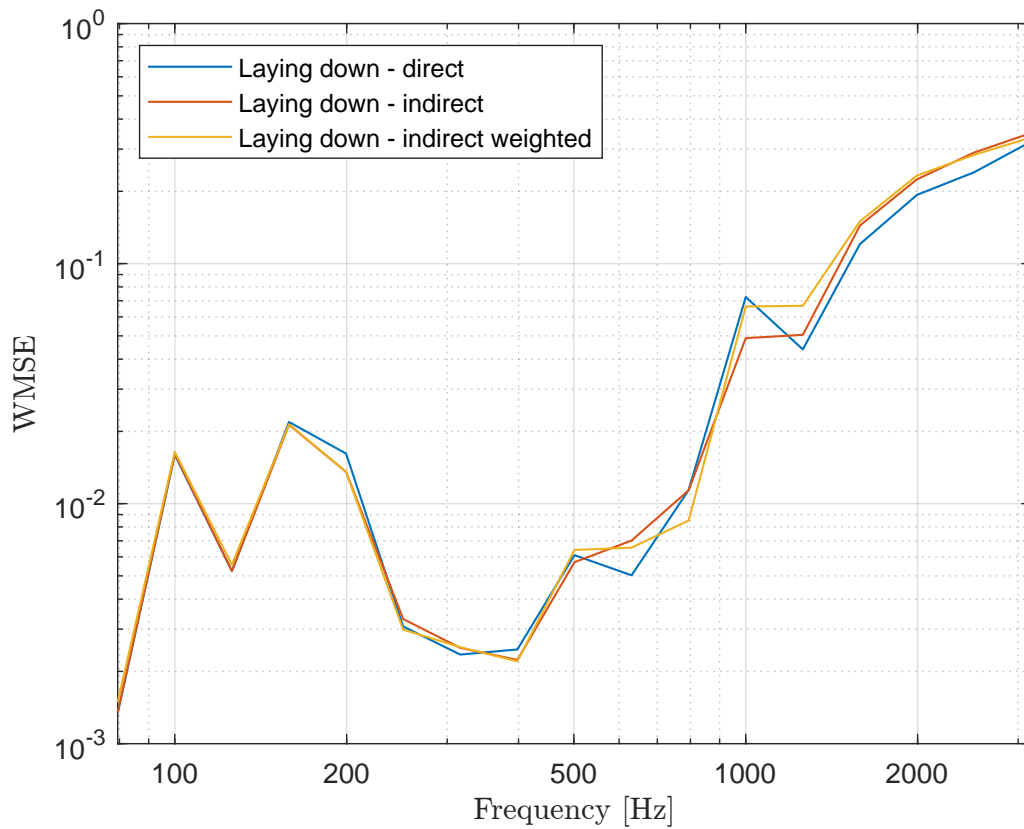
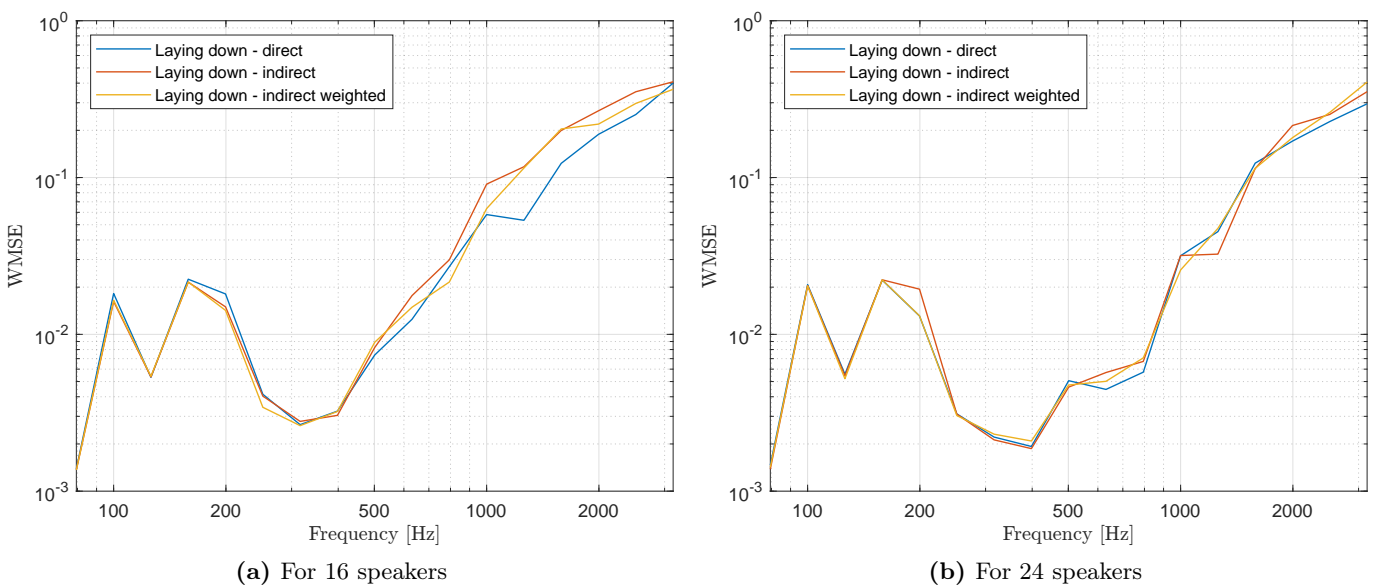


**Figure H.6:** *WMSE* for 20 speakers on the enclosure "Lying down"

Again it seems that the direct method gives a slightly better result at the higher frequencies but this time it is not as pronounced.

When a few more speakers get removed you can see the direct method gain a little more advantage on the indirect algorithms, as shown in Figure H.7.

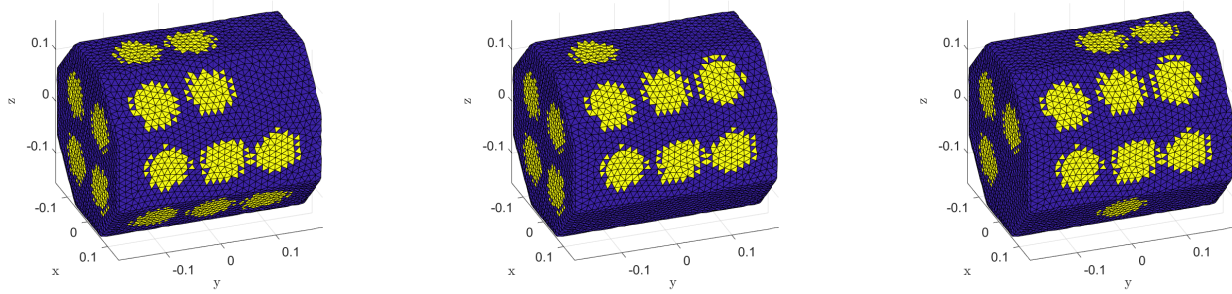


(a) For 16 speakers

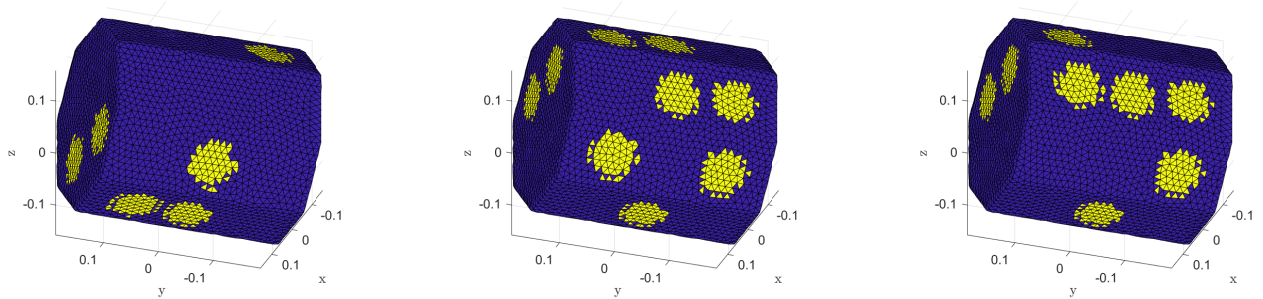
(b) For 24 speakers

**Figure H.7:** *WMSE* for 16 and 24 speakers of the "lying down" enclosure

Again, it is possible to see the placements of the 20 speakers for the different methods in Figure H.8.



(a) Direct method above and to the front (b) Indirect method above and to the front (c) Weighted indirect method above and to the front



(d) Direct method below and at the back (e) Indirect method below and at the back (f) Weighted indirect method below and at the back

**Figure H.8:** Speaker placement resulting from the three subtractive algorithms

### H.2.3 Comparison with Platonic Solid

In order to justify both the choice of the enclosure but also the speaker positions, a comparison between the direct subtractive method for the octagonal prism with 20 speakers and the icosahedron has also been made. The model and BEM matrices for the icosahedron are reused from Appendix F, so its corners are 20 cm away from the origin same as before.

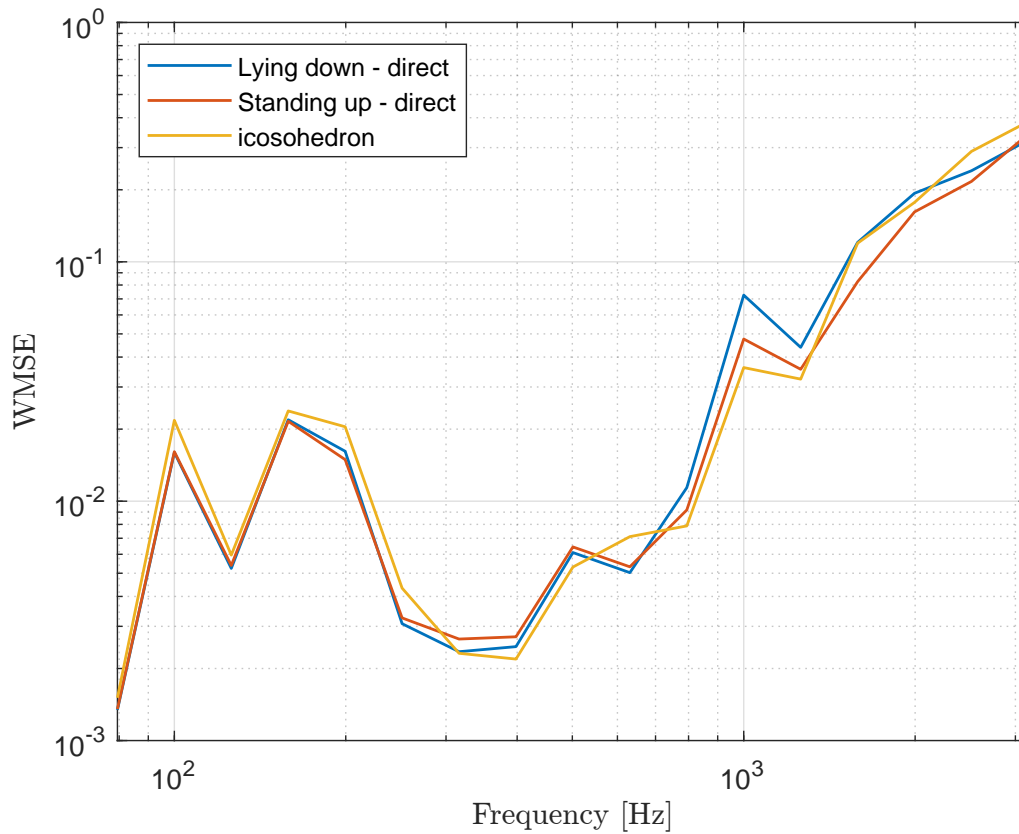


**Figure H.9:** Comparison between the direct subtractive placements on the octagonal prism and a icosahedron

The resulting *WMSE* from the direct subtractive method applied on both shapes from 32 initial speakers down to 20 remaining speakers, as well as the error for the icosahedron is shown on Figure H.9. Even though the icosahedron is slightly more compact as it has a significantly smaller surface area, the octagonal prism in the standing arrangement still outperforms the icosahedron at frequencies above  $\approx 1200$  Hz where the error is largest. Interestingly both octagonal prisms outperform the icosahedron in the lower frequencies below 300 Hz.

To give an overview of how well the different arrays match the target pattern at different frequencies, a series of balloon style plots can be seen in Figure H.10, H.11, H.12 and H.13

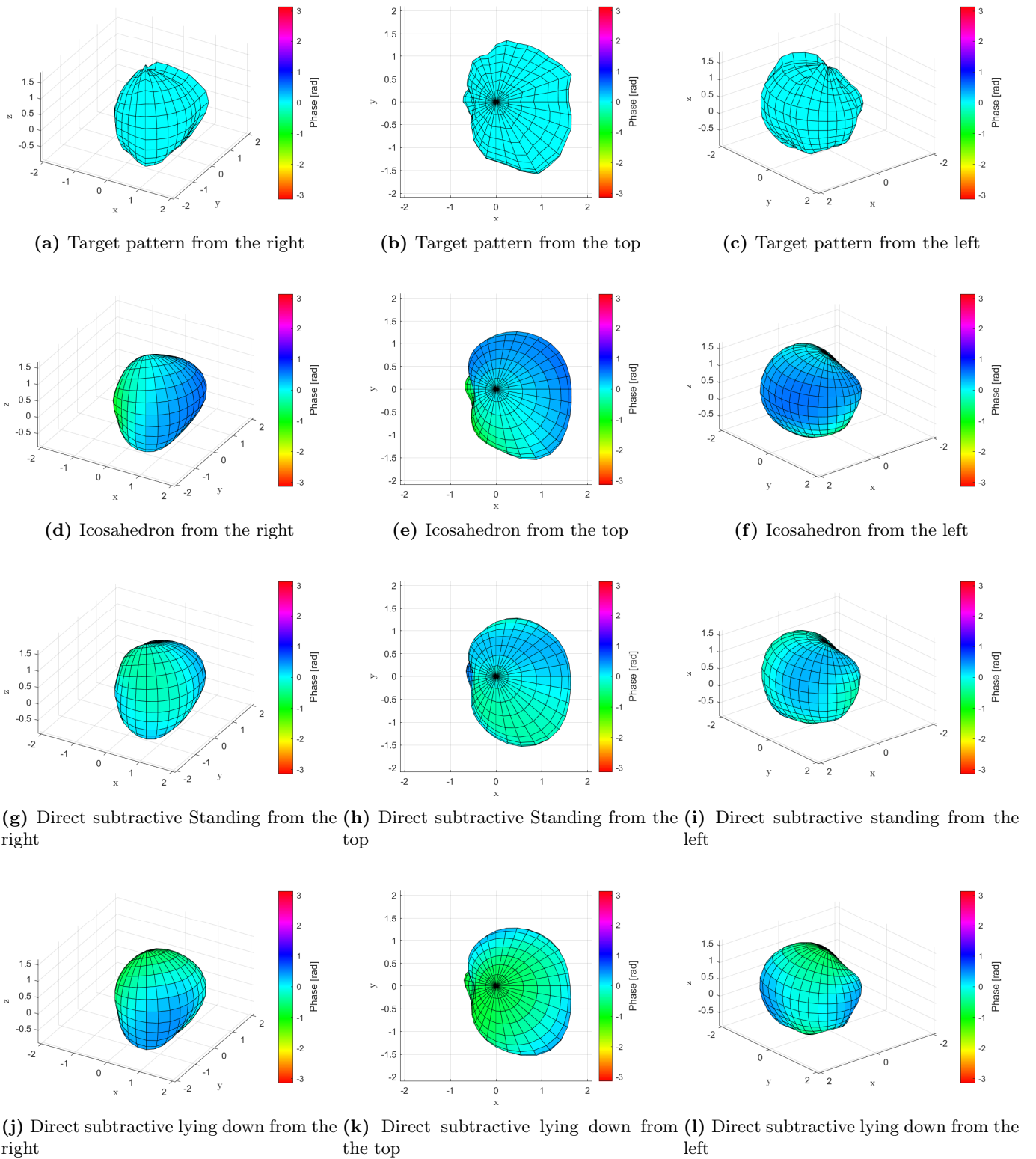


**Figure H.10:** Radiation patterns at 398 Hz seen from selected angles

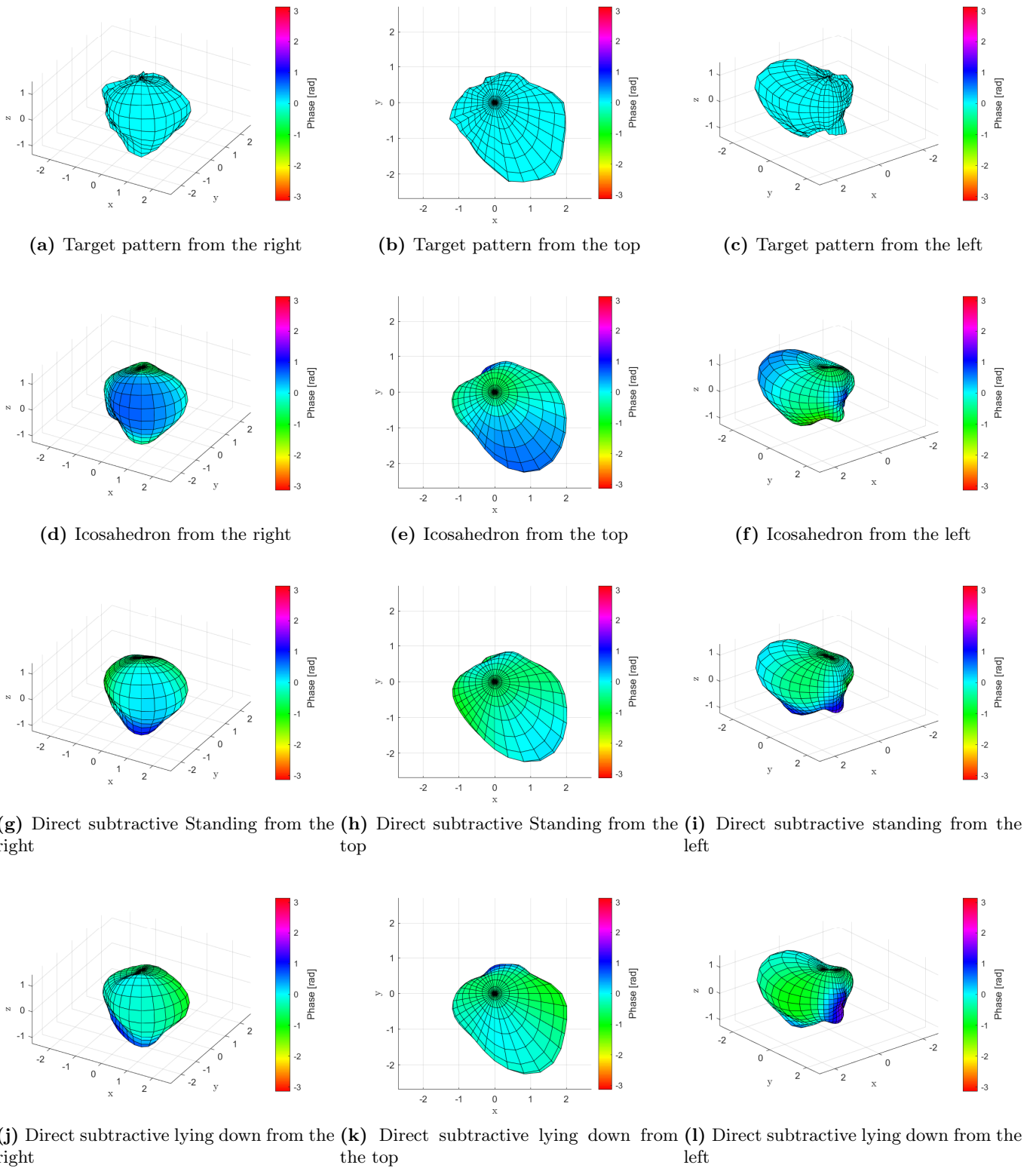


**Figure H.11:** Radiation patterns at 630.9573 Hz seen from selected angles

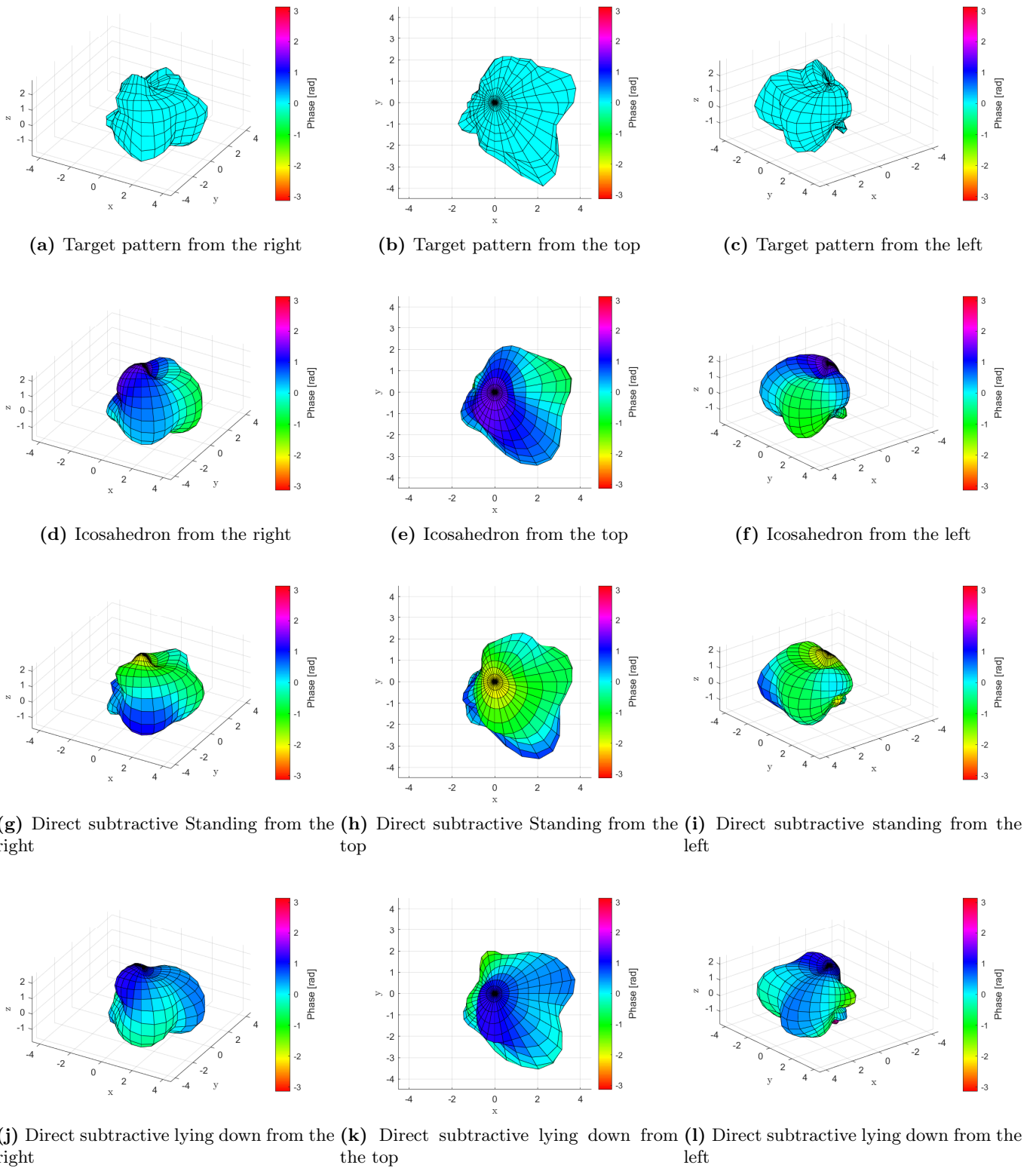
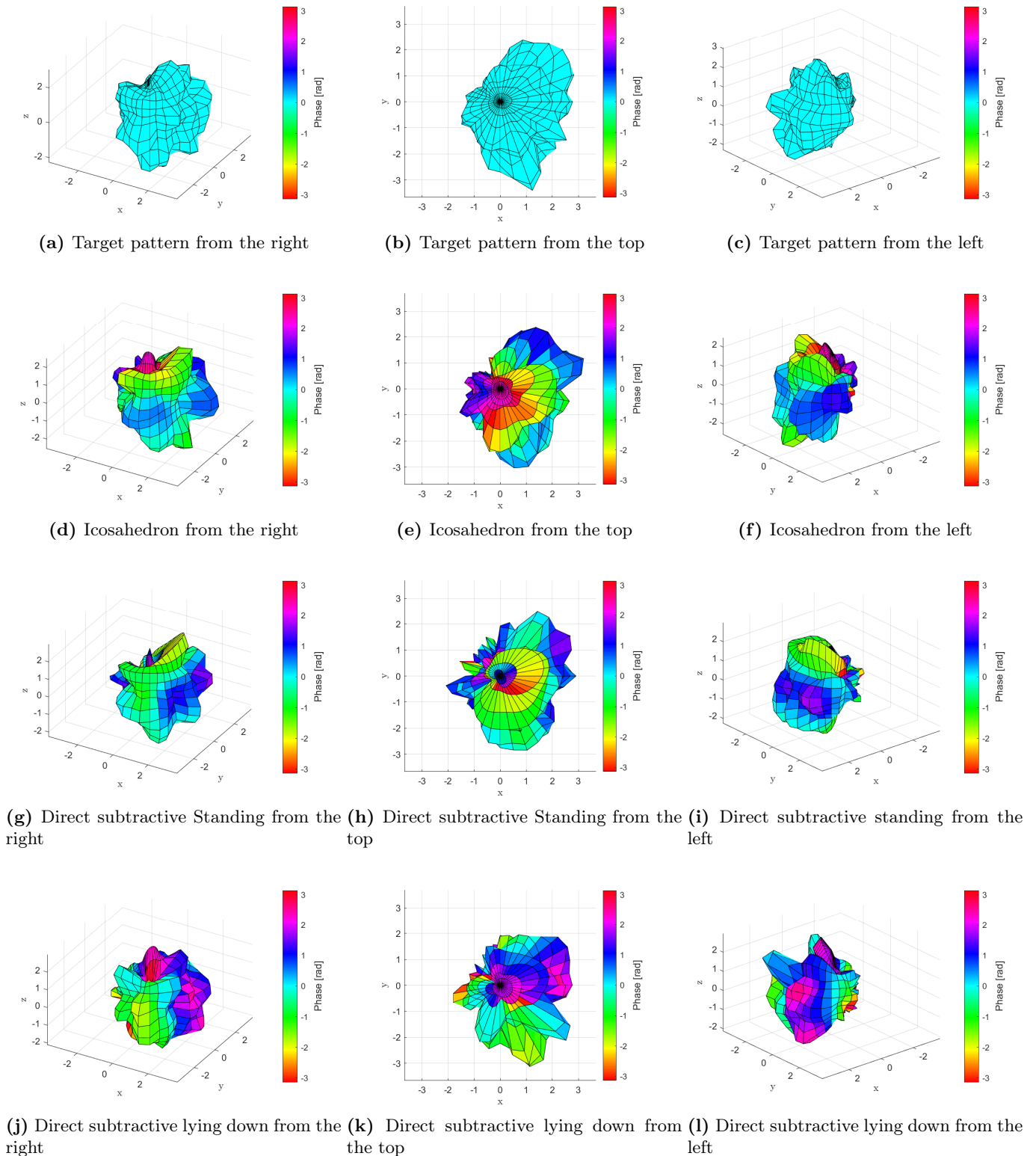


Figure H.12: Radiation patterns at 1000 Hz seen from selected angles



**Figure H.13:** Radiation patterns at 1995.2623 Hz seen from selected angles

At the lower frequencies at Figure H.10 and Figure H.11, all method seem to find an excellent match to the target function. The differences that can be seen are probably less than the inaccuracy of the target anyway.

At higher frequencies like in Figure H.12 and Figure H.13, larger differences exist between the synthesized patterns and the target, but it is hard to visually determine which one is "best". However, all synthesized

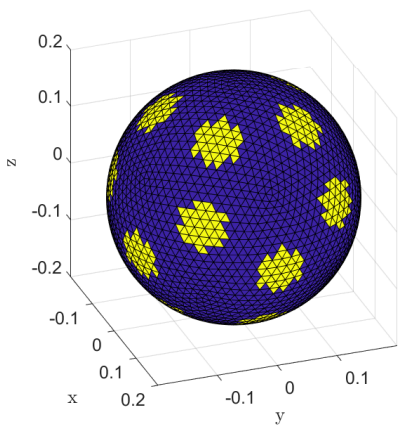
patterns seem to at least match the overall directivity of the target.

### H.2.4 Direct Subtractive Method Comparison on Sphere

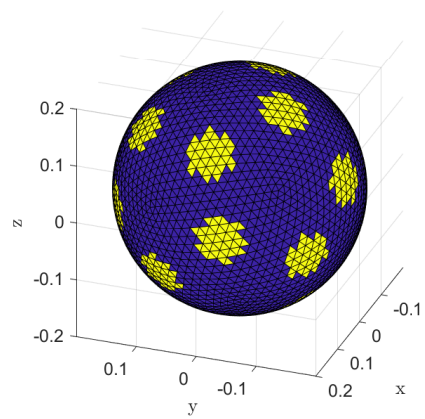
Perhaps a more "fair" comparison between a uniform speaker placement and the algorithm can be seen by comparing them on the same shape. On a sphere of radius 0.2 m, 48 pistons have been placed and removed one by one until only 20 speakers are left with the direct subtractive method.

This can then be compared to the same sphere with the same sized piston placed according to the faces of an icosahedron.

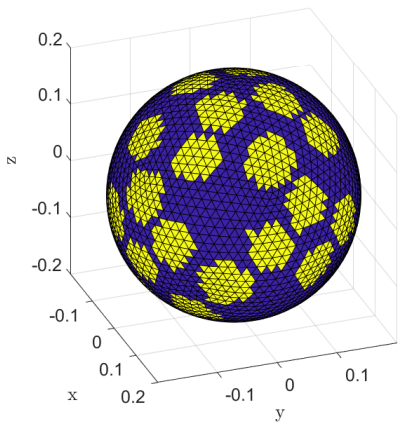
The two arrays in question can be seen on Figure H.14.



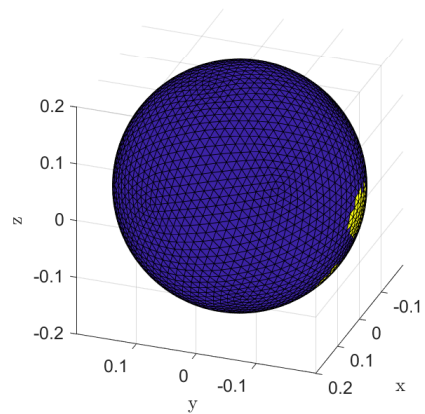
(a) Uniform speaker placement from the front and above



(b) Uniform speaker placement from the back and below



(c) Subtractive speaker placement from the front and above



(d) Subtractive speaker placement from the back and below

**Figure H.14:** 20 speakers placed on sphere, uniformly and through the subtractive algorithm

Clearly, the subtractive algorithm is placing way more speakers on the front side of the enclosure.

Like before we can look at the error across the simulated frequencies on Figure H.15.

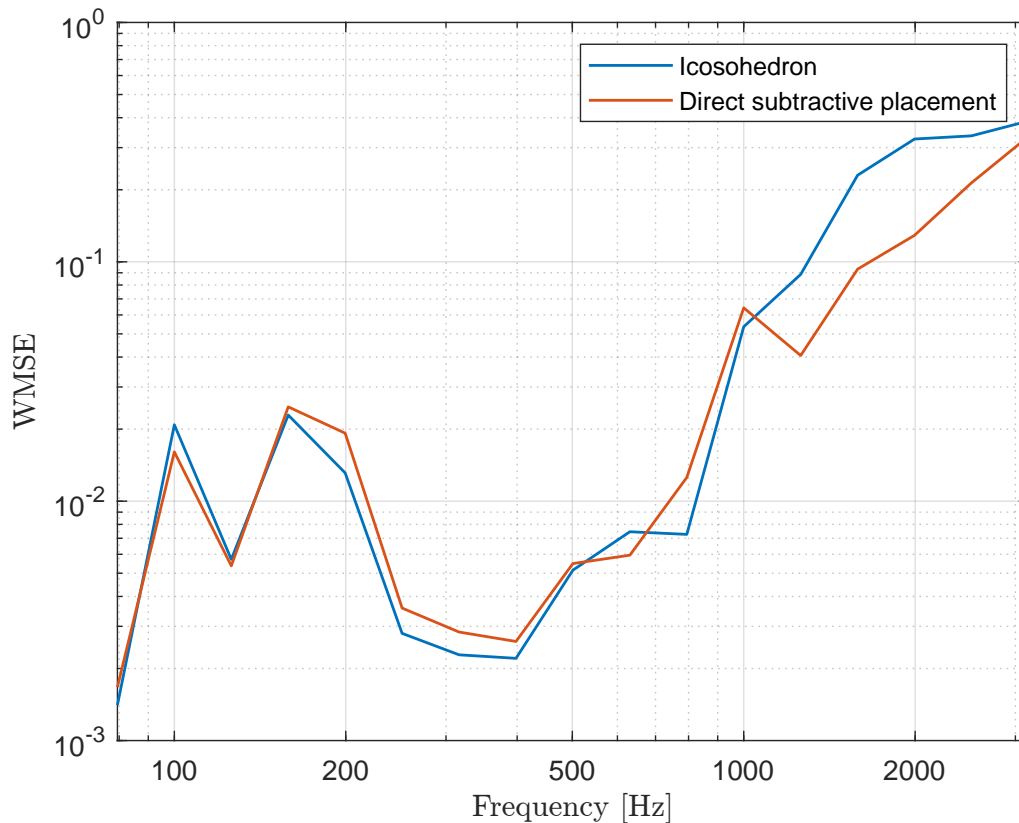


**Figure H.15:** Weighted MSE of a sphere with uniform speaker distribution vs. a sphere with speakers placed according to the direct subtractive algorithm

Like before we see the subtractive placement algorithm perform better at the higher frequencies. In fact, between  $\approx 1.2 - 2$  kHz, the error is around twice as large with a uniform placement compared to the subtractive placement strategy.

### H.3 Summary

To sum up the result from the preceding simulations: The direct subtractive placement strategy seems to produce a slightly better result when looking at the *WMSE* compared to the indirect methods, especially for the octagonal prism "standing up". When stopping at 20 speakers the octagonal prism standing up with speakers placed according to the direct subtractive algorithm gets the lowest *WMSE*, even lower than a simulation on a platonic solid with the same number of speakers at high frequencies.

The subtractive placement algorithm has also been simulated on a sphere and compared to a uniform speaker placement where it was also shown that the placement strategy achieved a better performance at the higher frequencies where the radiation pattern synthesis is more prone to error.

# Measurement of Speaker Impulse Responses

---

This appendix describes in detail the measurements of impulse responses for the chosen loudspeaker array. The measurements were carried on at the anechoic chamber B4-111 in the Acoustic Labs at Aalborg University, in Frederik Bajers Vej 7B, 9220 Aalborg Denmark while controlled from the control room B4-113 of the previously mentioned labs.

The impulse response of the chosen loudspeaker array to each observation/measurement point on a 3D sphere plays an important role in the design of filters for the sound radiation synthesis (see Chapter 6) as they are used to form the matrix of plant transfer functions  $\mathbf{H}(f)$ , by which the set of impulse responses have to be measured beforehand.

The description of the equipment list, measurement setup and procedure are reported in Section I.1, Section I.2 and Section I.3 respectively while the results of the measurement are grouped and presented in Section I.4.

## I.1 Equipment List

In this section, the equipment for the measurement is listed.

- 1x Arch of 1.7 m radius
- 17x G.R.A.S 40AZ 1/2" prepolarized free-field microphone
- 17x G.R.A.S 26CC 1/4" CCP standard preamplifier with SMB connector
- 1x B&K Type 4231 sound calibrator
- 3x RME Micstasy 8-channel full range pre-amp (Input level for 0 dBFS: +13 dBu)
- 2x RME M-16 DA, 16-channel high-end DA converter (Output level at 0 dBFS: +13 dBu)
- 1x RME Fireface UFX+
- 3x ICEpower class D amplifier (7 channels each at +30dB fixed gain)
- 1x Outilne ET 250-3D turning table
- 1x Mechanical turning table linked switcher
- 1x Loudspeaker array (20 channels)
- 1x Laptop with MATLAB
- 2x STANLEY CL-E laser

## I.2 Measurement Setup

The same microphone semicircle used in the 3D guitar radiation measurement (see Section C.2) was positioned again in the vertical plane, orthogonal to the floor for this measurement. The metal arch of 1.7 meters radius was still filled with 17 1/2" free-field microphones attached to plastic flat bars and distributed at every  $\phi = 10^\circ$  in the range  $-70^\circ < \phi < 90^\circ$ . This created a free-field microphone semicircle of 1.53m radius. As all microphones were already calibrated during the 3D measurement of the acoustic guitar, then

the same calibration factors were reused in this measurement to reduce any inequalities in between the microphones.

The loudspeaker array was positioned in the origin of the semicircle. The array was mounted on a tripod stand placed on the turntable, in such a way that the loudspeaker array would always remain located in the origin when being rotated over the turntable with the desired step size. In this measurement, the step size was fixed to  $\theta = 10^\circ$  to provide a spatial resolution of  $10^\circ$  in both azimuth and elevation angles. The turntable was able to be controlled from a switcher installed in the adjacent control room.

An overview of the measurement setup for the measurement loudspeaker array impulse responses can be seen in Figure I.1 while visualizations of the measurement setup in the anechoic chamber are shown in Figure I.2

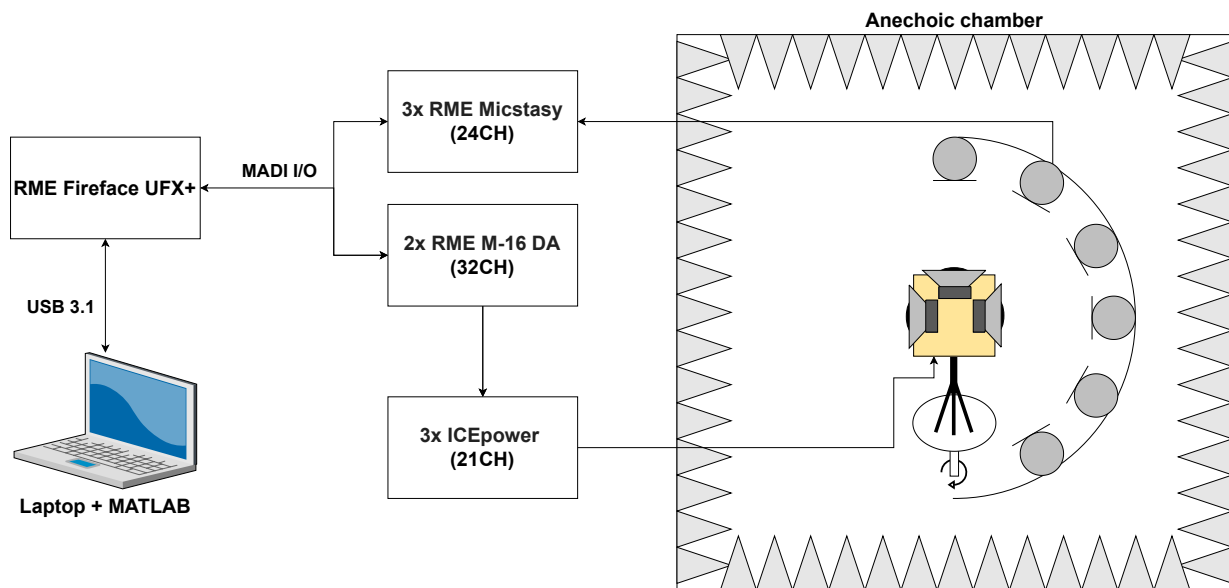
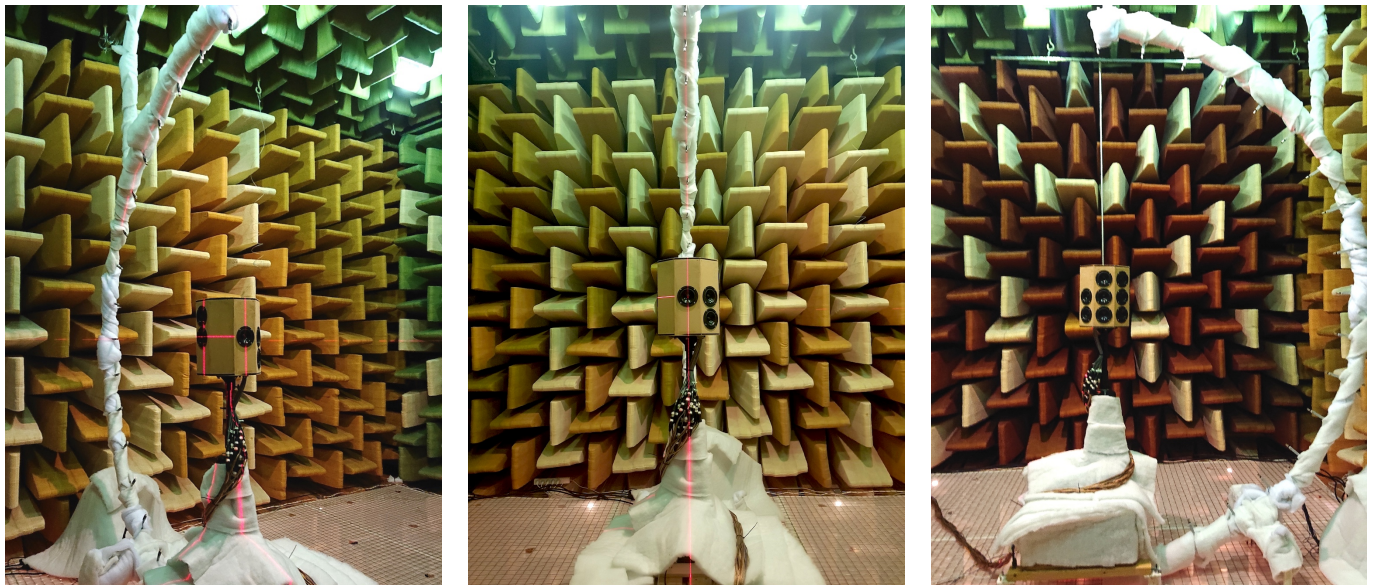


**Figure I.1:** Overview of setup for the equipment and connection used in the measurement procedure of the loudspeaker array impulse responses



(a) Picture of the setup from an angled left side.

(b) Picture of the setup from the back side.

(c) Picture of the setup from the right side.

**Figure I.2:** Pictures of the impulse response measurement setup in the anechoic chamber. The loudspeaker array located in the origin of the semicircle is mounted on a tripod-stand placed on top of the turning table

All the signals from the microphones were sent to three 8-channel RME Micstasy, microphone preamp, and AD converters, which were daisy-chained within MADI protocol. The two 16-channels RME M-16 DA converters were also connected to the MADI serial interface, such that the two DA converters were able to read each of the desired channels of the MADI stream before the three Micstasy AD converters had overwritten the MADI stream channels. In this way, the RME Fireface UFX+ soundcard situated in the control room was able to send a number of output signals digitally to the two DA converters through coaxial cable (MADI Interface) and simultaneously receive the signals from the microphones digitally over the same MADI serial interface. In addition, the soundcard could also adjust and control both the Micstasy and the DA converters settings from remote via MIDI over MADI.

The output signals received by the DA converters were passed to the three connected ICEpower amplifiers as analog signals. Each of the 20 channels of the loudspeaker was connected to a specified channel of the three ICEpower amplifiers from which each analog output signal could be played out by the correct channel of the loudspeaker array inside the anechoic chamber.

When daisy-chaining the three Micstasy within the MADI protocol, a small delay (3 samples) is introduced between each device. This is solved by manually activating a built-in delay compensation on the three Micstasy. In addition to that, a loop-back cable between the last unused channel of the two RME M-16 DA converters (Out=32) and the last unused channel of the three RME Micstasy (In=24) was used to measure the delay between the I/O of the sound card (including the serial communication and sampling latency of the RME M-16 DA and RME Micstasy), so to allow the measuring program to compensate for the delay of the measurement system later on.

Everything was controlled by a laptop connected to the soundcard through USB (ASIO protocol with a buffer size of 2048 samples) positioned in the control room, where the measurement could be analyzed and saved through MATLAB.

### I.3 Measurement Procedure

The exponential (or logarithmic) sine sweep (ESS) technique [70][71] is often employed to acquire impulse responses within audio and acoustics. For each individual driver of the loudspeaker array an ESS is used as the excitation signal  $x(t)$  given by:

$$x(t) = \sin \left[ \frac{\omega_1 \cdot T}{\ln \left( \frac{\omega_2}{\omega_1} \right)} \cdot \left( e^{\frac{t}{T} \cdot \ln \left( \frac{\omega_2}{\omega_1} \right)} - 1 \right) \right] = \sin \left[ \frac{2\pi \cdot f_1 \cdot T}{\ln \left( \frac{f_2}{f_1} \right)} \cdot \left( e^{\frac{t}{T} \cdot \ln \left( \frac{f_2}{f_1} \right)} - 1 \right) \right] \quad (\text{I.1})$$

Where  $\omega_1$  and  $\omega_2$  denote the angular start and stop frequency of the sweep (similarly,  $f_1$  and  $f_2$  denote the start and stop frequency in Hz) and where T provides the total sweep time in seconds.

The measurement procedure is controlled by MATLAB script/program and consists of the following steps:

1. The excitation signal  $x(t)$  is generated in MATLAB as a .wav file, consisting of 2 seconds of exponential sine sweep with a level of -40 dBFS, followed by 0.5 seconds of silence.
2. Several repetitions (5) of this combined sweep and silence signal are sent throughout the sound card and played back by one of the individual loudspeaker units at approximately 1.1Vrms (-40dB +13dBu +30dB = 3dBu) while the remaining units stay silenced.
3. The response  $y(t)$  at each of the 17 microphones on the semicircle is simultaneously measured and is then fed back to the sound card and to be analyzed in MATLAB.
4. In MATLAB the first of the measured sweep repetitions of each response  $y(t)$  is discarded because it only serves as a warm-up signal used to eliminate underrun or overrun of the measurement, which might occur because of start-connection delays within different hardware components in the signal chain.
5. The remaining sweep repetitions (4) of each response  $y(t)$  are then averaged to improve the SNR by averaging out any uncorrelated noise present in the measurement.
6. Each of the 17 measured responses  $y(t)$  and the excitation signal  $x(t)$  are then extended with zeros (zero-padding) to double their previous length in order to avoid cyclic deconvolution [71] later on.
7. Each of new zero-padded measured responses  $y(t)$  and excitation signal  $x(t)$  are then transformed to the frequency domain by taking the FFT of the signals
8. Using a linear deconvolution [71] in the frequency domain between each of the measured response  $Y(f)$  and the excitation response  $X(f)$ , then 17 transfer functions  $H(f)$  can be calculated.
9. Each impulse responses  $h(t)$  can then be found taking an IFFT of the each transfer functions  $H(f)$ .
10. The 2nd half of each impulse response  $h(t)$  is afterwards discarded in order to remove any harmonic distortion products [71].
11. Each impulse response  $h(t)$  is time-shifted a number of samples back corresponding to the latency of the measurement system, measured with the loopback cable.
12. (Optional) Each impulse response  $h(t)$  can be truncated to a shorter duration by multiplying an appropriate window function e.g. a half Hanning window or a half Tukey window of length  $N$ . In this project, the impulse responses are truncated to a length of 8192 samples to the same memory usage using a half Tukey window.

13. Lastly, each impulse response  $h(t)$  is scaled by the corresponding calibration factor of each microphone to reduce any inequalities in between the measurements and get the unit in Pa/FS.
14. The procedure is repeated from step 2 for loudspeaker units at all azimuth angle turntable steps ( $\theta = 0^\circ, 10^\circ, \dots, 350^\circ$ ) to obtain the impulse responses of all loudspeaker-microphone combination between the loudspeaker array and the full sphere of microphones.

An overview of the most important parts of the exponential sine sweep technique for obtaining the impulse responses for each loudspeaker-microphone combination can be seen in Figure I.3

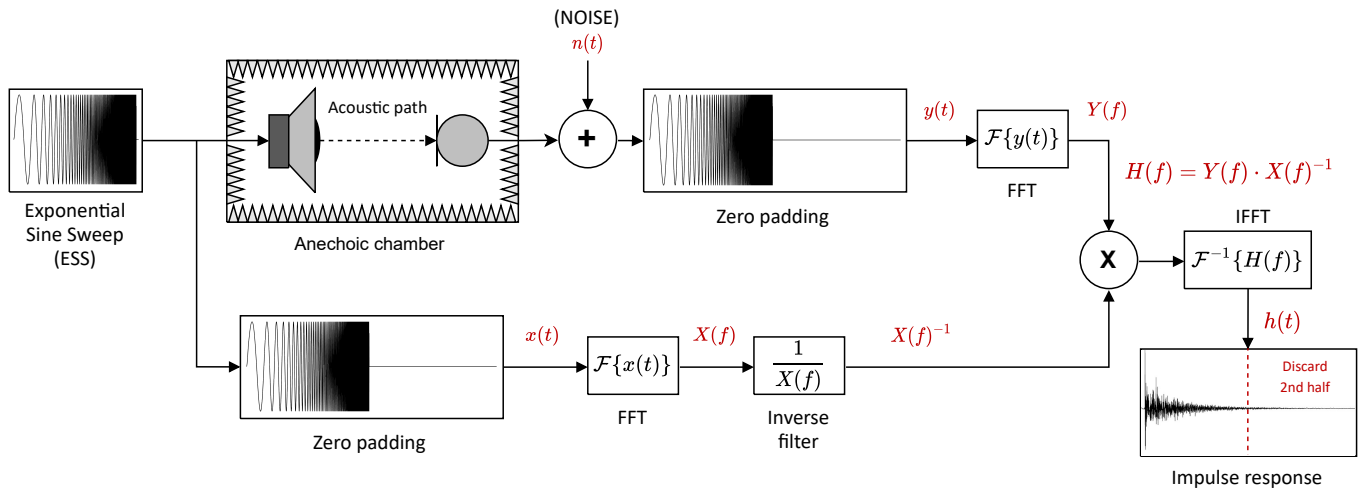


**Figure I.3:** Block diagram of the impulse response measurements using the exponential sine sweep technique for each loudspeaker-microphone combination between the loudspeaker array and the sphere of microphones

## I.4 Results

As a result of the measurements, a total of 12240 impulse responses were collected.

However, the measuring point at  $\phi = +90^\circ$  should only be measured as 1 impulse response for each of the 20 speakers. This is done by averaging the 36 repeated impulse responses at  $\phi = +90^\circ$  for each of the driver units.

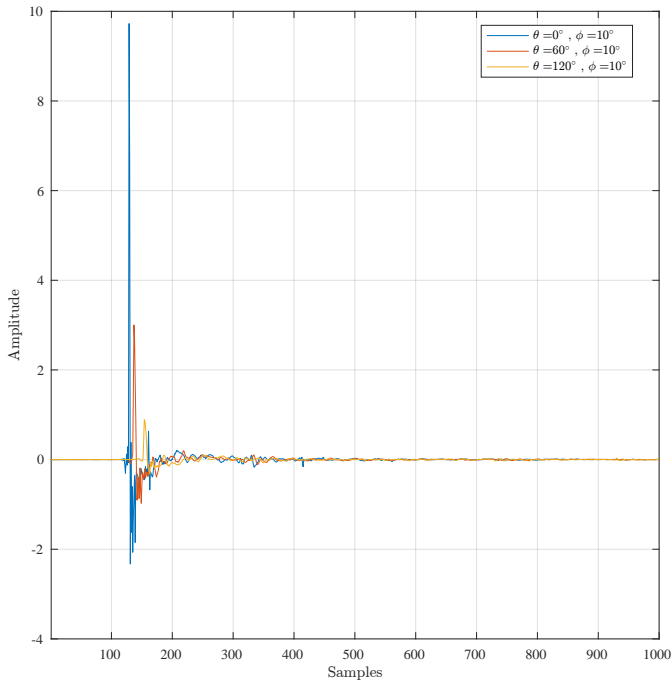
Hence, 11540 unique impulse responses are effectively measured, where each of the 20 driver units of the array is measured at 577 ( $16 \times 36 + 1$ ) uniquely defined measuring points with a resolution of  $\theta, \phi = 10^\circ$  within a range  $0^\circ < \theta < 360^\circ$  and  $-70^\circ < \phi < 90^\circ$ .

In addition to that, as no measurement point is located in the bottom of the measuring sphere at  $\phi = -90^\circ$ , a set of 20 impulse responses going to a virtual measurement point at  $\phi = -90^\circ$  is obtained by averaging all the 36 impulse responses at  $\phi = -70^\circ$  for each driver unit.

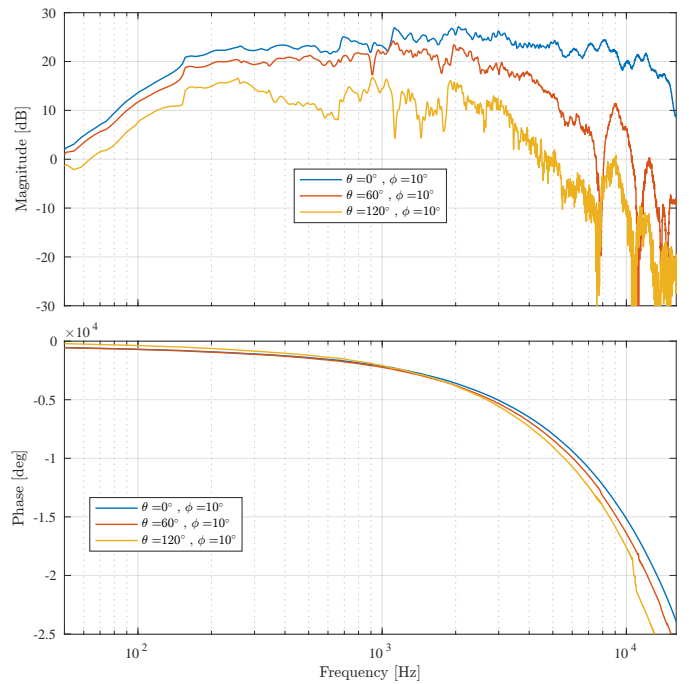
This results in a total of 577 unique measurement point + the virtual point at  $\phi = -90^\circ$  on a sphere from which a total 11560 impulse responses is obtained (578 impulse responses going from each of the 20 loudspeaker driver units to each of the measurement points).

It is these  $578 \times 20$  impulse responses that are used to form the  $M \times L$  matrix of the plant transfer function  $\mathbf{H}(f)$  employed in the design of filters for the sound radiation synthesis in Chapter 6.

Anyway, in Figure I.4, Figure I.5 and Figure I.6 the impulse responses for some selected angles and speaker units are plotted together with their respective magnitude response (50dB/decade) and phase response.

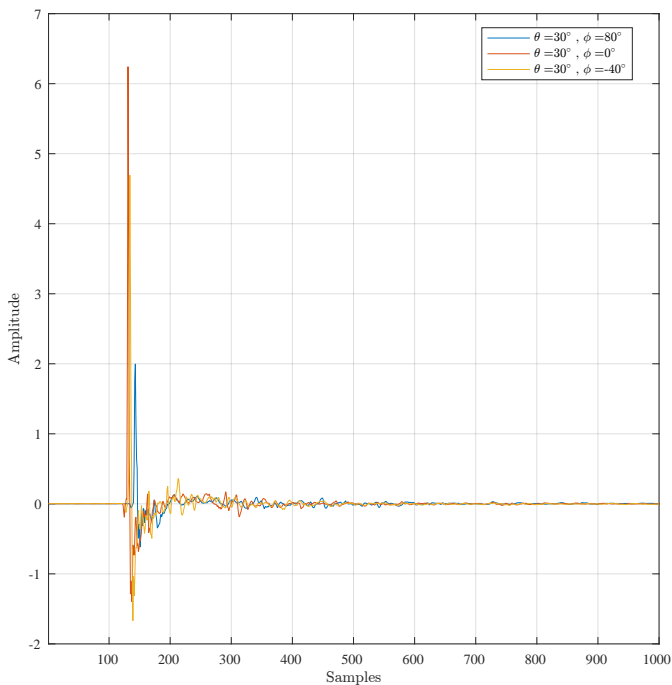


(a) Impulse responses for the speaker #2 (front center of the array).

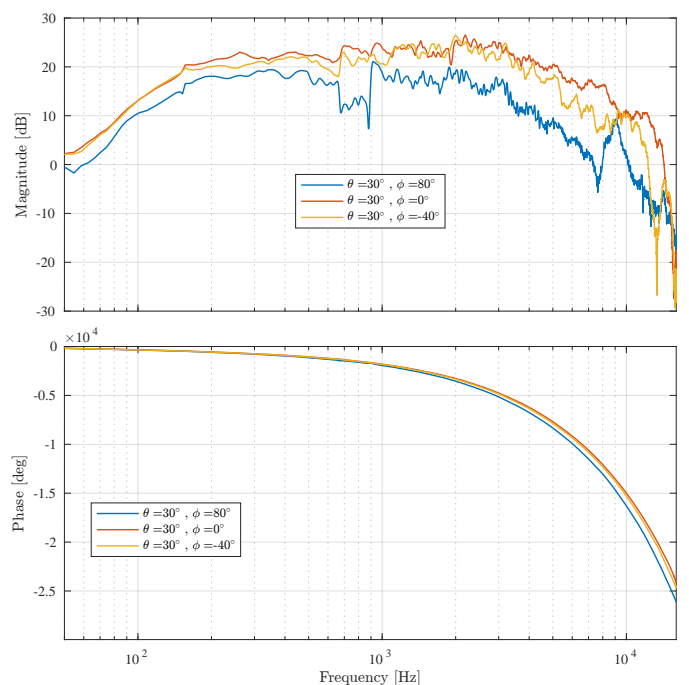


(b) Magnitude and phase response for the speaker #2 (front center of the array).

**Figure I.4:** Impulse response, Magnitude and phase response the speaker #2 (front center of the array) for three different azimuth angles  $\theta = 0^\circ, 60^\circ, 120^\circ$  at the same elevation angle  $\phi = 10^\circ$ .



(a) Impulse responses for the speaker #2 (front center of the array).



(b) Magnitude and phase response for the speaker #2 (front center of the array).

**Figure I.5:** Impulse response, Magnitude and phase response the speaker #2 (front center of the array) at the same azimuth angle  $\theta = 30^\circ$  for three different elevation angles  $\phi = 80^\circ, 20^\circ, -40^\circ$ .

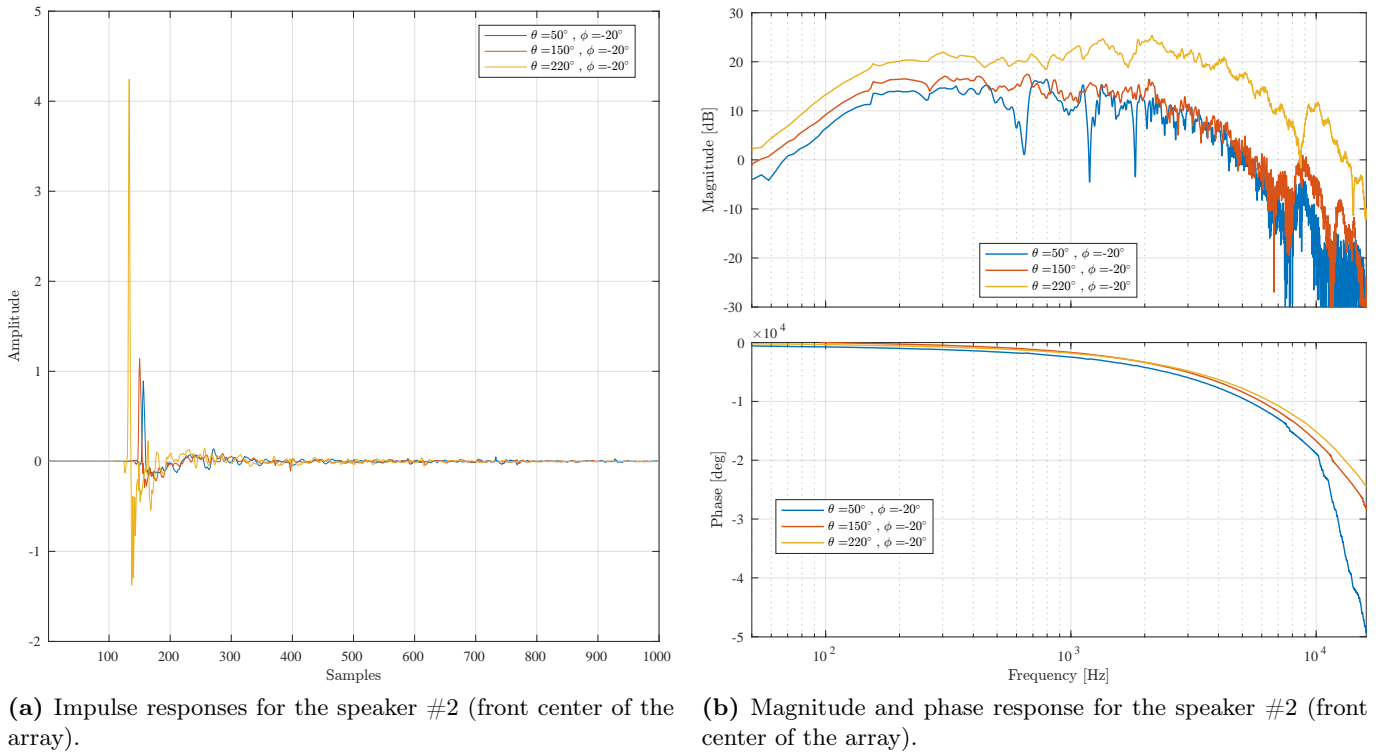


**Figure I.6:** Impulse response, Magnitude and phase response the speaker #9 (right bottom side of the array) for three different azimuth angles  $\theta = 50^\circ, 150^\circ, 220^\circ$  at the same elevation angle  $\phi = 10^\circ$ .

Figure I.4 shows the impulse responses and the respective magnitude and phase responses for the speaker #2 (front center) of the array. The responses are plotted for the same microphone ( $\phi = 10^\circ$ ) but for different azimuth angles  $\theta = 0^\circ, 60^\circ, 120^\circ$ . It is clearly seen how the difference in azimuth angles has an impact on both the amplitude/magnitude of the responses (the more the array turns from the starting position the more gets attenuated) and in the delay (the path to reach the microphone increases the more the array turns). The attenuation though is more effective at the high frequencies as shown in the magnitude response, where the directivity of the speaker as well as the shadowing effect of the array enclosure plays a decisive role.

Figure I.5 shows a different perspective of the same speaker, where the azimuth angle is fixed at a turn of  $\theta = 30^\circ$  and the responses are evaluated at three different microphones heights. As seen before, the responses show differences in amplitude/magnitude and delay/phase for different angles. Accordingly, for a fixed azimuth angle, the responses get more attenuated as the distance from the center of the speaker beam ( $\phi = 0^\circ$ ) increases.

The last Figure I.6 shows the plots for the speaker #9 (bottom speaker  $90^\circ$  to the right) of the array. The results are plotted for a fixed microphone at  $\phi = -20^\circ$  in elevation for three different azimuth angles. Once again, differences between the different measuring points are highlighted in both the impulse response (delay in samples and different amplitude) and from the magnitude and phase response (different magnitude and phase). As expected the magnitude responses deviate more as the frequency increases. Moreover, the attenuation increases as the measuring point get away from the position of the speaker, resulting in the response at  $\theta = 220^\circ$  being the highest in magnitude.

# Loudspeaker Balloon-style Directivity Plots



---

In this appendix, the balloon-style directivity plots of the loudspeaker array (20 channels) are shown both when using MLS (Section J.1) and MLS-CI (Section J.2) filters for every 1/3 octave bands from 79 Hz to 10000 Hz. The figures following plotted are presented in 3D as well as in 2D (from a topview) where their shapes define their radiation pattern and their magnitude on a linear scale. Anyway, further information on the magnitude are given by the color scale applied (dark blue to dark red), so to allow a zoom in without compromising the validity of the results.

The plots are obtained from the measurements conducted on the array in the same setup described in Appendix I. This time the array is fed with the pickup signal from the acoustic guitar measurements convolved with either the MLS or MLS-CI filters so to be played out by the loudspeaker.

Both types of filters, which have a length of 4096 taps, are applied a frequency-independent regularization factor  $\beta = 0.01$  to help at the frequencies where the matrix  $\mathbf{H}[k]$  is ill-conditioned.

However, a better description of the filters can be found in Chapter 6, while, some more information and analysis regarding the loudspeaker array and its comparison with the guitar target function (the 3D measurements of the acoustic guitar) can be found in Chapter 8.

J.1 MLS

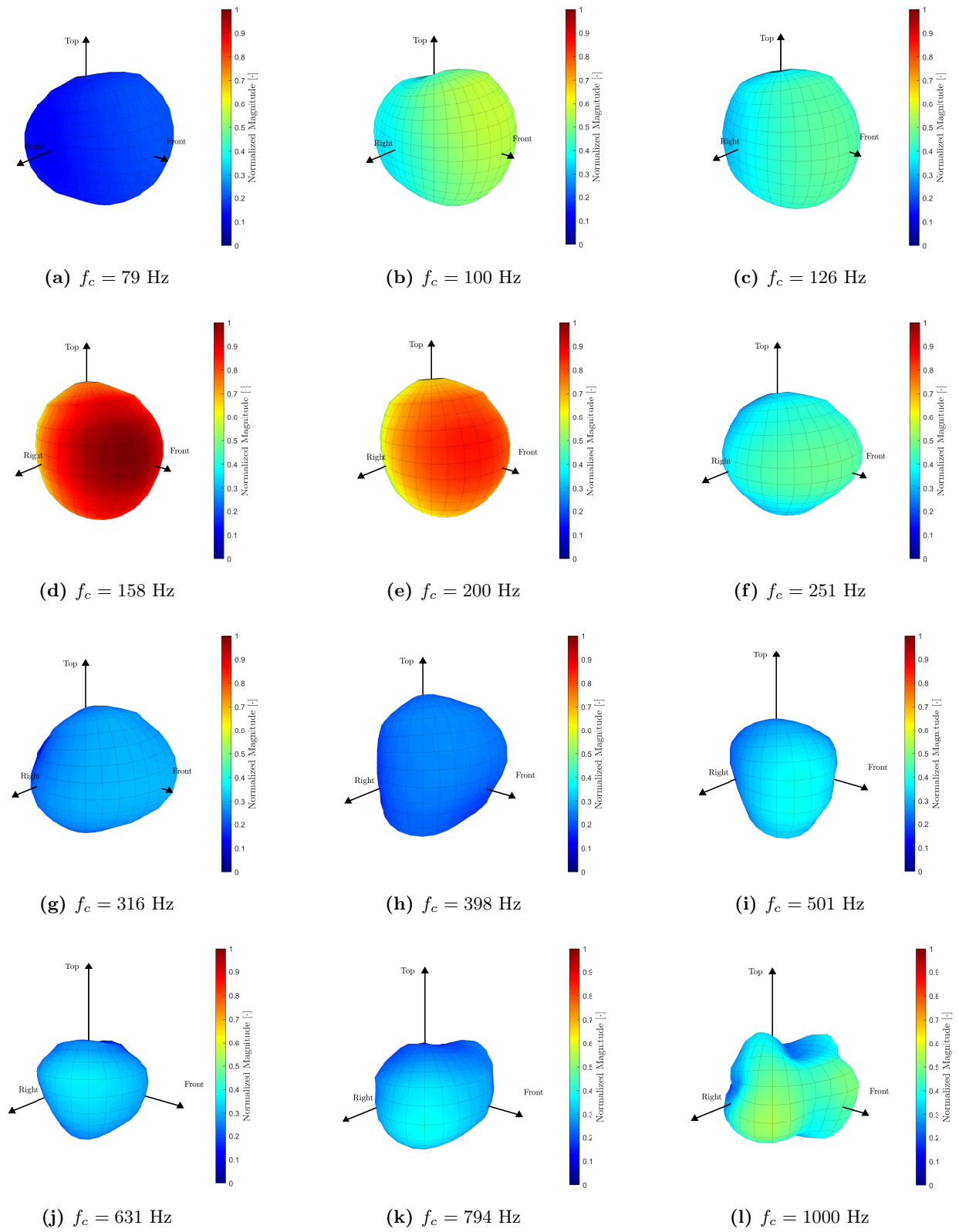


**Figure J.1:** 3D Balloon-style directivity plots (3D view) for the sound radiation of the loudspeaker array (using the MLS filters) in the 1/3 octave bands with  $10^\circ$  spatial resolution. The plots are normalized over the maximum magnitude for all 1/3 octave bands within 79 Hz to 10 kHz (Part 1)

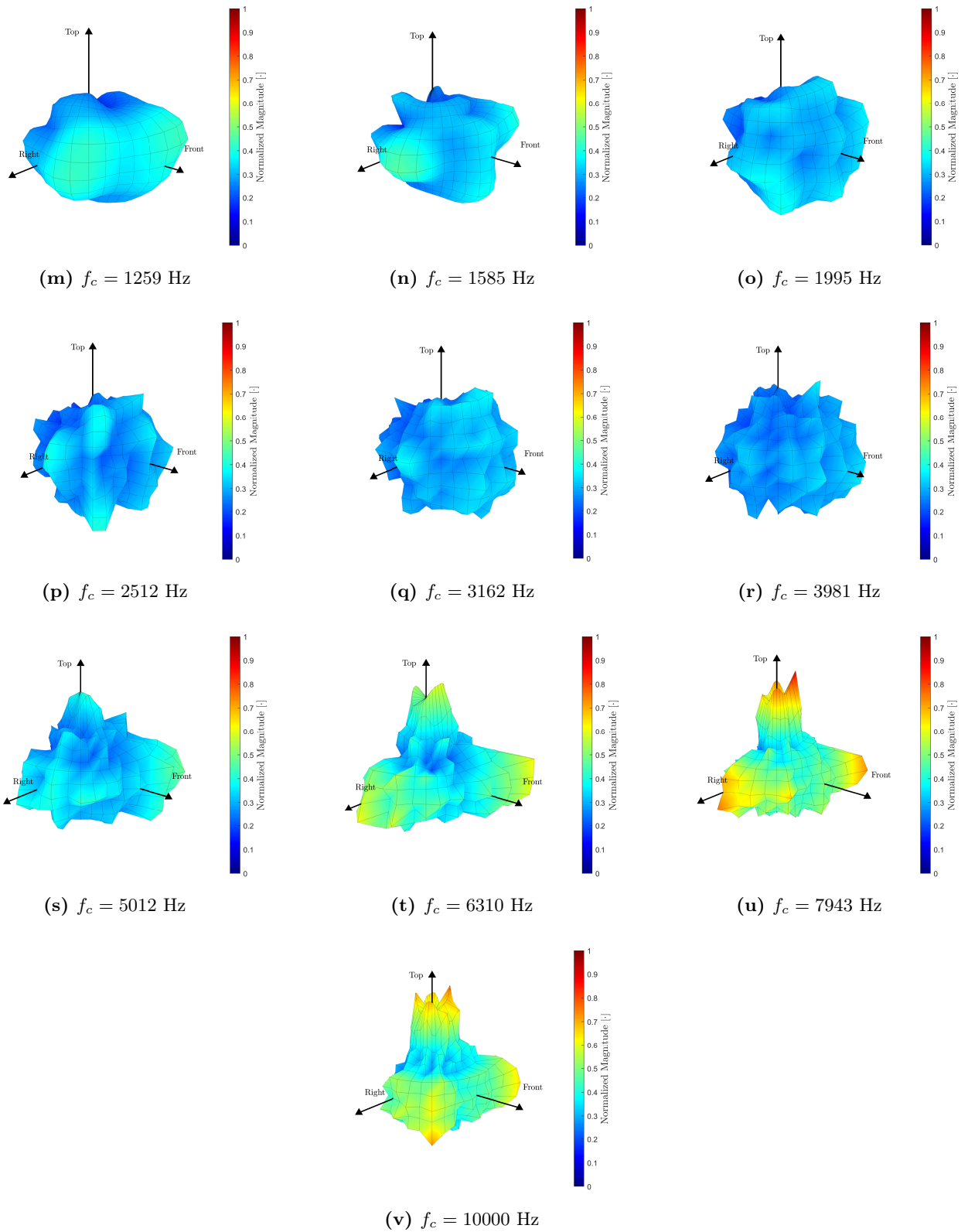


**Figure J.1:** 3D Balloon-style directivity plots (3D view) for the sound radiation of the loudspeaker array (using the MLS filters) in the 1/3 octave bands with  $10^\circ$  spatial resolution. The plots are normalized over the maximum magnitude for all 1/3 octave bands within 79 Hz to 10 kHz (Part 2)

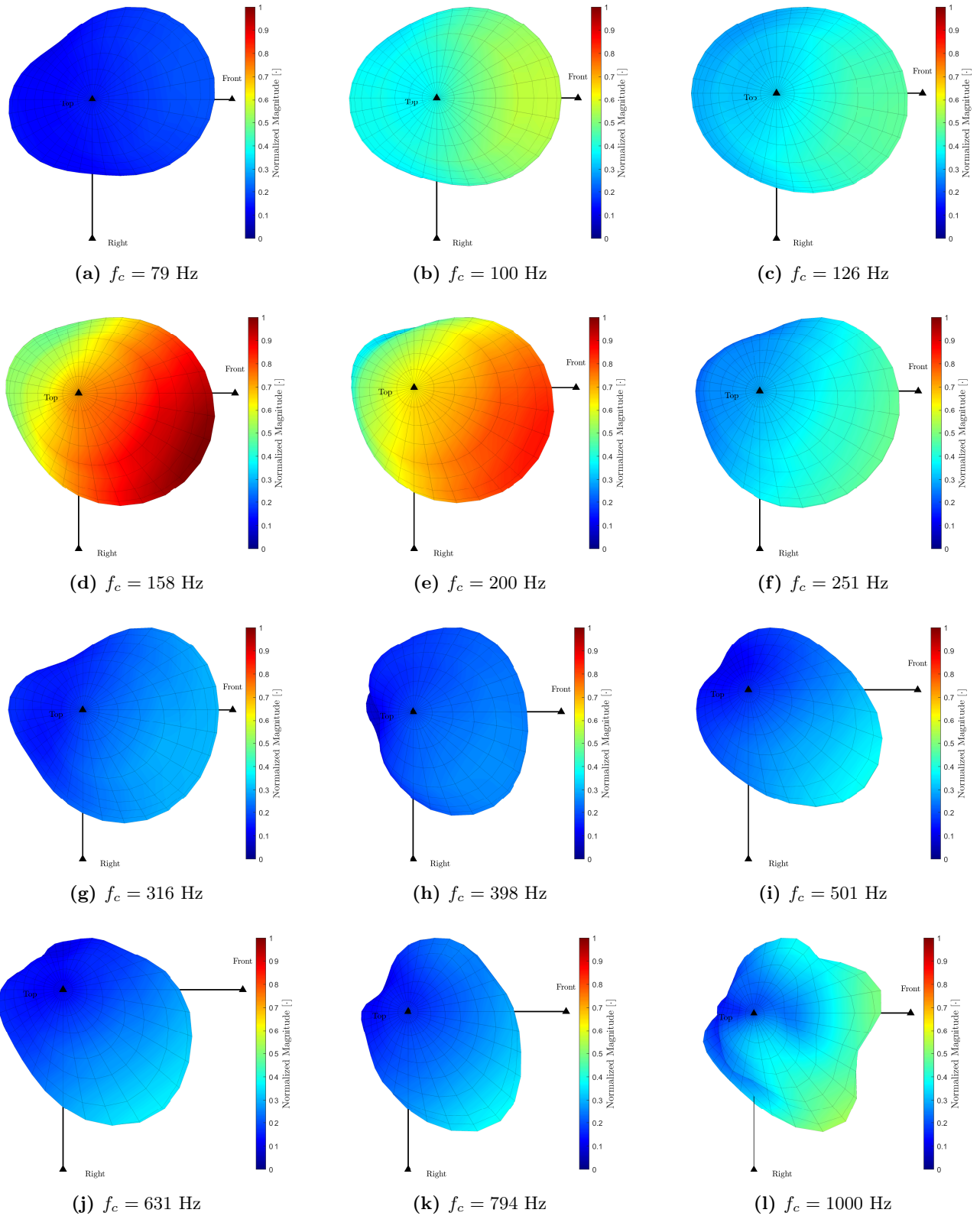


**Figure J.2:** 3D Balloon-style directivity plots (Top view) for the sound radiation of the loudspeaker array (using the MLS filters) in the 1/3 octave bands with  $10^\circ$  spatial resolution. The plots are normalized over the maximum magnitude for all 1/3 octave bands within 79 Hz to 10 kHz (Part 1)

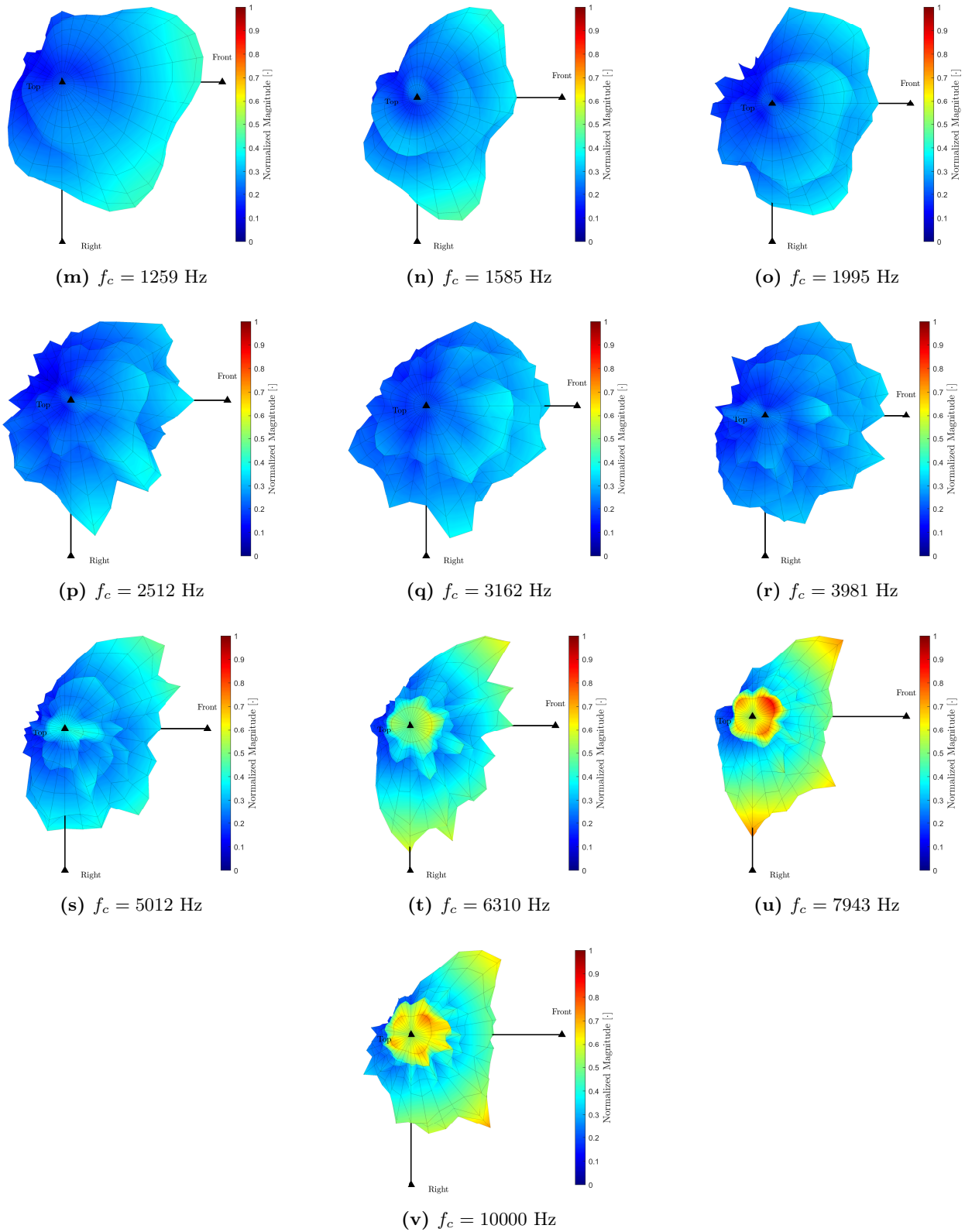


**Figure J.2:** 3D Balloon-style directivity plots (Top view) for the sound radiation of the loudspeaker array (using the MLS filters) in the 1/3 octave bands with  $10^\circ$  spatial resolution. The plots are normalized over the maximum magnitude for all 1/3 octave bands within 79 Hz to 10 kHz (Part 2)

J.2 MLS-CI

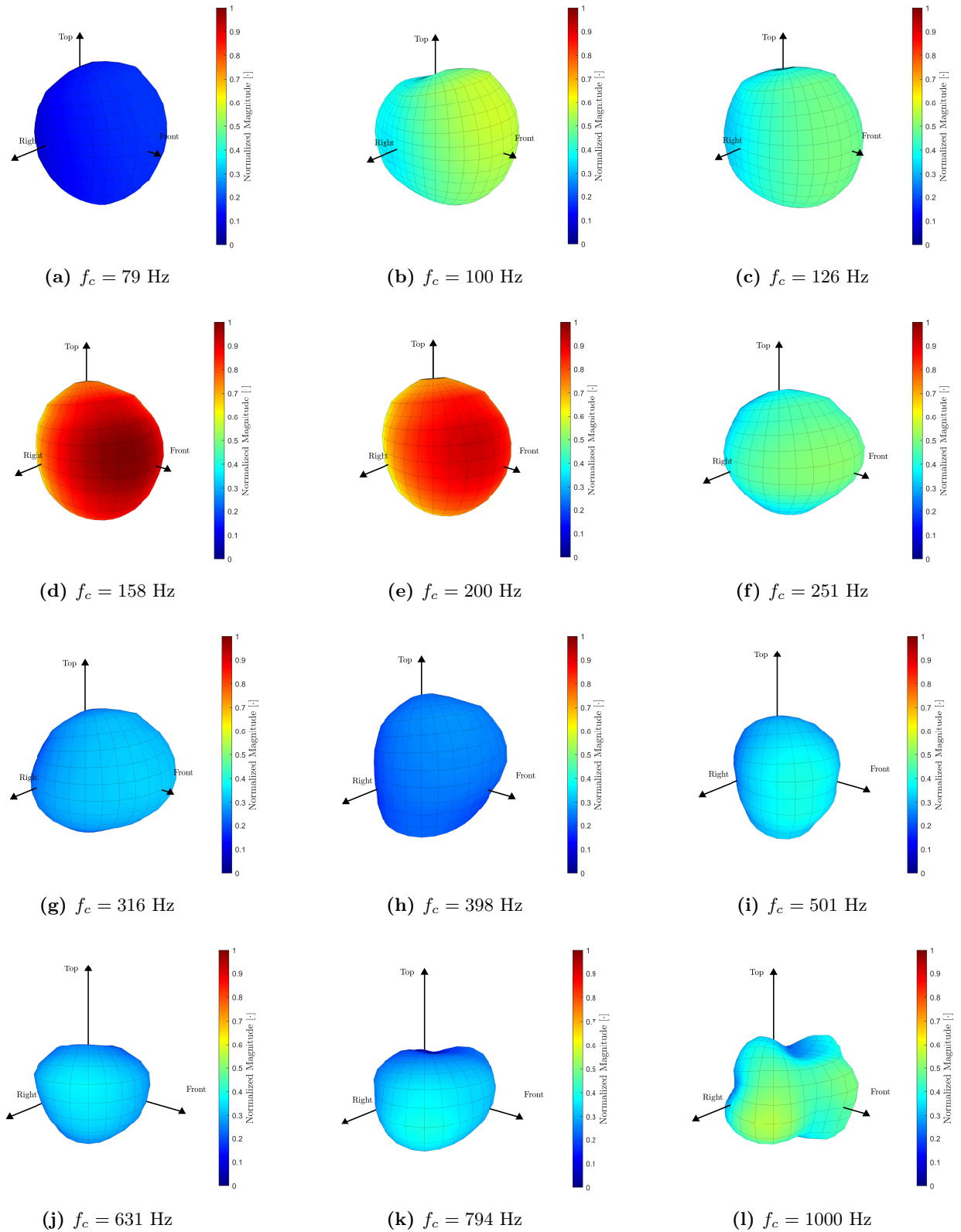


**Figure J.3:** 3D Balloon-style directivity plots (3D view) for the sound radiation of the loudspeaker array (using the MLS-CI filters) in the 1/3 octave bands with 10° spatial resolution. The plots are normalized over the maximum magnitude for all 1/3 octave bands within 79 Hz to 10 kHz (Part 1)

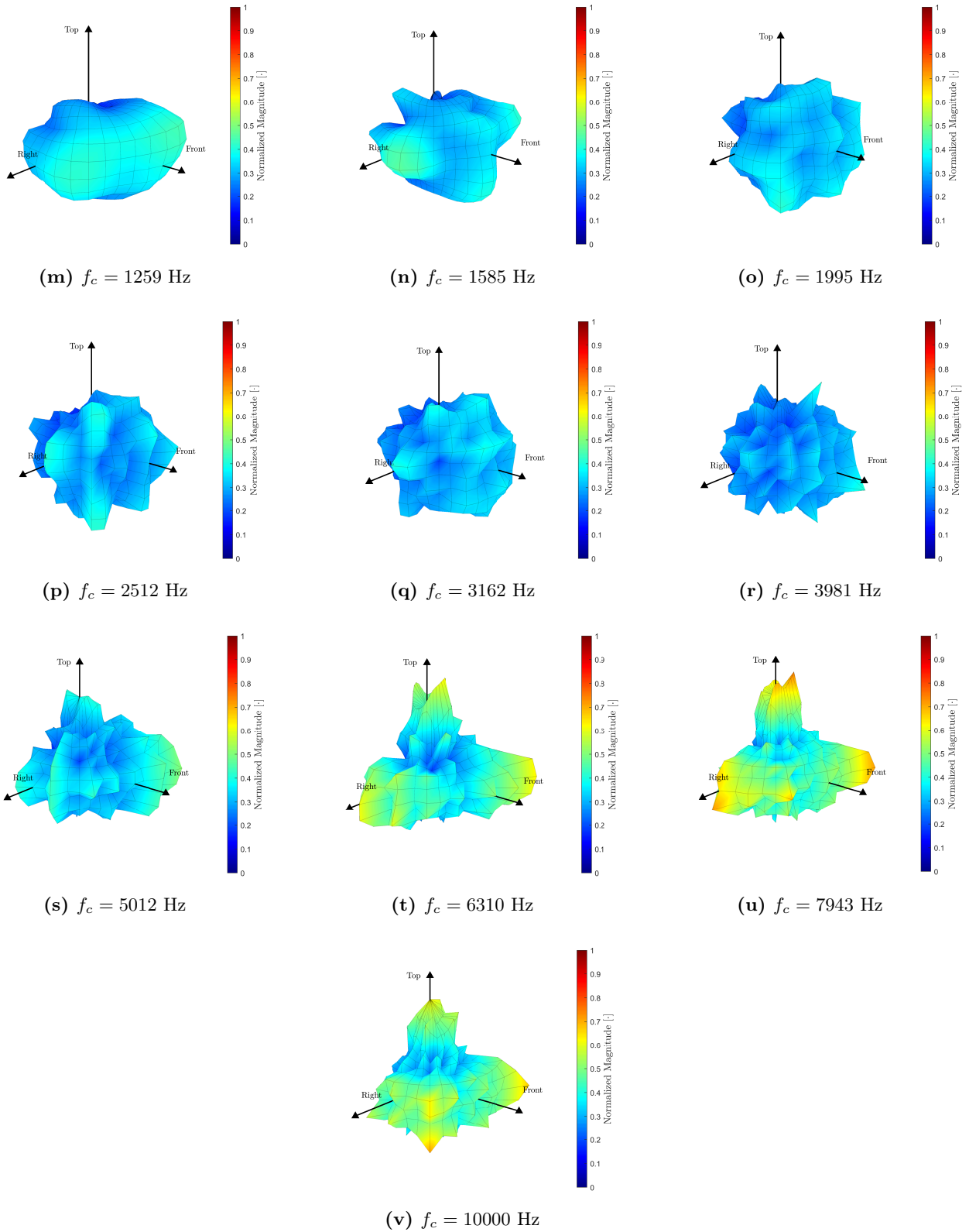


**Figure J.3:** 3D Balloon-style directivity plots (3D view) for the sound radiation of the loudspeaker array (using the MLS-CI filters) in the 1/3 octave bands with  $10^\circ$  spatial resolution. The plots are normalized over the maximum magnitude for all 1/3 octave bands within 79 Hz to 10 kHz (Part 2)

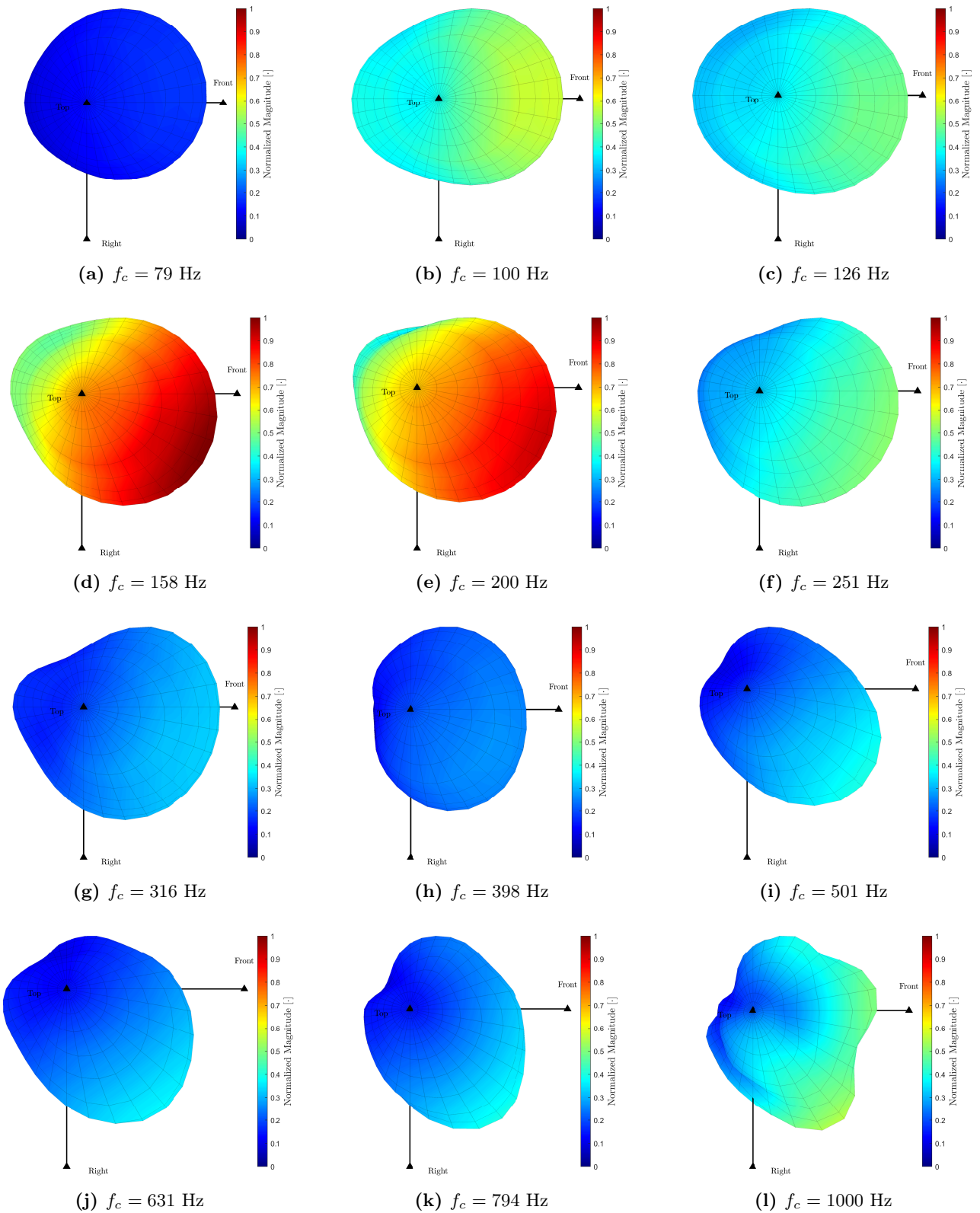


**Figure J.4:** 3D Balloon-style directivity plots (Top view) for the sound radiation of the loudspeaker array (using the MLS-CI filters) in the 1/3 octave bands with 10° spatial resolution. The plots are normalized over the maximum magnitude for all 1/3 octave bands within 79 Hz to 10 kHz (Part 1)

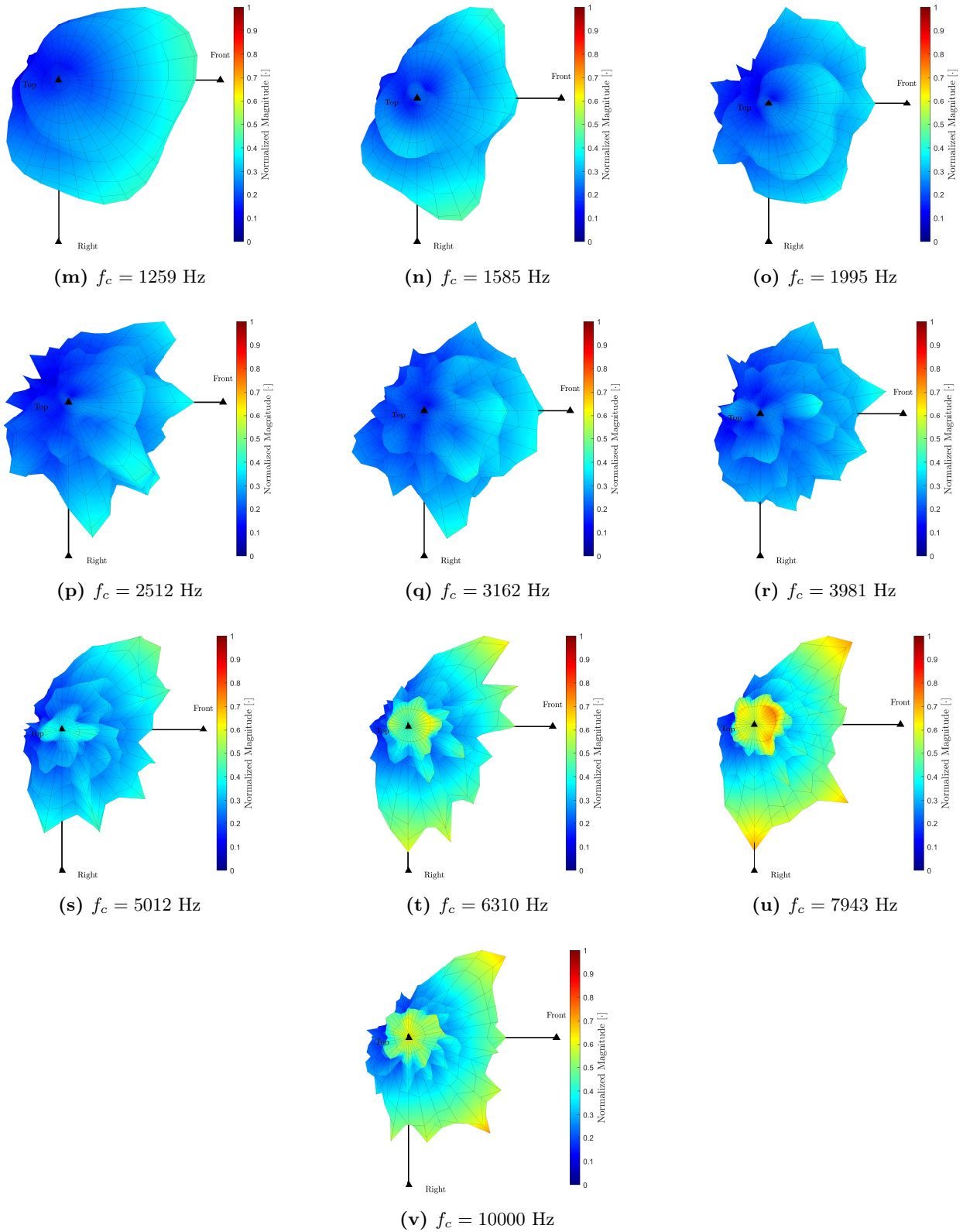


**Figure J.4:** 3D Balloon-style directivity plots (Top view) for the sound radiation of the loudspeaker array (using the MLS-CI filters) in the 1/3 octave bands with  $10^\circ$  spatial resolution. The plots are normalized over the maximum magnitude for all 1/3 octave bands within 79 Hz to 10 kHz (Part 2)